UNIVERSITÄT HAMBURG

DOKTORARBEIT

A matter of size: exploring atom-ion interactions on mesoscopic and macroscopic length scales

---

Dissertation

zur Erlangung des Doktorgrades

an der Fakultät für Mathematik, Informatik und Naturwissenschaften,

Fachbereich Physik,

der Universität Hamburg

vorgelegt von

Daniel Jordan BOSWORTH

geboren am 2. Juli 1997 in Bristol, Großbritannien.

Hamburg,

Juli 2024

Gutachter/innen der Dissertation:	Prof. Dr. Peter Schmelcher
	Prof. Dr. Henning Moritz
Zusammensetzung der Prüfungs-kommission:	Prof. Dr. Daniela Pfannkuche
	Prof. Dr. Peter Schmelcher
	Prof. Dr. Henning Moritz
	Prof. Dr. Ludwig Mathey
	Prof. Dr. Christof Weitenberg
Vorsitzende der Prüfungskommission:	Prof. Dr. Daniela Pfannkuche
Datum der Disputation:	14.11.2024
Vorsitzender Fach-Promotions-ausschusses PHYSIK:	Prof. Dr. Wolfgang J. Parak
Leiter des Fachbereichs PHYSIK:	Prof. Dr. Markus Drescher
Dekan der Fakultät MIN:	Prof. Dr. Norbert Ritter

To my grandfather, Philip Goode.

Abstract

The desire to further our understanding of complex physical phenomena and exploit quantum mechanics for useful applications has driven the development of controlled quantum systems which are well-isolated from their environment. Two of the earliest and most notable platforms are (i) trapped ultracold gases of neutral atoms and (ii) trapped ions. Due to the numerous achievements of these two platforms, interest emerged in combining both within a single setup for probing atom-ion interactions. Unlike interactions between neutral species, atom-ion interactions extend over mesoscopic length scales of hundreds of nanometres. Not only do atom-ion systems permit studies of charge-neutral chemistry - responsible among other things for the formation of water in the interstellar medium - they further provide a distinctive setup for quantum information processing and the simulation of many-body systems.

Today, many quantum information and simulation platforms make considerable use of the internal structure of single atoms. In particular, highly-excited atomic states have proved extremely useful for engineering entanglement between pairs of atoms over macroscopic distances. Within the context of atom-ion systems, the use of these so-called Rydberg atoms was initially proposed as a path to circumventing challenges in observing ultracold atom-ion collisions. More recently however, ion-Rydberg systems have proved themselves as attractive setups for observing fundamental chemical processes *in situ* due to their inherently slow vibrational dynamics on the order of microseconds.

The path to understanding and exploiting many-body phenomena often rests on intuition developed in systems with fewer numbers of particles – a notable example being the Rydberg blockade mechanism, which emerged out of the understanding of interactions between pairs of Rydberg atoms. To that end, this thesis is devoted to the study of few-body ultracold systems of atoms and ions from a theoretical perspective. We consider not only mesoscopic-scale atom-ion interactions present in the electronic ground-state, but also explore interactions between ions and Rydberg atoms, where interactions inflate to the macroscopic-scale. We present our results cumulatively in five successive scientific contributions, which can be roughly grouped into three different themes.

Our first theme examines how atom-ion interactions compete with other forces to influence a system's static properties. Here, we explore a trapped system of two ground-state bosonic atoms interacting with an ion. We characterise the energy and spatial structure of the lowest few eigenstates in different regimes of interatomic interaction and relative trapping strength of the two species.

Our second theme is quantum control. Here, we first consider the use of an externally-swept ion-like potential for deterministically driving trapped atoms between different vibrational states. In a subsequent work in collaboration with experiment, we examine the collisional dynamics of an interacting ion-Rydberg pair. We develop a semi-classical coupled-channel model to describe these collisions and explore the tunability of beyond Born-Oppenheimer physics exhibited by the colliding pair.

Our final theme concerns the formation and stability of weakly-bound triatomic Rydberg molecular ions. In one work, we reveal that a bound ion-Rydberg dimer can capture additional neutral ground-state atoms through attractive scattering with the Rydberg electron. Ion-induced mixing of different Rydberg states leads to distinctive patterns of maxima in the electronic density of the Rydberg electron, which support both linear and non-linear triatomic configurations. In our final work, we examine a system of two cations interacting with a Rydberg atom. The large repulsion between the cation pair means that such systems are generally unstable. However, we find that the ion-Rydberg interaction can stabilise the system against Coulomb explosion above a critical value of the principal quantum number. In other words, introducing additional energy to the system in the form of a Rydberg excitation can paradoxically make it more stable.

Zusammenfassung

Der Wunsch, unser Verständnis komplexer physikalischer Phänomene zu vertiefen und die Quantenmechanik für nützliche Anwendungen zu nutzen, hat die Entwicklung von kontrollierten Quantensystemen vorangetrieben, die von ihrer Umgebung gut isoliert sind. Zwei der frühesten und bemerkenswertesten Plattformen sind (i) gefangene ultrakalte Gase aus neutralen Atomen und (ii) gefangene Ionen. Aufgrund der zahlreichen Errungenschaften dieser beiden Plattformen entstand das Interesse an neuen Plattformen, die Ionen und neutrale Atome kombinieren, um deren Wechselwirkungen zu untersuchen. Im Gegensatz zu Wechselwirkungen zwischen neutralen Spezies erstrecken sich diese Wechselwirkungen über mesoskopische Längenskalen von Hunderten von Nanometern. Atom-Ion-Systeme ermöglichen nicht nur die Untersuchung der Atom-Ion-Chemie - die unter anderem für die Bildung von Wasser im interstellaren Medium verantwortlich ist -, sondern sie bieten auch eine unverwechselbare Versuchsanordnung für die Quanteninformationsverarbeitung und die Simulation von Vielteilchensystemen.

Viele Quanteninformations- und -simulationsplattformen nutzen heute in erheblichem Maße die innere Struktur einzelner Atome aus. Insbesondere hoch angeregte atomare Zustände haben sich als äußerst nützlich erwiesen, um die Verschränkung zwischen Atompaaren über makroskopische Entfernungen zu ermöglichen. Im Zusammenhang mit Atom-Ion-Systemen wurde die Verwendung dieser so genannten Rydberg-Atome ursprünglich als ein Weg zur Umgehung der Probleme bei der Beobachtung von ultrakalten Atom-Ion-Kollisionen vorgeschlagen. In jüngerer Zeit haben sich Ion-Rydberg-Systeme jedoch aufgrund ihrer inhärent langsamen Schwingungsdynamik in der Größenordnung von Mikrosekunden als attraktive Versuchsanordnung zur Beobachtung grundlegender chemischer Prozesse *in situ* erwiesen.

Wie bereits angedeutet, beruht der Weg zum Verständnis und zur Nutzung von Vielteilchenphänomenen häufig auf der Intuition, das sich in Systemen mit einer geringeren Anzahl von Teilchen, wie z.B. Paaren von Rydberg-Atomen, entwickelt hat. Aus diesem Grund widmet sich diese Arbeit der Untersuchung ultrakalter Systeme aus Atomen und Ionen mit wenigen Teilchen aus einer theoretischen Perspektive. Wir betrachten nicht nur die mesoskopischen Atom-Ion-Wechselwirkungen im elektronischen Grundzustand, sondern untersuchen auch die Wechselwirkungen zwischen Ionen und Rydberg-Atomen, wo Wechselwirkungen auf die makroskopische Skala aufblähen. Wir stellen unsere Ergebnisse in fünf aufeinanderfolgenden wissenschaftlichen Beiträgen vor, die sich grob in drei verschiedene Themen gliedern lassen.

Unser erstes Thema untersucht, wie Atom-Ion-Wechselwirkungen mit anderen Kräften konkurrieren, um die statischen Eigenschaften eines Systems zu beeinflussen. Hier untersuchen wir ein gefangenes System aus zwei bosonischen Atomen im Grundzustand, die mit einem Ion wechselwirken. Wir charakterisieren die Energie und räumliche Verteilung der niedrigsten Eigenzustände in verschiedenen Regimen der interatomaren Wechselwirkung und der relativen Fallenfrequenzen der beiden Spezies.

Unser zweites Thema ist die Quantenkontrolle. Hier betrachten wir zunächst die Verwendung eines von außen gewehten ionenähnlichen Potenzials, um gefangene Atome deterministisch zwischen verschiedenen Schwingungszuständen zu bewegen. In einer anschließenden Arbeit in Zusammenarbeit mit einem Experiment untersuchen wir die Kollisionsdynamik eines wechselwirkenden Ion-Rydberg-Paares. Wir entwickeln ein semiklassisches Modell mit gekoppelten Kanälen für die molekulare Dynamik und untersuchen die Abstimmbarkeit der Physik jenseits der Born-Oppenheimer-Näherung, die das kollidierende Paar aufweist.

Unser letztes Thema betrifft die Bildung und Stabilität von schwach gebundenen triatomischen

Rydberg-Molekülionen. In einer Arbeit zeigen wir, dass ein gebundenes Ion-Rydberg-Paar durch attraktive Streuung mit dem Rydberg-Elektron zusätzliche neutrale Grundzustandsatome einfangen kann. Die ioneninduzierte Vermischung verschiedener Rydberg-Zustände führt zu charakteristischen Mustern von Maxima in der elektronischen Dichte des Rydberg-Elektrons, die sowohl lineare als auch nicht-lineare triatomische Konfigurationen unterstützen. In unserer letzten Arbeit untersuchen wir ein System aus zwei Kationen, die mit einem Rydberg-Atom wechselwirken. Die große Abstoßung zwischen dem Kationenpaar bedeutet, dass solche Systeme im Allgemeinen instabil sind. Wir stellen jedoch fest, dass die Ion-Rydberg-Wechselwirkung das System oberhalb eines kritischen Werts der Hauptquantenzahl gegen Coulomb-Explosionen stabilisieren kann. Mit anderen Worten, wenn dem System zusätzliche Energie in Form einer Rydberg-Anregung zugeführt wird, kann es paradoxerweise stabiler werden.

Contents

List of Figures

List of Tables

List of Abbreviations

BO	Born-Oppenheimer
PEC	potential energy curve(s)
PES	potential energy surface(s)
ED	exact diagonalisation
FD	finite difference
(ML-)MCTDH(B)	(multi-layer) multi-configuration time-dependent Hartree method (for bosons)
SPF	single particle function(s)
DVR	discrete variable representation
RF	radio frequency
ULRM	Ultralong-range Rydberg molecule(s)
CG	Clebsch-Gordon

List of scientific contributions

[SC1] **D. J. Bosworth**, M. Pyzh, and P. Schmelcher, "Spectral properties of a three-body atom-ion hybrid system", Phys. Rev. A **103**, 033303 (2021).

[SC2] **D. J. Bosworth**, F. Hummel, and P. Schmelcher, "Charged ultralong-range Rydberg trimers", Phys. Rev. A **107**, 022807 (2023).

[SC3] **D. J. Bosworth**, M. Pyzh, and P. Schmelcher, "Excited-state preparation of trapped ultracold atoms via swept potentials", Phys. Rev. A **109**, 013311 (2024).

[SC4] M. Berngruber, **D. J. Bosworth**, O. A. Herrera-Sancho, V. S. V. Anasuri, N. Zuber, F. Hummel, J. Krauter, F. Meinert, R. Löw, P. Schmelcher, and T. Pfau, "In situ observation of nonpolar to strongly polar atom-ion collision dynamics", Phys. Rev. Lett. **133**, 083001 (2024).

[SC5] **D. J. Bosworth**, M. T. Eiles, and P. Schmelcher, "Metastable doubly charged Rydberg trimers", Phys. Rev. Res. **6**, 043164 (2024).

Declaration of personal contributions to [SC1–SC5]

In the works [SC1–SC3] and [SC5], I carried out the calculations, produced the results and prepared the figures and text of the manuscript. In the works that they co-authored, Maxim Pyzh and Frederic Hummel provided regular support in formulating the problems, working out which questions to ask and discussing and interpreting the results. Maxim Pyzh, Frederic Hummel, Peter Schmelcher and Matthew Eiles all provided comments on drafts of the figures and manuscripts. Peter Schmelcher provided his expert opinion and took responsibility for the instigation and long-term high-level supervision of all of my projects. Matthew Eiles provided additional high-level guidance throughout the project [SC5] and contributed significantly to the editing of the manuscript.

The work [SC4] was completed in collaboration with experimentalists at Universität Stuttgart. Moritz Berngruber, Nico Zuber, Óscar Andrey Herrera Sancho, Jennifer Krauter and Viraatt Anasuri built and maintained the experiment and took the measurements. The experiment was overseen by Robert Löw, Florian Meinert and Tilman Pfau. The theoretical calculations were primarily undertaken by myself, with assistance from Frederic Hummel in the formative stages of the project. I regularly discussed experimental and theoretical results with Moritz Berngruber, Nico Zuber, Frederic Hummel, Peter Schmelcher as well as Robert Löw, Florian Meinert and Tilman Pfau. The manuscript and figures were produced equally by Moritz Berngruber and I. All authors provided comments on the drafts of the figures and manuscript.

Outline of this thesis

Chapter 1 offers a thematic introduction to the topic of this thesis, namely few-body systems of atoms and ions. The goal of this chapter is to contextualise the scientific contributions of this thesis within a historical framework and clarify the broader motivation for the questions and problems tackled within them.

Chapters 2 and 3 build upon the discussion started in chapter 1, providing a more detailed and technical description of the research fields and physical systems explored in this thesis. Here, the goal is to introduce key theoretical concepts which support reading of the scientific contributions. In particular, chapter 2 begins with a review of the quantum mechanical description of diatomic systems, before proceeding to discuss interactions between ions and atoms in their electronic ground-state. In addition, this chapter provides a summary of the different numerical methodologies employed within the scientific contributions. In Chapter 3, we focus on Rydberg physics, beginning with a historical overview of the field leading up to the modern day and then discussing the interaction of Rydberg atoms with different species, including ground-state atoms and ions.

Reading of the scientific contributions is additionally supported by chapter 4, which provides further background information, discusses the specific motivations behind each project and summarises the major findings. The scientific contributions are then presented (in published form, where available) in chapter 5.

Chapter 6 offers a summary of this thesis and highlights the relevance of the scientific contributions for the broader atomic, molecular and optical physics community. Further, this chapter discusses perspectives for future work both directly and indirectly related to the scientific contributions of this thesis.

Finally, the appendices A, B, C and D contain additional technical details for the interested reader as well as a sample of currently unpublished results which may serve as the basis for future works.

Chapter 1

Introduction

Scientific progress over the last century has not only provided us with theoretical tools for understanding the basic building blocks of matter, such as individual atoms, ions and molecules; it has also devised techniques that enable us to study these species directly in the laboratory. This has opened up new possibilities for probing novel states of matter such as supersolids [1] and testing fundamental theories with tabletop experiments [2]. Nowadays, we are even in a position to begin exploiting the unique behaviours of quantum systems for applications such as secure satellite communication [3], compact and highly-tunable field sensing devices [4] and noisy intermediate-scale quantum computers [5].

These nascent quantum technologies require precise control over individual quantum states for which, among other things, it is necessary to suppress thermal fluctuations. Historically, the development of increasingly sophisticated cooling techniques has gone hand-in-hand with the realisation of new phenomena: from the remarkable discovery of superconductivity in cryogenically-cooled mercury in 1911 [6], to the observation of Bose-Einstein condensation (BEC) in laser- and evaporatively-cooled gases of alkali metal elements in 1995 [7–10]. The latter, also known as an ultracold quantum gas, is a prime example of a well-controlled quantum system. Ultracold quantum gases served initially as a toolbox for studying collective behaviour in regimes of weak interparticle interactions, where atomic ensembles behave as coherent matter waves [11]. Later, it became possible to explore strongly-correlated regimes by tuning the strength of interactions with Fano-Feshbach resonances [12] using external magnetic [13, 14] and optical fields [15]. Confining particles within quasi one- and two-dimensional traps offered an additional route to enhancing interparticle correlations [16–18]. Among other things, the ability to tune interparticle interactions has been used to associate ultracold molecules [19, 20] and observe novel few-body phenomena, such as Efimov trimers [21–23].

Ultracold atoms can also be loaded into lattice-like optical trapping potentials [24] with single-site resolution [25–27]. These experimental developments opened the door to a variety of prospects, including analogue quantum simulation of Hubbard models describing condensed matter phenomena [28, 29] and studies of open quantum systems [30–32]. In addition, neutral atoms in optical lattices can be used as precision optical atomic clocks [33–36].

More recently, experimentalists have developed techniques for constructing arrays of atoms with arbitrary shapes via piece-wise assembly of individual atoms in optical tweezer traps [37–40]. Meanwhile, tweezer arrays of several thousand atoms have now been reported [41]. The ability to develop arrays with increasingly greater numbers of atoms [42, 43] is a necessity for implementing effective quantum error correction [44]. These technological developments have made neutral atom arrays with Rydberg-mediated interactions attractive setups for pursuing analogue and digital quantum computing [45–47] and the simulation of spin models [48].

A further gold-standard for quantum control is exemplified by systems of cold trapped ions. For many years in fact, trapped ions were effectively the only game in town: radiofrequency trapping of ions was demonstrated [49, 50] over a decade before optical traps for neutral atoms were developed [51]. As a result of this initial advantage, many of the early breakthroughs in quantum control were achieved with trapped ions ahead of other platforms [52]. These milestones include the first demonstration of laser-cooling [53, 54] and its use for preparing trapped atoms in their vibrational ground-state [55]. The first working universal quantum gate was also developed with trapped ions [56]. Moreover, trapped ion quantum computers were amongst the earliest platforms to boast high gate fidelities [57] and have been used for quantum simulation [58–60], with applications ranging from quantum chemistry [61, 62] to high-energy physics [63]. Furthermore, record-breaking frequency standards have been established with the use of optically-driven narrow electronic transitions of single ions [36, 64, 65]

In view of the myriad successes of trapped neutral and charged atoms, it was only a matter of time before the notion took hold to integrate both species within a single hybrid system, providing a toolbox for exploring charge-neutral physics at cold temperatures [66–68]. This concept was first explored in a trilogy of works published in the early 2000s by Côté, Dalgarno, Kharchenko and Lukin [69–71]. Inspired by earlier experimental works on ultracold neutral plasmas [72] and frozen Rydberg gases [73, 74], these theoretical studies considered the collisional properties of charged impurities embedded within ultracold gases of neutral atoms. One key result revealed by Côté and co. was that the atom-ion elastic scattering and charge-exchange cross-sections remain large even at collision energies of hundreds of μK. In this regime, the elastic cross-section is more than two orders of magnitude larger than that for neutral atoms. One consequence of this strong attractive interaction is that the atom-ion binding potential supports greater numbers of rovibrational states compared to binding potentials of neutral ground-state atoms. Additionally, the most highly-excited atom-ion rovibrational states have sizes extending over hundreds of nanometres. These large, weakly-bound states were first investigated by Côté *et al.* in [71] and are referred to as mesoscopic molecular ions [75]. The authors further predicted that frequent three-body collisions should enable single ions to capture hundreds of atoms within weakly-bound states in the ultracold environment [71], forming mesoscopic charged polarons [75–78].

The long-range character of the atom-ion interaction brings with it a further consequence: unlike neutral systems, temperatures on the scale of μK or less are required in order to probe collisions in regimes of few partial-waves. Only at these temperatures will the collisional behaviour deviate significantly from semi-classical predictions [69, 79] and thereby exhibit distinctly-quantum effects, such as shape resonances. Therefore, whilst hybrid atom-ion trap setups have been available for nearly two decades [80–82], it is only in the last few years that signatures of ultracold atom-ion collisions have been observed [83–86]. Along the path toward studying these interactions in the single to few partial-wave regime, diverse experimental setups have been developed (for a comprehensive review of the experimental state-of-the-art, see [67] and [68]).

Among the various experimental approaches for realising atom-ion systems, in this thesis we are most interested in the use of Rydberg atoms. A striking example of this can be found in the work of Kleinbach *et al.* [87], who prepared an effective hybrid atom-ion system directly from an ultracold gas of ^{87}Rb atoms. This was achieved by exciting a single atom to a sufficiently high principal quantum number n state such that its valence electron orbited *outside* the spatial extent of the gas and thus, from the point of view of the remaining gas atoms, had been ionised. Subsequent works then demonstrated the creation of cold untrapped ions inside ultracold gases by photoionising Rydberg atoms just above the ionisation threshold, whereupon the ion's dynamics could be steered with controlled external fields [88] and observed using an ion microscope [89]. Further applications of Rydberg atoms to hybrid atom-ion systems include the

observation of an ion-induced Rydberg blockade mechanism [90] and the engineering of long-range atom-ion entanglement, which could remove the need for spatially-overlapping atom and ion traps and thereby avoid unwanted micromotion-induced heating of the system [91].

Whilst Rydberg atoms may serve as a tool for creating ultracold mixtures of atoms and ions, they additionally introduce the possibility of studying molecular ions on *macroscopic* length scales. In 2021, two independent works predicted that the scaling of the atom-ion interaction strength with n can give rise to weakly-bound bound states between an ion and a Rydberg atom with micrometre bond lengths [92, 93]. Unlike the kinds of molecules more familiar to us from chemistry, in this system there is no hybridisation of the electronic orbitals between the two atomic species [94]. Rather, the Rydberg electron remains localised at the Rydberg core and the charge exchange rate is vanishingly small [93]. The binding mechanism of these dimers is due to the long-range interaction between the ion and the Rydberg atom's induced dipole moment, which undergoes internal flipping at a critical internuclear separation around which the binding potential forms. Shortly after their prediction, the existence of these macroscopic ion-Rydberg dimers was confirmed in an experiment carried out by the group of Tilman Pfau at Universität Stuttgart [95].

As a result of their exaggerated properties, ion-Rydberg systems present a unique platform for exploring fundamental chemical processes [SC4, 96]. This is because their inherently slow vibrational dynamics allows the relative separations of ion-Rydberg pairs to be measured in real time using an ion microscope [89]. This opens the door to *in situ* observations of molecular dynamics without the need for ultrafast pulses and strong alignment fields [97, 98].

Combining the above ideas from the fields of ultracold atomic gases, trapped ions and Rydberg physics, this thesis explores the static properties and dynamical behaviours of few-body charge-neutral systems dominated by interactions spanning mesoscopic and macroscopic length scales. We aim to understand how the charge-neutral interaction competes with other forces in these systems and what influence this has on their electronic and vibrational structure, leading for example to the emergence of exotic molecular bound states. Furthermore, we explore dynamical effects which arise due to the action of of an external driving potential or the breakdown of the Born-Oppenheimer approximation in order to understand how these may be exploited for quantum state transfer and tunable molecular dynamics.

Chapter 2

Theoretical framework for few-body atom-ion systems

This chapter provides an introduction to the quantum-mechanical description of few-body atomic systems as well as numerical methods which can be used for solving the associated time-independent and time-dependent Schrödinger equations. We begin in section 2.1 by introducing a Hamiltonian describing a general diatomic system. Section 2.2 then discusses strategies for making the solution of this Hamiltonian more tractable through use of the Born-Oppenheimer (BO) approximation, a divide-and-conquer approach for solving the electronic and nuclear problems in a piecewise manner. Although it is a powerful tool for theoretical descriptions of molecular systems, the BO approximation is not always valid and a discussion of the conditions under which it breaks down is provided. Next, continuing within the framework of the BO approximation, in section 2.3 we turn to the problem of solving for the vibrational and rotational degrees of freedom of the nuclear Hamiltonian. Thereafter, since this thesis is chiefly focused on charge-neutral systems, section 2.4 provides an overview of interatomic interactions between a charged atom and a neutral atom which are in, or close to, their electronic ground-state for different regimes of internuclear separation. Finally, in section 2.5 we present an overview of the numerical methods employed throughout this thesis for determining the electronic and vibrational structure of various systems within the BO approximation as well as describing wavepacket dynamics.

2.1 Diatomic molecules

Let us begin by considering a system of two atoms described by the wavefunction $\psi = \psi(\mathbf{r}, \mathbf{R})$, where $\mathbf{r}$ and $\mathbf{R}$ describe the electronic and nuclear degrees of freedom, respectively. Due to the sheer number of electrons an atom can posses, seemingly inoffensive diatomic systems such as this are, in reality, many-body systems. The eigenstates $\Psi = \Psi(\mathbf{r}, \mathbf{R})$ of the system with energy E satisfy the time-independent Schrödinger equation $\hat{H}\Psi = E\Psi$ [99]. Expressing the Hamiltonian in the system's centre-of-mass (CM) frame, we find that the Hamiltonian describing the translation of the CM coordinate $\hat{H}_{\mathrm{CM}}$ decouples from the rest of the system, such that the problem reduces to solving of the remaining Hamiltonian describing the relative coordinates $\hat{H}_{\mathrm{rel}}$ in a molecule-fixed frame [94]:

$$\hat{H}_{\mathrm{rel}} = \hat{T}_n + \hat{T}_e + \hat{V}. \tag{2.1}$$

The terms denote the kinetic energy operators for the nuclei and electrons as well as the interactions between the particles in the system, respectively. Since $\hat{V}$ is composed of pairwise central forces [1], it

---

[1]In other words, $\hat{V}$ depends only on the relative separations of pairs of interacting particles.

is independent of the choice of reference frame. In contrast, the kinetic energy operators $\hat{T}_n$ and $\hat{T}_e$ are frame-dependent.

We now employ spherical coordinates and choose our coordinate frame such that the internuclear separation is orientated along $\hat{z}$, for which the internuclear separation vector is $\mathbf{R} = (R, 0, 0)$ and the nuclear kinetic energy operator reduces to $\hat{T}_n = -\nabla_R^2/2\mu$, where ∇_R^2 is the Laplace operator in spherical coordinates. Note that unless otherwise stated, atomic units of $m_e = 1$, $\hbar = 1$, $e = 1$, $c = 1$ will be assumed throughout this thesis.

In view of the considerable mass difference between electrons and their parent nuclei, the nuclear kinetic energy $\hat{T}_n$ is typically far smaller than that of the electrons $\hat{T}_e$. As a result, we may consider the Hamiltonian (2.1) as being composed of a zeroth-order Hamiltonian describing the electronic degrees of freedom with a fixed configuration of the nuclei $\hat{H}_e = \hat{T}_e + \hat{V}$, which is subject to a perturbation by the nuclear dynamics given by $\hat{T}_n$. The Schrödinger equation for the electronic Hamiltonian is:

$$(\hat{T}_e + \hat{V})\phi_k(\mathbf{r}; R) = \varepsilon_k(R)\,\phi_k(\mathbf{r}; R), \tag{2.2}$$

where $\phi_k(\mathbf{r}; R)$ describes the kth electronic state with energy $\varepsilon_k(R)$ for a given configuration of the nuclei R. Solutions to (2.2) are generally obtained by diagonalising the electronic matrix Hamiltonian [2] represented in a basis of the electronic states of the non-interacting atoms $\{\varphi_n\}$:

$$\phi_k(\mathbf{r}; R) = \sum_n c_n^{(k)}(R)\varphi_n(\mathbf{r}). \tag{2.3}$$

The states $\phi_k(\mathbf{r}; R)$ constitute a complete orthonormal basis, which we use to build our ansatz for the wavefunction of the full Hamiltonian (2.1):

$$\Psi(\mathbf{r}, R) = \sum_\alpha \chi_\alpha(R)\phi_\alpha(\mathbf{r}; R). \tag{2.4}$$

Here, $\chi_\alpha(R)$ are complex expansion coefficients which depend only on the nuclear configuration – in this case indicated solely by the separation between the nuclei, R. By substituting the ansatz (2.4) into the time-independent Schrödinger equation, then pre-multiplying by $\phi_\beta^*(\mathbf{r}; R)$ and finally integrating over $\mathbf{r}$, we arrive at the following set of coupled differential equations:

$$\left[\hat{T}_n + \varepsilon_\beta(R) - E\right]\chi_\beta(R) = \frac{1}{2\mu}\sum_\alpha \Lambda_{\beta\alpha}\,\chi_\alpha(R), \tag{2.5}$$

where μ is the reduced mass of the diatomic system. Note that this system of equations is further coupled to (2.2) through the R-dependent electronic eigenvalues $\varepsilon_\beta(R)$. The terms $\Lambda_{\beta\alpha}$ are coupling elements of the electronic states ϕ_β and ϕ_α due to the motion of the nuclei:

$$\Lambda_{\beta\alpha} = \langle\phi_\beta|\nabla_R^2|\phi_\alpha\rangle + 2\langle\phi_\beta|\nabla_R|\phi_\alpha\rangle\nabla_R. \tag{2.6}$$

The first and second terms in (2.6) are referred to as *scalar* and *derivative* non-adiabatic couplings, respectively.

---

[2]The matrix elements of the electronic Hamiltonian are denoted by $\langle\varphi_i|\hat{H}_e|\varphi_j\rangle = \int d\mathbf{r}\varphi_i(\mathbf{r}; R)\hat{H}_e\varphi_j(\mathbf{r}; R)$.

2.2 The Born-Oppenheimer approximation

Solving the complete set of coupled equations (2.5) is computationally expensive. Instead, we may first solve the problem in absence of the non-adiabatic coupling terms. Choosing $\Lambda_{\beta\alpha} = 0$, the coupled system of equations reduces down to only two equations:

$$(\hat{T}_e + \hat{V})\phi_\beta(\mathbf{r}; R) = \varepsilon_\beta(R)\,\phi_\beta(\mathbf{r}; R), \tag{2.7a}$$

$$\left[\hat{T}_n + \varepsilon_\beta(R)\right]\chi_\beta(R) = E\chi_\beta(R). \tag{2.7b}$$

The ansatz (2.4) is now given by $\Psi = \chi(R)\,\phi(\mathbf{r}; R)$, where $\chi(R)$ represents the wavefunction of the nuclei and $\phi(\mathbf{r}; R)$ represents the wavefunction of the electrons, which take the internuclear separation R as a parameter. The above simplification is referred to as the Born-Oppenheimer (BO) approximation [100] and treats the electronic and nuclear motion as being decoupled. Under this approximation, the R-dependent eigenvalues of the electronic Hamiltonian (2.7a) represent a potential term in the nuclear Hamiltonian (2.7b). $\varepsilon_\beta(R)$ is hence referred to as a *potential energy curve* (PEC). If the eigenvalues instead depend on more than a single nuclear coordinate, such as in a triatomic system, we speak of a *potential energy surface* (PES).

Non-adiabatic corrections beyond the BO approximation are typically small due to the considerable difference in mass between nuclei and electrons. Nonetheless, under certain conditions it can become necessary to account for them. As a first step beyond the BO approximation, the Born-Huang (BH) approximation [101–103] additionally includes the diagonal non-adiabatic coupling terms $\Lambda_{\beta\beta}$ in equation (2.5), which when finite are strictly greater than zero. Ultimately though, like the BO approximation, the BH approximation remains a *single-channel* description of the system, in which the nuclear wavepacket is confined to a single PEC or PES.

If off-diagonal non-adiabatic couplings become significant, we can no longer speak of distinct electronic and nuclear states anymore since the nuclear motion couples to different PEC or PES. We require thus a *multi-channel* description. Transitions of the nuclear wavepacket between channels, also known as non-adiabatic transitions, are radiationless and can occur on extremely short time scales, especially at conical intersections between PES where the avoided crossing gap vanishes and non-adiabatic couplings become singular [104–106]. Conical intersections are ubiquitous in nature, playing in a role in diverse processes from charge transfer to reactions supporting photosynthesis and the photostability of DNA [107].

Non-adiabatic couplings may also be significant at avoided crossings between nearly-degenerate PEC. Avoided crossings occur more frequently in excited states where the density of states is generally higher than it is close to the ground-state. As a rule of thumb however, the effect of non-adiabatic couplings will only be significant at avoided crossings which have a gap size comparable to the kinetic energy of the nuclear wavepacket. In such cases, the wavepacket is described with the multi-channel formalism of equation (2.5) whose solution is generally cumbersome.

To avoid the burden of solving the full coupled-channel problem described above, we can instead arrive at an approximate solution by treating the dynamics of the nuclear wavepacket as occurring on a single channel $\varepsilon_i(R)$ when it is far from the avoided crossing, whilst including a probability for it to transition to a neighbouring coupled channel $\varepsilon_j(R)$ when it is sufficiently close to the avoided crossing. The semi-classical Landau-Zener (LZ) formula [108] gives the probability P_{ij} of a wavepacket to transition, or "hop", between the channels $\varepsilon_i(R)$ and $\varepsilon_j(R)$ at their avoided crossing:

$$P_{ij} = \exp\left(\frac{-2\pi\Delta^2}{\dot{R}\,\alpha}\right). \tag{2.8}$$

The probability of a non-adiabatic transition depends on the gap Δ and gradient α parameters of the uncoupled (diabatic) PEC, which are fitted from the adiabatic PEC. In addition, the probability depends on the speed of the wavepacket $\dot{R}$ at the crossing point R_{cross} of the diabatic curves. Δ is defined as the energy gap between $\varepsilon_i(R)$ and diabatic curves at R_{cross}. α is similarly given by the absolute value of the difference in the gradient of the diabatic PEC at R_{cross}.

In general, non-adiabatic couplings serve as a funnel between electronic states and provide an additional mechanism for decay of excited molecular states. In [SC4], we consider non-adiabatic transitions occurring in collisions between an ion and a Rydberg atom and employ the LZ formula (2.8) to develop a stochastic model of the wavepacket's dynamics along the many coupled PEC of the system.

2.3 Rotation and vibration of diatomic molecules

In the previous sections, we considered two atomic nuclei whose separation vector had a fixed orientation along the $\hat{z}$ axis. However, unless cooled to its rovibrational ground-state, a molecular system will undergo vibrations and rotations such that we must specify the internuclear separation in vector form $\mathbf{R} = (R, \Theta, \Phi)$, assuming once again a spherical coordinate system. As we saw in section 2.2, under the BO approximation the nuclear Hamiltonian for a diatomic molecule in the CM frame is given by:

$$\left[-\frac{1}{2\mu}\nabla^2 + V(\mathbf{R}) \right]\chi_n(\mathbf{R}) = E\chi_n(\mathbf{R}). \tag{2.9}$$

A standard approach in solving the above is to use the separable rovibrational ansatz $\chi(R, \Theta, \Phi) = \frac{U(R)}{R}Y(\Theta, \Phi)$, where $U(R)$ is the component of the wavefunction describing the radial coordinate and $Y(\Theta, \Phi)$ is a spherical harmonic. Inserting this ansatz into (2.9) and noting that ∇^2 is the Laplace operator in spherical coordinates, we arrive at separate equations for the radial and angular degrees of freedom:

$$\frac{1}{2\mu}\frac{d^2U}{dR^2} + \left[E - V_j(R) - \frac{J(J+1)}{2\mu R^2} \right]U = 0, \tag{2.10a}$$

$$\frac{1}{\sin\Theta}\frac{\partial}{\partial\Theta}\left(\sin\Theta\frac{\partial Y}{\partial\Theta} \right) + \frac{1}{\sin^2\Theta}\frac{\partial^2 Y}{\partial\Phi^2} + J(J+1)Y = 0. \tag{2.10b}$$

Equation (2.10a) is equivalent to a single particle of mass μ moving in 1D with coordinate R subject to an effective potential $V_{\text{eff}} = V_j(R) + J(J+1)/2\mu R^2$ created from the combination of the PEC $V_j(R)$ of the jth electronic state and the centrifugal potential $J(J+1)/2\mu R^2$, depending on the total angular momentum J of the system. The eigenvalues of (2.10a) represent the different vibrational states of the molecule, whilst the solutions to (2.10b) yield the rotational spectrum. Taking $J = 0$, equation (2.10a) reduces to the form we had previously in equation (2.7b) for a non-rotating molecule.

2.4 Atom-ion interactions close to the electronic ground-state

After discussing the general theoretical treatment of diatomic systems in the sections above, in this section we consider a specific diatomic system of an atom and an ion close to their electronic ground-state. We assume the BO approximation throughout and neglect rotations $J = 0$, such that the problem reduces the solving the vibrational Hamiltonian (2.10a):

$$\frac{1}{2\mu}\frac{d^2U}{dR^2} + \left[E - V_j(R) \right]U = 0. \tag{2.11}$$

At this point, we are interested in determining the form of the atom-ion interaction potential given by $V_j(R)$. To develop some initial understanding about the functional form of $V_j(R)$ in the asymptotic limit, we can use some basic ideas from classical electrodynamics. The ion's electric field $\mathbf{E} = \hat{\mathbf{R}}/R^2$ polarises the neighbouring atom's charge distribution, such that it acquires a finite dipole moment $\mathbf{d} = \alpha\mathbf{E}$, where α is the polarisability of the neutral atom. The energy of the atom's induced dipole in the ion's field is then given by [109]:

$$V(R) = -\mathbf{d} \cdot \mathbf{E} = -\alpha/R^4. \tag{2.12}$$

Hence, we see that at large internuclear separations the atom-ion interaction is (i) species-dependent (ii) attractive and (iii) decays to the fourth-power of the internuclear separation [3].

Over what range of R is this interaction significant? To answer this, we compare the energy scale of the asymptotic interaction $|V(R)| = \alpha/R^4$ to that of the pair's kinetic energy $|T_n| = 1/2\mu R^2$, which is the only other relevant energy scale appearing in the Hamiltonian (2.11). Doing so, we arrive at a characteristic interaction range $R_4 = \sqrt{2\alpha\mu}$ and energy scale $E_4 = 1/2\mu R_4{}^2$. For the alkali metals, these typically take values of $R_4 \sim 100$ nm and $E_4 \sim \mu$K [111, cf. table 1.1]. To put this into perspective, the asymptotic interaction between neutral alkali metal atoms decays as $1/R^6$ and has characteristic length and energy scales of $R_6 \sim 1$ nm and $E_6 \sim 10$ mK, respectively [111, cf. table 1.1].

The above comparison highlights two important features of the atom-ion interaction. Firstly, it is a *long-range* interaction: it extends over a range of R roughly two orders of magnitude larger than the van der Waals' interaction between neutral atoms. Secondly, it indicates that atom-ion collisions need to be over *four orders of magnitude colder* than neutral atom collisions in order to enter a scattering regime where few partial waves contribute and quantum effects, such as shape resonances, become prominent.

For collisions with energy far greater than E_4, the centrifugal barrier term in equation (2.10a) smears out contributions from individual partial waves and prohibits collisions from probing the short-range limit of the atom-ion interaction potential $V_j(R)$. In this regime therefore, atom-ion collisions are dominated by the long-range part of the interaction and can be modelled accurately using semi-classical approximations [69, 112]. The strict requirements imposed by the μK energy scale of short-range atom-ion interactions is the reason that observing atom-ion collisions in the ultracold regime constitutes such an experimental challenge, as described in chapter 1. In contrast, gases of neutral atoms are routinely prepared at temperatures of $10 - 100$ μK, which is well below the energy scale E_6 of the van der Waals' interaction. Here, collisions of neutral atoms can be described using the *s*-wave scattering length as the sole scattering parameter.

Over the last five years however, experiments are now beginning to observe signatures of ultracold atom-ion collisions [83–85]. These experimental developments bring with them a demand for more accurate models of atom-ion PEC beyond semi-classical results. However, the description of interactions at short-range is hampered by the presence of electron-electron correlations, which can no longer be conveniently neglected as can be done for large internuclear separations.

Accounting for such correlations is non-trivial and computationally expensive. Determining accurate PEC at small internuclear separations requires the use of sophisticated *ab initio* methods which directly solve the full many-body Schrödinger equation without further approximation and account for electron correlations through approaches such as the Hartree-Fock formalism [113]. A couple of the most well-known approaches are the coupled cluster and configuration interaction methods [114].

---

[3]A similar classical argument may be used for the case of two interacting neutral atoms [94, 110], whereby an instantaneous dipole moment appearing in one of the atoms polarises the other atom, giving rise to a mutual interaction of the form $V = -\alpha_1\alpha_2/R^6$, where α_i are the atomic polarisabilities.

Another approach is to use quantum defect theory [115] to describe atom-ion interactions at short-range [116–118]. Here, the scattering problem is partitioned into a short-range region and a long-range region. At sufficiently small R, where the form of the interaction potential is unknown, the kinetic energy of the colliding pair is negligible compared to the interaction energy. Thus, the short-range region sets an energy-independent boundary condition for the solution in the asymptotic region, where the interaction potential is known and scattering solutions are analytically available. To obtain the full solution, the handful of energy-independent scattering parameters in the short-range region need to be determined experimentally.

In the interest of reducing the numerical overhead and employing the interaction in models of few- to many-body systems, it is convenient to instead fit a numerically-tractable model potential to the more accurate PEC obtained from *ab initio* or quantum defect methods. We now briefly introduce one such model potential which was originally proposed in [119] for studying a single ion immersed in a cloud of ultracold atoms and which we have subsequently employed in [SC1, SC3]. The model potential assumes that collisions occur within a single channel, meaning that it considers only a single PEC and thus neglects the possibility for processes such as spin-changing collisions. The model potential takes the form:

$$V(R) = a \exp(-bR^2) - \frac{1}{R^4 + 1/c}. \tag{2.13}$$

Where a, b and c are model parameters. For $R \to \infty$, we see that this gives the correct $-1/R^4$ dependence of the interaction. Equally, we see that the parameter c regularises the potential by suppressing the divergence of the $1/R^4$ term as $R \to 0$. Thus, the potential is well-defined for all values of R. In addition, the model parameters a and b control the shape of the short-range repulsive barrier in equation (2.13) and can be mapped to a wide range of possible quantum defect parameters such that it reproduces the exact scattering solutions [119].

Inserting (2.13) into the vibrational Hamiltonian (2.11), we find bound-state solutions $E < 0$, whose exact number depends on the choice of model parameters. Typically, we select the parameters such that only two weakly-bound states are present. We can safely neglect deeper bound-states of the potential since it has been shown that rates of spontaneous capture into the shallowest bound-states via three-body recombination are the most significant [71]. Three-body recombination has been further studied for atom-ion systems in the following works [120–124].

2.5   Numerical methods

This final section provides an overview of the main numerical approaches used throughout the scientific contributions of this thesis [SC1–SC5]. In these works, we concerned ourselves with few-body systems of particles and sought to determine either time-independent quantities, such as PEC and vibrational spectra, or model the time-evolution of a wavepacket subject to a potential. For the former, we relied on methods such as exact diagonalisation and finite difference, which will be discussed in sections 2.5.1 and 2.5.2. For the latter, we employed the multi-configuration time-dependent Hartree method (MCTDH) and its multi-layer extension for bosonic species ML-MCTDHB which are the subject of section 2.5.3.

2.5.1   Exact diagonalisation

Exact diagonalisation (ED) refers to methods for determining the eigenstates and energy eigenvalues of a Hamiltonian by rewriting the Hamilton function in matrix form and then subsequently diagonalising

it, often numerically. Given a system described by the time-independent Schrödinger equation $\hat{H}\ket{\Psi_n} = E_n\ket{\Psi_n}$, we represent the eigenstates of our Hamiltonian in some known orthonormal basis $\ket{\Psi_n} = \sum_\alpha c_\alpha \ket{\phi_\alpha}$, where the complex coefficients c_α and real eigenvalues E_n are to be determined.

We now reformulate the Schrödinger equation as a matrix eigenvalue problem using the finite set of basis states $\{\ket{\phi_\alpha}\}$. First, we premultiply the Schrödinger equation with the state $\bra{\phi_\beta}$, giving: $\bra{\phi_\beta}\hat{H}\ket{\Psi_n} = \bra{\phi_\beta}E_n\ket{\Psi_n}$. Inserting the expansion for $\ket{\Psi_n}$ yields the result:

$$\sum_\alpha c_\alpha \bra{\phi_\beta}\hat{H}\ket{\phi_\alpha} = E_n c_\beta. \tag{2.14}$$

For each value of β, we have a corresponding equation with the form of (2.14), comprising a system of linear equations. Combining these altogether, we can write these in terms of a single matrix equation:

$$\underline{\underline{H}}\mathbf{c}_n = E_n\mathbf{c}_n. \tag{2.15}$$

Here, $\underline{\underline{H}}$ is the matrix Hamiltonian with elements $\bra{\phi_\alpha}\hat{H}\ket{\phi_\beta}$, $\mathbf{c}_n$ is a column eigenvector whose elements are the complex coefficients $\{c_i\}$ and E_n is the corresponding eigenvalue.

Given a finite-sized basis of N basis states, the first task of our ED routine is to build the $N \times N$ matrix Hamiltonian by evaluating the integrals $\bra{\phi_\beta}\hat{H}\ket{\phi_\alpha}$ for the matrix elements. However, since the Hamiltonian is hermitian, not all matrix elements are unique. The next step is to diagonalise the matrix to obtain solutions to the eigenproblem, which can be accomplished with the help of standard linear algebra packages such as `numpy.linalg` for Python [125], which employs functions from the LAPACK software library [126].

The choice of basis has a strong influence on the efficiency of the ED approach. Where possible, knowledge gained from related problems or physical intuition about the system should be used to choose a basis appropriate to the problem at hand. This will help minimise the overall number of basis states required and ensure that values of the obtained results (e.g. eigenvalues) converge quickly to a final value with increasing basis size. For example, to diagonalise a Hamiltonian of the form $\hat{H}' = \hat{H}_0 + \hat{V}$, a natural choice of basis would be the eigenstates of the unperturbed Hamiltonian $\hat{H}_0$ when the interaction term $\hat{V}$ is neglected.

ED has been used in several of the scientific contributions of this thesis, in particular for the Rydberg systems studied in [SC2, SC4, SC5]. ED is well-suited to such systems because the atomic states of a single Rydberg atom are separable into radial and angular components and many of their integrals admit analytical solutions. In particular, most integrals involving the angular degrees of freedom are analytically-solvable [127], as are several integrals involving the radial components of non quantum-defect states in alkali metals [128].

2.5.2 Finite-difference

Finite difference (FD) approaches are used for solving differential equations. Here, the functions and their derivatives appearing in a differential equation are approximated on a discrete grid describing each independent variable, e.g. a spatial grid. The grid's dimensionality is determined by the number of independent variables. The approximated form of the differential equation can then be written as a system of linear equations, which can be combined into a single matrix and then diagonlised to obtain solutions for the eigenvectors and eigenvalues as was the case in ED. Unlike ED however, FD does not require a choice of basis or the evaluation of integrals in constructing the matrix Hamiltonian. However,

sufficient grid points must be used in order to accurately represent the differential equation. This can make the diagonalisation inefficient, especially for large and multi-dimensional grids.

In what follows, we provide a basic overview of the idea of FD and present an example relevant to the works of this thesis. The core idea of FD is that, assuming a sufficiently fine-spacing between grid points, exact differentials may be discretised as, for example:

$$\frac{\partial f(x)}{\partial x}\bigg|_{x=x_i} \approx \frac{f(x_{i+1}) - f(x_{i-1})}{x_{i+1} - x_{i-1}}. \tag{2.16}$$

This particular representation is known as *central finite difference.* However, different definitions for the first derivate exist and these may be generalised to higher-order derivatves, as well as multivariate functions. A detailed review can be found here [129].

Let us now consider the vibrational Hamiltonian for a non-rotating diatomic molecule (2.10a):

$$\frac{1}{2\mu}\frac{d^2 U}{dR^2} + \big[E - V_j(R)\big]U = 0. \tag{2.17}$$

The second-order derivative appearing in (2.17) can be approximated using a central finite different representation as follows:

$$\frac{d^2 U}{dR^2}\bigg|_{R=R_i} \approx \frac{U(R_{i+1}) - 2U(R_i) + U(R_{i-1})}{h^2}, \tag{2.18}$$

where h is the spacing of the discrete R-grid with N grid points. By inserting equation (2.18) into (2.17), the Schrödinger equation reduces to:

$$\frac{1}{2\mu h^2}[U(R_{i+1}) - 2U(R_i) + U(R_{i-1})] + [E - V_j(R_i)]U(R_i) = 0, \tag{2.19}$$

which amounts to a system of N linear equations. Similar to the ED method described in section 2.5.1, these linear equations can be formulated as an $N \times N$ matrix eigenvalue problem $\underline{H}\mathbf{U} = E\mathbf{U}$, where $\underline{H}$ is a sparse tri-diagonal matrix and $\mathbf{U}$ is a vector of length N whose elements correspond to the amplitude of the eigenvector $U(R)$ with energy E at each grid point. By diagonalising the matrix Hamiltonian $\underline{H}$, we obtain solutions to the time-independent Schrödginer equation.

The accuracy of finite difference representations like (2.16) and (2.18) can be increased by using a large number of grid points. Convergence of the energy eigenvalues should be ensured with respect to the number of grid points N and additionally one should be mindful of the boundary conditions assumed at the edges of the grid.

Notably, in this thesis we used the FD approach to solve a second-order differential equation with three independent variables. This was done in order to determine the vibrational states of an $^{87}\text{Rb}_3^{2+}$ trimer molecule [SC5]. The finite difference representation of the corresponding three-body vibrational Hamiltonian is given in appendix D.

2.5.3   Wavepacket propagation with tensor network methods

Tree tensor networks provide a convenient mathematical representations of wavefunctions and are widely used throughout quantum physics [130]. Various tensor-based algorithms have been developed, most notably the density matrix renormalization group (DMRG) [131, 132], which emerged in the early 1990s and has been used extensively for treating one-dimensional lattice problems [133–135]. Around the

same time as the arrival of DMRG, another algorithm known as the multi-configuration time-dependent Hartree method (MCTDH) was developed in the field of quantum chemistry [136–138] for propagating nuclear wavepackets on high-dimensional and coupled PES. Whilst thorough introductions to the algorithm can be found in [139] and [140], we provide here an overview of the MCTDH wavefunction ansatz and discuss its key advantages compared to other methods.

Given a molecular system with distinguishable nuclear degrees of freedom x_1, x_2 and x_3, the wavefunction describing the nuclei is written in MCTDH as follows:

$$\Psi(x_1, x_2, x_3, t) = \sum_{i=1}^{n_1} \sum_{j=1}^{n_2} \sum_{k=1}^{n_3} A_{ijk}(t)\, \psi_i^{(1)}(x_1, t)\, \psi_j^{(2)}(x_2, t)\, \psi_k^{(3)}(x_3, t). \tag{2.20}$$

Here, $A_{ijk}(t)$ describes a 3-tensor whose components are time-dependent coefficients of the top-layer and $\{\psi_i^{(m)}\}_{i=1}^{n_m}$ are the set of n_m basis states describing the mth degree of freedom. These basis states are also known as single particle functions (SPF). The salient advantage of the MCTDH ansatz is that both the complex A-coefficients as well as the basis states are time-dependent. Thus, in contrast to other approaches which used truncated *time-independent* bases, the MCTDH basis itself evolves dynamically in order to optimally span the active region of the Hilbert space at each instance of time. The time-dependent SPF are themselves expanded in terms of a time-independent discrete variable representation (DVR) basis [139]:

$$\psi_i^{(m)}(x_m, t) = \sum_{j=1}^{\mathcal{M}_m} C_{ij}^{(m)}(t)\, \chi_j^{(m)}(x_m). \tag{2.21}$$

$C_{ij}^{(m)}(t)$ are time-dependent bottom-layer coefficients. The DVR functions $\chi_j^{(m)}$ are orthonormal and define a finite grid of $\mathcal{M}_m$ points for the mth degree of freedom.

The proportion of the full Hilbert space spanned by the MCTDH ansatz can be controlled through changing the number of SPF and DVR functions in (2.20) and (2.21). In this way, the ansatz can be tailored in order to treat the problem as efficiently as possible. For example, if x_1 is only weakly correlated with the remaining two degrees of freedom, fewer x_1 configurations will be required and hence computational cost can be reduced by lowering the number of SPF for that degree of freedom.

The time evolution of the ansatz (2.20) subject to the Hamiltonian $\hat{H}$ is determined in the MCTDH algorithm by solving the equations of motion for the expansion coefficients $A_{ijk}(t)$ and $C_{ij}^{(m)}(t)$. The equations of motion are derived from the Dirac-Frenkel variational principle [139]:

$$\langle \delta \psi | \left(i\partial_t - \hat{H} \right) | \psi \rangle = 0. \tag{2.22}$$

In addition to solving time-dependent problems, MCTDH can also propagate the ansatz (2.20) in imaginary time, such that the wavefunction converges to the ground-state of the Hamiltonian for sufficiently long propagation times. This method is known as *relaxation* [141, 142]. Beyond this, the *improved relaxation* algorithm [142–146] allows MCTDH to access excited eigenstates. Here, in order to ensure that the wavefunction eventually converges to the nth eigenstate of the Hamiltonian times, there must be a finite overlap between the initial wavefunction at $t = 0$ and the target eigenstate. The improved relaxation algorithm performs phases of imaginary time relaxation, in-between which it updates the values of the top-layer coefficients $A_{ijk}(t)$ with the components of the nth eigenstate of the top-layer Hamiltonian. If applied to find an eigenstate which is degenerate with another, the algorithm will yield a superposition of the two eigenstates.

MCTDH has distinguished itself as a powerful method for simulating dynamics of distinguishable

degrees of freedom describing the wavepacket dynamics of molecules [147, 148]. Furthermore, MCTDH has proved useful for simulating strongly-correlated few-body systems with indistinguishable degrees of freedom, such as bosonic atoms in ultracold quantum gases [149–152].

To efficiently treat systems with increased numbers of degrees of freedom and stronger correlations, such as many-body interacting systems, MCTDH has been extended in several ways. One approach has been to represent the Hilbert space more efficiently by grouping together SPF for degrees of freedom which exhibit strong correlations. These groups of correlated SPF now form the nodes of a new, higher layer in the tensor network. The total number of configurations in the MCTDH ansatz can now be reduced by using as few configurations as possible in this higher layer. Such approaches are known as multi-layer MCTDH (ML-MCTDH) [153, 154].

ML-MCTDH is effective at describing wavefunctions of systems which can be partitioned into sub-systems with strong intra-subsystem correlations and weak inter-subsystem correlations. Bath-impurity type problems, such as polaron models, are particularly amenable to mutli-layering approaches [155–159]. However, subsystem partitioning is applicable in a much wider variety of physical systems. For example, the weak correlation between different-sized vortices appearing in turbulent flows has been exploited by similar tensor network methods for efficient computational fluid dynamics simulations [160].

MCTDH has also been extended to account for quantum statistics in order to more efficiently describe systems of indistinguishable bosonic and fermionic degrees of freedom, known as MCTDHB [161, 162] and MCTDHF [163, 164], respectively. In such approaches, the wavefunction is expanded in terms of symmetrised time-dependent number state configurations $|\mathbf{n}, t\rangle$, in which $\mathbf{n} = (n_1, n_2, \ldots, n_m)$ gives the occupation of each of the n_m time-dependent basis function within a single configuration. Using wave-function symmetrisation in conjunction with multi-layering is a powerful approach and implementations have been developed over the years for ML-MCTDH for bosons (ML-MCTDHB) [165, 166] as well as mixtures of bosons and fermions (ML-MCTDHX) [167]. ML-MCTDHX is an incredibly versatile tool and has been used to explore a plethora of physical systems, including dynamics of particles in colliding wells [168], nonequilibrium dynamics of strongly-correlated bosonic mixtures in double-wells [169, 170] and optical lattices [171, 172], spontaneous symmetry-breaking in ultracold Fermi gases [173], quench dynamics of ULRM in external fields [174] as well as stationary and dynamical properties of hybrid atom-ion systems [75, 119, 175, 176]. More recently, an extension for ML-MCTHDX for treating lattice systems has been developed, opening the door to studies of many-body spin systems [177].

To give an example of how the multi-layering approach works in conjunction with symmetrisation, consider a mixture of two bosonic species of particles α and β. First, the total wavefunction is expanded in a basis of species wavefunctions

$$|\Psi(t)\rangle = \sum_{i=1}^{n_\alpha} \sum_{j=1}^{n_\beta} A_{ij}^1(t) \, |\phi_i^\alpha(t)\rangle \, |\phi_j^\beta(t)\rangle \,. \tag{2.23}$$

This forms the top-layer of the MCTDH tensor tree. The species wavefunctions are then further expanded in terms of time-dependent number states $|\mathbf{n}\rangle_t^\sigma$

$$|\phi_i^\sigma(t)\rangle = \sum_{\mathbf{n}|N_\sigma} A_{i;\mathbf{n}}^{2;\sigma}(t) \, |\mathbf{n}, t\rangle^\sigma \,. \tag{2.24}$$

The use of number states is important in order to impose the correct quantum statistics of the wavefunction. The number states $|\mathbf{n}\rangle^\sigma = (n_1, \ldots, n_{m_\sigma})$ are comprised of $m_\sigma \in \mathbb{N}$ time-dependent SPF $\{|\psi_i^\sigma(t)\rangle\}_{i=1}^{m_\sigma}$. (2.24) only includes number state configurations $\mathbf{n}|N_\sigma$ which respect the particle number conservation

$\sum_{i=1}^{m_\sigma} n_i = N_\sigma$. As we saw already for the case of MCTDH, the SPF $|\psi_i^\sigma(t)\rangle$ are further written in terms of time-independent DVR functions (2.21) and the time-evolution of the coefficients on each layer is determined from the Dirac-Frenkel variational principle (2.22).

In this thesis, methods from the MCTDH family have been used for determining the low-energy spectrum of few-body atom-ion mixtures [SC1], solving for the vibrational states of Rydberg trimer molecules [SC2] and simulating dynamics of trapped bosons subject to driven potentials [SC3].

Chapter 3

Rydberg atoms and their interactions

In the previous chapter, we discussed interaction potentials between atoms close to their electronic ground-state, in particular for atom-ion pairs. In this chapter, we turn our attention to interactions involving highly-excited atoms, also known as Rydberg atoms. We begin with an overview of the broader field of Rydberg physics, whose goal is to explore and exploit the exaggerated properties of highly-excited atoms across a wide range of contexts spanning few-body quantum chemistry [178, 179], condensed-matter physics [180–182], field sensing [183], non-linear quantum optics [184] and quantum information [185, 186]. In section 3.1, we give a short account of the major developments within the field over the last century leading up to the study of ultralong-range Rydberg molecules, a class of exotic macroscopic-sized molecule first predicted at beginning of the 2000s, whose origins however date back to experiments undertaken almost a century ago. Then in section 3.2, we provide a detailed discussion of the interaction potentials of Rydberg atoms with different atomic species. In particular, we will focus on interactions with (i) other Rydberg atoms (ii) ground-state atoms and (iii) ions. Among other things, we will highlight the zoo of possible long-range molecular states which arise due to these interactions.

3.1 Rydberg atoms

Rydberg atoms are atoms with one or more electrons occupying states close to the dissociation threshold of the Coulomb potential [1]. Rydberg atoms distinguish themselves from their less-excited counterparts through their exaggerated properties, such as the extent of the outermost electron's orbit which scales as n^2, where n is the principal quantum number. Some of the largest Rydberg atoms created in the lab were excited to $n \sim 300$ [187], where the Rydberg electron's orbit achieves proportions of 10 μm – a size which is comparable to the width of a human hair!

Quite surprisingly perhaps, Rydberg atoms have appeared frequently in several seminal works of the late nineteenth and early twentieth centuries related to the fields of spectroscopy, quantum mechanics and scattering theory. Indeed, their name is taken from Swedish physicist Johannes Rydberg, who in the late 1800s extended prior models for the spectrum of hydrogen by deriving an empirical formula for the spectra of alkali atoms [188]. Later, Niels Bohr provided a physical foundation for Rydberg's formula in his atomic model [189], whereby spectral lines are interpreted as transitions between quantised electron orbits. Ultimately, Bohr's theory was superseded by the theory of quantum mechanics developed in the 1920s by Heisenberg, Born, Schrödinger, Jordan, Dirac and co. At this point, new versions of Rydberg's original formula appeared, derived by Pauli [190] and Schrödinger [191] in quick succession of

---

[1]"Close" is generally taken to mean states with $n \geq 10$.

one another. In its modern form, Rydberg's formula for the spectra of alkali metal elements is:

$$\varepsilon_{n,l} = -\frac{1}{2[n - \delta_l(n)]^2},$$ (3.1)

which relates the energy of the valence electron to the quantum numbers n, l and a small number of so-called quantum defect parameters $\delta_l(n)$ which account for modifications to the pure Coulomb potential experienced by the valence electron due to the presence of the core-shell electrons close to the nucleus [192] [2].

The earliest studies of Rydberg spectra were performed in hot gases with broadband sources of light, which severely restricted the ability to resolve high-n states due to the increasingly narrow spacing between neighbouring states [3]. Despite these limitations, spectroscopic measurements made in the 1930s for Rydberg atoms immersed within buffer gases of neutral atoms revealed a strikingly inexplicable result: the spectra showed not only the expected red-shifts, but additional unexpected blue-shifts [193–196]. The cause of this confusion was the mistaken assumption that any lineshifts should stem solely from the attractive long-range interaction between the Rydberg electron and buffer gas atoms. The true mechanism behind the lineshifts was found by Enrico Fermi, who demonstrated that low-energy electron-atom scattering could give rise to both red- and blue-shifts depending on the sign of the scattering length [197]. By introducing concepts such as scattering length and zero-range pseudopotentials, Fermi's ideas gave birth to the field of scattering theory.

Until the 1970s, the only reliable source for observing high-n spectral transitions was through radioastronomical observations [198, 199], which recorded radiative transitions of Rydberg atoms present in interstellar space. Things changed dramatically however with the arrival of tunable high-frequency lasers with narrow linewidths [200] and techniques for field ionising excited atoms, which for the first time enabled precision Rydberg spectroscopy [201–203] over a broad range of n values. This newfound ease of exciting high-n states in the lab, coupled with the large electric dipole moments of Rydberg atoms, opened the door to studies of light-matter interaction in the strong-coupling regime, giving rise to the field of cavity quantum electrodynamics [204]. This led to remarkable experimental achievements ranging from the creation of Rydberg masers [205] to non-destructive single-photon detection [206].

The 1990s witnessed the advent of ultracold quantum gases [11] and with that the creation of so-called frozen Rydberg gases [73, 74] in which the interaction energy between pairs of Rydberg atoms exceeds their kinetic energy to become the dominant energy scale in the system. In such regimes, two-body collision processes are suppressed and many-body effects dominate energy transfer processes in the system. Around the same time, Coulomb crystals formed by ions were also studied [207, 208]. However unlike the Coulomb interaction, the interaction strength of a pair of neutral atoms is strongly-dependent on the atoms' internal states. Therefore, the interactions can be controlled by driving atoms between low- and high-n states using lasers.

This ability to deterministically switch interatomic interactions "on" and "off" lay at the heart of landmark proposals in the early 2000s for performing quantum gate operations [209] and generating controlled collective excitations in atomic ensembles by means of a Rydberg excitation blockade mechanism [210]. These works set the stage for the field of neutral atom quantum computing [45–47, 185, 211], which at the time of writing boasts the largest quantum computers in terms of numbers of qubits [41–43]. The inherent tunability of Rydberg interactions has further played an important role in many other

---

[2] In the absence of core-shell electrons, $\delta_l(n) = 0$ for all n and l and equation (3.1) reduces to the energy spectrum of hydrogen. In this regard, Rydberg states of alkali atoms are in principle hydrogenic, differing only in the minor energy shifts of electronic states which have significant probability density close to the nucleus.

[3] From Rydberg's formula (3.1), we find that the spacing of neighbouring states should decreases as n^{-3}.

areas of physics, including nonlinear quantum optics [184, 212], the formation of ultralong-range bound Rydberg macrodimers [179, 213–220] and studying many-body correlations and ordered phases emerging in long-range interacting spin systems [221–229].

A further pioneering work of the early 2000s was the prediction of ultralong-range weakly-bound states between Rydberg atoms and neutral ground-state atoms [230]. In this work, Greene *et al.* made use of the pseudopotential developed by Fermi in the 1930s [197] to determine PEC of a Rydberg atom interacting with a single ground-state atom. They found that attractive scattering between the Rydberg electron and the ground-state atom leads to the formation of shallow potentials wells which at ultracold temperatures may support bound states [231–234]. The bond length is determined by the extent of the electron charge density and hence can quickly become macroscopic for sufficiently large n. As a result, these states were dubbed ultralong-range Rydberg molecules (ULRM).

Depending on the angular momentum character of the electronic state forming the binding potential, ULRM can have considerable permanent electric dipole moments on the order of $\sim 10^3 \, ea_0$ – despite the system being homonuclear. ULRM have been observed in ultracold quantum gases [231, 234, 235] and experimental works have further revealed that ULRM lifetimes are significantly shorter than the atomic lifetime of the parent Rydberg state [236], existing typically only for tens of microseconds. Their rapid decay is triggered through collisions with background gas atoms or via autoionisation processes initiated by the tunnelling of the molecular wavepacket to smaller internuclear separations.

Experimental and theoretical research into ULRM is now well into its third decade and the field has expanded along several different lines of enquiry. For example, more complex molecular arrangements have been studied where Rydberg atoms bind multiple ground-state atoms, forming polyatomic ULRM [237–243] as well as bound states with polar diatomic molecules [244–247]. Pushing the number of ground-state atoms to the many-body limit, one may study polaron physics [248–250] and explore solid-state phenomena in so-called Rydberg composites [182, 251], where systems of Rydberg atoms interacting with ordered arrangements of ground-state atoms have been shown to exhibit properties such as Anderson localisation [252] and symmetry-protected edge states [253]. Furthermore, ULRM have been employed experimentally for probing interatomic correlations in ultracold Bose and Fermi gases [254] and for precise spectroscopy of negative-ion resonances [255, 256], which may lead to the formation of bound ion pairs [257]. In recent years, interest has grown in using ULRM to explore physics beyond the BO approximation [103, 258–260]. In the work [258], Hummel and co. demonstrated that the synthetic dimension offered by the Rydberg atom's internal structure can be used to explore different regimes of non-adiabatic couplings between PEC and even engineer conical intersections in diatomic systems.

3.2 Interatomic interactions involving Rydberg atoms

This section focuses on Rydberg interactions between different atomic species. Section 3.2.1 will cover interactions between pairs of Rydberg atoms and discuss Rydberg-Rydberg bound states, known as macrodimers. Section 3.2.2 then provides further information on the formation of ULRM between Rydberg atoms and ground-state atoms beyond what was covered in the section 3.1. Finally, in section 3.2.3 we turn to interaction of Rydberg atoms with ions, which is one of the major focus points of the scientific works comprising this thesis. We will discuss the interaction potentials, ion-Rydberg bound states and give an overview of relevant works on the subject from recent years.

3.2.1   Rydberg – Rydberg interactions

Assuming the BO approximation, the electronic Hamiltonian describing a pair of interacting Rydberg atoms is given by:

$$\hat{H}_e = \hat{H}_0^{(1)} + \hat{H}_0^{(2)} + \hat{V}, \tag{3.2}$$

where $\hat{H}_0^{(i)}$ is the Hamiltonian describing the ith Rydberg electron in the orbit of its parent nucleus, with energy levels $\epsilon_\nu^{(i)}$ given by the Rydberg formula (3.1) and atomic wavefunctions $\phi_\nu^{(i)}(\mathbf{r}_i)$. $\hat{V}$ describes the interaction between the two Rydberg atoms. We consider the internuclear separation to be larger than the Le Roy radius [261], such that there is vanishing overlap between the atomic charge distributions. In this limit, electron-electron correlations can be safely neglected and it is sufficient to only include electrostatic interaction terms:

$$\hat{V} = \frac{1}{|\mathbf{R}|} + \frac{1}{|\mathbf{r}_1 - \mathbf{r}_2 - \mathbf{R}|} - \frac{1}{|\mathbf{r}_1 - \mathbf{R}|} - \frac{1}{|\mathbf{r}_2 + \mathbf{R}|}. \tag{3.3}$$

$\mathbf{R}$ is the separation between the nuclei and $\mathbf{r}_i$ defines the displacement of the ith Rydberg electron relative to its parent nucleus. The first and second terms describe the mutual repulsion between the two positively-charged Rydberg cores and the two negatively-charged Rydberg electrons, respectively. The third and fourth terms describe attractive interactions between each Rydberg electron and the core of the neighbouring atom. Since we are in the regime $|\mathbf{r}_i| \ll |\mathbf{R}|$, one may expand the last three terms in equation (3.3) in terms of multipoles [262–264], leading to the net result:

$$\hat{V} = \sum_{\lambda_1, \lambda_2 = 1}^{\infty} \frac{\hat{V}_{\lambda_1, \lambda_2}}{R^{\lambda_1 + \lambda_2 + 1}}. \tag{3.4}$$

Here, for convenience we have chosen the internuclear axis $\hat{\mathbf{R}}$ to be parallel with the z-axis. Explicit definitions of the multipole terms in equation (3.4) are given in appendix A.

Before discussing numerical solutions to (3.2), we first consider the leading-order term of the multipole expansion (3.4). Explicitly, this takes the form of:

$$\hat{V}^{(1,1)} \propto -\frac{r_1 r_2}{R^3}, \tag{3.5}$$

which represents an interaction between a pair of permanent dipoles. However, for two identical Rb atoms in non-polar states, for example the pair state $|35S_{1/2}35S_{1/2}\rangle$, the leading-order energy correction is given in perturbtation theory by (3.5) to second-order. Given that the extent of the Rydberg electron's orbit scales as n^2 and the spacing among neighbouring Rydberg states scales as n^{-3}, the second-order energy correction to the pair state is found to be $\epsilon \propto -n^{11}/R^6$. The rapid n-scaling of the interaction term is precisely why Rydberg atoms can be used to facilitate long- and ultralong-range interactions between atoms which, in their electronic ground-state, would be non-interacting.

We now discuss numerical solutions to the electronic Hamiltonian (3.2). For this, we employ an ansatz which is a linear combination of unperturbed Rydberg pair states $|\psi(\mathbf{r}_1, \mathbf{r}_2)\rangle = \sum_{ij} \alpha_{ij} |\phi_i^{(1)}(\mathbf{r}_1)\phi_j^{(2)}(\mathbf{r}_2)\rangle$. The electronic wavefunctions and PEC are then determined by diagonalising the electronic Hamiltonian in this finite basis of Rydberg pair states, which are coupled through the action of the interaction operator (3.4). Figure 3.1 shows results for pair interaction potentials near the $|35P_{1/2}35P_{3/2}\rangle$ asymptote calculated with the `pairinteraction` software package [265, 266] for pair states with 0_g^+ symmetry [4].

---

[4]A breakdown of molecular term symbol notation. Molecular states denoted by 0_g^+: (0) the total projection of the orbital angular momentum along the internuclear axis is zero, (+) the electronic states are symmetric under reflection through a plane containing the internuclear axis and (g) the electronic states have even (*gerade*) symmetry under point inversion.
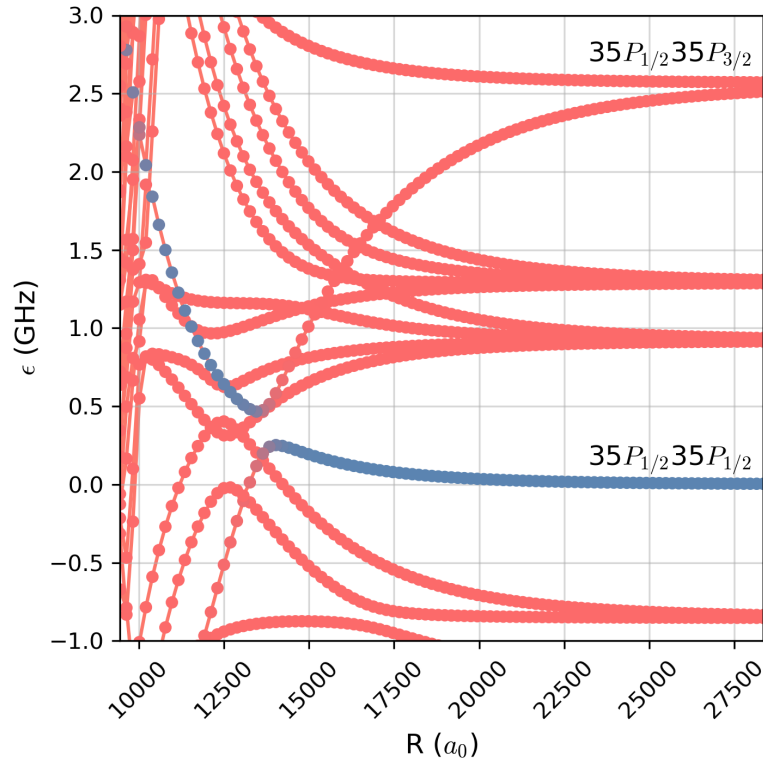
FIGURE 3.1: Adiabatic PEC for a pair of Rydberg atoms near the $|35P_{1/2}35P_{1/2}\rangle$ pair state. A binding potential with an approximate depth of 2 GHz, supporting Rydberg-Rydberg bound "macrodimer" states, is formed due to an anti-crossing with the attractive $|35P_{1/2}35P_{3/2}\rangle$ pair state. These curves were calculated using `pairinteraction` [265] and only states with 0_g^+ symmetry are shown. Higher-order effects, such as the hyperfine-splitting of atomic levels, are much smaller than the energy of the Rydberg interactions and have been neglected. Energies are given in GHz relative to the $|35P_{1/2}35P_{1/2}\rangle$ pair state.

The figure highlights two important features of Rydberg interactions. First, we see that an avoided crossing between the attractive branch of the $|35P_{1/2}35P_{3/2}\rangle$ state and the repulsive $|35P_{1/2}35P_{1/2}\rangle$ state at approximately $R = 14000 \, a_0$ leads to the formation of a potential well with a depth of approximately 2 GHz. Wells such as these can support multiple bound vibrational states (not shown) with 100 MHz energy spacing. Such bound states, known as Rydberg *macrodimers*, were first predicted in the early 2000s [213, 214] and have been subsequently observed and studied experimentally [179, 218–220]. In addition, long-range bound states between three Rydberg atoms exist, known as *macrotrimers* [267, 268].

The second important feature visible in figure 3.1 is that the size of the energy shift of an unperturbed pair state depends on the internuclear separation. This has important implications for experiment. To understand this, let us consider a finite-linewidth laser setup which is calibrated to photoexcite a pair of Rydberg atoms close to the asymptote of the pair potential $|35P_{1/2}35P_{1/2}\rangle$. Due to the shift in energy of the pair potential from the Rydberg interaction, we see that photoassociation will be forbidden for pairs of atoms below a certain critical internuclear separation, where the pair potential is no longer in resonance with the excitation laser. For example, at $R = 17500 \, a_0$ the energy shift of the unperturbed state is of the order of 100 MHz and will thus no longer be accessible to a MHz-linewidth laser whose frequency is calibrated to the asymptotic state $|35P_{1/2}35P_{1/2}\rangle$. This effect is referred to as the *Rydberg blockade mechanism* [210] and enables the precise control of the number of Rydberg excitations in the

system. Equally, by calibrating the laser such that it has a fixed detuning from the asymptotic energy of the pair potential, only Rydberg pairs at a specific internuclear separation will be photoassociated, which is often referred to as Rydberg *antiblockade* or *facilitation* [269, 270].

3.2.2 Rydberg – Ground-state interactions

As discussed in section 3.1, the earliest studies involving interactions of Rydberg atoms with neutral ground-state atoms were conducted in the 1930s in Rome [196] and Rostock [193–195]. These experiments performed spectroscopy of Rydberg states prepared inside different kinds of buffer gases. Their results revealed that lineshifts of the atomic states in the presence of the gases were not consistently to the red, but also exhibited blueshifts for particular buffer gas species. These observations contradicted contemporary theoretical understanding, which expected only redshifts stemming from the long-range attractive interaction between the Rydberg electron and the surrounding neutral atoms. Enrico Fermi provided the answer to this puzzle [197] by developing a model for interactions at short-range, namely *s*-wave scattering of the Rydberg electron from the buffer gas atoms. He described the scattering with an effective zero-range pseudopotential, which is attractive or repulsive depending on the momentum of the Rydberg electron. Fermi's model explained the anomalous lineshifts and even allowed the experimentalists to measure scattering lengths [271]. Thereafter, the model played an integral part in understanding collisions involving Rydberg atoms [272], which helped shed light on collisional broadening in spectral lines observed in the atmospheres of stars [273]. Fermi's pseudopotential was later extended in the 1970s to account for higher partial-wave scattering [274].

Almost seventy years after Fermi's original publication, the pseudopotential model was used again within the context of the newly-emerged field of ultracold quantum gases [230]. In the ultracold regime, authors Greene *et al.* predicted that attractive scattering could support the formation of weakly-bound macroscopic-sized homonuclear molecules possessing large permanent electric dipole moments. They considered a Rydberg atom interacting with a neutral ground-state atom, described by the electronic Hamiltonian $\hat{H}_e = \hat{H}_0 + \hat{V}$. Here, $\hat{H}_0$ describes the unperturbed Rydberg atom with energy spectrum (3.1) and $\hat{V}$ is the Fermi pseudopotential interaction operator [230, 275, 276]:

$$\hat{V} = 2\pi a_s[k(R)]\delta^{(3)}(\mathbf{r} - \mathbf{R}) + 6\pi a_p^3[k(R)]\overleftarrow{\nabla}_{\mathbf{r}}\,\delta^{(3)}(\mathbf{r} - \mathbf{R})\overrightarrow{\nabla}_{\mathbf{r}} - \frac{\alpha_c}{2R^4}. \qquad (3.6)$$

The first two terms describe *s*- and *p*-wave scattering in the dominant spin-polarised (triplet scattering) channel. The third term is the charge-neutral interaction between the positively-charged Rydberg core and the perturber, relevant only at short-range.

The strength of the scattering interaction depends on the magnitude of the scattering lengths [5] as well as the Rydberg electron's probability density at the position of the ground-state atom, given to first-order by $|\phi(\mathbf{R})|^2$, where ϕ is the unperturbed atomic Rydberg state. The oscillatory shape of this probability density gives rise to shallow potential wells for negative scattering lengths, centred around areas of electron density maxima.

Figure 3.2 shows exemplary adiabatic PEC for an energy window around the $|33S\rangle$ atomic Rydberg state. The PEC exhibit wells with depths ranging from tens of MHz to several GHz. At ultracold temperatures, these are sufficiently deep to support long-range vibrationally-bound states between the

---

[5]The scattering length and volume are defined as $a_s[k(R)] = -\tan\delta_s[k(R)]/k(R)$ and $a_p^3[k(R)] = -\tan\delta_p[k(R)]/k(R)$, respectively. $\delta_s[k(R)]$ and $\delta_p[k(R)]$ are energy-dependent *s*- and *p*-wave phase shifts of an electron with wavenumber k at the position R of the perturber relative to the Rydberg core.
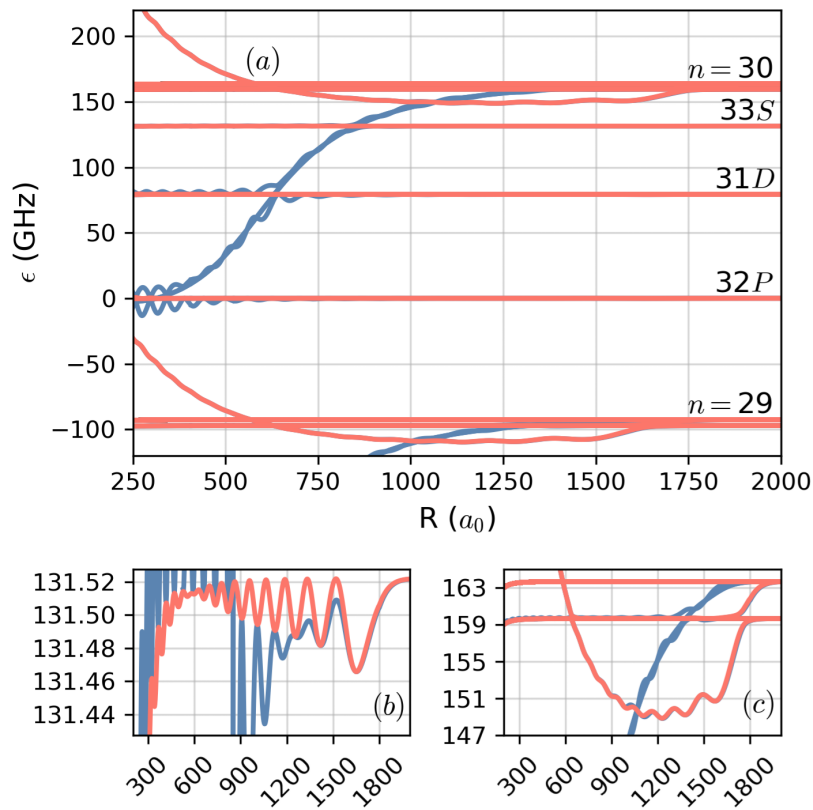
FIGURE 3.2: (a) Adiabatic PEC for a Rydberg atom interacting with a ground-state atom ^{87}Rb for only *s*-wave (red curves) and *s*- and *p*-wave interactions (blue curves). (b) Close-up of the PEC asymptotically connected with the $|33S\rangle$ Rydberg state. Note the oscillatory potential wells with characteristic depth on the order of MHz and the crossing with the butterfly state at approximately $R = 900\,a_0$. (c) Shows a close-up of the near-degenerate hydrogenic manifold with trilobite and butterfly curves present. These electronic states have depths of the order GHz and posses large permanent electric dipole moments. The PEC were determined using exact diagonalisation of the electronic Hamiltonian $\hat{H}_e$ (see section 3.2.2). Energies are given in GHz relative to the $|32P\rangle$ atomic Rydberg state.

Rydberg and perturber (not shown). Due to the large bond lengths, these states have been dubbed ultralong-range Rydberg molecules (ULRM).

Broadly speaking, ULRM can be classified into two types. The first kind are formed by low angular momentum Rydberg states *S*-, *P*- and *D*-states. Low-*l* ULRM have binding energies on the order of tens of MHz. In addition, the relatively large energy gap betwen low-*l* states and their neighbouring states means that coupling between different *l* states due to the presence of the perturber is marginal. This class of ULRM therefore do not have large electric dipole moments and are referred to as non-polar ULRM.

On the other hand, high-*l* states connected asymptotically with hydrogenic manifold undergo significant *l*-mixing which gives rise electronic states whose probability density is maximised around the position of the perturber atom. Consequently, these states acquire an electric dipole moment proprtional to the internuclear separation R and thus can have dipole moments on the order of $10^3\,ea_0$. The *s*-wave scattering term in (3.6) leads to a GHz-depth well visible in figure 3.2. The shape of the electronic structure of the vibrational states in this well is reminiscent of ancient trilobite fossils and hence these states are

often referred to in the literature as trilobite states [276].

Including the higher-order *p*-wave scattering term leads to an additional strongly-perturbed electronic state, which has been dubbed the butterfly state on account of its distinct shape [276]. The butterfly PEC undergoes a sharp drop for decreasing R, such that it crosses all other PEC. This feature is specific to alkali metal elements for values of R at which the energy of the Rydberg electron approaches a negative ion resonance. In ^{87}Rb, this $^-$Rb shape resonance occurs at approximately 25 meV. As a consequence of the shape resonance, the butterfly state exhibits anticrossings with the other ULRM states, which serve as decay channels whereby bound vibrational states tunnel inward to smaller R along the steep butterfly curve. Such tunnelling leads to short-range processes which can result in autoionisation and dissociation of the molecule, limiting the ULRM molecular lifetime to tens of microseconds [112, 236].

3.2.3   Rydberg – Ion interactions

Interest in employing Rydberg states to engineer stronger, longer-range atom-ion interactions has existed for over twenty years now. Already as early as the year 2000, Côté proposed replacing a gas of neutral ground-state atoms with Rydberg atoms in order to study electron mobility in atomic gases at more favourable experimental temperatures, which is possible due to the scaling of the charge exchange cross-section with *n* [70].

Later in the 2010s, several works revisited ion-Rydberg interactions as an approach for circumventing the restrictive lower-bound on atom-ion collision energies imposed by micromotion-induced heating of ions confined in Paul traps [87, 88, 90, 91, 277–279]. It was predicted, and later demonstrated, that Rydberg atoms could be used to create atom-ion entanglement over macroscopic distances [91, 279], which relies on the fact that the atomic polarisability α featuring in the charge-induced dipole interaction (2.12) scales in proportion to n^7.

Further proposals suggested the use of off-resonant coupling to engineer repulsive atom-ion interactions that would be resistant to heating from the time-dependent fields present in Paul traps [277]. An ion-Rydberg blockade mechanism was also observed [90] and an effective ground-state charged impurity was created inside an ultracold gas of neutral atoms by exciting a giant Rydberg atom of $n = 190$ which suppressed electron-atom scattering [87]. Moreover, the idea emerged that Rydberg states could be used as precursors for initiating ultracold collisions between ions and ground-state atoms by exploiting either the short decay times of ULRM [278] or using tailored pulsed field-ionisation of a Rydberg atom to produce a single ion in a nominally field-free environment within an ultracold gas [88]. The overarching goal of these works was to prepare a hybrid atom-ion system in the quantum regime, which would be a decisive step toward realising proposals such as atom-ion quantum gates [280] and the use of atom-ion Feshbach resonances for precision control of interactions [118].

These aforementioned works focused almost exclusively on interactions between ions and low-*l* Rydberg-state atoms in the asymptotic limit, whose interaction potential is described by (2.12). The focus on low-*l* states was necessitated in part due to the restrictions imposed by dipole selection rules. That said, the production of dipole-forbidden Rydberg states was reported in 2019 [279] and an earlier work [91] had suggested using high-*l* states to explore more exotic functional forms of atom-ion interactions beyond the classic charge-induced dipole interaction (2.12), such as charge-dipole and charge-quadrupole interactions which vary as $1/R^2$ and $1/R^3$, respectively.

Exploring ion-Rydberg interactions in the regime of strong coupling really begain in 2021, when two independent works predicted ultralong-range vibrationally-bound ion-Rydberg dimers [92, 93]. These bound states were predicted to exist within potential wells formed by avoided crossings between pairs of

high- and low-field seeking Rydberg states. It did not take long before these molecules were first observed *in situ* through selective photoassociation out of an ultracold gas of neutral atoms [95]. Similar to the Rydberg macrodimers discussed in section 3.2.1, these wells form at internuclear separations for which there is vanishing overlap between the charge distributions of the Rydberg atom and the ion. These singly-charged macroscopic dimers can be considered Rydberg-analogues of the dihydrogen cation H_2^+, which is one of the earliest problems considered in quantum mechanics [281].

The electronic Hamiltonian describing an interacting ion-Rydberg pair is given by $\hat{H}_e = \hat{H}_0 + \hat{V}$, where $\hat{H}_0$ describes the unperturbed Rydberg atom and the operator $\hat{V}$ describes the electrostatic interactions between the Rydberg atom and the ion

$$\hat{V} = \frac{1}{|\mathbf{R}|} - \frac{1}{|\mathbf{r} - \mathbf{R}|}. \tag{3.7}$$

$\mathbf{R}$ is the separation between the nuclei and $\mathbf{r}$ defines the displacement of the Rydberg electron relative to its parent nucleus. Since we are in the regime $|\mathbf{r}_i| \ll |\mathbf{R}|$, one may expand the final term of equation (B.1) as a series of multipoles [262–264], leading to the net interaction

$$\hat{V} = -\sum_{\lambda=1}^{\infty} \sqrt{\frac{4\pi}{2\lambda+1}} \frac{r^\lambda}{R^{\lambda+1}} Y_{\lambda,0}(\theta, \phi). \tag{3.8}$$

Here, we have chosen the internuclear axis $\hat{\mathbf{R}}$ to be parallel with the z-axis. Further details of this derivation, including a more general result for the case that $\hat{\mathbf{R}}$ is not parallel to $\hat{\mathbf{z}}$, is provided in appendix B.

In the spectra of certain alkali metal elements, such as Rb and Cs, the Rydberg nP-state lies close above the $n-3$ hydrogenic manifold of quasi-degenerate high-l states. In the presence of the ion, the states naturally undergo level shifts. As discussed previously, low-l dipole-allowed states such as nS and nP acquire an induced dipole moment and the leading-order correction to their energies in the asymptotic limit is of the form $\epsilon_P \propto -n^7/R^4$. In contrast, the degenerate manifolds of high-l dipole-forbidden states acquire permanent dipole moments due to strong l-mixing and their leading-order energy correction is $\epsilon_L \propto \pm n^2/R^2$ such that the degenerate manifold splits up into a "fan" of non-degenerate states – similar to the spectra of atoms in homogeneous electric fields. The prefactor of ϵ_L determines whether the states in the fan are high- or low-field seeking states. For decreasing R, the attractive nP state will eventually cross through the fan of low-field seeking high-l states. By equating the energy scaling of the low-l state with that of the high-field seeking states, we find that positions of crossings between the two should scale approximately as $R_c \propto n^{5/2}$. Therefore, for sufficiently large n the crossing will occur at internuclear separations which far exceed the extent of the Rydberg electron's orbit [6]. Indeed, the dimers observed in [95] were bound over distances exceeding ten times the radius of the Rydberg electron's orbit. As a result of their large bond lengths, these dimers are expected to be stable against charge transfer [93].

We now solve for the adiabatic PEC of an interacting ion-Rydberg pair by diagonalising the electronic Hamiltonian in a finite basis of atomic Rydberg states. Typically, including only the first few multipole terms in the series of equation (3.8) is sufficient to ensure convergence of the PEC to the nearest 1 MHz, which for a reasonable range of n is at least one order of magnitude smaller than the smallest relevant molecular energy scale (namely, the spacing of the vibrational states). Solutions in the region of the energy spectrum near the $|32P\rangle$ atomic Rydberg state are provided in figure 3.3. The avoided crossings between the nP and high-l states create potential wells with depths up to tens of GHz (though the depth of the wells inside the fan is considerably shallower than the outermost well, as shown in figure 3.3 (c)). The wells support vibrational bound states with spacing typically on the order of 100 MHz for the case of

---

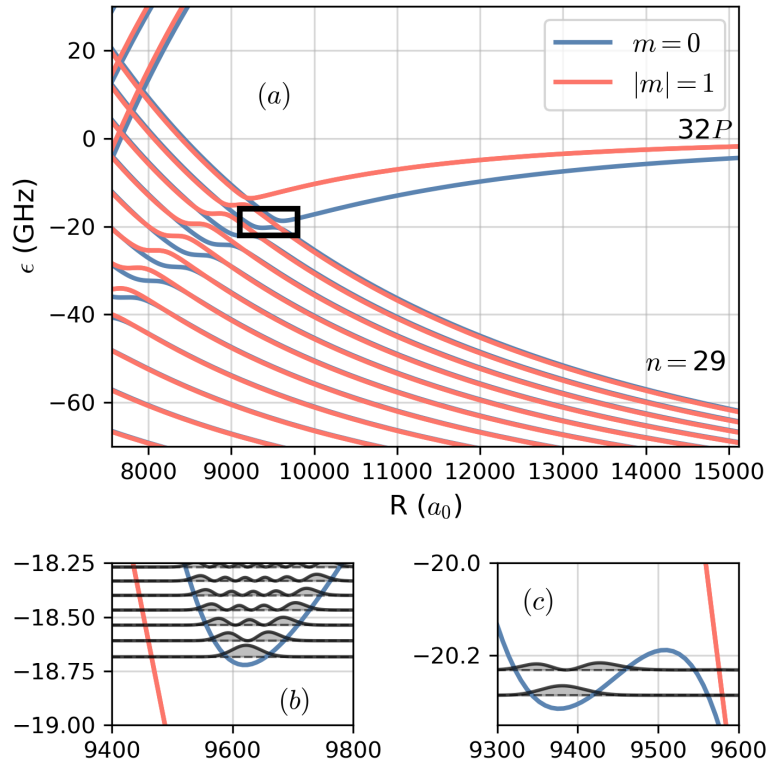[6]The extent of the Rydberg orbit scales in proportion to n^2.

FIGURE 3.3: (a) Adiabatic PEC for a ^{87}Rb Rydberg atom interacting with a singly-charged positive ion at separation R near the $|32P\rangle$ atomic Rydberg state. Vibrationally-bound states inside the first (b) and second (c) potential wells formed between the $|32P\rangle$ state and low-field seeking high-l states are shown. The PEC were determined using exact diagonalisation of the electronic Hamiltonian $\hat{H}_e$ (see section 3.2.3). Energies are given in GHz relative to the $|32P\rangle$ atomic Rydberg state.

^{87}Rb, which have been observed in experiment [95]. The rotational splitting of the dimer is on the order of kHz and hence rotation occurs on time scales which exceed the radiative lifetime of the Rydberg state [95]. Interestingly, due to the superposition of high- and low-field seeking states in the electronic state, the dipole moment changes sign across the well's minimum [96] - similar to the electronic ground-state of carbon monoxide [282].

At this point, we remark that the leading-order interaction term in (3.8) is equivalent to the energy of a neutral atom in a homogeneous electric field, which means that the PEC bear some resemblance to atomic DC Stark spectra. The higher-order interaction terms (3.8) cause the PEC to deviate from DC Stark spectra, especially for smaller R. This is because the radially-symmetric shape of the ion's electric field becomes more relevant for smaller internuclear distances.

Due to the fact that the vibrationally-bound states exist close to an avoided crossing between PEC, recent works have examined the influence of non-adiabatic couplings on these molecular states [93, 283]. These works employed both the Landau-Zener formula [93] (see also equation (2.8)) as well as more sophisticated coupled-channel models [283] and predict that decay due to non-adiabatic coupling terms occurs on time scales longer than the radiative lifetime of the Rydberg state. This theoretical evidence is further supported by spectroscopic measurements of the vibrational series [95] which show no visible deviation from the BO calculations at current experimental precision. Therefore, contrary to what one

might expect given the presence of so many avoided crossings, the approximation of the wavepackets existing on an isolated adiabatic PEC appears to hold.

However, given that the spacing between vibrational states (approx. 100 MHz) is smaller than the avoided crossing gap size (approx. few GHz), it is perhaps not surprising that the non-adiabatic couplings are so seemingly insignificant. A similar effect has been reported in the vibrational spectrum of Rydberg macrodimers [284], where an external magnetic field **B** controlled the size of the avoided crossing between pair potentials. The crossing was exact for $B = 0$ and grew in size with increasing field strength B. As the field was turned on, the width of the vibrational resonances were observed to increase. However, the resonances became narrower again at high field strengths when the size of the avoided crossing grew considerably large. Nonetheless, a true quantitative understanding of the impact of non-adiabatic couplings on the dynamics and lifetime of ion-Rydberg dimers remains open. Furthermore, although non-adiabatic couplings appear to be insignificant for the range of n explored so far, they may become more relevant at higher n due to the smaller size of the avoided crossings between PEC. Similar ideas have been explored already for ULRM [259].

Therefore, from a theoretical perspective, it seems that the lifetime of ion-Rydberg dimers should be limited only by radiative decay of the Rydberg atom. Despite this, recent experimental measurements report lifetimes over an order of magnitude smaller than this [95], indicating some additional unexplained decay mechanism. A potential candidate for this may be collisions between the dimer and neutral ground-state atoms in the surrounding gas, which is discussed in appendix C. Using a straightforward semi-classical approach, we predict decay rates in good agreement with the experimentally-observed lifetimes. Additionally, in our work [SC2] we predict that neutral ground-state atoms can additionally bind to the dimer via attractive scattering with the Rydberg electron. In such cases, we expect the lifetime of the trimer state to be limited by rapid autoionisation of the Rydberg – ground-state pair, as is the case for ULRM [236].

Finally, we remark on the dynamics of ion-Rydberg pairs. In contrast to conventional diatomic molecules, the spacing of the vibrational states of ion-Rydberg dimers is extremely narrow (approximately 10-100 MHz) and as a consequence, their vibrational dynamics occurs over microsecond time scales. In contrast, deeply-bound molecular systems close to their electronic ground-state exhibit picosecond dynamics [98]. This fact has been exploited to perform *in situ* observation of wavepacket oscillations excited by preparing the system in a superposition of several bound vibrational states using a quenched external electric field [96]. However, currently observations are limited by the short lifetimes of the dimers reported in [95]. Our joint work [SC4] presents direct observations of collisions between an ion and an *S*-state Rydberg atom. In contrast the Rydberg *P*-state, the *S*-state does not form any binding potentials due to the ion's field. Nonetheless, the dynamics unfolds over a rich landscape of coupled collision channels due to the presence of high-field seeking high-l states from the *S*-state's neighbouring hydrogenic manifold.

Chapter 4

Summary of scientific contributions

This chapter serves as an overview of the scientific contributions of this thesis, discussing the motivation behind each project and summarising their key results. Section 4.1 focuses on the scientific works [SC1] and [SC3], which consider systems with mesoscopic-scale atom-ion interactions between ions and ground-state atoms. In contrast, section 4.2 is dedicated to the works [SC2], [SC4] and [SC5], in which we explore macroscopic interactions between ions and Rydberg atoms. At the beginning of each section, we briefly review some key literature relevant to the topic of the scientific works in that section. This provides additional context for readers unfamiliar with these topics and highlights the relevance of our works for the wider research community. We then discuss each work in turn, outlining the methods used and the main results obtained. Explicit details of the author's contributions to each of the projects [SC1–SC5] are provided in the preface on page xxiii.

4.1 Mesoscopic atom-ion systems

Charged species, such as ions and molecular ions, have important functions in various chemical processes throughout nature. Even relatively simple molecular ions can play a pivotal role. For instance, the formation of more complex molecules in the interstellar medium, such as water, is brought about through proton transfer reactions of trihydrogen cations H_3^+ with heavier atomic species [285]. We see therefore that the study of charge-neutral collisions and chemistry can contribute to our understanding of some of the most basic questions we have about nature. Clean, controlled quantum systems of atoms and ions provide an ideal platform for such fundamental investigations.

The earliest experiments which embedded charged particles inside ultracold atomic gases were performed with ultracold plasmas [72, 286, 287] and ionisation experiments in BECs [288]. Nonetheless, these approaches suffered from the drawback that the ions were free-floating and therefore could escape on relatively short time scales. As a result, proposals emerged for hybrid trap setups, in which both atoms and ions are trapped simultaneously [289, 290]. Since their earliest demonstration two decades ago [80], experiments with hybrid atom-ion trap setups have proceeded to study controlled chemical reactions and collisions [86, 291, 292], state-resolved chemistry [293, 294], charge transport [88] and collisional ion-qubit decoherence [295]. Furthermore, trapped ions have been used for probing the density of atomic gases [82, 296].

These experimental achievements have been complimented by numerous theoretical studies, ranging from the development of a quantum description of atom-ion collisions [118] to the study of charged polarons [75, 77, 78]. Moreover, proposals have emerged for performing controlled collisions with movable trap potentials [297], realising atom-ion quantum gates [280] and performing ion thermometry [298]. Further theoretical works have explored hybrid atom-ion systems for the purpose of simulating bosonic

Josephson junctions [176, 299, 300], extended Hubbard Hamiltonians [301] and electrons in solid-state systems [302].

In addition to this broad body of literature, several theoretical works have explored the formation and properties of weakly-bound molecular ions inside ultracold gases [71, 75, 119]. In such states, an atom-ion pair occupies a highly-excited rovibrational state close to the dissociation limit. Due to the long-range nature of the atom-ion interaction, varying at large separations as $-1/R^4$, the bond lengths of these highly-excited states are on the order of 100 nm, which is comparable to the average interparticle separation in dilute atomic gases. Moreover, it is predicted that hundreds of atoms may become bound by a single ion [71] and the properties of these many-body molecular ions in quasi-1D systems have been explored using *ab initio* techniques [75].

For many years however, the aforementioned theoretical works have largely been decoupled from experimental reality. This is because observing the quantum effects studied by theorists requires atom-ion experiments prepared at sub-µK temperatures. This presents a significant technical challenge, as this temperature scale is at least two orders of magnitude colder than the ultracold temperature regime for neutral systems [111]. An additional challenge is presented by the micromotion dynamics of ions confined in radiofrequency (RF) Paul traps [303–306]. Ion micromotion limits the effectiveness of buffer gas cooling techniques, since energy imparted to the ion by the driving RF field can be transferred to the buffer gas through collisions [307, 308]. This has prompted researchers to consider alternative trapping technologies, such as optical ion traps [309–314]. Whilst free from micromotion heating effects, optical ion traps bring with them a unique set of challenges, including shallower trap depths [315]. Other approaches in recent years have created cold free-floating ions by means of controlled pulsed field-ionisation [88]. Here, atoms are photoionised slightly above the ionisation threshold, such that their net kinetic energy corresponds to tens of µK. If stray fields are sufficiently compensated, the ions remain trapped for tens of µs. Their collisional dynamics can be steered using external fields and monitored with high spatial- and temporal-resolution using an ion microscope [89].

Despite the new possibilities opened up with these two innovative experimental approaches, experiments with ions in Paul traps continue to break new ground in the pursuit of ultracold atom-ion systems. These achievements were driven by the development of approaches for mitigating the ion's micromotion by means of mass-imbalanced atom-ion mixtures [307, 316, 317] and trap parameter optimisation [318]. In 2020, Feldker and co. performed cooling of a single ^{171}Yb$^+$ ion with an ultracold buffer gas of ^{6}Li and measured collision energies at the boundary of the *s*-wave scattering regime [83]. Then in 2021, Weckesser *et al.* raised the bar yet again by observing the first atom-ion Feshbach resonances in a ^{6}Li-^{138}Ba$^+$ system [84]. This work was extended in 2024 by introducing external electric fields for tuning atom-ion collision energies over several orders of magnitude [85]. Here, Thielemann *et al.* used electric fields to control the excess kinetic energy of the ^{138}Ba$^+$ ion, enabling them to probe atom-ion collisions in both classical and quantum regimes and assign the partial wave character of several Feshbach resonances. Furthermore, in 2022 Pinkas *et al.* reported the trap-assisted formation of weakly-bound molecular ions created via binary collisions of ^{87}Rb and ^{88}Sr$^+$ [319].

These exciting advancements highlight the rapidly narrowing gap between experiment and theory and provide fresh motivation for expanding our theoretical understanding of atom-ion systems. In this regard, we now introduce two scientific contributions related to interactions between ions and ground-state atoms [SC1, SC3]. In [SC1], we perform an extensive analysis of the low-energy excitations of a three-body system of two bosons interacting with an ion. We explore the impact of competing atom-atom and atom-ion correlations on the energy and structure of the eigenstates, focusing particularly on mesoscopic atom-ion bound states. Exploring few-body quantum systems such as this can be beneficial because whilst

being simpler to describe than many-body systems, they can still exhibit complex and rich behaviours with implications for fundamental physics and quantum technology. Building on this understanding, in [SC3] we explore the dynamics of trapped atoms interacting with a mobile ion, which we employ as an external drive for realising quantum state transfer of the atoms between different vibrational trap states. The ability to control and manipulate quantum states enables researchers to simulate and study complex quantum phenomena, opening the door to a deeper understanding of many-body physics, condensed matter systems, and chemical reactions.

4.1.1   The low-energy spectrum of a few-body atom-ion system [SC1]

Using the model potential (2.13) discussed in section 2.4, *ab initio* theoretical studies have investigated the ground-state properties of mesoscopic molecular ions in the few- to many-body regime [75, 119]. However, a thorough treatment of the excited states of such systems was missing. This was the primary motivation behind our first published work [SC1], in which we present an in-depth study of the low-energy spectrum of a few-body atom-ion system.

Specifically, we focus on a one-dimensional hybrid trapped system consisting of a pair of neutral bosonic atoms interacting with a single ion and explore how the competition between the zero-range interatomic interaction and the long-range atom-ion interaction impacts the low-energy spectrum and structure of the eigenstates. The Hamiltonian describing such a system in the laboratory frame is written as:

$$\hat{H} = \sum_{\substack{i=1 \\ \sigma \in \{A, I\}}}^{N_\sigma} \left[-\frac{\hbar^2}{2m_\sigma} \frac{\partial^2}{\partial z_{\sigma,i}^2} + \frac{1}{2} m_\sigma \omega_\sigma^2 z_{\sigma,i}^2 \right] + \sum_{i<j}^{N_A} g\, \delta(r_{ij}^{AA}) + \sum_{i=1}^{N_A} \hat{V}_{AI}(r_i^{AI}). \tag{4.1}$$

The first sum describes the non-interacting species sub-Hamiltonian consisting of N_σ particles of mass m_σ with position $z_{\sigma,i}$ and longitudinal trapping frequency ω_σ, where $\sigma \in \{A, I\}$ for the atomic and ionic species, respectively. The second sum describes the interaction between two atoms with separation $r_{ij}^{AA} = |z_{A,i} - z_{A,j}|$, which is modelled by a zero-range potential whose strength g is determined solely by a single scattering parameter, the *s*-wave scattering length [320]. The third sum accounts for interactions between an atom-ion pair at separation $r_i^{AI} = |z_{A,i} - z_I|$ using the model potential (2.13), whose parameters are chosen such that it includes only the two most weakly-bound states.

To obtain the few lowest-energy eigenstates of (4.1), we make use of the multi-layer multi-configuration time-dependent Hartree method for bosons (ML-MCTDHB) described in section 2.5.3. ML-MCTDHB makes use of a product ansatz, which can be tailored to account for the level of correlation between degrees of freedom by changing the number of configurations in the summation. In the laboratory frame Hamiltonian (4.1), the long-range nature of the atom-ion interaction means that z_A and z_I are strongly correlated, especially for atom-ion bound states. Therefore, greater numbers of terms in the product ansatz are required, which can make ensuring convergence of the results more challenging. For this reason, we instead work with relative coordinates, for example in a reference frame defined relative to the system's centre-of-mass or the absolute position of the ion, as discussed in section II B of [SC1].

The ground-state of the system is determined by propagating the initial ansatz in imaginary time, which leads to exponential decay of contributions to the state from excited eigenstates such that over sufficiently long time scales the wavefunction relaxes to the lowest-energy state [141]. To obtain excited states, we make use of the improved relaxation algorithm [142–146]. In this case, the overlap of the target state with the initial state as well as the energy separation of the eigenstates will determine how quickly the result converges to the target state. Since there is no guarantee that the initial state will converge to the desired excited eigenstate, we performed multiple relaxation runs using initial wavefunctions with added

random noise to ensure we achieve sufficient overlap with the target eigenstate. In this way, we determine the first five lowest energy eigenstates of the system for varying interatomic interactions strength g and interspecies mass ratio $\beta = m_A/m_I$. We explore how the changing values of these parameters influence the competition between the atom-atom and atom-ion correlations and how this subsequently impacts the character of the states in the energy spectrum. In particular, we investigate both mass-balanced $\beta = 1$ and mass-imbalanced $\beta \neq 1$ mixtures in regimes of interatomic interactions ranging from $g = 0$ up to large positive values approaching the Tonks-Girardeau limit [321–323].

We then carry out a careful classification of the properties of the low-excited states by examining the distribution of energy among the various components of the Hamiltonian (4.1), the two-body correlations in the system and changes to further observables, such as the expected atom-atom and atom-ion separations. We found that certain effects, such as an ion-induced bunching of the repelling atom pair, could be described qualitatively using a mean-field approach, which assisted in developing a greater intuitive understanding of the system.

The work completed in [SC1] could be extended to ions interacting with mixtures of bosons and fermions, akin to triple-mixture systems which have received increasing attention in recent years [156, 158, 159]. In particular, ML-MCTDHB is well-suited as a numerical tool for investigating such problems due to its ability to efficiently capture intra- and interspecies correlations. In addition, one could consider systems combining atom-ion interactions with other long-range interactions, such as dipole-dipole interactions. When taken alone, the latter already give rise to exotic phases such as quantum droplets [324–327] and supersolidity [328–330]. Other avenues of future research could explore ultracold gases interacting with lattice-like arrangements of ions for the purpose of simulating condensed matter phenomena.

4.1.2   Facilitating quantum state transfer with a driven ion-like potential [SC3]

Using the intuition developed from the time-independent system of [SC1], in our follow-up work we shifted our focus to atom-ion dynamics. Prior works have examined non-equilibrium dynamics of gases of ultracold atoms in the presence of *static* ions, such as the sudden immersion of an ion within a BEC [175] and the use of the atom-ion interaction for controlled atom tunnelling in a bosonic Josephson junction [176]. We go beyond these works by investigating dynamics involving a *mobile* ion, such as collisions between atoms and ions in separate traps, in the spirit of similar works for neutral systems [168].

We began by simulating the dynamics of single ions moving at a constant velocity through a gas of atoms trapped in one-dimension. For certain choices of the ion's initial position and speed, we found that striking patterns emerged in the atomic probability density. A prime example of one of these early results is shown in figure 4.1. We see that regular periodic oscillations in the atomic density emerge out of seemingly-disordered fluctuations at intermediate times. Fourier analysis of the signal revealed that these oscillations emerge because the ion's motion excites the atoms into a superposition of the first few vibrational trap states. This excitation is possible because the ion's presence breaks the parity symmetry of the trapped atoms, leading to position-dependent couplings between neighbouring trap eigenstates (see figure 1 in [SC3]).

This realisation motivated us to shift our focus toward deterministic state transfer of trapped atoms into excited states using the ion's motion as a control, where we seek to maximise the fidelity between the atoms's final state and some pre-defined target state. Knowing which state your system is in, preventing unwanted coupling with its environment and transfering it to other states in a reliable and efficient manner is the basis of quantum state engineering [331–333]. These abilities are essential for realising the potential of quantum effects for applications ranging from information processing [334] to metrology [335].
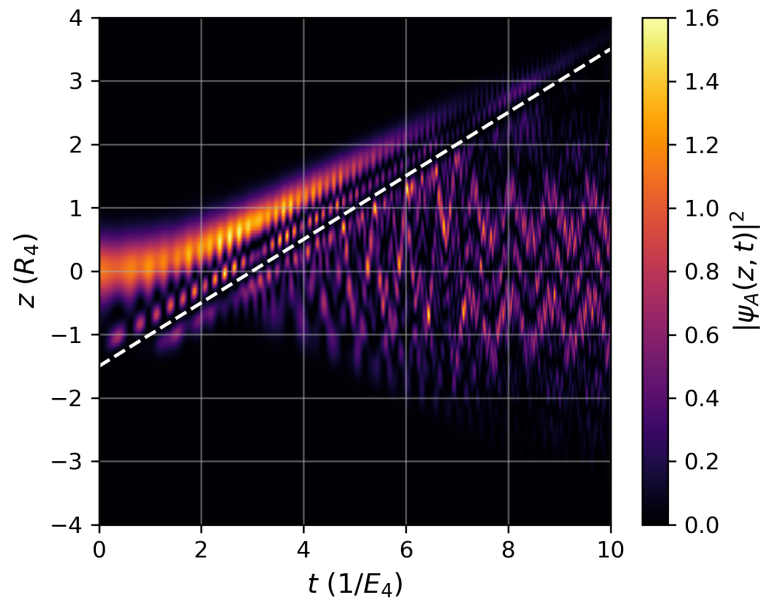
FIGURE 4.1: Time evolution of the probability density of a single harmonically-trapped atom $|\psi_A(z,t)|^2$ interacting with an ion modelled by (2.13) which moves through the system at a constant velocity. The ion's trajectory is shown by the dashed line. At $t = 0$, the atom is in the vibrational ground-state of the trap. For $t > 0$, the atom-ion interaction is switched on, perturbing the atomic state. Out of the highly-disordered density pattern in the interval $4 < t < 7$ emerges a regular oscillation for $t \gtrsim 7$. Position and time are plotted in units defined by the characteristic length R_4 and energy scale E_4 of the atom-ion interaction (see section 2.4).

Quantum state engineering with trapped ultracold quantum gases can be performed by driving the system externally, such as by varying the underlying trapping potential [336–338] or moving external potentials through the system [339–344].

In our work, the atom-ion model potential serves as the external drive. To simplify the problem, we neglect the ion's degree of freedom and treat it instead as a time-dependent one-body potential. This could be realised experimentally by re-creating (2.13) using designer optical potentials [345] or by using a tightly-trapped ion. The form of the atom-ion interaction potential (2.13) is unique among other external drives considered in the literature because it has both a short-range repulsive barrier as well as an attractive long-range tail, which offer additional flexibility. These two features each give rise to a unique series of avoided crossings in the vibrational spectrum of the trapped atoms (see figure 1 (b) and (c) in [SC3]), which can be exploited for transferring atoms to excited states.

We manipulate the external drive's motion in such a way as to confine the atomic state to evolve in time along an ideal "state path" (see figure 3 in [SC3]) and minimise loss to other states in the Hilbert space. For this purpose, we devise two kinds of protocols for moving the external potential through the atom trap. The *adiabatic* protocol relies on adiabatic-sweeping of the potential at certain critical points to achieve state transfer. Whilst the performance of this protocol proves to be the comparatively robust to errors in the position and shape of the external potential, it suffers from the fact that the sweep must be slow enough to satisfy the adiabatic condition, leading to long protocol times which may be unrealistic for experimental setups. In contrast, the *tunnelling* protocol offers faster state transfer because it exploits the inherently short tunnelling time scales set by the size of the avoided crossings in the vibrational energy

spectrum. However, this latter protocol is more sensitive to noise than the adiabatic protocol and requires precise control over the external potential's position and speed in order to deliver the best results.

Future extensions of [SC3] could explore state transfer in many-body bosonic systems, which even in the non-interacting limit would present a challenge since the fidelity to the target state would decay to the power of the number of atoms N. It could also be interesting to explore such systems in regimes of finite interactions, such as quench dynamics triggered in atoms occupying excited trap states. Furthermore, by considering binary or triple mixtures of atoms in excited trap states, one could explore the role of particle statistics and study phononic excitations through preparing one species in an excited state, whose density then acts as a lattice-like potential for the other species.

4.2   Macroscopic atom-ion systems

The works discussed in the previous section focused on interactions between ions and ground-state atoms. We were particularly interested in effects arising from the mesoscopic scale of this interaction, whose effective range is roughly two orders of magnitude larger than interactions between neutral atoms in their ground-state. In this section, we now turn our attention to *macroscopic* atom-ion interactions which exist between ions and atoms in highly-excited Rydberg states. Whilst a more thorough introduction to Rydberg physics can be found in chapter 3, for the purpose of this section the most important piece of information is that the atom-ion interaction strength strongly depends on the value of the principal quantum number n. Specifically, the leading-order long-range interaction term scales as $V \propto -n^7/R^4$ for neutral atoms without permanent dipole moments. In this way, we may exploit the atomic structure as a further control knob for modifying the interaction strength of atom-ion pairs.

This scalability of the atom-ion interaction was initially capitalised upon in proposals for creating hybrid atom-ion systems free from unwanted heating effects due to the excess micromotion of ion's confined in Paul traps. Notably, Secker and co. recognised that by exciting atoms to Rydberg states, the atom-ion interaction range could be scaled-up from the mesoscopic regime of 0.1 μm to the macroscopic regime of several μm [91]. They proposed using this exaggerated interaction range to build hybrid atom-ion setups in which the trapped atoms and ion do not overlap in space, thereby mitigating heating of the atomic gas through collisions with the RF field driven ion. In a subsequent work [277], they additionally proposed using Rydberg dressing to engineer *repulsive* atom-ion interactions, preventing short-range collisions which cause ground-state atoms to sample the ion's micromotion. Over the years, other theoretical works have studied cold ion-Rydberg collisions [346] and proposed the use of Rydberg dressing for optical shielding schemes to facilitate controlled atom-ion collisions [347]. Macroscopic ion-Rydberg interactions have also been observed in experiment [90, 279, 348], including the demonstration of an analogous Rydberg blockade mechanism resulting from the ion-Rydberg interaction [90].

More recently, it was found that Rydberg-enhanced atom-ion interactions can in fact become strong enough for pairs of ions and Rydberg atoms to bind together over macroscopic distances [92, 93]. The local minima of the binding potential was found to scale approximately as $n^{5/2}$ [SC2], such that in principle the ion-Rydberg bond length may grow arbitrarily large. However, in reality it is limited by the decreasing depth of the binding potential which decays as n^{-3} [SC2, 93].

These ion-Rydberg dimers were observed for the first time in 2022 in cold dilute gases of ^{87}Rb [95]. Here, Zuber et al. photoassociated the vibrationally-bound ion-Rydberg states in a two-step process by first producing a single low-energy ion out of the ^{87}Rb gas [88]. They subsequently photoassociated the bound pair with help of a second laser scheme in resonance with vibrational states in the dimer binding potential. Not only were they able to measure the vibrational spectrum, their high-resolution

ion microscope setup [89] enabled them to additionally measure the bond length and orientation of individual dimers. Furthermore, introducing time delays allowed them to perform mass-spectroscopic measurements, confirming that the pairs were truly bound. Similar time-of-flight measurements were also used to determine the lifetime of the molecules, which they found to be on the order of 1 - 10 μs depending on the value of n.

In what follows, we discuss three scientific contributions [SC2, SC4, SC5] which explore systems involving interacting ion-Rydberg pairs. In section 4.2.1, we discuss our contribution [SC4] in which we worked in collaboration with an experiment at Universität Stuttgart performing *in situ* observations of ion-Rydberg dynamics. The motion of the pair takes place in a regime where non-adiabatic couplings give rise to myriad possible collision channels, essentially constituting a branching-problem for the colliding ion-Rydberg pair. In order to gain additional insight beyond what can be deduced from experimental measurements, we developed a model to describe the dynamics of the pair on this landscape of coupled PEC and explored ways in which the experimental control parameters may be used to steer the branching ratio of the ion-Rydberg pairs along the collision channels. In section 4.2.2, we then discuss the remaining works [SC2, SC5] which focus on the stability of ion-Rydberg systems in the presence of other atomic species. In particular, we explore the possibility for the formation of charged triatomic molecules of $^{87}\mathrm{Rb}_3^+$ and $^{87}\mathrm{Rb}_3^{2+}$.

4.2.1   Observing ion-Rydberg nuclear dynamics *in situ* [SC4]

Due to their large bond lengths and shallow binding potentials, ion-Rydberg dimers exhibit rotational splittings on the scale of 100 - 1000 Hz and vibrational splittings of 10 - 100 MHz, depending on the value of n. This has two important consequences for their molecular dynamics. First, the narrow rotational splitting means that time scales for rotational motion exceed the radiative lifetime of the Rydberg state. Thus, over the lifetime of the Rydberg atom, the molecule can be considered to have a fixed orientation. Second, the narrow vibrational splitting translates to vibrational wavepacket dynamics on time scales of μs, approximately six orders of magnitude *slower* than vibrational dynamics in molecules which are close to their electronic ground-state.

These two properties make ion-Rydberg systems attractive as a platform for observing molecular dynamics and other fundamental chemical processes. For conventional molecules, such observations are challenging because ultrafast pulses are required to resolve the dynamics and strong external fields are needed to ensure the alignment of the molecules [98]. In contrast, ion-Rydberg dynamics can be resolved using imaging techniques with only ns or 100 ns resolution. Additionally, the ion-Rydberg pair is highly-sensitive to external fields, such that aligned molecules can be prepared using comparably weak fields of mV/cm.

These features have been exploited recently in the group of Tilman Pfau at Universität Stuttgart to perform *in situ* observations of ion-Rydberg dynamics. Pfau's group first reported observations of the dynamics of a bound ion-Rydberg pair triggered by an external field and imaged using an ion microscope [96]. In an extension of this work, we collaborated with them on a joint project studying the collisions of unbound ion-Rydberg pairs [SC4]. To provide some further background to our contribution [SC4], we begin by discussing the results of the first experiment [96].

Here, authors Zou and co. prepared ion-Rydberg dimers at $t = 0$ in the presence of a weak electric field, which breaks the symmetry of the system and enables selective photoassociation of molecules with a specific orientation relative to the field axis. For $t > 0$, the field is quenched to zero and the system is knocked out of equilibrium, such that the molecular wavepacket undergoes oscillatory dynamics within

the binding potential. Due to the range of the ion-Rydberg interaction, the wavepacket oscillates with an amplitude of roughly 0.5 μm. The variation in internuclear separation was imaged destructively over an interval of roughly 1 μs using the ion microscope. Due to the anharmonicity of the binding potential, the amplitude of the oscillation undergoes collapse and revival dynamics [349]. Whilst the wavepacket's amplitude was observed to decay over time, observing subsequent revival of the amplitude was hindered by the short lifetime of the molecules in the experiment.

Whilst the work [96] studied wavepacket dynamics confined within a binding potential connected asymptotically with the Rydberg *P*-state, in [SC4] we sought to understand and control the vibrational dynamics on PEC connected asymptotically with the Rydberg *S*-state. In the asymptotic limit, the leading-order energy corrections to the *P* and *S* Rydberg states are both described by a polarisation potential $V \propto -n^7/R^4$. However, at decreasing internuclear separations the shape of their PEC deviate significantly as they couple to different neighbouring PEC. The *P*-state PEC forms a series of binding potentials due to avoided crossings with neighbouring low-field seeking states. In contrast, the *S*-state PEC exhibits no binding potential because it couples instead to high-field seeking states. Therefore, ion-Rydberg pairs interacting through PEC in this part of the spectrum experience a consistently attractive interaction, causing them to collapse inward to $R \to 0$ instead of oscillating as was the case in [96]. For this reason, *S*-state Rydberg atoms interacting with ions provide a platform for studying collisions, which is relevant for gaining insight into a broad range of phenomena, such as thermalisation [350], the catalysis of chemical reactions through enzymes [351] and properties of plasmas [352].

Another characteristic which fundamentally alters the nature of the dynamics near the *S*-state are the non-adiabatic couplings to neighbouring PEC, which are stronger than those to neighbouring curves of the *P*-state due to the smaller size of the avoided crossings. As a result, whilst the dynamics in [96] occurs essentially on a single PEC, the dynamics observed in [SC4] involves multiple coupled collision channels. The stark difference in gradient of the PEC of the shallow *S*-state polarisation potential and the steep high-field states gives rise to distinct collisional time scales, depending on which channel the wavepacket follows. Furthermore, the dynamics in this regime exhibits the counterintuitive property that wavepackets with higher collision energies will collide slower. This is because faster wavepackets are more likely to undergo non-adiabatic transitions and remain on the shallow polarisation potential. Therefore, initially fast pairs experience a weaker inward acceleration than their slower counterparts.

Our contribution to the project was to model the dynamics of ion-Rydberg pairs on the series of coupled PEC near the Rydberg *S*-state. These theoretical results provide a comparison to and insight into the experimental observations. For a given set of initial conditions, we simulated the wavepacket's trajectory across all open collision channels and weighted the results with the probability of following each channel, determined from the Landau-Zener transition probability (2.8). Furthermore, in order to compare the results of the simulations with the measurements in a meaningful way, it was necessary to account for various experimental parameters and additional time-delays present in the measurement scheme as well as the projection of the true internuclear distance on the 2D micro-channel detection plate.

Whilst we initially used our model to better understand the system, we later explored the possibility for controlling the dynamics using experimental control parameters. We focused in particular on the detuning of the Rydberg excitation laser, which determines the initial separation of the ion-Rydberg pair R_0. The value of R_0 has a strong influence over the time scale of the collision, since it affects the branching ratio of pairs along the steep and shallow collision channels. For example, pairs excited at smaller R_0 are more likely to exhibit adiabatic dynamics and follow steep collision channels, since the energy gaps of avoided crossings between neighbouring adiabatic PEC grow larger at smaller internuclear separations. Equally, pairs excited at larger R_0 have a higher probability of undergoing non-adiabatic transitions since

they not only encounter avoided crossings with a smaller gap size, but also gain additional kinetic energy from rolling inward on the polarisation potential. As a result, pairs formed at larger R_0 show a greater tendency to follow the shallow collision channel and collide more slowly.

By controlling R_0, it should therefore be possible to observe a change in the nature of the dynamics from slow non-adiabatic motion of the nuclei along the polarisation potential at large R_0 to fast adiabatic motion at small R_0. In addition, varying the principal quantum number n of the Rydberg state should also have an impact on the dynamics. For example, with increasing n the crossings between the S-state and the high-field seeking states become narrower such that non-adiabatic transitions are more likely.

Our simulations showed that this intuition indeed holds on the single-particle level. However, this trend cannot be observed as clearly when accounting for the uncertainty in the initial separation of the ion-Rydberg pair due to the finite linewidth of the excitation laser (approximately a few MHz) and the temperature of the gas (approximately 20 μK). Since the nature of the dynamics is strongly dependent on the initial separation, the variation in R_0 between measurements limits the degree of control over the branching ratio of ion-Rydberg pairs in the experiment.

Nonetheless, the works [SC4, 96] represent an important step toward realising experiments that can perform state-to-state chemistry and steer reactions along specific pathways with a small number of experimental control parameters. In the more immediate future, one could extend our work by exploring collisional association of ion-Rydberg dimers, where an unbound ion-Rydberg pair is excited onto the asymptotic region of the P-state's polarisation potential and then rolls inward along the binding potential. This experiment could be performed already with the setup available in Stuttgart and our code developed for modelling the dynamics could be straightforwardly ported.

4.2.2 Triatomic ion-Rydberg molecules [SC2, SC5]

In this remaining section, we outline our final two scientific contributions which study three-body systems of an ion-Rydberg pair interacting with an additional atomic species. In particular, in [SC2] we examine an ion-Rydberg pair in the presence of an additional ground-state atom and in [SC5] we study a Rydberg atom interacting with a pair of ions. We focus specifically on the existence of metastable three-bound bound states.

As discussed in section 3.2.3 as well as in the introduction of section 4.2, a Rydberg atom can bind to a distant ion over macroscopic distances due to the long-range electrostatic interaction between the ion's charge and the induced dipole moment of the Rydberg atom [92, 93]. These dimers have been photoassociated in cold atomic gases [95] and their lifetime was measured to be on the scale of 1 - 10μs. This result came as quite a surprise, since the current theoretical understanding suggests that the lifetime of these molecules should be limited only by radiative decay of the Rydberg atom [93, 283], which takes place on time scales of 100 - 1000 μs. Since charge exchange and non-adiabatic decay rates are also too low to explain the measured lifetimes [93, 283], we decided to investigate the possible influence of the background neutral gas on the lifetime of the molecule. It is out of these considerations that our project [SC2] emerged.

The clue that led us to consider that the background gas may be of relevance came from the range of gas densities that were reportedly used in the experiment in [95]. In particular, we found that the corresponding average interparticle spacings are comparable to, or even smaller than, the expected size of the Rydberg electron's orbit. Therefore, it seems plausible that collisions between the Rydberg atom and background gas atoms could occur on the lifetime of the Rydberg state. Using the reported experimental parameters, we determined that the classical scattering rate between the Rydberg atom

and the background gas atoms is the same order of magnitude as the decay rates measured in [95]. The details of this calculation are provided in appendix C. As has been done for similar works studying collisional-decay of ULRM [236], the results of the classical scattering model could be tested by performing measurements of the molecular lifetime at variable background gas densities, for which the classical model predicts a linear dependency. Beyond providing an explanation for the measured molecular lifetimes, confirming the validity of this hypothesis would offer a path to observing molecular vibrations over longer time scales than was possible in the work [96] discussed in section 4.2.1, thus enabling the observation of collapse and revival dynamics of vibrational wavepackets.

Whilst collisions with background gas atoms may indeed destabilise ion-Rydberg dimers, the presence of the background gas may also enable the formation of more complex polyatomic molecular species. This idea was the focus of our work [SC2], in which we consider an interacting three-body system of an ion, a Rydberg-state atom and a background gas atom in its electronic ground-state. Employing the Fermi pseudopotential formalism to describe the scattering between the Rydberg electron and the ground-state atom (see section 3.2.2 and in particular equation (3.6)), we demonstrate that ground-state atoms can become bound within regions of high electron density in the orbit of the Rydberg electron, whilst the Rydberg atom itself is electrostatically-bound to the ion.

We first determine adiabatic PES for the three-body system by diagonalising the system's electronic Hamiltonian in a finite basis of atomic Rydberg states. These exhibit local minima formed by the mixing of electronic states with low and high angular momentum character, which are coupled due to the ion's electric field. Two series of minima emerge, differing in the magnetic quantum number m of the underlying electronic states, which results in distinct nodal structures in the Rydberg electron's charge density. Inspired by the shape of their charge density, we classify these series as "snow angels" and "squids". We determine the vibrational states of the system using the multi-configuration time-dependent Hartree (MCTDH) method, described in section 2.5.3. These results reveal that the wells support both linear as well as nonlinear three-body bound states, where the ground-state atom is bound to regions of high electron density via attractive scattering.

The triatomic states considered in this work can be thought of as a non-polar ULRM bound to a distant ion. Future work could instead study the interaction of an ion interacting with a *polar* ULRM, such as a trilobite molecule. The large permanent dipole moment of the trilobite molecule would make such a system attractive for exploring the old problem of a charge interacting with a polar molecule [353–357], a system which in principle supports an infinite number of bound states above a critical value of the molecule's dipole moment given by the Fermi-Teller limit [358, 359].

We now turn to the final scientific contribution of this thesis [SC5]. Before describing the work however, we note that in both of the works previously discussed [SC2, SC4], the ion-Rydberg interaction potentials are dominated by the interaction of the Rydberg atom's dipole moment with the electric field of the ion (see discussion of ion-Rydberg interactions in section 3.2.3). The higher-order terms in the multipole interaction series provide mainly quantitative corrections to the PEC [360]. However, we have also found that these terms have a non-trivial impact on the strength of the non-adiabatic couplings between neighbouring PEC. For example, changing the sign of the ion's charge from positive to negative causes the avoided crossing associated with the ion-Rydberg binding potential to shrink by an order of magnitude, leading to considerably larger predictions for the non-adiabatic decay rates. This effect is chiefly caused by the quadrupole moment of the Rydberg electron and the results are discussed in appendix B.

The motivation of our work [SC5] was thus to explore regimes in which the role of the charge-dipole interaction term is reduced, or even absent entirely, such that other terms in the multipole expansion

dominate the physics of the system. One way to realise such a scenario is by considering a system of two cations arranged symmetrically on either side of a Rydberg atom, such that the Rydberg's dipole moment averages to zero. Hence, the leading-order term in the interaction series (3.8) is now the interaction of the ions with the Rydberg atom's quadrupole moment. However, the presence of the second ion also introduces a repulsive Coulomb interaction between the ion pair, which threatens to dominate the ion-Rydberg interaction entirely. In the electronic ground-state, this indeed appears to be the case, where analogous systems such H_3^{2+} are not expected to be stable [361–363]. However, since Rydberg interactions scale with n, it may be possible to find regimes in which the ion-Rydberg interaction can compete against the Coulomb repulsion.

To investigate this, we study a three-body system of an ^{87}Rb Rydberg atom interacting with two ^{87}Rb$^+$ cations. Using perturbation theory, we compare the scaling of the relative strengths of the ion-Rydberg and Coulomb interactions with the principal quantum number n. We find that above a critical value of $n \approx 66$, the ion-Rydberg interaction begins to dominate the Coulomb repulsion and can in principle lead to the formation of long-range binding potentials through mixing of Rydberg states in neighbouring hydrogenic manifolds. These predictions are supported by numerical results, where we determine the adiabatic PES of the ^{87}Rb$_3^{2+}$ system by diagonalising the electronic Hamiltonian in a finite basis of atomic Rydberg states. The PES reveal a host of potential wells with depths of several GHz formed by avoided crossings between Rydberg states in neighbouring hydrogenic manifolds at internuclear separations approximately 2 - 3 times the size of the extent of the Rydberg electron's orbit. Importantly, our numerical results reveal that binding potentials can form at smaller values of n than was predicted by first-order perturbation theory.

Using finite difference methods, we then show that these wells are deep enough to support several bound vibrational states of ^{87}Rb$_3^{2+}$ (see appendix D for details). Whilst the depths of the wells quickly diminish with increasing n, they should be deep enough to support bound states in the range $24 < n < 40$. Next, we investigate the stability of the molecular states by determining decay rates for Coulomb explosion and charge transfer processes. We describe the former process through semi-classical tunnelling of the bound vibrational wavepackets out of the potential well created in the adiabatic PES. Similarly, we model the latter process by determining the semi-classical tunnelling rate of the Rydberg electron between ionic cores. Our results indicate that the rate of Coulomb explosion is only relevant for the highest excited vibrational states, whilst the rate of charge transfer is strongly dependent on the value of n. In particular, we expect a difference of over two orders of magnitude in the charge transfer rate between states bound in wells at $n = 35$ and $n = 38$. The charge transfer rate decreases with n, such that at $n = 38$ the rate should be comparable or less than the rate of radiative decay of the Rydberg atom.

In summary, we have explored a metastable system which counterintuitively becomes more stable as additional energy, in the form of a Rydberg excitation, is provided to it. The strong dependence of the charge transfer rate on n may make such systems an interesting playground with which to study charge exchange in future. In addition, we could also explore the role of non-adiabatic decay, which are generally relevant in Rydberg molecular systems due to their high density of electronic states.

Chapter 5

Scientific contributions

Spectral properties of a three-body atom-ion hybrid system [SC1]

Spectral properties of a three-body atom-ion hybrid system

Daniel J. Bosworth [1,2,*] Maxim Pyzh,[1] and Peter Schmelcher[1,2]

[1]*Zentrum für Optische Quantentechnologien, Universität Hamburg, Luruper Chaussee 149, 22761 Hamburg, Germany*
[2]*Hamburg Centre for Ultrafast Imaging, Universität Hamburg, Luruper Chaussee 149, 22761 Hamburg, Germany*

We consider a hybrid atom-ion system consisting of a pair of bosons interacting with a single ion in a quasi-one-dimensional trapping geometry. Building upon a model potential for the atom-ion interaction developed in earlier theoretical works, we investigate the behavior of the low-energy eigenstates for varying contact interaction strength g among the atoms. In particular, we contrast the two cases of a static ion and a mobile ion. Our study is carried out by means of the multilayer multiconfiguration time-dependent Hartree method for bosons, a numerically exact *ab initio* method for the efficient simulation of entangled mixtures. We find that repulsive atom interactions induce locally distinct modifications of the atomic probability distribution unique to each eigenstate. While the atoms on average separate from each other with increasing g, they do not necessarily separate from the ion. The mobility of the ion leads in general to greater separations among the atoms as well as between the atoms and the ion. Notably, we observe an exchange between the kinetic energy of the atoms and the atom-ion interaction energy for all eigenstates, which is both interaction and mobility induced. For the ground state, we provide an intuitive description by constructing an effective Hamiltonian for each species, which aptly captures the response of the atoms to the ion's mobility. Furthermore, the effective picture predicts enhanced localization of the ion, in agreement with our results from exact numerical simulations.

I. INTRODUCTION

Over the past decades, our understanding of the physics of neutral ultracold atom and laser-cooled ion systems has seen unprecedented development, which has borne deep insights into their underlying and emergent physical phenomena. The superb degree of control achieved over these two quantum systems enables a high degree of accuracy and precision at both the single- and many-particle levels and has established them at the forefront of modern quantum many-body research. Recently, the two fields have been combined [1–4], creating a versatile experimental platform for exploring fundamental interaction processes between atoms and ions at milli-Kelvin to micro-Kelvin temperatures [5,6]. The most prominent experimental and theoretical accomplishments to date include studies on atom-ion collisions and reactions [7–11] and related phenomena, such as the formation of chemical bonds [12,13], sympathetic cooling [4,14,15], and charge transport [16,17]; quantum simulation of condensed matter physics [18] and polaron models [19,20]; quantum information investigations in the context of controlled entanglement generation [21,22] and decoherence effects [23]; and precision measurements where the ion acts as a local probe of the host gas's properties [3,4,24].

One of the ongoing challenges faced by experimentalists in the field of atom-ion research is to create hybrid systems at nano-Kelvin temperatures. The nano-Kelvin scale marks the boundary of the ultracold regime, in which quantum

phenomena dominate. The earliest hybrid traps were based on a straightforward superposition of optically trapped atoms with ions confined in a Paul trap. The drawback of this scheme was found to be a heating mechanism caused by the excess micromotion of the ion [25,26]. In an effort to overcome this perceived limitation, several alternative schemes are currently being pioneered, such as photoionization of an atomic cloud using a femtosecond laser [27], optical traps for ions [28–32], and highly excited Rydberg atoms within an atomic cloud [17,33,34].

In addition to the endeavors with alternative trapping schemes, proposals were also made to use the established Paul trap approach with a ^{6}Li - ^{174}Yb$^+$ hybrid mixture [35], whose high mass imbalance was predicted to undermine the micromotion-induced heating. This setup was realized in a recent experimental breakthrough [36], reaching temperatures in the s- and p-wave scattering regime. In this regime of few partial waves, the increasingly weighty quantum effects lead to deviations away from classical predictions and may enable the experimental observation of hitherto-unseen atom-ion Feshbach resonances [37]. The presence of such a resonance would allow for complete control over the scattering parameters and thus, over the atom-ion interaction itself.

These recent experimental advances provide fresh impetus to extend the current theoretical understanding about the nature of the long-range atom-ion interaction at zero temperature. In this $T = 0$ regime, the inelastic processes dominate the system's scattering dynamics and atoms can be captured in the weakly bound states of the atom-ion polarization potential. These bound states enable the formation of so-called mesoscopic molecular ions, which are typically hundreds of

*dan.bosworth@physnet.uni-hamburg.de

nanometres in size [38,39]. The amount of atoms captured by the ion is limited by the interaction strength among the atoms. The kinetic energy released during the capture process is distributed via phonon excitations among the unbound fraction and a density disturbance is created at the ion position [40,41] or even, in the limit of a Tonks-Giradeau gas, a density bubble [42].

In our previous studies, we performed detailed analysis of the ground-state properties and dynamical behavior of an atom-ion hybrid system for a static ion in a quasi-1D system [41,43], analogous to the aforementioned ^{6}Li - ^{174}Yb$^+$ mixture. We have also examined the case of an equal mass system [39], analogous to optically trapped ions subject to the same external potential as the neutral atoms. In this work, we present an extension of both these investigations to the lowest energy eigenstates of a few-body system composed of a single ion and two neutral bosonic atoms at zero temperature, with both species parabolically confined in a quasi-1D geometry. The eigenstates of our few-body hybrid mixture are obtained via the multilayer multiconfiguration time-dependent Hartree method for mosons (ML-MCTDHB) [44,45], a numerically exact *ab initio* method that efficiently accounts for the intra- and interspecies correlations via a time-dependent, variationally optimized basis. Previously, ML-MCTDHB has been successfully applied to solve similar problems in mixtures of neutral bosonic species [46,47] and there is also an extension for dealing with mixtures of both bosonic and fermionic species [48–50]. Our chosen numerical method requires interactions to be finite valued at all spatial grid points of the system, including at distances below the range of validity R_0 of the atom-ion interaction's long-distance tail, which varies with the atom-ion separation r as $-1/r^4$. To this end, we employ a model interaction potential whose parameters can be mapped to the real scattering parameters by means of quantum defect theory [43]. We characterize the five lowest-energy eigenstates of our few-body hybrid mixture across regimes of weak to strong atomic interactions through using the atom-atom and atom-ion distance correlations, number state composition, and distribution of the total energy among the energy components.

This work is organized as follows. In Sec. II, we introduce our model Hamiltonian, describe the form of the atom-ion interaction, and present our numerical methodology. In Sec. III, we present the eigenstate spectrum of our three-body molecular ion system, before proceeding to examine the effects of varying interatomic interactions and ion mobility on the individual eigenstates in Sec. IV. In Sec. V, we conclude with a summary of our findings, examine the experimental viability of our model, and discuss prospective directions for future work.

II. ATOM-ION HYBRID MODEL AND NUMERICAL APPROACH

In this section, we first present the Hamiltonian describing the atom-ion hybrid system in the laboratory frame (Sec. II A). We then introduce two alternative coordinate frames, which will prove themselves useful for the numerical treatment and physical analysis (Sec. II B). Finally, we provide a brief overview of the computational approach used throughout

this work (Sec. II C) and define several physical quantities, which we will use to characterize the low-energy eigenstates (Sec. II D).

A. Atom-ion hybrid model

We consider a system composed of a single ion of mass m_I and N neutral bosonic atoms of mass m_A at zero temperature. We assume that both species are confined within quasi-1D parabolic traps, such that they can only move along the z direction, with axial trapping frequency ω_A for the atoms and ω_I for the ion. The atom-atom interactions are of s-wave character and are described by a contact pseudopotential.

When approaching a charged particle, the neutral atoms become polarized, resulting in long-range interactions between the ion and the induced dipole moments of the atoms. At large separations, the interaction between an atom at position z_A and an ion at position z_I behaves as $-\alpha e^2/2(z_A - z_I)^4$, where α is the polarizability of the atom and e is the elementary charge. This interaction introduces a new length $R^* = \sqrt{\alpha e^2 m_A/\hbar^2}$ and energy scale $E^* = \hbar^2/2m_A R^{*2}$ to the system, in addition to those set by the external traps. In atom-ion hybrid experiments [6], the interaction range is typically $R^* \approx 100$ nm.

To properly account for interactions between the atomic and ionic species at all distances, while also ensuring our model is numerically tractable, we introduce a short-distance cutoff to the $1/r^4$ potential and describe the interaction at small separations by a repulsive barrier. The explicit model interaction used was developed previously in earlier works based on quantum defect theory [41,43] and can be expressed in units of E^* and R^* as

$$V_{AI}(r) = v_0 e^{-\gamma r^2} - \frac{1}{r^4 + \frac{1}{\kappa}}, \tag{1}$$

where $r = z_A - z_I$ denotes the atom-ion separation, v_0 is the height, and γ is the width of the repulsive short-range barrier, while κ sets the short-range cutoff to the attractive tail and determines the number of bound states. It has been shown theoretically that at ultracold temperatures the rate of inelastic atom-ion collisions is larger for states with smaller binding energies [38]. Accordingly, we choose our model parameters to be $v_0 = 3\kappa$, $\gamma = 4\sqrt{10\kappa}$, and $\kappa = 80$, in units of E^*, R^{*-2}, and R^{*-4}, respectively. This choice accounts for the two uppermost bound states closest to the continuum $E = 0$ [43].

The species Hamiltonians H_A and H_I take the following form in units of E^* and R^*:

$$H_A = \sum_{i=1}^{N} \left(-\frac{\partial^2}{\partial z_{Ai}^2} + \frac{z_{Ai}^2}{l_A^4} \right) + \sum_{i<j}^{N} g\delta(z_{Ai} - z_{Aj}) \tag{2a}$$

$$= K_A + P_A + V_{AA},$$

$$H_I = -\beta \frac{\partial^2}{\partial z_I^2} + \frac{z_I^2}{l_A^4 \beta \eta^2} = K_I + P_I, \tag{2b}$$

where z_{Ai} denotes the position of the ith atom, $l_A = \sqrt{\hbar/m_A \omega_A}/R^*$ is the oscillator length of the parabolically confined atoms rescaled by R^*, g is the effective strength of the atom-atom interaction, $\beta = m_A/m_I$ is the interspecies mass ratio, z_I is the position of the ion, and $\eta = \omega_A/\omega_I$ is the ratio of the trapping frequencies. K_A and K_I abbreviate the kinetic
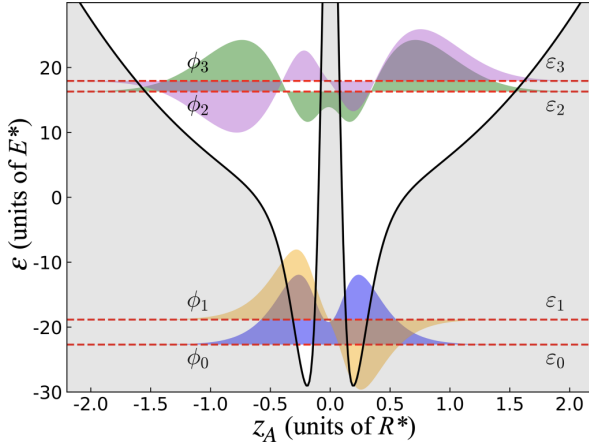
FIG. 1. The first four lowest-energy solutions to the single-particle eigenvalue problem $h_{1b}\phi_i(z_A) = \varepsilon_i\phi_i(z_A)$ [see Eq. (3)], describing a single atom in a harmonic trap interacting with a static ion localized at $z = 0$. The effective potential experienced by the atom is given by the solid black curve. The eigenstates $\{\phi_i(z_A)\}_{i=0}^3$ (filled curves) are shown along red dashed lines, which indicate their eigenenergies $\{\varepsilon_i\}_{i=0}^3$. Energies and lengths are given in units of E^* and R^* set by the atom-ion interaction. The harmonic trap length is $l_A = 0.5$, in units of R^*.

terms, P_A and P_I are the external potentials, and V_{AA} is the contact interaction. We fix $l_A = 0.5$, $\eta = 1$, and $N = 2$ for the remainder of this work.

To provide some basic intuition for the system at hand, we assume that the ion is localized at the origin (i.e., $l_I = 0$, well approximated by either a heavy ion or a tight trap) and that the atoms are noninteracting ($g = 0$). In this case, the ion acts as a one-body potential for the atoms and does not receive any feedback from them. Our model reduces to a single-particle problem,

$$h_{1b} = -\frac{\partial^2}{\partial z_A^2} + \frac{z_A^2}{l_A^4} + V_{AI}(z_A), \tag{3}$$

which describes a single atom in an effective potential, being the superposition of the harmonic trap and atom-ion potential (see solid black curve in Fig. 1). The Schrödinger equation belonging to the one-body Hamiltonian h_{1b} can be solved straightforwardly using exact diagonalization. We choose to use a fast Fourier transform (FFT) discrete variable representation (DVR) basis.[1] The four lowest-energy single-particle eigenstates $\{\phi_i(z)\}_{i=0}^3$ of the eigenvalue problem $h_{1b}\phi_i = \varepsilon_i\phi_i$ are depicted in Fig. 1. As mentioned above, our choice of parameters for the model interaction (1) results in two bound states in the atom-ion potential: ϕ_0 and ϕ_1. Due to the steep $-1/z^4$ contribution, these two bound states share a similar spatial extent ($\sim R^*$) and the peaks of their probability amplitudes coincide with the potential minima at $\approx \pm 0.3 R^*$. In

---

[1]Specifically, we use a FFT DVR basis of size $n = 333$, which ensures the single-particle eigenenergies are converged up to the sixth decimal place.

contrast, the higher energy eigenstates ϕ_2 and ϕ_3 are extended across the harmonic trap ($\sim 2R^*$) with a significantly smaller probability amplitude at the potential minima. From now on, we will refer to ϕ_0 and ϕ_1 as *molecular orbitals* and ϕ_2 and ϕ_3 will be called *vibrational orbitals*.

In this work, we perturb this single-particle picture h_{1b} in two ways: first by considering interactions between the trapped pair of bosons and second by including the motion of the ion. The former is parameterized by the contact interaction strength g and the latter is parameterized by the mass ratio β, which determines the relative localization between the two trapped species.

B. Nonlaboratory reference frames

We emphasize that in the laboratory frame (LF), the atomic and ionic degrees of freedom are highly entangled because atoms can be bound to the mobile ion, which possesses a spatially extended probability density. This fact makes it difficult to obtain well-converged numerical results. To account for these correlations, we replace the atom coordinates z_{Ai} with the relative distances with respect to the ion $r_i = z_{Ai} - z_I$. The remaining ion coordinate z_I can be retained (ion frame, IF) or replaced by the combined center of mass $R = (m_I z_I + m_A \sum_i z_{Ai})/M$ of the system, where $M = m_I + N m_A$ is the system's total mass (center of mass frame, CMF).

The primary frame used for the numerical simulations was the CMF, whose main advantage is its numerical stability during eigenstate acquisition and its more rapid convergence compared to the other frames. The corresponding CMF Hamiltonian is given by

$$
\begin{aligned}
H = &\sum_{i=1}^N \left(-(1+\beta)\frac{\partial^2}{\partial r_i^2} + (1-d)\frac{r_i^2}{l_A^4} \right) \\
&+ \sum_{i=1}^N \left(v_0 \exp\left(-\gamma r_i^2\right) - \frac{1}{r_i^4 + \frac{1}{\kappa}} \right) \\
&+ \sum_{i<j} \left(g\delta(r_i - r_j) - 2\beta\frac{\partial}{\partial r_i}\frac{\partial}{\partial r_j} - \frac{2d}{l_A^4}r_i r_j \right) \\
&- d\frac{\partial^2}{\partial R^2} + \frac{1}{l_A^4\beta\eta^2}(1+N\beta\eta^2)R^2 + \frac{2d}{l_A^4\beta\eta^2}(\eta^2-1)\sum_{i=1}^N R r_i,
\end{aligned}
\tag{4}
$$

where the parameters have the same meanings as discussed in Sec. II A and $d = \beta/(1 + N\beta)$. For equal trapping frequencies $\eta = 1$, the above Hamiltonian decouples into two sub-Hamiltonians: one for the center of mass coordinate R and the other for relative coordinates $\{r_i\}$. The center of mass sub-Hamiltonian $H_R(\eta = 1) = -d\frac{\partial^2}{\partial R^2} + \frac{R^2}{l_A^4 d}$ describes a quantum harmonic oscillator of mass $M = 1/2d$ and frequency $\Omega = 2/l_A^2$ and can be solved analytically. The atom-ion interaction now takes the form of a one-body potential, as was also the case for the static ion example discussed in Sec. II A. However, the ion's motion induces two additional interactions between the relative coordinates, namely the positional ($r_i r_j$) and the derivative ($\frac{\partial}{\partial r_i}\frac{\partial}{\partial r_j}$) couplings. In the limit of a static ion ($\beta \to 0$), these additional interactions vanish, and for $g = 0$,

we recover the one-body Hamiltonian (3) describing a single boson interacting with a static ion.

The other frame used for analysis was the IF. While the IF is less efficient than the CMF, it is nonetheless more efficient than the LF since the entanglement between the interspecies degrees of freedom is reduced. Due to numerical instabilities, however, it is challenging to obtain higher excited states in the IF, which limits the analysis in this frame solely to the ground state. Nevertheless, in contrast to the CMF, the IF provides access to the single-particle atomic $\rho_1(z_A)$ and ionic $\rho_1(z_I)$ density distributions, which are laboratory frame quantities and thus allow for an easier interpretation (see Supplementary Material in Ref. [39]). The IF Hamiltonian is given by

$$
\begin{aligned}
H = \sum_{i=1}^{N} & \left(-(1+\beta)\frac{\partial^2}{\partial r_i^2} + \frac{r_i^2}{l_A^4} \right) \\
& + \sum_{i=1}^{N} \left(v_0 e^{-\gamma r^2} - \frac{1}{r^4 + \frac{1}{\kappa}} \right) \\
& - \beta\frac{\partial^2}{\partial z_I^2} + \frac{1}{l_A^4}\left(N + \frac{1}{\beta\eta^2} \right)z_I^2 \\
& + \sum_{i<j} \left(g\delta(r_i - r_j) - 2\beta\frac{\partial}{\partial r_i}\frac{\partial}{\partial r_j} \right) \\
& + 2\sum_{i=1}^{N} \left(\frac{z_I r_i}{l_A^4} + \beta\frac{\partial}{\partial z_I}\frac{\partial}{\partial r_i} \right).
\end{aligned}
\tag{5}
$$

Note that the derivative coupling term $(\frac{\partial}{\partial r_i}\frac{\partial}{\partial r_j})$ is also present in this frame and that z_I and r_i cannot be decoupled for any choice of parameters.

C. Computational approach

To solve for the lowest energy eigenstates of our three-body problem, we employ the multilayer multiconfiguration time-dependent Hartree method for bosons (ML-MCTDHB) [44,45]. ML-MCTDHB is a numerically exact *ab initio* method for performing time-dependent simulations of many-body quantum dynamics and it belongs to a wider family of multiconfiguration Hartree-Fock methods [51–54]. In the same manner as its sibling methods, ML-MCTDHB utilizes a variationally optimized time-dependent basis which enables us to perform efficient calculations in a truncated Hilbert space, while ensuring that we fully cover the active subspace of the complete Hilbert space. The multilayer expansion allows for adopting the wave-function ansatz to system-specific intra- and interspecies correlations. As a result, it is able to more efficiently treat mixtures with large numbers of particles in comparison to approaches that do not utilize multilayering [55].

The construction of the ML-MCTDHB wave-function ansatz describing our three-body system proceeds as follows. In the first step, we group together the indistinguishable degrees of freedom (DOF) and assign to them $S_\sigma \in \mathbb{N}$ species wave functions $\{|\psi_i^\sigma(t)\rangle\}_{i=1}^{S_\sigma}$, with σ denoting the distinct species. For our case, there are only two distinct species, corresponding to the atomic and ionic DOF. Next, the total many-body wave function is written as a linear combination

of product states:

$$
|\psi(t)\rangle = \sum_{i=1}^{S_I}\sum_{j=1}^{S_A} A_{ij}^1(t) \left|\psi_i^I(t)\right\rangle \left|\psi_j^A(t)\right\rangle,
\tag{6}
$$

where $A_{ij}^1(t)$ are time-dependent top-layer coefficients and $\sigma = A$ stands either for z_i or r_i, while $\sigma = I$ for z_I or R, depending on the chosen frame. For $\eta = 1$, the CMF DOF (r_i and R) decouple, such that (6) becomes a single product state: $|\psi(t)\rangle = |\psi^I(t)\rangle |\psi^A(t)\rangle$. In such cases, the step in Eq. (6) is usually skipped as solving the sub-Hamiltonians independently using single-layer MCTDHB is more efficient.

In the second step, the species wave functions $|\psi_i^\sigma\rangle$ for indistinguishable DOF are expanded in time-dependent number states $|\mathbf{n}\rangle_t^\sigma$ to incorporate proper, in our case bosonic, quantum statistics:

$$
\left|\psi_i^{(\sigma)}(t)\right\rangle = \sum_{\mathbf{n}|N_\sigma} A_{i;\mathbf{n}}^{2;\sigma}(t) |\mathbf{n}\rangle_t^\sigma,
\tag{7}
$$

with time-dependent species-layer coefficients $A_{i;\mathbf{n}}^{2;\sigma}(t)$. The number states $|\mathbf{n}\rangle^\sigma = (n_1, \ldots, n_{s_\sigma})$ are composed of $s_\sigma \in \mathbb{N}$ time-dependent single-particle functions (SPFs) $\{|\phi_i^\sigma(t)\rangle\}_{i=1}^{s_\sigma}$ and the sum goes over all possible number state configurations $\mathbf{n}|N_\sigma$ which fulfil the constraint of a fixed number of particles $\sum_{i=1}^{s_\sigma} n_i = N_\sigma$.

Finally, the time-dependent SPFs are represented on a one-dimensional discrete variable representation (DVR) basis $\{|\chi_i^\sigma\rangle\}_{i=1}^{\mathcal{M}_\sigma}$ (in our case, a FFT DVR basis),

$$
\left|\phi_i^\sigma(t)\right\rangle = \sum_{j=1}^{\mathcal{M}_\sigma} A_{ij}^{3;\sigma}(t) \left|\chi_j^\sigma\right\rangle,
\tag{8}
$$

with time-dependent particle-layer coefficients $A_{i;j}^{3;\sigma}(t)$ [56].

The Hilbert space of our system is truncated at each layer and controlled through the values of S_σ, s_σ, and $\mathcal{M}_\sigma$. This allows us to tailor our ansatz to suit the degree of intra- and interspecies correlations present in the system. Note that in contrast to standard approaches, the SPFs are time dependent, allowing for a considerable boost in computation time.

The equations of motion for the three layers of coefficients A_{ij}^1, $A_{i;\mathbf{n}}^{2;\sigma}$, and $A_{i;j}^{3;\sigma}$ outlined above are derived from the Dirac-Frenkel variational principle [52]:

$$
\langle\delta\psi| (i\partial_t - \hat{H}) |\psi\rangle = 0.
\tag{9}
$$

The ground state and higher excited states are obtained by means of improved relaxation of an initial input state. Specifically, ML-MCTDHB propagates the non-top-layer coefficients $A_{i;\mathbf{n}}^{2;\sigma}$ and $A_{i;j}^{3;\sigma}$ in imaginary time to a fixed point, at which point it diagonalizes the top-layer A_{ij}^1 matrix. This process is performed recursively until the top-layer and non-top-layer coefficients become constant during the diagonalization and imaginary-time propagation, respectively. This converged result is a stationary state of the system, which lies in the truncated Hilbert space given by the ML-MCTDHB ansatz. Different stationary states can be obtained by carefully selecting the initial input wave function provided to the improved relaxation routine.

Working in the CMF and IF offers a distinct numerical advantage to working in the LF since, as discussed in Sec. II B,

position correlations between the atom and ion in a bound pair are accounted for implicitly within the relative coordinate $r_i = z_{Ai} - z_I$. This enables us to further truncate our active Hilbert space on the top layer (6) in these frames, resulting in greater computational efficiency. We emphasize that this additional level of truncation is only possible due to the multilayer structure of our wave function ansatz.

D. Observables

Here we introduce several physical quantities used to characterize the eigenstates in Sec. IV.

1. Interatomic and interspecies separation distributions

In the decoupled CMF ($\eta = 1$), we focus on the relative sub-Hamiltonian [see Eq. (4)] with bosonic DOF r_i. For a system of two atoms with relative positions r and r' to the ion, the wave function takes the form $\psi(r, r')$ and the probability density for finding the atoms in the configuration (r, r') is given by the density $\rho_2(r, r') = \psi(r, r')^* \psi(r, r')$.

We are now able to extract a useful quantity related to LF coordinates, namely the interatomic separation distribution $\rho_1(z_A - z_A')$. To this end, we note that

$$\int dr\,dr'\, \rho_2(r, r') = \int dX\,dY\, \tilde{\rho}_2(X, Y) = 1, \qquad (10)$$

where in the second step we do a coordinate transformation $X = r - r'$, $Y = (r + r')/2$, and $\tilde{\rho}_2(X, Y) = \rho_2(r(X, Y), r'(X, Y))$. Now by integrating out the coordinate Y, we obtain the reduced one-body density $\rho_1^{AA}(X)$:

$$\rho_1^{AA}(X = z_A - z_A') = \int dY\, \tilde{\rho}_2(X, Y). \qquad (11)$$

Additionally, in both the CMF and IF, we can evaluate the expectation values for the atom-atom and atom-ion separations:

$$\langle d_{AA} \rangle = \int dX\, |X| \rho_1^{AA}(X), \qquad (12)$$

$$\langle d_{AI} \rangle = \int dr\, |r| \rho_1(r), \qquad (13)$$

where in the IF $\rho_1(r) = \int dz_I dr'\, \psi^*(z_I, r, r') \psi(z_I, r, r')$. Whereas in the CMF, $\rho_1(r) = \int dr'\, \rho_2(r, r')$ is the one-body probability density of the relative coordinate $r = z_A - z_I$, giving us the interspecies separation distribution.

2. Bunching probability

In this paper, we often refer to the atoms as being *bunched* or *antibunched*. To clarify what is meant by this quantitatively, we define the so-called bunching probability as the total probability for the atoms to be found on the same side of the ion, irrespective of their separation. This can be written explicitly as follows:

$$P_{\text{bunched}} = \int_{-\infty}^{0} \int_{-\infty}^{0} dr\,dr' \rho_2(r, r') + \int_{0}^{\infty} \int_{0}^{\infty} dr\,dr' \rho_2(r, r'), \qquad (14)$$

i.e., the probability to be found in the lower-left or upper-right quadrants of the two-particle density $\rho_2(r, r')$. Naturally, $P_{\text{antibunched}} = 1 - P_{\text{bunched}}$. In the bunched configuration, atoms
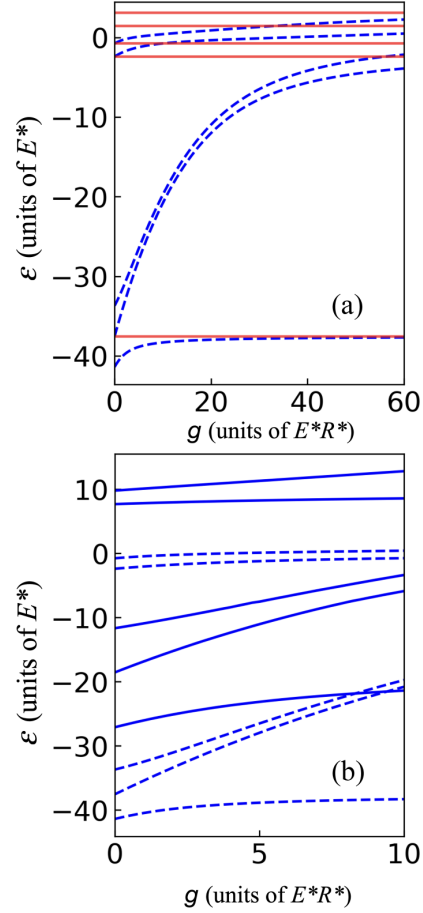

FIG. 2. Low-energy spectrum of two bosons coupled to a single ion as a function of the atom-atom contact interaction strength g for (a) a static ion $\beta = 0$ (dashed lines) and (b) a mobile ion $\beta = 1$ (solid lines). The corresponding energies for two noninteracting fermions are indicated in panel (a) by the horizontal solid red lines. Note that the eigenenergies should approach the fermionic values in the Tonks-Girardeau limit $g \to \infty$. The static ion spectrum from panel (a) is given additionally for reference in panel (b) (dashed lines). Note the different range of g values in the subfigures (a) and (b).

favor the same side of the ion $P_{\text{bunched}} > P_{\text{antibunched}}$, whereas in the antibunched configuration, the atoms are more likely to be found on opposite sides of the ion $P_{\text{bunched}} < P_{\text{antibunched}}$.

III. LOW-ENERGY SPECTRUM

In this section, we analyze how the five lowest lying eigenenergies of our hybrid model (see Sec. II) change under variation of the interatomic interaction strength g and elaborate on the differences between a static and a mobile ion.

We first discuss the spectrum for the case of a static ion pinned at $z_I = 0$, where the atom-ion interaction [see Eq. (1)] reduces to an effective one-body potential. The first five eigenenergies are given by the blue dashed lines in Fig. 2(a). They increase monotonically with g and approach the Tonks-Girardeau (TG) energies ($g \to \infty$), equivalent to those of

two noninteracting fermions subject to the same one-body potential (solid red lines) [57]. The ground state at $g = 0$ corresponds to the bosonic number state $|2, 0, 0, 0\rangle$ built from SPFs of h_{1b} [Eq. (3)] (see also Fig. 1). It saturates rapidly to the corresponding TG energy of the fermionic number state $|1, 1, 0, 0\rangle$, tapering off beyond $g = 4$.

The first and second excited states at $g = 0$ correspond to excitations of one or both atoms to the second molecular orbital, i.e., $|1, 1, 0, 0\rangle$ and $|0, 2, 0, 0\rangle$. We observe that with increasing g, the energy gap between these states, given by $\epsilon_2 - \epsilon_1$, first decreases up to $g = 10$ before increasing again and then tapering off at large g as the system approaches the TG limit ($g \to \infty$). In this limit, the interacting bosons which constitute the first and second excited states are energetically mapped to pairs of noninteracting fermions with number state configurations $|1, 0, 1, 0\rangle$ and $|1, 0, 0, 1\rangle$, respectively. The energy gap between these states is equal to the gap at $g = 0$ between the third and fourth excited states $\epsilon_4 - \epsilon_3$. The third and fourth excited states at $g = 0$ correspond to excitations of a single atom to one of the vibrational orbitals, i.e., $|1, 0, 1, 0\rangle$ and $|1, 0, 0, 1\rangle$. They are quite robust to g variation, being a consequence of the reduced spatial overlap between the molecular and vibrational orbitals. In the TG limit, they map to the fermionic states $|0, 1, 1, 0\rangle$ and $|0, 1, 0, 1\rangle$ and as a result, they have the same energy gap as at $g = 0$.

The ion's mobility has two effects on the spectrum [blue solid lines in Fig. 2(b)]: (i) a positive energy shift for all states and (ii) increased energy separation among the eigenstates. Aside from this, we still observe a monotonous increase of the energies with g. Interestingly, we also observe a tapering off of the energy of the ground state at large g, which is reminiscent of the energy mapping between hard-core bosons and noninteracting fermions. Formally, however, the criteria for the TG mapping are not fulfilled since first we do not have a single- but rather a two-component system and second the hard-core interaction exists only between the atoms.

IV. ANALYSIS OF EIGENSTATES

In this section, we will examine in detail the individual eigenstates composing the low-energy spectrum presented in Sec. III, from the ground state up to the fourth excited state (Secs. IV A–IV E). In particular, we will explore the effect of varying atomic interactions and ion mobility on the properties of the eigenstates. For each state considered, we will analyze the distribution of energy among the various energy components and discuss what implications this has for the interatomic and interspecies separation distributions introduced in Sec. II D 1. Moreover, we will also consider to what extent the single-particle picture h_{1b} based on Eq. (3) is modified by exploring the number state composition of each eigenstate. Each subsection focuses on a specific eigenstate and begins with a short summary of the main physical properties of that state.

A. Ground state

In the ground state, both atoms bind to the ion in the lowest bound state and show no preference for bunching or antibunching when they are noninteracting and the ion is

static. Finite interactions between the atoms cause them to separate to opposite sides of the ion (see Sec. IV A 1). For an equal mass system ($\beta = 1$), the ion's mobility results in a slight preference for the noninteracting atoms to be bunched, which can be understood using an effective potential model that shows the atom pair clusters at the trap center when the ion is mobile (see Sec. IV A 2). This interspecies correlation effect competes against the interatomic anticorrelations, delaying the onset of complete separation of the atoms. The fully separated atom pair pins the mobile ion from either side, such that it becomes increasingly localized at the trap center (see Sec. IV A 3).

1. Static ion

The ground state of two noninteracting ($g = 0$) atoms coupled to a static ($\beta = 0$) ion located at the trap center $z_I = 0$ is given by the number state $|2, 0, 0, 0\rangle$ with regard to the single-particle eigenstates of h_{1b} [see Eq. (3)]; i.e., both atoms occupy the lowest molecular orbital ϕ_0 in Fig. 1. The bunched and antibunched configurations are equally probable [see Fig. 4(a)], which is further indicated by the two peaks in the interatomic separation distribution $\rho_1^{AA}(z_A - z_A')$ [dashed curve with blue circles in Fig. 3(a)].

With increasing g, we observe in Fig. 3(a) a depletion of the central peak at $z_A = z_A'$ in favor of the side humps, which smoothly shift their position to larger separations. As a result, the atom-atom separation d_{AA} increases [dashed line in the inset of Fig. 3(a)]. The sharp initial growth in the total energy [see Fig. 2(b)] can be mainly attributed to the behavior of the intra-atomic interaction V_{AA}, which increases monotonously for $g < 3$ and decreases thereafter as the probability for the atoms to occupy the same position gradually vanishes [dashed curve with blue circles in Fig. 3(e)]. In addition, there is a near 1:1 exchange between the atomic kinetic K_A and the atom-ion interaction V_{AI} energies with increasing interaction strength g: The increased probability for the antibunched configuration enables the atoms to localize more around the atom-ion potential minimum [increasing K_A, dashed curve with black circles in Fig. 3(c)] and slide down within the V_{AI} potential [decreasing V_{AI}, pink dashed line in Fig. 3(d)]. Thus, the distance between the atoms and the ion d_{AI} [dashed line in the inset of Fig. 3(b)] is almost unchanged, though it shows a gradual increase due to the increasingly depleted $z_A = z_I$ region [see dashed curves in Fig. 3(b)], which is further reflected in the gentle increase of the atomic trap potential energy P_A [dashed curve with triangles in Fig. 3(e)] since the atoms have a reduced probability to be found at the origin $z_A = 0$.

At stronger interactions ($g = 10$), the bunched configuration becomes completely suppressed and the atoms exist on opposite sides of the ion [see Fig. 4(b)]. While approaching the TG regime, all energies begin to saturate and d_{AA} approaches the corresponding limit of the separation between two noninteracting fermions ≈ 0.6, i.e., the distance between the V_{AI} minima (see Fig. 1). V_{AA} decreases for large g and will approach zero in the TG limit.

2. Mobile ion: Impact on the atoms

Let us now consider the impact of the ion's mobility ($\beta = 1$) on the ground-state properties. The two-body
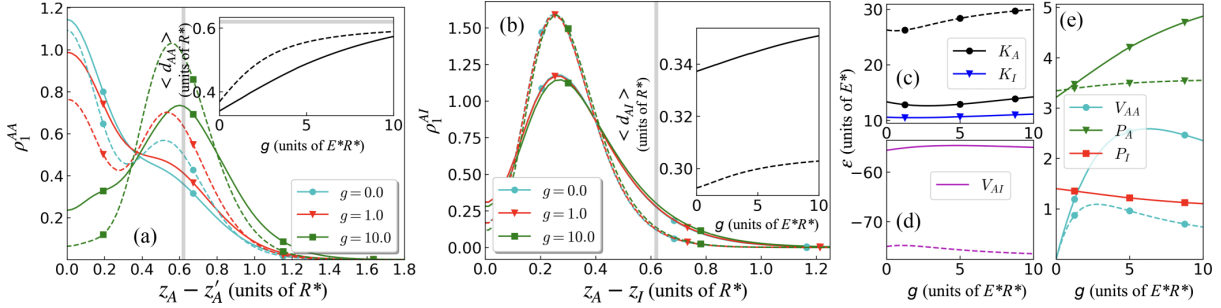
FIG. 3. Key observables for the ground state. (a) Interatomic separation distribution $\rho_1^{AA}(z_A - z_A')$ for different atom-atom coupling strengths g. The inset shows the expectation value $\langle d_{AA} \rangle$ for the atom-atom separation as a function of g [Eq. (12)]. (b) Interspecies separation distribution $\rho_1^{AI}(z_A - z_I)$ for varying atom-atom coupling strengths g. The inset shows the expectation values $\langle d_{AI} \rangle$ for the atom-ion separation as a function of g [Eq. (13)]. [(c)–(e)] The evolution of the laboratory frame energy components with atom-atom coupling strength g. Note that for panels (a) and (b) the gray lines indicate the distance between the minima of the atom-ion interaction potential (1). Due to the parity symmetry, it is sufficient to show only the positive semiaxis. All subfigures: the solid curves indicate results for a mobile ion, while dashed curves correspond to results for a static ion.

density $\rho_2(r, r')$ becomes more spread out [compare Figs. 4(a) and 4(c)], which results in a decrease of the kinetic energy of the atoms K_A and a positive shift in the atom-ion interaction energy V_{AI} (see middle and upper solid curves in Figs. 3(c) and 3(d), respectively). Similarly, the atom-ion separation distribution $\rho_1^{AI}(r)$ broadens, leading to an increase in the atom-ion separation d_{AI} [compare curves in inset of Fig. 3(b)]. By comparing the interatomic separation distributions ρ_1^{AA} between the static and mobile cases [dashed and solid lines in Fig. 3(a)], we infer that the additional derivative and positional coupling terms in Eq. (4), introduced by the ion mobility, impede the process of particle separation. Thus, when $\beta = 1$, the average atom-atom distance d_{AA} reaches values of the static ion system only at a stronger coupling g [compare curves in the inset of Fig. 3(a)].

To obtain a better understanding of this mobility-induced bunching effect [see Fig. 4(c)], we now examine the ground state through the lens of species mean-field (SMF) theory. This will allow us to extract for each species an effective one-body potential induced by the other component, effectively decoupling the equations of motion between the distinguishable DOF. As already discussed in Sec. II B, the LF is badly suited for this purpose. On the other hand, the IF incorporates the correlations of a bound atom-pair following the ion movement and moreover allows us to obtain several useful physical quantities of the LF. In the notation of ML-MCTDHB, the IF

SMF ansatz assumes a single product state on the top layer (6):

$$\psi(z_I, r_1, \ldots, r_N) \approx \psi_A(r_1, \ldots, r_N)\psi_I(z_I). \quad (15)$$

In Fig. 5(a), we compare the one-body density $\rho_1(z_A)$ of the atoms obtained with the SMF ansatz (blue triangles) to that of the exact ML-MCTDHB solution (black squares) in the IF for noninteracting atoms $g = 0$ bound to a mobile ($\beta = 1$) as well as a heavy, near-static ($\beta = 0.034$) ion. The latter mass ratio corresponds to the species pairing ^{6}Li - ^{174}Yb$^+$. We additionally show the results obtained via the SMF ansatz in the LF (pink circles) for comparison. For a heavy ion, the SMF ansatz is well justified in both frames [compare dashed curves in Fig. 5(a)]. The atoms are most likely to be found around the minima of the atom-ion potential at $\approx \pm 0.3R^*$. For a mobile ion ($\beta = 1$), the exact result shows that the atoms are now most likely to be found at the trap center [see solid curve with black squares in Fig. 5(a)]. While the IF SMF ansatz approximately captures this feature, it nonetheless shows substantial quantitative deviations from the exact result. Thus, the entanglement between the DOF z_I and r_i, neglected in the IF SMF, favors increased bunching of atoms around the center of the harmonic trap. The LF SMF ansatz, which neglects entanglement between the DOF z_I and z_A^i, still predicts that the atoms are most likely to be found around the minima of the static ion potential. The entanglement between the DOF
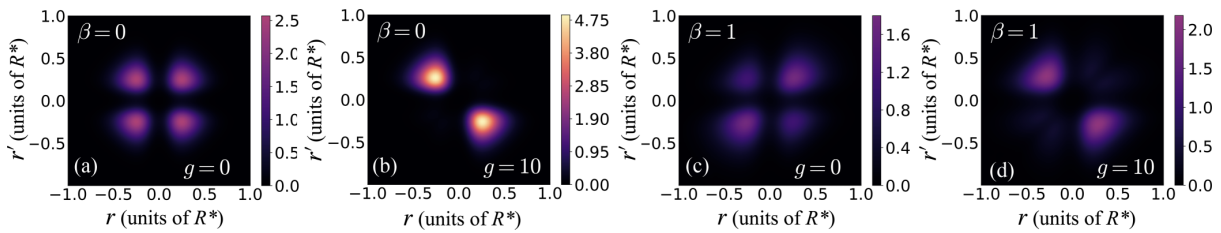

FIG. 4. Snapshots of the atomic probability density $\rho_2^{AA} = |\psi(r, r')|^2$ of the ground state for different interaction strengths g for a static ion [(a), (b)] and a mobile ion [(c), (d)].
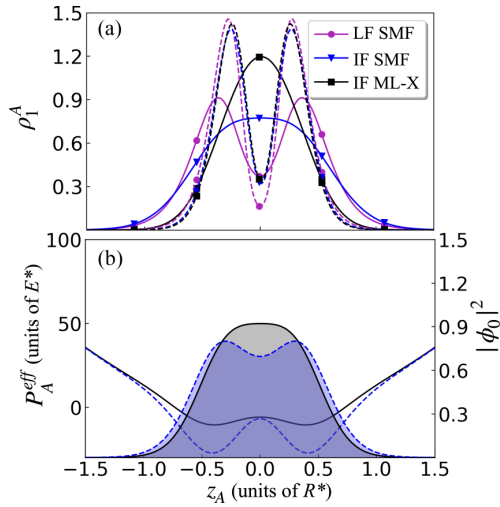
FIG. 5. (a) Atomic density $\rho_1(z_A)$ for the case of a heavy ion ($\beta = 0.034$, dashed lines) and a mobile ion ($\beta = 1$, solid lines), obtained via the laboratory frame species mean field (LF SMF) ansatz, the ion frame SMF (IF SMF) ansatz, and the exact IF result from the full ML-MCTDH ansatz [see Eq. (6)] (IF ML-X). (b) Effective potential $P_A^{\text{eff}}(z_A)$ experienced by the atoms due to the IF ML-X density $\rho_1^{\text{IF}}(z_I)$ (solid black line) and that obtained with the IF SMF ansatz $\tilde{\rho}_1^{\text{IF}}(z_I)$ (dashed blue line), derived from Eq. (16) with $\beta = 1$. The filled curves denote the respective ground-state orbitals $|\phi_0|^2$ calculated from the potential. Note for both subfigures that the atoms are noninteracting $g = 0$.

z_I and z_A^i is therefore crucial for capturing the correct form of the probability density.

In the following, we ignore the entanglement between z_I and r_i and aim at understanding the qualitative features of $\rho_1(z_A)$ for a mobile ion ($\beta = 1$) with noninteracting atoms ($g = 0$). To this end, we perturb atomic Hamiltonian in the LF (2a) with an effective atom-ion interaction potential found by integrating out the ionic degree of freedom in the interspecies interaction (1). The result is

$$H_A^{\text{eff}} = K_A + P_A + V_{AA} + \sum_{i=1}^{N} \int dz_I \, V_{AI}(z_{Ai}, z_I) \tilde{\rho}_1^{\text{IF}}(z_I)$$
$$= K_A + P_A^{\text{eff}} + V_{AA}, \tag{16}$$

where $\tilde{\rho}_1^{\text{IF}}(z_I)$ is the approximate one-body density of the ion obtained with the IF SMF ansatz. Note, $\tilde{\rho}_1^{\text{IF}}(z_I)$ is different than the density $\tilde{\rho}_1^{LF}(z_I)$ one would normally use based on the LF SMF ansatz. Since $\tilde{\rho}_1^{\text{IF}}(z_I)$ incorporates some of the many-body correlations between laboratory DOF, we expect this effective Hamiltonian to better capture the behavior of the atomic species than $\tilde{\rho}_1^{LF}(z_I)$. Indeed, we observe for a mobile ion ($\beta = 1$) that the extended ion density flattens out the V_{AI} minima and central barrier, yielding an effective potential which takes the form of a harmonic potential with a small modulation around the origin [dashed lines in Fig. 5(b)]. The corresponding ground-state orbital $|\phi_0|^2$ [filled dashed curve in Fig. 5(b)] shows increased probability for the atom to be found at the center of the harmonic trap,
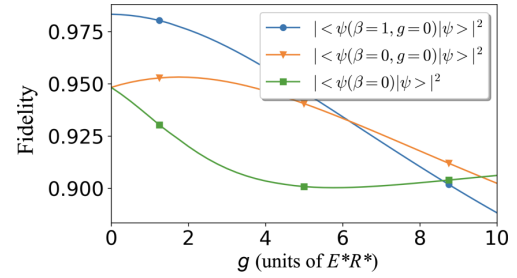

FIG. 6. Uhlmann fidelity between the exact ground state $|\psi\rangle$ at $\beta = 1$ and the state describing a mobile ion with noninteracting atoms $|\psi(\beta = 1, g = 0)\rangle$ (blue line), a static ion with noninteracting atoms $|\psi(\beta = 0, g = 0)\rangle$ (orange line), and a static ion with interacting atoms $|\psi(\beta = 0)\rangle$ (green line).

though it still displays peaks around the remnants of potential minima. The effective potential obtained from Eq. (16) with the exact ion density $\rho_1^{\text{IF}}(z_I)$ is qualitatively similar; however, the modulation around the origin is considerably weaker and therefore its ground-state orbital $|\phi_0|^2$ bears closer resemblance to a Gaussian [solid lines in Fig. 5(b)], in accordance with the shape observed in Fig. 5(a). While the effective picture obtained using the IF SMF ansatz provides a qualitatively correct description of the mobility-induced atomic bunching, accounting for entanglement between z_I and r_i is necessary for quantitative correctness.

3. Mobile ion: Impact on the ion

We now perform a complementary analysis on how the mobile ion is affected by the interatomic coupling strength g. In Fig. 3(e), we observe that the ion's potential energy P_I slightly decreases with g (solid curve with red squares), while its kinetic energy K_I slightly increases (solid curve with blue triangles). From this, we can infer that with increasing g the ion density $\rho_1(z_I)$ becomes squeezed and more localized at the trap center.

This observation is further confirmed by examining the Uhlmann fidelity $|\langle \chi | \psi \rangle|^2$ between the numerically exact ground state $|\psi\rangle$ for the mobile ion system and several states $|\chi\rangle$ describing different limiting cases (see Fig. 6). At weak couplings, $|\psi\rangle$ bears strongest similarity to the state describing a mobile ion with noninteracting atoms $|\psi(\beta = 1, g = 0)\rangle$. Then around $g \approx 6$, the dominant overlap is with the state describing a static ion with noninteracting atoms $|\psi(\beta = 0, g = 0)\rangle$, having no correlations at all. Finally, for $g > 9$ it shares the greatest overlap with the state $|\psi(\beta = 0)\rangle$, describing a static ion with interacting atoms. The latter exhibits only atom-atom correlations.

To develop a intuitive picture of what is happening to the ion, we first perform a comparison in terms of the SMF ansatz and exact solution in the IF for the ion density $\rho_1(z_I)$, similar to what was done for the atoms in Sec. IV A 2. Note that the SMF prediction for $\rho_1(z_I)$ is independent of g, since here the DOF are decoupled [dashed line in Fig. 7(a)]. Thus, the ion localization phenomenon cannot be captured by the SMF ansatz alone. For weak coupling $g \leqslant 1$, the ion density $\rho_1(z_I)$

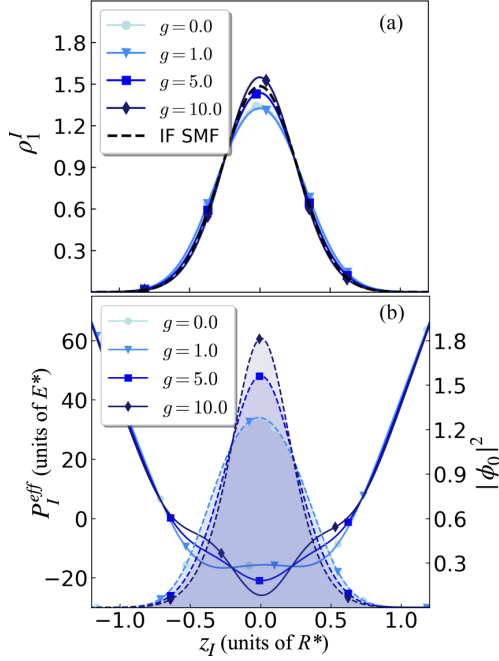FIG. 7. (a) The ion density $\rho_1(z_I)$ at various coupling strengths g, obtained via the ion frame species mean field (IF SMF) ansatz (dashed black line) and full ML-MCTDH ansatz (solid lines). Note the IF SMF has only a single solution for all g, since the z_I and r_i degrees of freedom decouple in the SMF ansatz [see Eq. (15)]. (b) The effective potential $P_I^{\text{eff}}(z_I)$ experienced by the mobile ion due to the exact atomic density $\rho_1^{\text{IF}}(z_A)$ at various coupling strengths g. The filled curves denote the corresponding ground-state orbitals $|\phi_0|^2$.

obtained via the exact result spreads out subtly (note the dip in probability at $z_I = 0$ between $g = 0$ and $g = 1$), before gradually becoming higher and narrower [see solid curves in Fig. 7(a)], in line with our prior observations of K_I and P_I discussed in the paragraph above.

Next, we construct an effective Hamiltonian for the ion due to the atomic density, in the same manner as we did for the atoms:

$$H_I^{\text{eff}} = K_I + P_I + N \int dz_A \, V_{AI}(z_A, z_I)\rho_1^{\text{IF}}(z_A) = K_I + P_I^{\text{eff}},$$
(17)

where $\rho_1^{\text{IF}}(z_A)$ is the exact one-body density of the atoms obtained in the IF. The effective potential P_I^{eff} is given in Fig. 7(b) for various interatomic couplings. The exact one-body densities $\rho_1(z_I)$ fit well inside P_I^{eff}. At $g = 0$, the effective trap takes the form of a harmonic trap with a shallow double-well modulation near the origin. As the intraspecies correlations build up, the double-well structure inverts, making the ion profile narrower due to the new minimum at the origin.

B. First excited state

In the first excited state, both of the atom-ion bound states are occupied by a single atom. The opposite symmetries of the bound states force the atoms to reside on the same side with regard to the ion, such that the atoms share a large spatial overlap (see Sec. IV B 1). The spatial overlap leads to a swift rise in the total energy of the first excited state at finite interatomic interactions. To minimize their overlap at greater interaction strengths, one of the atoms is released from the ion and occupies a vibrational trap state. While the ion's mobility leads to an overall positive shift in the total energy of the state, as well as increased inter- and intraspecies separations, it does not qualitatively affect the underlying physics (see Sec. IV B 2).

1. Static ion

The first excited state for two noninteracting ($g = 0$) atoms coupled to a static ($\beta = 0$) ion is given by the number state $|1, 1, 0, 0\rangle$ with respect to the single-particle eigenstates of h_{1b} [see Eq. (3)]; i.e., each molecular orbital ϕ_0, ϕ_1 in Fig. 1 is occupied by a single atom. Unlike in the ground state, the atoms here are completely bunched [note the single peak in Fig. 8(a)]. This is caused by the fact that $\phi_0(r) \approx$
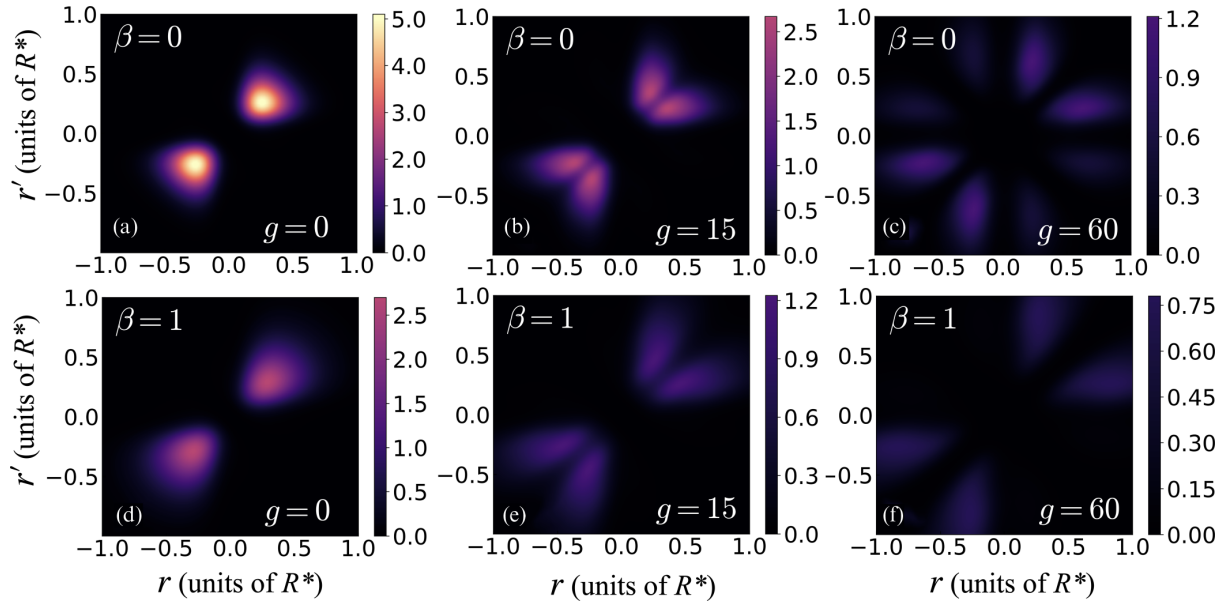

FIG. 8. Key observables for the first excited state. (a) Interatomic separation distribution $\rho_1^{AA}(z_A - z_A')$ for different atom-atom coupling strengths g. The inset shows the expectation value $\langle d_{AA} \rangle$ for the atom-atom separation as a function of g [Eq. (12)]. (b) Interspecies separation distribution $\rho_1^{AI}(z_A - z_I)$ for varying atom-atom coupling strengths g. The inset shows the expectation values $\langle d_{AI} \rangle$ for the atom-ion separation as a function of g [Eq. (13)]. [(c)–(e)] The evolution of the laboratory frame energy components with atom-atom coupling strength g. Note for panels (a) and (b) that the gray lines indicate the distance between the minima of the atom-ion interaction potential (1). Due to the parity symmetry, it is sufficient to show only the positive semiaxis. In all subfigures, the solid curves indicate results for a mobile ion, while dashed curves correspond to results for a static ion.

FIG. 9. Snapshots of the atomic probability density $\rho_2^{\mathrm{AA}} = |\psi(r, r')|^2$ of the first excited state for different interaction strengths g for a static ion [(a)–(c)] and a mobile ion [(d)–(f)].

$-\mathrm{sgn}(r)\phi_1(r)$ (compare ϕ_0 and ϕ_1 in Fig. 1). The suppression of the antibunched probabilities can be seen explicitly by inserting this relation into the two-body density:

$$\rho_2(r, r') = \frac{1}{4}[|\phi_0(r)|^2|\phi_1(r')|^2 + |\phi_1(r)|^2|\phi_0(r')|^2$$
$$+ 2\phi_0^*(r)\phi_1(r)\phi_1^*(r')\phi_0(r')] + \text{c.c.}, \quad (18)$$

where the first two terms cancel out the last two terms whenever $\mathrm{sgn}(r) \neq \mathrm{sgn}(r')$.

With increasing g, the interatomic separation distribution ρ_1^{AA} spreads and the peak at $z_A = z_A'$ for $g = 0$ is shifted to larger distances [dashed curves in Fig. 8(a)]. Even though the average distance d_{AA} between the atoms gradually increases [dashed curve in the inset of Fig. 8(a)], they insist on staying in the bunched configuration, i.e., on the same side with respect to the ion, which results in the formation of a nodal structure on the diagonal of the probability density [see Figs. 9(b) and 9(c)]. Thus, the interspecies separation distribution peak broadens [dashed curves in Fig. 8(b)], which leads to a monotonous increase of d_{AI} [dashed curve in the inset of Fig. 8(b)].

The above observations clarify the rapid increase of the total energy with g [see Fig. 2(a)]. One major contribution comes from the atom-atom interaction energy V_{AA} given by $g\rho_1^{AA}(r = 0)$. Thus, considering a large initial amplitude $\rho_1^{AA}(r = 0) > 1$ at $g = 0$ and that it decreases slowly with g, we identify a fast linear increase of V_{AA} up to approximately $g = 20$ [dashed curve with blue circles in Fig. 8(e)]. Once the amplitude drops significantly below the value of 1.0, V_{AA} starts decreasing. Another significant contribution stems from the atom-ion interaction potential V_{AI}. Drawing away from the ion requires the atoms to climb the V_{AI} potential, which costs energy [purple dashed line in Fig. 8(d)]. For $g < 10$, this energy is compensated by decreasing atomic kinetic energy

K_A [dashed curve with black circles in Fig. 8(c)], but V_{AI} keeps increasing even after K_A has saturated.

The atoms stay on one side of the ion while increasing their separation with g because of the growing contribution of the number state $|1, 0, 0, 1\rangle$ (see dashed lines in Fig. 10). The eigenstate is continuously transitioning to a regime in which one atom remains bound to the ion and the other is released into the harmonic trap. This can be seen clearly from the additional peak around $\approx \pm 0.7R^*$ that emerges in the interspecies separation distribution [see the dashed curve with green diamonds in Fig. 8(b)]. This causes a monotonous increase of the atomic trap potential energy P_A [dashed line with green triangles in Fig. 8(e)]. Beyond $g = 40$, the overlap with $|1, 0, 0, 1\rangle$ becomes dominant. Since the odd vibration
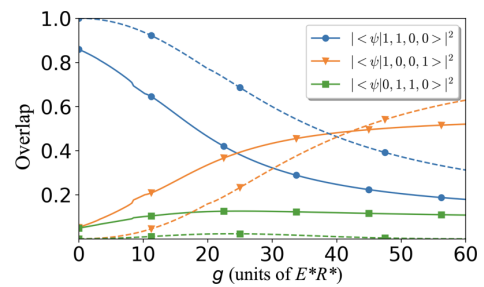

FIG. 10. Overlap spectrum $|\langle\psi|\mathbf{n}\rangle|^2$ between the first excited state $|\psi\rangle$ and the separate SPF number states $|\mathbf{n}\rangle$ calculated from the static ion model in Eq. (3) for a static ion (dashed curves) and a mobile ion (solid curves). For the sake of clarity, we show here only the dominant overlap coefficients. The complete representation of the mobile ion state in the static ion basis requires numerous additional small contributions from higher order number states.
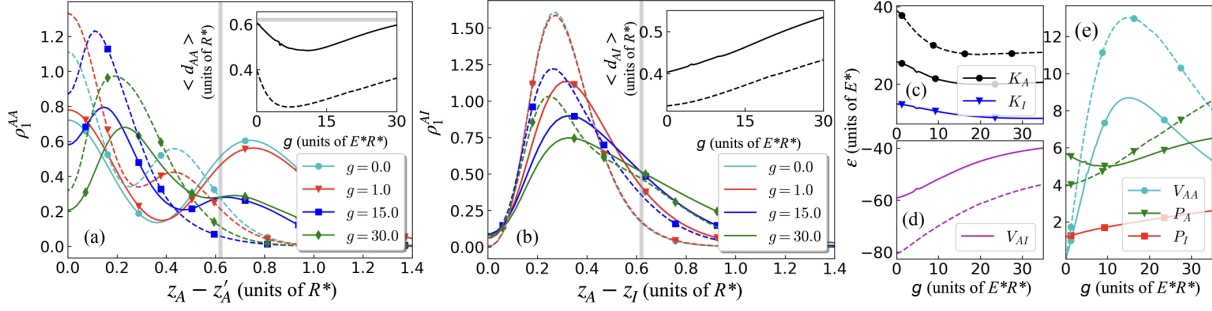
FIG. 11. Key observables for the second excited state. (a) Interatomic separation distribution $\rho_1^{AA}(z_A - z_A')$ for different atom-atom coupling strengths g. The inset shows the expectation value $\langle d_{AA} \rangle$ for the atom-atom separation as a function of g [Eq. (12)]. (b) Interspecies separation distribution $\rho_1^{AI}(z_A - z_I)$ for varying atom-atom coupling strengths g. The inset shows the expectation values $\langle d_{AI} \rangle$ for the atom-ion separation as a function of g [Eq. (13)]. [(c)–(e)] The evolution of the laboratory frame energy components with atom-atom coupling strength g. Note for panels (a) and (b) that the gray lines indicate the distance between the minima of the atom-ion interaction potential (1). Due to the parity symmetry, it is sufficient to show only the positive semiaxis. All subfigures: the solid curves indicate results for a mobile ion, while dashed curves correspond to results for a static ion.

orbital ϕ_3 features a smaller probability density to be found at the minimum of the atom-ion potential than ϕ_0, we observe an emergence of antibunching probability in the upper left and lower right quadrants of ρ_2 [see Fig. 9(c)].

2. Mobile ion

The ion's mobility causes a mixture of the number state $|0, 1, 1, 0\rangle$ (solid line with green squares in Fig. 10), whose contribution to the eigenstate amounts to $\approx 10\%$ and is approximately unchanged by the atom-atom coupling strength g. Thus, the impact on the physical quantities from the static ion case is expected to be qualitatively similar at all g.

The positive offset of the total energy of the first excited state [see Fig. 2(b)] is mainly due to the energy of the ion itself $K_I + P_I$ [see solid lines with blue triangles and red squares in Figs. 8(c) and 8(d), respectively]. With increasing g, there is

an exchange of energy between K_I and P_I, with K_I decreasing and P_I increasing, indicating the delocalization of the ion. The ion's mobility induces an additional energy exchange between K_A and V_{AI}, with V_{AI} increasing and K_A decreasing [compare the solid black curve with circles and purple curve in Figs. 8(c) and 8(d) to their dashed counterparts], implying that the atoms separate from each other. This is also evident from the patterns of $\rho_2(r, r')$, which remain qualitatively the same, albeit with a slightly enhanced overall spread (compare rows in Fig. 9) that is further imprinted on the interatomic ρ_1^{AA} and interspecies ρ_1^{AI} separation distributions [compare dashed and solid lines in Figs. 8(a) and 8(b)]. Accordingly, the distance among the atoms d_{AA} increases [see inset of Fig. 8(a)]. This is in contrast to the ground state, where the ion's mobility decreased d_{AA}. Due to the overall decreased amplitude of $\rho_1^{AA}(r = 0)$ compared to $\beta = 0$, the atom-atom interaction energy V_{AA} reaches the turning point already at a slightly weaker coupling g [solid
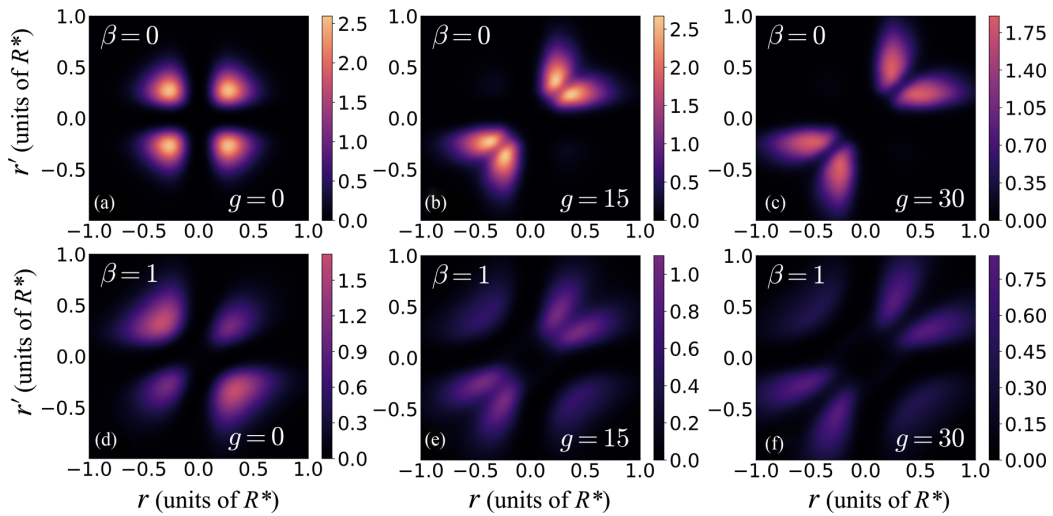

FIG. 12. Snapshots of the atomic probability density $\rho_2^{AA} = |\psi(r, r')|^2$ of the second excited state for different interaction strengths g for a static ion [(a)–(c)] and a mobile ion [(d)–(f)].
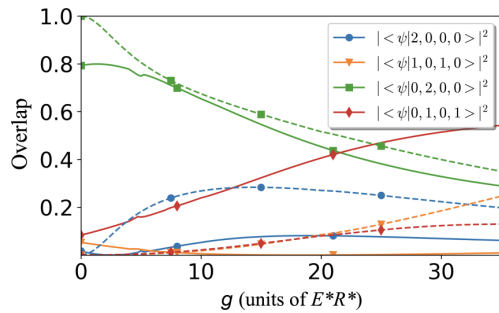
FIG. 13. Overlap spectrum $|\langle\psi|\mathbf{n}\rangle|^2$ between the second excited state $|\psi\rangle$ and the separate SPF number states $|\mathbf{n}\rangle$ calculated from the static ion model in Eq. (3) for a static ion (dashed curves) and a mobile ion (solid curves). For the sake of clarity, we show here only the dominant overlap coefficients. The complete representation of the mobile ion state in the static ion basis requires numerous additional small contributions from higher order number states.

curve with blue circles in Fig. 8(e)]. In summary, at $\beta = 1$ the atoms separate further from each other and from the ion as compared to $\beta = 0$.

C. Second excited state

In the noninteracting second excited state, both atoms occupy the upper bound state in the atom-ion interaction potential and display preference neither for bunching nor antibunching (see Sec. IV C 1). The response of the second excited state to finite atomic interactions closely resembles that of the first excited state, namely that at intermediate interactions, the atoms become preferentially bunched and at large interaction strengths, one of the atoms frees itself from the ion. In addition, the ion's mobility does not produce significant qualitative differences to the results for the static case (see Sec. IV C 2). These similarities between the states are to be expected, considering that their energy gap initially narrows [see Fig. 2(a)]. There are however, two crucial differences between the first and second excited states: (i) The bunching of the atoms in the latter state does not stem from an inherent symmetry of the single particle states but rather is a consequence of state mixing with other number states, such as $|2, 0, 0, 0\rangle$, and (ii) the atomic kinetic energy is consistently higher in the second excited state.

1. Static ion

The second excited state for two noninteracting ($g = 0$) atoms coupled to a static ($\beta = 0$) ion is given by the number state $|0, 2, 0, 0\rangle$ with respect to the single-particle eigenstates of h_{1b} [see Eq. (3)], with both atoms occupying the molecular orbital ϕ_1 (see Fig. 1). Similarly to the ground state, the atoms show no preference for either bunched or antibunched configurations [see Fig. 12(a)].

As g is increased, there is a mixture of the number state $|2, 0, 0, 0\rangle$ up to $g = 15$ (dashed curve with blue circles in Fig. 13). This leads to an increased bunching of the atoms [dashed curve with red triangles in Fig. 11(a)], decreasing the average distance d_{AA} among them [dashed line in the inset of Fig. 11(a)] until finally the antibunched configuration

is completely suppressed and a nodal structure emerges on the diagonal of the probability density [see Fig. 12(b)]. The increasingly bunched repulsive atoms create an increase in the interspecies separation d_{AI} [see dashed line in the inset of Fig. 11(b)]. Beyond $g > 10$, we observe a mixture of the number states $|1, 0, 1, 0\rangle$ and $|0, 1, 0, 1\rangle$ (see dashed curves with orange triangles and red diamonds in Fig. 13) featuring stronger separations among the atoms, which causes them to draw away from each other [see dashed curve in the inset of Fig. 11(a)]. The number states $|1, 0, 1, 0\rangle$ and $|0, 1, 0, 1\rangle$ feature one of the atoms unbound from the ion in a trap state. As such, the interspecies separation distribution broadens significantly [see dashed curves in Fig. 8(b)]. At the same time, the contribution of $|2, 0, 0, 0\rangle$ displays only a slight decay. Consequently at larger g, we anticipate the preservation of the bunched configuration with an increased spread of the two-body density $\rho_2(r, r')$ and a depletion of the diagonal at $r = r'$. [See Fig. 12(c).]

We note a strong similarity between the atomic probability densities shown in Figs. 9(b) and 12(b), which is due to a small energy gap between the first and second excited states [see Fig. 2(b)]. The two eigenstates also display a similar energy dependence on the coupling g [compare Figs. 8(c) to 8(e) and 11(c) to 11(e)]. The major difference between them is that the second excited state has a greater atomic kinetic energy K_A.

2. Mobile ion

Similar to the ground state and first excited state, the ion's mobility leads to a shift in the energies [compare solid and dashed curves in Figs. 2(b) and 11(c) to 11(e)] and of the interatomic and interspecies separations [inset of Figs. 11(a) and 11(b)]. Specifically, the atoms exhibit an increase in separation between each other of $\approx 0.2R^*$ and an increase in separation to the ion by $\approx 0.1R^*$. Contrary to the first excited state however, which featured a g-independent mixture of an additional number state, the number state composition of the second excited state undergoes substantial structural changes at $\beta = 1$ (see Fig. 13). Thus, the roles of $|1, 0, 1, 0\rangle$ and $|2, 0, 0, 0\rangle$ are substantially suppressed in favor of $|0, 1, 0, 1\rangle$. As a result, we observe a strong enhancement of the antibunched off-diagonal probability in $\rho_2(r, r')$ at all g (compare rows in Fig. 12).

D. Third excited state

In the third excited state, one atom remains bound to the ion in the lowest energy bound state and the other occupies the lowest energy trap state. As shown in Sec. III, the total energy of this eigenstate is not markedly affected by varying atomic interactions. Unsurprisingly, the principle observables for the state (probability density, energy components, and number state composition) are likewise largely unaffected by these changes (see Sec. IV D 1). This robustness of the third excited state stems from the relatively small spatial overlap of the two atoms, due to the contrasting length scales of the bound and trap states (see discussion in Sec. II A). The state is further robust to the ion mobility (see Sec. IV D 2), displaying only a positive shift in the total energy due to an increased spread between the atomic and ionic species, in accordance with the weaker localization of the ion.
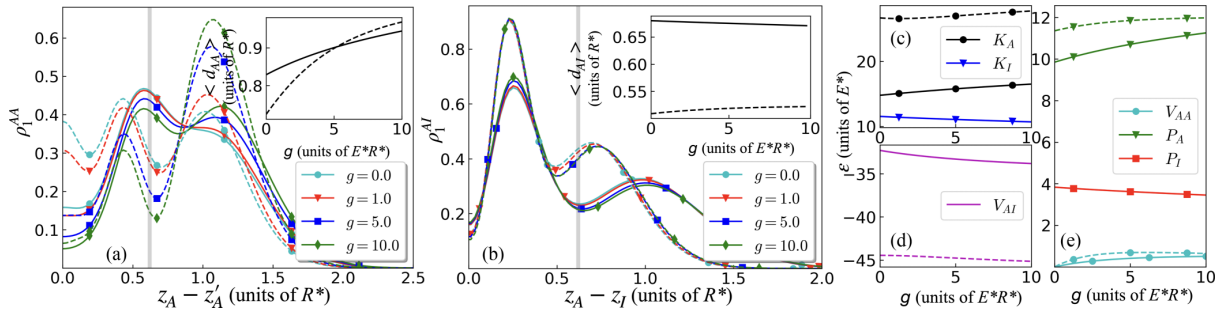
FIG. 14. Key observables for the third excited state. (a) Interatomic separation distribution $\rho_1^{AA}(z_A - z_A')$ for different atom-atom coupling strengths g. The inset shows the expectation value $\langle d_{AA} \rangle$ for the atom-atom separation as a function of g [Eq. (12)]. (b) Interspecies separation distribution $\rho_1^{AI}(z_A - z_I)$ for varying atom-atom coupling strengths g. The inset shows the expectation values $\langle d_{AI} \rangle$ for the atom-ion separation as a function of g [Eq. (13)]. [(c)–(e)] The evolution of the laboratory-frame energy components with atom-atom coupling strength g. Note for panels (a) and (b) that the gray lines indicate the distance between the minima of the atom-ion interaction potential (1). Due to the parity symmetry, it is sufficient to show only the positive semiaxis. In all subfigures, the solid curves indicate results for a mobile ion, while dashed curves correspond to results for a static ion.

1. Static ion

The third excited state for two noninteracting ($g = 0$) atoms coupled to a static ($\beta = 0$) ion is given by the number state $|1, 0, 1, 0\rangle$, where one atom is bound in the even molecular orbital ϕ_0 and the other occupies the even vibrational orbital ϕ_2 (see Fig. 1).

Previously, we have seen that the total energy of the vibrational eigenstates depends only weakly on g [see Fig. 2(b)]. This also holds for the energy components, which show only a slight exchange between V_{AI} and K_A [see Figs. 14(c) and 14(d)]. On the level of energies, the eigenstate seems quite robust to perturbations by atom-atom interactions, though the atom-atom separation distribution ρ_1^{AA} features significant structural changes with increasing g, leading to increased separation among the atoms d_{AA} [dashed curve in the inset of Fig. 14(a)].

At $g = 0$, there are three pronounced humps in ρ_1^{AA} [dashed curve with blue circles in Fig. 14(a)]. Comparing this to $\rho_2(r, r')$ [Fig. 15(a)], we can see that these correspond to (i) atoms being bound to the same side of the ion ($r_A = z_A - z_A' = 0$), (ii) atoms being bound to opposite sides of the ion ($r_A \sim 0.4R^*$), and (iii) one atom being bound to the ion while the other is unbound ($r_A \sim 1.0R^*$). With increasing g, we observe a depletion of the central peak at $r_A = 0$ in favor of the outer peak, which additionally shifts to larger separations [dashed curves in Fig. 14(a)]. The middle peak is essentially

unaffected. The bunching of atoms becomes suppressed and at $g = 10$ one ends up with atoms located on different sides with respect to the ion [see Fig. 15(b)].

The structure of ρ_1^{AI} at $g = 0$ has two distinct peaks at $\approx 0.3R^*$ and $\approx 0.8R^*$, reflecting the different length scales of the molecular and vibrational orbitals comprising the number state [dashed curves in Fig. 14(b)]. ρ_1^{AI} is largely unaffected by the interatomic coupling strength, though there is a peak shift around $\approx 0.8R^*$, indicating that the increase in d_{AI} [dashed curve in inset of Fig. 14(b)] arises solely from the unbound atom spreading out as the atom pair grows increasingly repulsive.

2. Mobile ion

Several patterns in $\rho_2(r, r')$ are enhanced for $\beta = 1$ (compare rows in Fig. 15). When both atoms are in the vicinity of the ion ($r < 0.3$, $r' < 0.3$), the antibunching is amplified, while when one atom is further away ($r \lesssim 0.3R^*$, $r' \gtrsim 0.3R^*$), the antibunching is suppressed and atoms are most likely to be found on the same side with respect to the ion. This causes further depletion of the interparticle separation distribution at $r_A = 0$ and suppresses the outer peak at $r_A \sim 1.0R^*$ [compare dashed and solid lines in Fig. 14(a)]. The relative magnitudes of these effects are different depending on the value of g, resulting in larger d_{AA} at small g and smaller d_{AA} at large g, compared to the static ion case [see the inset of Fig. 14(a)]. The ion's mobility creates a positive shift in d_{AI} from the
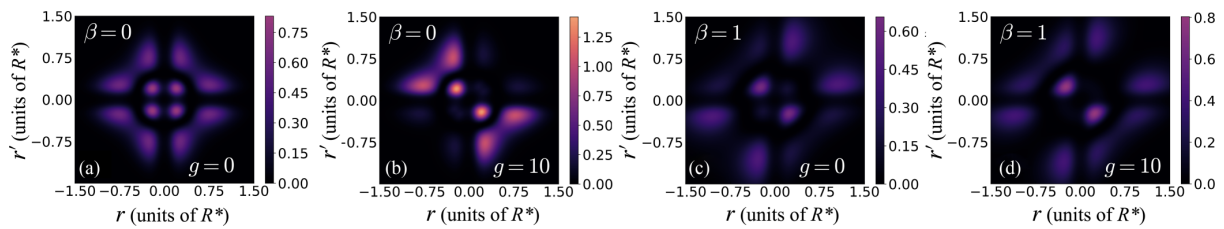

FIG. 15. Snapshots of the atomic probability density $\rho_2^{AA} = |\psi(r, r')|^2$ of the third excited state for different interaction strengths g for a static ion [(a), (b)] and a mobile ion [(c), (d)].
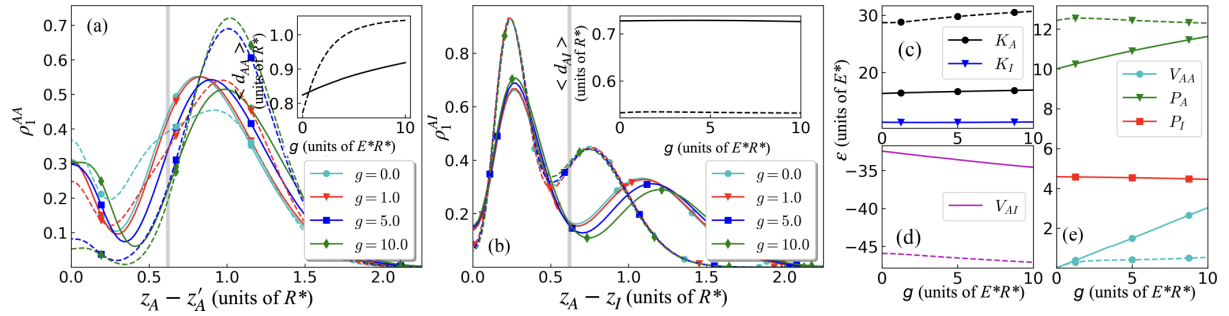
FIG. 16. Key observables for the fourth state. (a) Interatomic separation distribution $\rho_1^{AA}(z_A - z_A')$ for different atom-atom coupling strengths g. The inset shows the expectation value $\langle d_{AA} \rangle$ for the atom-atom separation as a function of g [Eq. (12)]. (b) Interspecies separation distribution $\rho_1^{AI}(z_A - z_I)$ for varying atom-atom coupling strengths g. The inset shows the expectation values $\langle d_{AI} \rangle$ for the atom-ion separation as a function of g [Eq. (13)]. [(c)–(e)] The evolution of the laboratory frame energy components with atom-atom coupling strength g. Note for panels (a) and (b) that the gray lines indicate the distance between the minima of the atom-ion interaction potential (1). Due to the parity symmetry, it is sufficient to show only the positive semi-axis. In all subfigures, the solid curves indicate results for a mobile ion, while dashed curves correspond to results for a static ion.

greater spread of ρ_1^{AI}. Although the vibrational orbital peak shifts to greater separations, the molecular orbital peak at $\approx 0.3R^*$ is enhanced, leading to a slow decrease of d_{AI}.

E. Fourth excited state

The noninteracting fourth excited state bears similarity to the third excited state, except that the trap-state atom occupies the next highest energy vibrational orbital. Here, the opposing symmetries of the single-particle states suppress the off-diagonal elements ($z_A = -z_A'$) of the probability density, as was observed already in the first excited state. For the case of a static ion, the atoms fully separate to opposite sides of the ion even at extremely weak atomic interaction strengths and thereafter, further changes are negligible (see Sec. IV E 1). For the case of an equal mass system, however, the ion's mobility reinforces the overlap of the atoms, which competes against the anticorrelations produced by the repulsive interatomic interaction. As a result, the total energy of the state grows rapidly and the onset of the fully antibunched configuration is delayed (see Sec. IV E 2).

1. Static ion

The fourth excited state for two noninteracting ($g = 0$) atoms coupled to a static ($\beta = 0$) ion is given by the number state $|1, 0, 0, 1\rangle$, with one atom in the even molecular orbital ϕ_0 and the other in the odd vibrational orbital ϕ_3 (see Fig. 1).
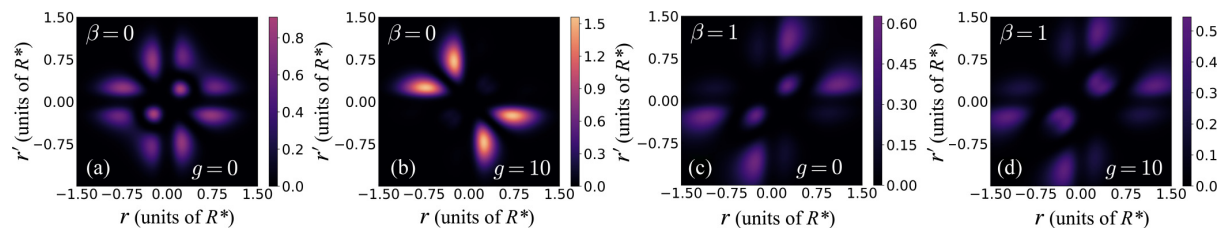
Similar to the third excited state, the total energy [given in Fig. 2(b)] and the energy components [see Figs. 16(c)–16(e)] are robust to g variation. The small energy gap between the third and fourth eigenstates is due to a difference in the potential energy P_A of the atoms. Nevertheless, this state also exhibits structural changes in the interatomic separation distribution ρ_1^{AA} [dashed curves in Fig. 16(a)]. Contrary to the third excited state, here we observe two humps: a narrow hump at $r_A = z_A - z_A' = 0$ and a broad hump at $r_A \sim 1.0R^*$. As g increases, the hump at $r_A = 0$ becomes smaller and broader, while the other becomes higher and narrower. As a result, the distance among the atoms d_{AA} increases with g [dashed curve in the inset of Fig. 16(a)].

In the two-body density $\rho_2(r, r')$ at $g = 0$ [see Fig. 17(a)], we observe the absence of antibunched regions in close proximity to the ion ($r < 0.3R^*$, $r' < 0.3R^*$). This is in contrast to the third excited state and explains the absence of the third peak at $r_A = 0.4R^*$. Additionally, since the occupied orbitals ϕ_0 and ϕ_3 are of opposite parity symmetry, the off-diagonal at $r = -r'$ is zero. At stronger coupling $g = 10$ [see Fig. 17(b)], the only eligible configurations are the ones, where one atom is bound to ion and the other is unbound on the opposite side with respect to the ion.

2. Mobile ion

For $\beta = 1$, the total energy and energy components are not as robust to variations in g. Notably, there is a rapid increase in V_{AA} given by $g\rho_1^{AA}(r = 0)$ [see solid curve with blue circles

FIG. 17. Snapshots of the atomic probability density $\rho_2^{AA} = |\psi(r, r')|^2$ of the fourth excited state for different interaction strengths g for a static ion [(a), (b)] and a mobile ion [(c), (d)].

in Fig. 16(e)], since the probability amplitude at $\rho_1^{AA}(r = 0)$ is unaffected by g [see solid curves in Fig. 16(a)]. As a result, the energy gap between the third and fourth excited state widens with growing g [see Fig. 2(b)].

V. SUMMARY AND OUTLOOK

In this study, we have analyzed the low-energy eigenstates of an atom-ion hybrid system consisting of a pair of bosons interacting with a single ion, where both species are confined in a quasi-1D trapping geometry. The eigenstates were obtained by means of the multilayer multiconfiguration time-dependent Hartree method for bosons (ML-MCTDHB), an *ab initio* method for simulating entangled mixtures with significant intracomponent correlations. We described the eigenenergies' dependence on the atom-atom coupling strength g for the case of an infinitely heavy ion ($\beta = 0$) and contrasted this to the case of an equal mass system ($\beta = 1$). The former we termed the *static* ion system and the latter the *mobile* ion system. Each eigenstate has been characterized in terms of its interatomic and interspecies separation distributions, average separations among the particles, and energy allocation in different Hamiltonian components.

In general, the repulsive interaction between the atoms increases their average separation, accompanied by a broadening of the interatomic separation distribution and an energy exchange between atomic kinetic and atom-ion interaction energies. The average distance to the ion does not necessarily change in the process, however. When it does change, the atoms separate, while simultaneously remaining on the same side with respect to the ion (first and second excited states). On the other hand, a constant atom-ion distance indicates that the atoms have transitioned to a configuration in which the ion lies in between them. In this case, both atoms are either bound (ground state) or one atom moves freely in the harmonic trap (third and fourth excited states). Contrary to the repulsive interatomic interaction, the mobility of the ion works to increase the average separation between all particles, irrespective of the species.

We explained the apparent ion mobility-induced bunching effect observed in the ground state through use of an effective potential, which predicts that the ion mobility morphs the standard double-well-like potential produced by the static ion into a pseudoharmonic potential, such that the atoms cluster together at the trap center. Likewise, the effective potential for the ion predicts that for strong interatomic interactions, the antibunched atom pair acts like a pincer, which confines the ion at the center of the trap. These predictions agree with the trend in the ion's energy components obtained via exact numerical methods.

Regarding possible experimental realization of our hybrid model, it is important to note that we have neglected all three-body recombination processes. However, considering the low particle density in few-body systems such as ours, the loss rate is expected to be insignificant. For larger particle numbers in one spatial dimension, such decay channels may be suppressed by strong repulsion among the atoms [58]. We have additionally neglected charge transfer and radiative loss resulting from reactions between the ion and the atoms. For certain heteronuclear atom-ion pairings, these inelastic processes happen to be of low probability [59], and for other pairings the chemical reactivity can be controlled through the use of a magnetic field [35]. We have further assumed our system is at temperatures low enough for pure s-wave scattering, which has long been the goal of atom-ion experiments. Recent experiments have attained temperatures at the threshold of this regime via buffer gas cooling of a single ion in a Paul trap for species pairings with a large mass imbalance [36], corresponding to a static ion system. As for the mobile ion system, the recent advent of optical traps for ions [30] provides a promising platform that could be used for experiments with atoms and ions of the same element.

This work has mapped out the landscape of stationary states for an exemplary few-body mixture characterized by long-range interspecies interactions. It lays the foundation for the route to more exotic and complex systems, such as solid-state emulation in Coulomb crystals and dipolar quantum gases. Additionally, exploring how the properties of the present atom-ion hybrid system evolve with greater particle numbers, alternative species pairings, and differing trapping frequencies ($\eta \neq 1$) would be an interesting avenue for future study. This work also focused solely on a time-independent problem, and therefore a natural extension would be to consider many-body dynamics, e.g., ion immersion in an atomic gas and time-resolved monitoring of atom capture, leading to the formation of mesoscopic molecules. Other theoretical investigations into atom-ion hybrid systems have employed a variety of techniques, including exact diagonalization [60], quantum Monte Carlo [61,62], density matrix renormalization group (DMRG) [63], variational methods [64], semiclassical methods [65], and hyperspherical coordinates [66], for which our work may serve as a useful numerical benchmark.

ACKNOWLEDGMENTS

[1] W. W. Smith, O. P. Makarov, and J. Lin, J. Mod. Op. **52**, 2253 (2005).

[2] A. T. Grier, M. Cetina, F. Oručević, and V. Vuletić, Phys. Rev. Lett. **102**, 223201 (2009).

[3] S. Schmid, A. Härter, and J. H. Denschlag, Phys. Rev. Lett. **105**, 133202 (2010).

[4] C. Zipkes, S. Palzer, C. Sias, and M. Köhl, Nature (London) **464**, 388 (2010).

[5] A. Härter and J. Hecker Denschlag, Contemp. Phys. **55**, 33 (2014).

[6] M. Tomza, K. Jachymski, R. Gerritsma, A. Negretti, T. Calarco, Z. Idziaszek, and P. S. Julienne, Rev. Mod. Phys. **91**, 035001 (2019).

[7] L. Ratschbacher, C. Zipkes, C. Sias, and M. Köhl, Nat. Phys. **8**, 649 (2012).

[8] F. H. J. Hall and S. Willitsch, Phys. Rev. Lett. **109**, 233202 (2012).

[9] A. Härter, A. Krükow, A. Brunner, W. Schnitzler, S. Schmid, and J. H. Denschlag, Phys. Rev. Lett. **109**, 123201 (2012).

[10] Z. Meir, T. Sikorsky, R. Ben-shlomi, N. Akerman, Y. Dallal, and R. Ozeri, Phys. Rev. Lett. **117**, 243401 (2016).

[11] J. Pérez-Ríos, Mol. Phys. **0**, 1881637 (2021).

[12] A. Krükow, A. Mohammadi, A. Härter, and J. Hecker Denschlag, Phys. Rev. A **94**, 030701(R) (2016).

[13] A. Krükow, A. Mohammadi, A. Härter, J. H. Denschlag, J. Pérez-Ríos, and C. H. Greene, Phys. Rev. Lett. **116**, 193201 (2016).

[14] C. Zipkes, L. Ratschbacher, C. Sias, and M. Köhl, New J. Phys. **13**, 053020 (2011).

[15] K. Ravi, S. Lee, A. Sharma, G. Werth, and S. A. Rangwala, Nat. Commun. **3**, 1126 (2012).

[16] R. Côté, Phys. Rev. Lett. **85**, 5316 (2000).

[17] T. Dieterle, M. Berngruber, C. Hölzl, R. Löw, K. Jachymski, T. Pfau, and F. Meinert, Phys. Rev. Lett. **126**, 033401 (2021).

[18] U. Bissbort, D. Cocks, A. Negretti, Z. Idziaszek, T. Calarco, F. Schmidt-Kaler, W. Hofstetter, and R. Gerritsma, Phys. Rev. Lett. **111**, 080501 (2013).

[19] W. Casteels, J. Tempere, and J. Devreese, J. Low Temp. Phys. **162**, 266 (2011).

[20] K. Jachymski and A. Negretti, Phys. Rev. Research **2**, 033326 (2020).

[21] R. Gerritsma, A. Negretti, H. Doerk, Z. Idziaszek, T. Calarco, and F. Schmidt-Kaler, Phys. Rev. Lett. **109**, 080402 (2012).

[22] J. M. Schurer, R. Gerritsma, P. Schmelcher, and A. Negretti, Phys. Rev. A **93**, 063602 (2016).

[23] L. Ratschbacher, C. Sias, L. Carcagni, J. M. Silver, C. Zipkes, and M. Köhl, Phys. Rev. Lett. **110**, 160402 (2013).

[24] C. Veit, N. Zuber, O. A. Herrera-Sancho, V. S. V. Anasuri, T. Schmid, F. Meinert, R. Löw, and T. Pfau, Phys. Rev. X **11**, 011036 (2021).

[25] M. Cetina, A. T. Grier, and V. Vuletić, Phys. Rev. Lett. **109**, 253201 (2012).

[26] M. Krych and Z. Idziaszek, Phys. Rev. A **91**, 023430 (2015).

[27] P. Wessels, B. Ruff, T. Kroker, A. K. Kazansky, N. M. Kabachnik, K. Sengstock, M. Drescher, and J. Simonet, Commun. Phys. **1**, 32 (2018).

[28] C. Schneider, M. Enderlein, T. Huber, and T. Schätz, Nat. Photon. **4**, 772 (2010).

[29] M. Enderlein, T. Huber, C. Schneider, and T. Schaetz, Phys. Rev. Lett. **109**, 233004 (2012).

[30] T. Schaetz, J. Phys. B **50**, 102001 (2017).

[31] A. Lambrecht, J. Schmidt, P. Weckesser, M. Debatin, L. Karpa, and T. Schaetz, Nat. Photon. **11**, 704 (2017).

[32] J. Schmidt, P. Weckesser, F. Thielemann, T. Schaetz, and L. Karpa, Phys. Rev. Lett. **124**, 053402 (2020).

[33] K. S. Kleinbach, F. Engel, T. Dieterle, R. Löw, T. Pfau, and F. Meinert, Phys. Rev. Lett. **120**, 193401 (2018).

[34] T. Schmid, C. Veit, N. Zuber, R. Löw, T. Pfau, M. Tarana, and M. Tomza, Phys. Rev. Lett. **120**, 153401 (2018).

[35] M. Tomza, C. P. Koch, and R. Moszynski, Phys. Rev. A **91**, 042706 (2015).

[36] T. Feldker, H. Fürst, H. Hirzler, N. Ewald, M. Mazzanti, D. Wiater, M. Tomza, and R. Gerritsma, Nat. Phys. **16**, 413 (2020).

[37] Z. Idziaszek, T. Calarco, P. S. Julienne, and A. Simoni, Phys. Rev. A **79**, 010702(R) (2009).

[38] R. Côté, V. Kharchenko, and M. D. Lukin, Phys. Rev. Lett. **89**, 093001 (2002).

[39] J. M. Schurer, A. Negretti, and P. Schmelcher, Phys. Rev. Lett. **119**, 063001 (2017).

[40] P. Massignan, C. J. Pethick, and H. Smith, Phys. Rev. A **71**, 023606 (2005).

[41] J. Schurer, A. Negretti, and P. Schmelcher, New J. Phys. **17**, 083024 (2015).

[42] J. Goold, H. Doerk, Z. Idziaszek, T. Calarco, and T. Busch, Phys. Rev. A **81**, 041601(R) (2010).

[43] J. M. Schurer, P. Schmelcher, and A. Negretti, Phys. Rev. A **90**, 033601 (2014).

[44] S. Krönke, L. Cao, O. Vendrell, and P. Schmelcher, New J. Phys. **15**, 063018 (2013).

[45] L. Cao, S. Krönke, O. Vendrell, and P. Schmelcher, J. Chem. Phys. **139**, 134103 (2013).

[46] K. Keiler, S. I. Mistakidis, and P. Schmelcher, New J. Phys. **22**, 083003 (2020).

[47] F. Theel, K. Keiler, S. I. Mistakidis, and P. Schmelcher, New J. Phys. **22**, 023027 (2020).

[48] L. Cao, V. Bolsinger, S. Mistakidis, G. Koutentakis, S. Krönke, J. Schurer, and P. Schmelcher, J. Chem. Phys. **147**, 044106 (2017).

[49] J. Chen, J. M. Schurer, and P. Schmelcher, Phys. Rev. Lett. **121**, 043401 (2018).

[50] J. Kwasniok, S. I. Mistakidis, and P. Schmelcher, Phys. Rev. A **101**, 053619 (2020).

[51] H.-D. Meyer, U. Manthe, and L. Cederbaum, Chem. Phys. Lett. **165**, 73 (1990).

[52] M. H. Beck, A. Jäckle, G. A. Worth, and H.-D. Meyer, Phys. Rep. **324**, 1 (2000).

[53] O. E. Alon, A. I. Streltsov, and L. S. Cederbaum, Phys. Rev. A **77**, 033613 (2008).

[54] T. Kato and H. Kono, Chem. Phys. Lett. **392**, 533 (2004).

[55] O. E. Alon, A. I. Streltsov, and L. S. Cederbaum, Phys. Rev. A **76**, 062501 (2007).

[56] J. C. Light, I. P. Hamilton, and J. V. Lill, J. Chem. Phys. **82**, 1400 (1985).

[57] M. D. Girardeau and A. Minguzzi, Phys. Rev. Lett. **96**, 080404 (2006).

[58] D. M. Gangardt and G. V. Shlyapnikov, Phys. Rev. Lett. **90**, 010401 (2003).

[59] M. Tomza, Phys. Rev. A **92**, 062701 (2015).

[60] M. A. García-March, B. Juliá-Díaz, G. E. Astrakharchik, J. Boronat, and A. Polls, Phys. Rev. A **90**, 063605 (2014).

[61] M. A. Garcia-March, B. Juliá-Díaz, G. E. Astrakharchik, T. Busch, J. Boronat, and A. Polls, Phys. Rev. A **88**, 063604 (2013).

[62] G. E. Astrakharchik, L. A. P. Ardila, R. Schmidt, K. Jachymski, and A. Negretti, arXiv:2005.12033.

[63] A. B. Michelsen, M. Valiente, N. T. Zinner, and A. Negretti, Phys. Rev. B **100**, 205427 (2019).

[64] S. P. Rath and R. Schmidt, Phys. Rev. A **88**, 053632 (2013).

[65] V. S. Melezhik, Z. Idziaszek, and A. Negretti, Phys. Rev. A **100**, 063406 (2019).

[66] J. Pérez-Ríos and C. H. Greene, Phys. Rev. A **98**, 062707 (2018).

Charged ultralong-range Rydberg trimers [SC2]

Charged ultralong-range Rydberg trimers

Daniel J. Bosworth [1,2,*] Frederic Hummel [3,†] and Peter Schmelcher [1,2]

[1]*Zentrum für Optische Quantentechnologien, Universität Hamburg, Luruper Chaussee 149, 22761 Hamburg, Germany*
[2]*The Hamburg Centre for Ultrafast Imaging, Universität Hamburg, Luruper Chaussee 149, 22761 Hamburg, Germany*
[3]*Max Planck Institute for the Physics of Complex Systems, Nöthnitzer Straße 38, 01187 Dresden, Germany*

We show that the recently observed class of long-range ion-Rydberg molecules can be divided into two families of states, which are characterized by their unique electronic structures resulting from the ion-induced admixture of quantum defect-split Rydberg nP states with different low-field-seeking high-l states. We predict that in both cases, these diatomic molecular states can bind additional ground-state atoms lying within the orbit of the Rydberg electron, thereby forming *charged* ultralong-range Rydberg molecules (ULRMs) with binding energies similar to that of conventional nonpolar ULRMs. To demonstrate this, we consider a Rydberg atom interacting with a single ground-state atom and an ion. The additional atom breaks the system's cylindrical symmetry, which leads to mixing between states that would otherwise be decoupled. The electronic structure is obtained using exact diagonalization over a finite basis and the vibrational structure is determined using the multiconfiguration time-dependent Hartree method. Due to the lobelike structure of the electronic density, bound trimers with both linear and nonlinear geometrical configurations of the three nuclei are possible. The predicted trimer binding energies and excitation series are distinct enough from those of the ion-Rydberg dimer to be observed using current experimental techniques.

I. INTRODUCTION

Hybrid atom-ion systems serve as a testbed for fundamental quantum physics research [1–3], enabling studies of cold collisions and chemistry [4–9] such as the formation of cold molecular ions [10–12]. They also provide a platform for precision measurements [13–15] and quantum simulation [16,17]. Recent milestones in this field include the first reports of *s*-wave atom-ion collisions [18] and the observation of atom-ion Feshbach resonances [19].

Over the last two decades, there has also been growing interest in combining ions with Rydberg atoms in order to engineer atom-ion interactions [20,21] and control cold collisions and charge hopping [22–25]. Additionally, an ion-induced Rydberg blockade effect has been established [26] and Rydberg atoms have been used to realize hybrid atom-ion systems in the quantum regime without the need for an ion trap [27]. Recent theoretical works predicted bound molecular states between ions and Rydberg states of Rb and Cs [28,29] and their existence and vibrational dynamics were observed shortly after [30,31]. These ion-Rydberg molecules have bond lengths and energies ranging from nm to μm and MHz to GHz, respectively.

Such extreme bonding lengths and energies are seen in another exotic type of Rydberg molecule formed between a Rydberg atom and one or more ground-state atoms which become bound due to attractive electron scattering. These are known as ultralong-range Rydberg molecules (ULRMs) [32,33]. The

importance of electron scattering for describing Rydberg atoms in atomic gases originated with Fermi [34]. Fermi's model was later applied within the context of ultracold atomic gases, leading to the prediction of ULRMs in 2000 [35]. These molecules were first observed in 2009 [36] and over the past decade they have been used for probing spatial correlations in ultracold atomic gases [37–39], studying low-energy electron-atom collisions [40–42], and the formation of Rydberg polarons in the high-density regime [27,43–45]. Furthermore, the formation of polyatomic ULRMs and Rydberg composites has been a topic of major interest [46–53] as well as the behavior of ULRMs in external electric and magnetic fields [54–61].

In light of recent developments, combining ULRMs with ions is a natural step forward: it constitutes a system for studying Rydberg molecules exposed to *inhomogeneous* electric fields created by the ion and in which Rydberg atoms may become bound to both ions and ground-state atoms simultaneously. In contrast to neutral ULRMs where the ground-state atom is bound within the Rydberg cloud, ions bind with Rydberg atoms far outside the orbit of the Rydberg electron. The ion-Rydberg potential wells are formed due to couplings between neighboring electronic states, reminiscent of Rydberg macrodimer potential wells [62].

In this work, we begin by examining the electronic structure of a two-body system consisting of an ion and a Rydberg atom. We focus in particular on the electronic density distributions of ion-Rydberg bound states that exist within different potential wells present in the adiabatic potential energy curves (PECs). These reveal patterns of pronounced density maxima that are unique to each potential well due to the ion-induced admixture of different high- and low-l Rydberg states. Despite their differences, we show that the electronic density

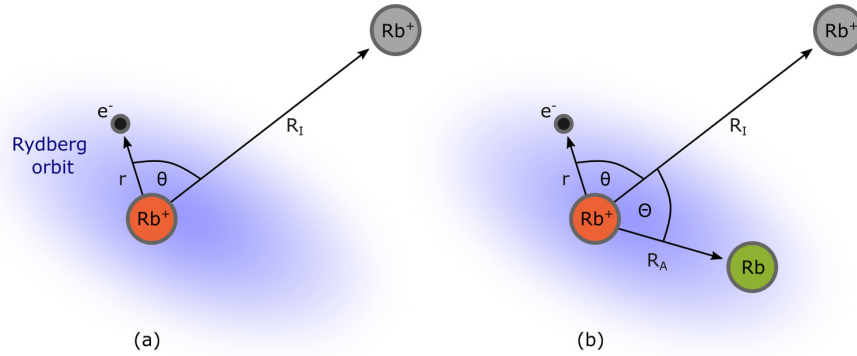*dboswort@physnet.uni-hamburg.de
†hummel@pks.mpg.de

FIG. 1. Schematic illustration of the two- and three-body systems. (a) A Rydberg atom (ionic core and valence electron) interacting with an ion. (b) A Rydberg atom interacting with an ion and a ground-state atom.

structures can be grouped into two families of states, which differ primarily in their angular arrangement of the density maxima. We remark that the Rydberg electron's probability density in one of these wells has been discussed previously within the context of the Rydberg atom's flipping electric dipole moment around the well minimum and the electronic oscillations accompanying nuclear dynamics in this well [30,31]. Building on our considerations of the two-body system's electronic structure, we then introduce an additional ground-state atom into the system. We determine adiabatic potential energy surfaces (PESs) near the $32P$ atomic Rydberg state and uncover that their local minima support weakly bound trimer states with unique excitation spectra for different geometrical arrangements of the three species. The properties of the trimer states are compared against those of the dimer for principal quantum numbers ranging from 17 to 90.

This work is organized as follows. Section II presents an overview of the current understanding of ion-Rydberg molecules as well as a discussion of their electronic structure. In Sec. III, we introduce our three-body system and analyze the corresponding adiabatic PES. Section IV discusses the resulting vibrational states supported by these surfaces and compares their properties to those of ion-Rydberg dimers, including possible experimental aspects. Our conclusions are provided in Sec. V.

II. ELECTRONIC STRUCTURE OF ION-RYDBERG DIMERS

This section first provides some background information on ion-Rydberg molecules. We then present results for the electronic structure of different molecular states, which motivate the discussion of the three-body system in Secs. III and IV.

A. Squid and snow angel states

We consider a Rydberg atom in the presence of an ion at internuclear distances in which there is vanishing spatial overlap between the charge distribution of the Rydberg atom and the ion, as illustrated in Fig. 1(a). This holds for internuclear distances greater than the so-called LeRoy radius R_{LR} [63], which for this system is approximately defined by the diameter of the Rydberg cloud.

The system's electronic structure is described by the Hamiltonian $H_e = H_0 + V_{ei}(R_I)$.[1] H_0 describes the Rydberg electron interacting with the positively charged Rydberg core and $V_{ei}(R_I)$ is the net multipole interaction between the ion and Rydberg atom for a given internuclear separation R_I [28,29],

$$V_{ei}(R_I) = -\sum_{\lambda=1}^{\infty} \sqrt{\frac{4\pi}{2\lambda+1}} \frac{r^\lambda}{R_I^{\lambda+1}} Y_\lambda^0(\theta,\phi). \qquad (1)$$

We choose our coordinate system such that the Rydberg core is located at the origin and the ion-Rydberg internuclear axis lies along the z axis. The position of the Rydberg electron relative to the Rydberg core is given by (r,θ,ϕ) in spherical coordinates. Y_λ^μ are the spherical harmonics with angular momentum λ and angular momentum projection μ, which should not be confused with the orbital angular momentum quantum numbers defining the Rydberg state, namely, l and m. Since we have chosen $\mathbf{R}_I = R_I \hat{z}$, μ is restricted to $\mu = 0$. The order of the multipole expansion in (1) is typically truncated at $\lambda = 6$ since higher-order terms only provide energy corrections on the sub-MHz level, which can be safely neglected here.

The time-independent Schrödinger equation for the electronic Hamiltonian reads $H_e \psi_\nu(\mathbf{r};R) = \varepsilon_\nu(R)\psi_\nu(\mathbf{r};R)$, which depends parametrically on the internuclear separation R, while ν labels the separate adiabatic electronic states. The Born-Oppenheimer PECs $\{\varepsilon_\nu\}$ obtained from the exact diagonalization of H_e in a finite Rydberg basis are shown in the region of the Rydberg $32P$ state in Fig. 2. Note that we neglect the fine and hyperfine structures in our analysis since they are not responsible for the primary features and results obtained here.

As predicted in [28,29], the ion-Rydberg interaction potential $V_{ei}(R_I)$ couples nearby Rydberg states of different angular momentum l character, leading to a series of potential wells in the vicinity of the Rydberg p state which support bound vibrational states with a spacing of the order of 100 MHz (see inset of Fig. 2). The color bar in Fig. 2 encodes the l-character of the electronic states, which changes in particular around the avoided crossings. In principle, these

---

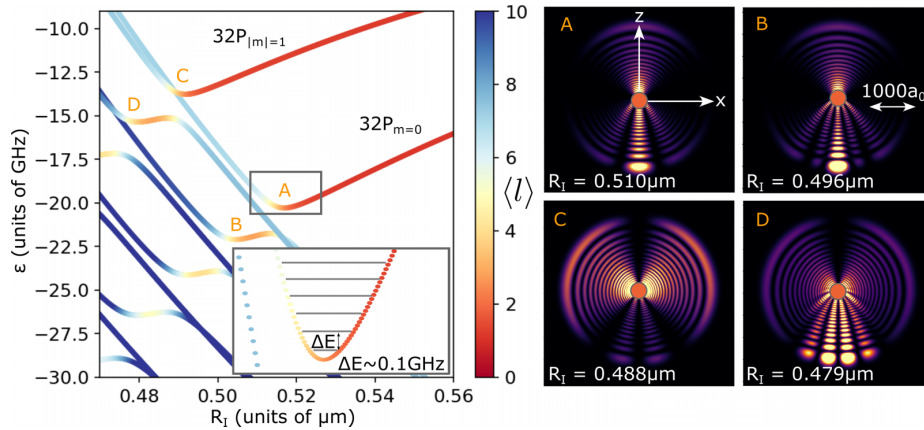[1]Unless stated otherwise, atomic units are assumed throughout.

FIG. 2. Adiabatic potential energy curves and electronic density of the ion-Rydberg dimer system. Left: adiabatic PEC near the $32P$ atomic Rydberg state. The color bar indicates the l-character $\langle l \rangle$ of the corresponding electronic states. Energies are given relative to the field-free $32P$ atomic Rydberg state. Inset: close-up of well A showing the energies of the first few vibrational states. Right: the electronic density $|\psi(r, \theta, \phi)|^2$ in the $y = 0$ plane at the four minima A–D shown in (a). Plots are normalized such that $\int r^2 \sin\theta |\psi(r, \theta, \phi)|^2 dr d\theta d\phi = 1$. Note that the ion (not shown) lies outside the Rydberg cloud.

avoided crossings should introduce nonadiabatic corrections to the Born-Oppenheimer approximation, yet remarkably the vibrational energies calculated using the adiabatic approximation are in excellent agreement with current measurements [30]. Moreover, a recent theoretical study determined that the nonadiabatic decay rate of ion-Rydberg molecules should be far smaller than the radiative decay of the parent Rydberg atom [64].

As a direct result of the admixture of low- and high-l states, the electronic densities of these molecules display interesting lobelike patterns. These can be seen in Fig. 2, which shows two-dimensional (2D) slices of the Rydberg electron's probability density in the $y = 0$ plane for the first four potential wells, marked A to D. The lobes differ in the degree of their azimuthal localization. Additionally, the number of lobes present in the probability density increases for potential wells lying deeper in the fan of electronic states, thereby forming a series of unique electronic densities. We choose to classify the series of electronic densities formed by states of $m = 0$ character [Figs. 2(A) and 2(B)] as "squid states" from their resemblance to a head with several appendages, while the winglike features of the density patterns formed by $|m| = 1$ states [Figs. 2(C) and 2(D)] are reminiscent of an angel pattern made in the snow.

We emphasize that the potential wells shown near the $32P$ atomic Rydberg state in Fig. 2 are a general feature of the ion-Rydberg system and should appear in the adiabatic PEC over a wide range of principal quantum numbers. Indeed, molecular states have already been observed at different principle quantum numbers [30]. Furthermore, a perturbative treatment of the ion-Rydberg interaction given by Eq. (1) yields leading-order energy corrections to the Rydberg p state and quasidegenerate high-l states of $\varepsilon_p \propto -n^7/R^4$ and $\varepsilon_{l>3} \propto \pm n^2/R^2$, respectively. From these results, it is expected that the equilibrium separation and binding energy of the ion-Rydberg molecule should scale as $R_e \propto n^{2.5}$ and $\varepsilon_b \propto n^{-3}$, similar to the scaling laws of Rydberg macrodimer binding potentials [62].

B. From the charged dimer to the trimer

The interaction of a Rydberg atom and a ground-state atom is determined by the scattering of the highly excited Rydberg electron off the ground-state atom. The corresponding s-wave scattering term is described by the Fermi pseudopotential $V_{ea} = 2\pi a_s[k(R_A)]\delta(\mathbf{r} - \mathbf{R_A})$. This model predicts the appearance of wells in the PEC for regions where the scattering length $a_s[k(R_A)]$ is negative. These wells support weakly bound vibrational states with binding energies in the range of MHz to GHz, as first shown in [35]. These bound molecular states are *ultralong-range Rydberg molecules* (ULRMs) and examples include the polar trilobite state and the nonpolar s state ULRMs [32].

Motivated by this fact, we now turn to the question of whether the same mechanism could enable ion-Rydberg molecules to bind an additional ground-state atom within the orbit of the Rydberg electron, forming a *charged* ULRM trimer. To that end, we consider an additional ground-state atom within the Rydberg cloud, as shown by the schematic in Fig. 1(b). If this binding is possible, the various lobes of high electron density present in the squid and snow angel states would enable the formation of both linear and nonlinear bound configurations of the atoms, akin to the d-state angular trimers reported in [51].

III. ELECTRONIC STRUCTURE OF THE TRIMER

In this section, we consider the effect of an additional ground-state atom on the first squid and snow angel states, whose unperturbed electronic densities are shown in Figs. 2(A) and 2(C), respectively.

A. Setup and interactions

With the Rydberg core at the origin of our coordinate system, the ion and ground-state atom are located at positions $(R_I, 0, 0)$ and $(R_A, \Theta, 0)$, respectively. A schematic for this three-body system is provided in Fig. 1(b). Within the
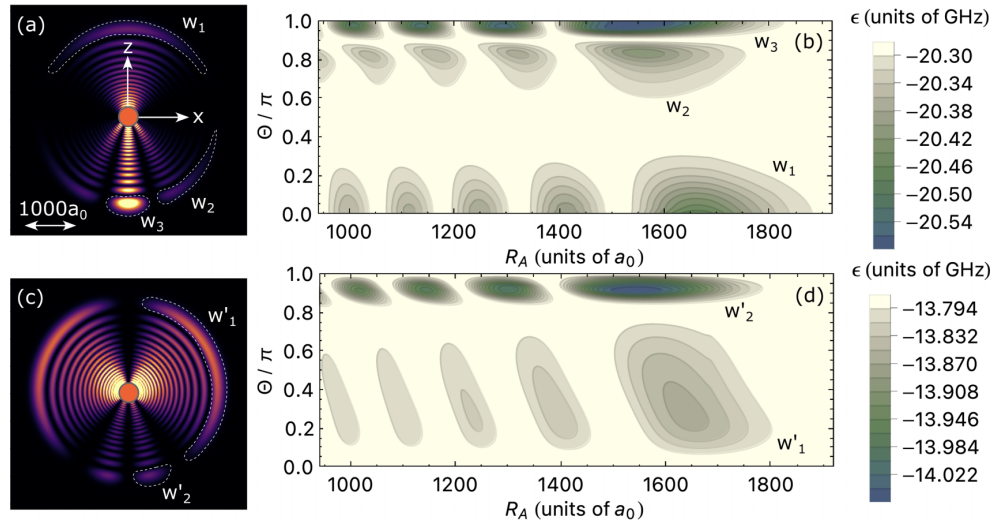
FIG. 3. Adiabatic potential energy surfaces of the squid and snow angel states for the trimer system. (a) The electronic density of the three-legged squid state in the dimer system. (b) 2D slice taken at $R_I = 0.510$ μm of the squid state's PES with major local minima denoted by $\{w_i\}$. (c) The electronic density of the snow angel state in the $y = 0$ plane. (d) 2D slice taken at $R_I = 0.488$ μm of the snow angel state's PES with major local minima denoted by $\{w'_i\}$. Energies are given relative to the field-free $32P$ atomic Rydberg state.

Born-Oppenheimer approximation, the electronic structure of the Rb^+-Rb^*-Rb system is based on the following Hamiltonian:

$$H_e = H_0 + V_{ei}(R_I) + V_{ea}(R_A) + V_{ca}(R_A) + V_{ia}(R_I, R_A, \Theta).$$

$$(2)$$

V_{ei} describes the electron-ion interaction (1) and V_{ea} represents the s-wave scattering between the electron and the ground-state atom. V_{ca} and V_{ia} are the interactions between the Rydberg core and the ion with the neutral atom, respectively. These interactions take the form of a charge-induced dipole (polarization potential) interaction, e.g., $V_{ca} \propto -1/R_A^4$.

We obtain the adiabatic PES $\{\varepsilon_\nu(R_I, R_A, \Theta)\}$ from the exact diagonalization of the electronic Hamiltonian (2) using a finite basis of unperturbed Rydberg states $\{|n, l, m\rangle\}$, where the quantum numbers take their usual meaning. Specifically, our electronic basis includes all states enclosed by the nearest six hydrogenic manifolds centered around the $32P$ atomic Rydberg state, up to a maximum magnetic quantum number of $|m| = 4$.

Besides introducing additional interactions, the presence of the ground-state atom breaks the dimer's cylindrical symmetry, such that m is no longer a good quantum number. This means couplings between states of different m-character are no longer prohibited, though generally this will only be relevant where states become near degenerate. One example of this occurs close to the minimum of the first snow angel state, labeled as C in Fig. 2. In principle, this requires that we enlarge our basis to account for the additional couplings that arise between different m states.

B. Adiabatic potential energy surfaces

Let us analyze in the following the relevant adiabatic PES of the trimer. Figure 3 shows the electronic densities of

the squid and snow angel states in the dimer system alongside 2D slices of the corresponding Born-Oppenheimer PES $\varepsilon(R_I, R_A, \Theta)$ for the trimer system at fixed R_I. Each lobe in the electronic density leads to a unique local minimum along Θ. Along R_A, the surfaces exhibit a series of local minima due to the oscillatory electronic density along each lobe. The deepest minima are found at $R_A \approx 1700\,a_0$ and have a depth of the order of 100 MHz, similar to a conventional nonpolar ULRM at this principal quantum number.

For the squid state, we focus on three local minima labeled w_1, w_2, and w_3 in Fig. 3(b). These minima occur at angles $\Theta = 0$, $\Theta = 0.8\pi$, and $\Theta = \pi$, respectively, which map directly to the three unique lobes in the electronic density in Fig. 3(a). Well w_3 is the deepest of these, which is not surprising since the electronic probability density is highly localized at this position. For the snow angel state, we focus on the two minima labeled w'_1 and w'_2. The depths of these wells are similar in magnitude to those of the squid state. Since the electronic probability density vanishes along the z axis, no local minima appear along $\Theta = 0$ and $\Theta = \pi$ and, as such, it should not be possible for the snow angel to support linear trimer configurations.

C. Coupling among states of different magnetic quantum number

We now discuss couplings among PESs of different magnetic quantum number m that arise due to the presence of the ground-state atom. Figure 4(a) shows an angular cut of the squid state's PES $\varepsilon(\Theta)$ for $R_I = 9756\,a_0$ and $R_A = 1653\,a_0$, with a color bar denoting the m-character of the state. The surface exhibits potential wells at $\Theta = 0$, $\Theta = 0.8\pi$, and $\Theta = \pi$, which correspond to the local minima w_1, w_2, and w_3 defined in Fig. 3(b), respectively. Along this cut, the m-character is pure $m = 0$ and no other surfaces are present in
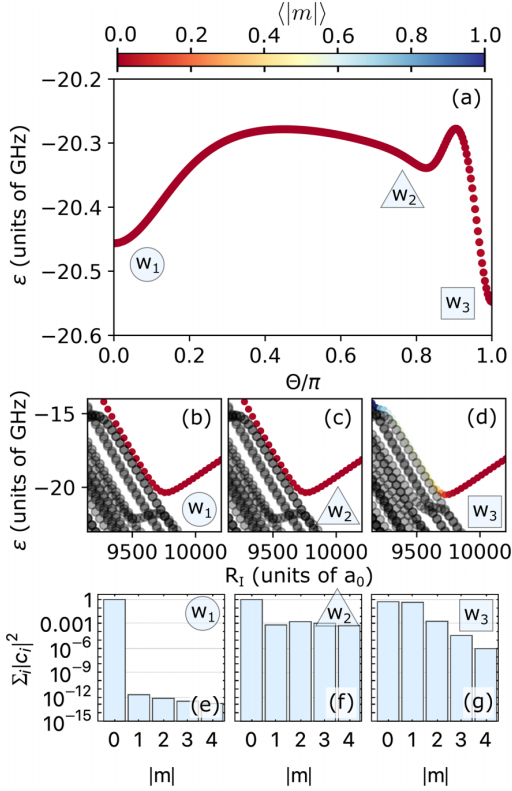
FIG. 4. The m-admixture in the three-body squid state. (a) Angular slice of the squid state's PES with color bar denoting the electronic state's m-character $\langle|m|\rangle$. (b)–(d) Radial slices of the PES near the w_1, w_2, and w_3 local minima, respectively. (e)–(g) The squid states' composition in terms of Rydberg basis states grouped by their m quantum number at the w_1, w_2, and w_3 local minima, respectively. Energies are given relative to the field-free $32P$ Rydberg state.

FIG. 5. The m-admixture in the three-body snow angel state. (a) Angular slice of the snow angel state's PES with color bar denoting the electronic state's m-character $\langle m\rangle$. (b),(c) Radial slices of the PES near the w_1' and w_2' local minima, respectively. (d),(e) The snow angel state's composition in terms of Rydberg basis states grouped by their m quantum number at the w_1 and w_2 local minima, respectively. Energies are given relative to the field-free $32P$ Rydberg state.

the energy window shown. However, as is visible from Fig. 2, the ion-Rydberg dimer's potential well exists above a fan of high-l Stark-split states. Figures 4(b)–4(d) show slices of the PES along R_I for values of Θ and R_A taken around the three local minima in Fig. 4(a). For wells w_1 and w_2, the PES are qualitatively similar to those of the dimer and show only marginal deviation from the $m = 0$ character. This is further illustrated by Figs. 4(e) and 4(f), which show the cumulative overlap coefficients $|c_i|^2 = |\langle\psi(R_I, R_A, \Theta)|\varphi_i\rangle|^2$ of the squid state $\psi(R_I, R_A, \Theta)$ for each local minimum with atomic Rydberg basis states $\{\varphi_i\}$, grouped by their magnetic quantum number m. The lack of coupling is perhaps most surprising for the case of well w_2, which corresponds to a nonlinear configuration of the three atoms and is hence the least symmetric of all three wells. In contrast, the slice along R_I for well w_3 in Fig. 4(d) shows that the local minimum is shifted to slightly lower R_I, such that it crosses into the fan of high-l states. This observed shift does not seem to modify the l-character, but it does result in an admixture with states of finite m at small angles around the local minimum, $\Theta = \pi + \epsilon$. This admixture is primarily with $|m| = 1$ states, as shown in Fig. 4(g). Note that these couplings vanish at $\Theta = \pi$ since cylindrical symmetry is restored, i.e., the three atoms are colinear.
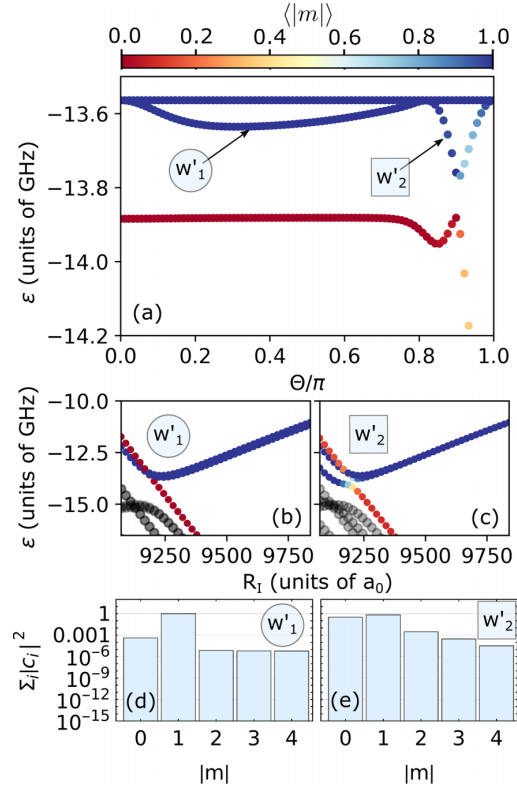
As already mentioned in Sec. III A in the context of the dimer system, the squid state's PEC crosses the curve of the snow angel state near the snow angel's potential well (cf. well C in Fig. 2). In the dimer system, this crossing is exact since there can be no coupling among surfaces of different magnetic quantum number m. In the trimer system, this no longer holds and a finite coupling between the $m = 0$ squid surface and the $|m| = 1$ snow angel surfaces is observed in Fig. 5. This admixture is most significant near the w_2' well, for which a pronounced avoided crossing arises, as shown in Figs. 5(a) and 5(c). While the shallower w_1' well also shows minor admixture [Fig. 5(d)], it is nevertheless orders of magnitude smaller than for w_2' and, if any avoided crossing is present, its gap cannot be discerned on the energy scale of Fig. 5(b).

From here on, we limit our analysis of the vibrational structure to those local minima which show only relatively weak m admixture (w_1, w_2, and w_1') because we expect the Born-Oppenheimer approximation to continue to hold for these. We treat crossings with states of different m-character near these minima as being approximately exact, though this only applies to w_1' since no crossings were observed in the vicinity of the minima of wells w_1 and w_2. For the remaining wells (w_3 and

w_2'), we expect strong nonadiabatic couplings to exist with neighboring PES.

IV. VIBRATIONAL STRUCTURE OF THE TRIMER

In this section, we explore the vibrational structure of the three-body system defined by the nuclear Hamiltonian H_n in the vicinity of the local minima w_1, w_2, and w_1' of the electronic squid and snow angel states. We begin by discussing our computational approach and afterward present the analysis of the vibrational structure.

A. Methodology and computational approach

The total Hamiltonian of our trimer system reads $H = H_e + H_n$. In the previous section, we have discussed solutions to the electronic Hamiltonian H_e obtained via exact diagonalization in a finite basis of Rydberg states $\{|n, l, m\rangle\}$. Here, we focus on the vibrational motion of the nuclei, assuming that the system possesses zero angular momentum, $J = 0$. Accordingly, the full vibrational Hamiltonian [65–67] is given by

$$
\begin{aligned}
H_n &= \frac{1}{m}\left[-\frac{\partial^2}{\partial R_I^2} - \frac{\partial^2}{\partial R_A^2} - \cos(\Theta)\frac{\partial}{\partial R_I}\frac{\partial}{\partial R_A} \right] \\
&\quad - \frac{1}{m}\left(\frac{1}{R_I^2} + \frac{1}{R_A^2} - \frac{\cos(\Theta)}{R_I R_A} \right)\left[\frac{\partial^2}{\partial \Theta^2} + \cot(\Theta)\frac{\partial}{\partial \Theta} \right] \\
&\quad - \frac{1}{m}\left(\frac{1}{R_I R_A} - \frac{1}{R_A}\frac{\partial}{\partial R_I} - \frac{1}{R_I}\frac{\partial}{\partial R_A} \right) \\
&\quad \times \left[\cos(\Theta) + \sin(\Theta)\frac{\partial}{\partial \Theta} \right] + \varepsilon_\nu(R_I, R_A, \Theta),
\end{aligned}
\tag{3}
$$

where m is the atomic mass of Rb and $\varepsilon_\nu(R_I, R_A, \Theta)$ is the νth adiabatic electronic PES satisfying $H_e\psi_\nu(\mathbf{r}; R_I, R_A, \Theta) = \varepsilon_\nu(R_I, R_A, \Theta)\psi_\nu(\mathbf{r}; R_I, R_A, \Theta)$. The time-independent Schrödinger equation for the vibrational Hamiltonian in the Born-Oppenheimer approximation reads

$$
H_n \chi_i(R_I, R_A, \Theta) = E_i \chi_i(R_I, R_A, \Theta),
\tag{4}
$$

with vibrational eigenstates $\{\chi_i(R_I, R_A, \Theta)\}$ and associated eigenenergies E_i.

In order to efficiently solve the above vibrational problem, we utilize the powerful multiconfiguration time-dependent Hartree method (MCTDH) [68–74]. A thorough introduction to MCTDH can be found in [71,73]. In the following, we provide a brief account of the approach in order to be self-contained. MCTDH is an *ab initio* method for multimode wave-packet propagation in high-dimensional spaces. The MCTDH representation of our vibrational wave function $\chi(R_I, R_A, \Theta, t)$ is written as a series of Hartree products,

$$
\begin{aligned}
\chi(R_I, R_A, \Theta, t) &= \sum_{i_1=1}^{n_1}\sum_{i_2=1}^{n_2}\sum_{i_3=1}^{n_3} A_{i_1, i_2, i_3}(t) \\
&\quad \times \varphi_{i_1}^{(1)}(R_I, t)\varphi_{i_2}^{(2)}(R_A, t)\varphi_{i_3}^{(3)}(\Theta, t),
\end{aligned}
\tag{5}
$$

where $A_{i_1, i_2, i_3}(t)$ are time-dependent coefficients and $\{\varphi_{i_d}^{(d)}\}_{i_d=1}^{n_d}$ are the so-called single-particles functions (SPFs) for the dth degree of freedom, for which a total of n_d SPFs are used.

MCTDH reduces computational effort by employing a small time-dependent basis that evolves according to the Dirac-Frenkel variational principle $\langle \delta\chi|(i\partial_t - \hat{H})|\chi\rangle = 0$. This ensures that the basis follows the active part of the complete Hilbert space as it evolves over time. The time-dependent SPFs are described using a time-independent discrete variable representation (DVR) [75]. In this work, we use sine DVRs for the radial degrees of freedom and a Legendre DVR for the angular degree of freedom. SPFs for the radial degrees of freedom are normalized as $\int dR|\varphi(R)|^2 = 1$ and the angular SPFs are normalized according to $\int d\Theta \sin\Theta|\varphi(\Theta)|^2 = 1$.

The vibrational ground state can be obtained by propagating the starting wave packet in imaginary time, whereas excited states are obtained using so-called improved relaxation. Here, the time-dependent coefficients $\{A_{i_1, i_2, i_3}(t)\}$ are set equal to an eigenvector $\mathbf{A}$ of the Hamiltonian in the instantaneous SPF basis, $\{\varphi_{i_d}^{(d)}\}_{i_d=1}^{n_d}$. The coefficients are then kept constant while the SPFs are relaxed using imaginary-time propagation. This process is repeated until χ converges to a stationary state of the Hamiltonian. For our analysis, we seek the lowest few eigenstates in the potential wells w_1, w_2, and w_1' of the squid and snow angel PES. These are obtained by first performing a block improved relaxation scheme [73], which provides approximate results for the first 30–40 lowest-energy eigenstates. Out of this set, we select the states of interest and relax each of them individually using improved relaxation until convergence is achieved.

We consider a calculation to be converged when the change in energy between time steps remains consistently less than 1 Hz over a period of 100 time steps. Additionally, we assure that the occupation of the n_d-th orbital for each degree of freedom is less than 0.1% and that the occupations $\{A_{i_1, i_2, i_3}(t)\}$ decrease exponentially. For the majority of our calculations, 100 grid points and 10 single-particle functions for each degree of freedom were sufficient to converge all eigenenergies.

B. Vibrational structure

Figure 6 shows results for the reduced angular and radial densities of the four lowest vibrational states in the squid state's w_1 potential well. Table I summarizes the properties of the lowest vibrational states in all three trimer wells and compares these with the vibrational states of the squid and snow angel dimer.

In Figs. 6(a) and 6(b), we observe that the energetically lowest states in the potential well w_1 are localized around $\Theta = 0$ such that the three atoms are arranged along a common internuclear axis, i.e., in a collinear configuration. The well's ground state is approximately 180 MHz lower in energy than the ground state of the squid state dimer and exhibits a positive shift of the ion-Rydberg bond length and corresponding electric dipole moment, as shown in Table I. From Fig. 6(b), we find that the reduced angular density of the first excited state exhibits an additional node, indicating that this is a bending mode. The excitation energy of this mode is about 20 MHz above the ground-state energy. In contrast, the first excited state of the dimer is approximately 88.1 MHz. The second excited state is also a bending mode, with an additional node along the reduced angular density in Fig. 6(b). The third excited state's energy lies close to that of the second excited
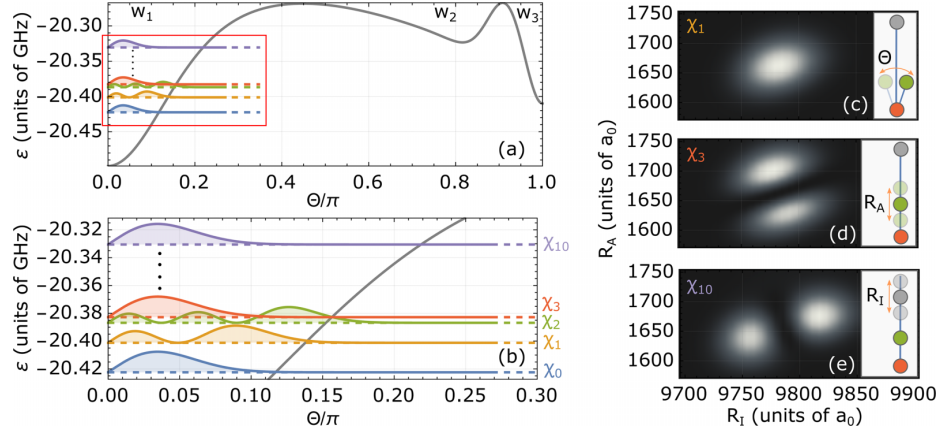
FIG. 6. Selection of vibrational states of the squid state trimer's w_1 potential well. (a) Angular cut through the potential energy surface (gray) near the local minimum $(R_I, R_A, \Theta) = (9782a_0, 1657a_0, 0)$. (b) Reduced angular densities $\rho_\nu(\Theta) = \int dR_I dR_A |\chi_\nu(R_I, R_A, \Theta)|^2$ of the vibrational states $\nu = \{0, 1, 2, 3, 10\}$ (filled curves) offset by their energy (dashed lines). (c),(d),(e) Reduced radial densities $\rho_\nu(R_I, R_A) = \int d\Theta |\chi_\nu(R_I, R_A, \Theta)|^2$ of χ_1, χ_3, and χ_{10}, respectively. The eigenstates are normalized as $\int dR_I dR_A d\Theta |\chi_\nu(R_I, R_A, \Theta)|^2 = 1$. All energies given relative to the field-free $32P$ atomic Rydberg state.

state, yet its reduced radial density in Fig. 6(d) confirms that it is an excitation in R_A, a stretching mode. The energy gap to the first excitation in R_I is 91.6 MHz, which is of the same order of magnitude as the energy gap between vibrational states of the dimer.

We now examine some global trends of properties among the three wells evident from Table I. Surprisingly, the ground-state atom's presence appears to contribute to a consistent positive shift of 20 Debye in the Rydberg atom's electric dipole moment $\langle d_z \rangle$, independent of which well it inhabits and regardless of whether the expected ion-Rydberg binding length $\langle R_I \rangle$ has increased or decreased with respect to the dimer. On the other hand, the energy gap to the first R_I stretching mode is essentially unchanged by the presence of the perturber. The energy gaps of the bending and R_A stretching modes do vary among the different potential wells. In particular, in the w_1' well, 3 MHz are necessary to excite its first bending mode, while the same gap in the w_1 well is an order of magnitude larger. From the 2D graphs of the PES in Figs. 3(b) and 3(d), we see that w_1 and w_1' are reasonably extended along Θ, which implies a weak angular confinement in both cases. Nevertheless, the w_1 well is considerably deeper than the w_1' well, which leads to the greater excitation gap.

In an experimental setting, it should be possible to distinguish trimer states from dimer states due to the trimer's deeper binding energies and distinguishable excitation series for bending and stretching modes depending on the geometric configuration of the nuclei. Moreover, mass spectroscopy techniques such as that employed in [30] could be used to distinguish the two based on their mass difference. In principle, the trimer's shift in ion-Rydberg binding length could serve as a further indicator for the presence of trimer states. The shifts predicted in Table I are, however, of the order of a few Bohr radii, which is clearly too small to be observed with current techniques. As first shown in [29], the equilibrium separation of the ion-Rydberg dimer R_e scales with the principal quantum number n and, in Fig. 7(a), we find this scaling to be $R_e \propto n^{2.80 \pm 0.18}$, which is close to the value expected from perturbation theory as described in Sec. II A. However, we see no clear trend for the change in the equilibrium separation $\Delta R_e = R_e^{\text{trimer}} - R_e^{\text{dimer}}$ for the well w_1, shown in Fig. 7(b).

On the other hand, there is an evident trend in the difference of the local energy minima, $\Delta \epsilon_{\min} = \epsilon_{\min}^{\text{dimer}} - \epsilon_{\min}^{\text{trimer}}$, between the PES of the dimer and trimer. Figure 7(c) shows $\Delta \epsilon_{\min}$ for the trimer w_1 well and we find $\Delta \epsilon_{\min} \propto n^{-5.97 \pm 0.06}$. This can be understood as follows. To first order, the interaction of the

TABLE I. Contrasting properties of the dimer and trimer vibrational states. From left to right, the first three columns give the difference in the vibrational ground state's (I) expected ion-Rydberg separation $\Delta \langle R_I \rangle = \langle R_I^{\text{trimer}} \rangle - \langle R_I^{\text{dimer}} \rangle$, (II) expected electric dipole moment of the Rydberg atom $\Delta \langle d_z \rangle = \langle d_z^{\text{trimer}} \rangle - \langle d_z^{\text{dimer}} \rangle$, and (III) energy $\Delta E_{000} = E_{000}^{\text{trimer}} - E_{000}^{\text{dimer}}$. The last three columns contain the trimer's excitation energies with respect to the trimer ground state of the first (IV) Θ bending mode $\tilde{E}_{001} = E_{001} - E_{000}$, (V) R_A stretching mode $\tilde{E}_{010} = E_{010} - E_{000}$, and (VI) R_I stretching mode $\tilde{E}_{100} = E_{100} - E_{000}$. Where applicable, corresponding values for the dimer are given in brackets. All quantities are rounded to the nearest decimal place.

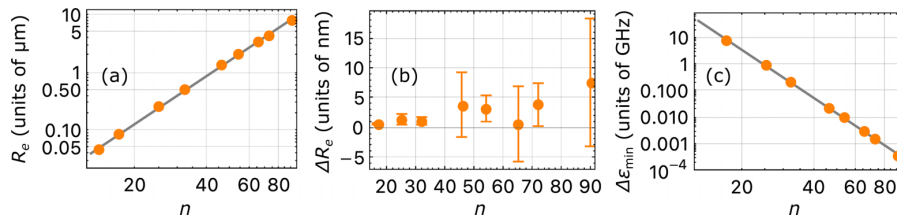|	$\Delta \langle R_I \rangle / a_0$	$\Delta \langle d_z \rangle$/Debye	ΔE_{000}/MHz	$\tilde{E}_{001}$/MHz	$\tilde{E}_{010}$/MHz	$\tilde{E}_{100}$/MHz
Squid w_1	14.1	18.2	−181.9	21.2	39.6	91.9 (88.1)
Squid w_2	−5.3	20.8	−102.8	7.4	31.1	92.6 (88.1)
Angel w_1'	5.9	19.3	−79.9	3.0	29.3	86.6 (86.6)

FIG. 7. (a) Scaling of the squid dimer's bond length with principal quantum number n. (b) Difference in ion-Rydberg equilibrium separation and (c) potential well minima between the squid dimer and squid trimer for the w_1 potential well (cf. well Fig. 3). Error bars in (b) represent the error in ΔR_e, which arises due to the fact that the potential energy surfaces are represented on a discrete grid. Error bars for R_e^{dimer} have been left out since their size is negligible on the scale of (a).

ground-state atom with the Rydberg electron contributes an energy shift proportional to the electron's probability density $\Delta\epsilon \propto |\psi(R_A)|^2$, whose sign depends on the s-wave scattering length $a_s[k(R_A)]$. The electron's probability density scales with the radius of the Rydberg orbit as $|\psi(r)|^2 \propto 1/r^3$, which in turn scales quadratically with n. This gives $\Delta\epsilon \propto n^{-6}$, which is close to our fitted value. Since $\Delta\epsilon_{\min}$ decays with n, the trimer's vibrational spectrum will lie energetically closer to the dimer's at higher principal quantum numbers, making them harder to distinguish. By modulating the density of the background gas of atoms, signals of trimer states can be suppressed or enhanced.

V. CONCLUSIONS

In this work, we first studied the case of an ion interacting with a Rydberg atom and determined the electronic structure of bound states which exist in various potential wells in the spectrum of adiabatic potential energy curves. For atomic species such as Rb and Cs, the ion's presence mixes the quantum defect-split p state with its neighboring quasidegenerate manifold of high-l states. This results in the formation of a twofold series of potential wells, one for each $|m|$ sublevel of the p state. We found that the Rydberg electron's probability density exhibits several lobes, which vary in their size and number between the wells. Due to their distinctive shapes, we classify the electronic density patterns along the $m = 0$ series as squid states, while those along the $|m| = 1$ series are termed snow angel states.

We predict that the lobes in the electronic density admit the binding of additional ground-state atoms via the same binding mechanism as conventional polar and nonpolar ULRMs. We have demonstrated this for a three-body system of a Rydberg atom interacting with a ground-state atom and a single ion, in the limit of nonoverlapping charge distributions. Bound

vibrational states exist among the three species, forming a charged ultralong-range Rydberg trimer. The ground-state atom can become bound within different lobes in the electronic density, such that linear as well as nonlinear geometric configurations of the nuclear framework are possible.

The ground-state atom leads to a significant shift in the energy of the trimer's vibrational ground state and the additional nuclear degrees of freedom give rise to distinct excitation series for bending and stretching modes, which vary between the local minima associated with different lobes in the electronic structure. Using current spectroscopic techniques, it should thus be possible to distinguish the trimer and dimer states. Similarly to the ion-Rydberg dimer, we expect nonadiabatic couplings between neighboring potential energy surfaces to be a significant channel for molecular decay in our system. Indeed, the effect may even be stronger in the trimer system since crossings between states of different m are no longer symmetry protected. Corresponding investigations are left to future studies.

Our work lays the foundation for exploring ULRMs in inhomogeneous electric fields. Future work could consider the interaction of an ion with polyatomic ULRMs and wave-packet dynamics in the ion's field. Additionally, conical intersections can occur between adiabatic potential energy surfaces in triatomic systems and thus one could examine the role of beyond Born-Oppenheimer physics in our system in the spirit of recent work in this direction [76].

ACKNOWLEDGMENTS

[1] C. Zipkes, L. Ratschbacher, S. Palzer, C. Sias, and M. Köhl, J. Phys.: Conf. Ser. **264**, 012019 (2011).

[2] M. Tomza, K. Jachymski, R. Gerritsma, A. Negretti, T. Calarco, Z. Idziaszek, and P. S. Julienne, Rev. Mod. Phys. **91**, 035001 (2019).

[3] R. S. Lous and R. Gerritsma, in *Advances In Atomic, Molecular, and Optical Physics*, Advances in Atomic, Molecular, and

Optical Physics, Vol. 71, edited by L. F. DiMauro, H. Perrin, and S. F. Yelin (Academic Press, San Diego, 2022), pp. 65–133.

[4] L. Ratschbacher, C. Zipkes, C. Sias, and M. Köhl, Nat. Phys. **8**, 649 (2012).

[5] F. H. J. Hall and S. Willitsch, Phys. Rev. Lett. **109**, 233202 (2012).

[6] A. Härter, A. Krükow, A. Brunner, W. Schnitzler, S. Schmid, and J. H. Denschlag, Phys. Rev. Lett. **109**, 123201 (2012).

[7] Z. Meir, T. Sikorsky, R. Ben-shlomi, N. Akerman, Y. Dallal, and R. Ozeri, Phys. Rev. Lett. **117**, 243401 (2016).

[8] J. Pérez-Ríos, Mol. Phys. **119**, e1881637 (2021).

[9] L. Oghittu and A. Negretti, Phys. Rev. Res. **4**, 023069 (2022).

[10] R. Côté, V. Kharchenko, and M. D. Lukin, Phys. Rev. Lett. **89**, 093001 (2002).

[11] J. M. Schurer, A. Negretti, and P. Schmelcher, Phys. Rev. Lett. **119**, 063001 (2017).

[12] D. J. Bosworth, M. Pyzh, and P. Schmelcher, Phys. Rev. A **103**, 033303 (2021).

[13] S. Schmid, A. Härter, and J. H. Denschlag, Phys. Rev. Lett. **105**, 133202 (2010).

[14] C. Zipkes, S. Palzer, C. Sias, and M. Köhl, Nature (London) **464**, 388 (2010).

[15] C. Veit, N. Zuber, O. A. Herrera-Sancho, V. S. V. Anasuri, T. Schmid, F. Meinert, R. Löw, and T. Pfau, Phys. Rev. X **11**, 011036 (2021).

[16] R. Gerritsma, A. Negretti, H. Doerk, Z. Idziaszek, T. Calarco, and F. Schmidt-Kaler, Phys. Rev. Lett. **109**, 080402 (2012).

[17] J. M. Schurer, R. Gerritsma, P. Schmelcher, and A. Negretti, Phys. Rev. A **93**, 063602 (2016).

[18] T. Feldker, H. Fürst, H. Hirzler, N. V. Ewald, M. Mazzanti, D. Wiater, M. Tomza, and R. Gerritsma, Nat. Phys. **16**, 413 (2020).

[19] P. Weckesser, F. Thielemann, D. Wiater, A. Wojciechowska, L. Karpa, K. Jachymski, M. Tomza, T. Walker, and T. Schaetz, Nature (London) **600**, 429 (2021).

[20] T. Secker, R. Gerritsma, A. W. Glaetzle, and A. Negretti, Phys. Rev. A **94**, 013420 (2016).

[21] N. V. Ewald, T. Feldker, H. Hirzler, H. A. Fürst, and R. Gerritsma, Phys. Rev. Lett. **122**, 253401 (2019).

[22] T. Secker, N. Ewald, J. Joger, H. Fürst, T. Feldker, and R. Gerritsma, Phys. Rev. Lett. **118**, 263201 (2017).

[23] T. Schmid, C. Veit, N. Zuber, R. Löw, T. Pfau, M. Tarana, and M. Tomza, Phys. Rev. Lett. **120**, 153401 (2018).

[24] R. Côté, Phys. Rev. Lett. **85**, 5316 (2000).

[25] T. Dieterle, M. Berngruber, C. Hölzl, R. Löw, K. Jachymski, T. Pfau, and F. Meinert, Phys. Rev. Lett. **126**, 033401 (2021).

[26] F. Engel, T. Dieterle, T. Schmid, C. Tomschitz, C. Veit, N. Zuber, R. Löw, T. Pfau, and F. Meinert, Phys. Rev. Lett. **121**, 193401 (2018).

[27] K. S. Kleinbach, F. Engel, T. Dieterle, R. Löw, T. Pfau, and F. Meinert, Phys. Rev. Lett. **120**, 193401 (2018).

[28] A. Duspayev, X. Han, M. A. Viray, L. Ma, J. Zhao, and G. Raithel, Phys. Rev. Res. **3**, 023114 (2021).

[29] M. Deiß, S. Haze, and J. Hecker Denschlag, Atoms **9**, 34 (2021).

[30] N. Zuber, V. S. V. Anasuri, M. Berngruber, Y.-Q. Zou, F. Meinert, R. Löw, and T. Pfau, Nature (London) **605**, 453 (2022).

[31] Y.-Q. Zou, M. Berngruber, V. S. V. Anasuri, N. Zuber, F. Meinert, R. Löw, and T. Pfau, Phys. Rev. Lett. **130**, 023002 (2023).

[32] M. T. Eiles, J. Phys. B: At. Mol. Opt. Phys. **52**, 113001 (2019).

[33] C. Fey, F. Hummel, and P. Schmelcher, Mol. Phys. **118**, e1679401 (2020).

[34] E. Fermi, Nuovo Cim **11**, 157 (1934).

[35] C. H. Greene, A. S. Dickinson, and H. R. Sadeghpour, Phys. Rev. Lett. **85**, 2458 (2000).

[36] V. Bendkowsky, B. Butscher, J. Nipper, J. P. Shaffer, R. Löw, and T. Pfau, Nature (London) **458**, 1005 (2009).

[37] T. Manthey, T. Niederprüm, O. Thomas, and H. Ott, New J. Phys. **17**, 103024 (2015).

[38] J. D. Whalen, S. K. Kanungo, R. Ding, M. Wagner, R. Schmidt, H. R. Sadeghpour, S. Yoshida, J. Burgdörfer, F. B. Dunning, and T. C. Killian, Phys. Rev. A **100**, 011402(R) (2019).

[39] J. D. Whalen, R. Ding, S. K. Kanungo, T. C. Killian, S. Yoshida, J. Burgdörfer, and F. B. Dunning, Mol. Phys. **117**, 3088 (2019).

[40] D. A. Anderson, S. A. Miller, and G. Raithel, Phys. Rev. Lett. **112**, 163201 (2014).

[41] H. Saßmannshausen, F. Merkt, and J. Deiglmayr, Phys. Rev. Lett. **114**, 133201 (2015).

[42] F. Böttcher, A. Gaj, K. M. Westphal, M. Schlagmüller, K. S. Kleinbach, R. Löw, T. C. Liebisch, T. Pfau, and S. Hofferberth, Phys. Rev. A **93**, 032512 (2016).

[43] R. Schmidt, H. R. Sadeghpour, and E. Demler, Phys. Rev. Lett. **116**, 105302 (2016).

[44] F. Camargo, R. Schmidt, J. D. Whalen, R. Ding, G. Woehl, S. Yoshida, J. Burgdörfer, F. B. Dunning, H. R. Sadeghpour, E. Demler, and T. C. Killian, Phys. Rev. Lett. **120**, 083401 (2018).

[45] J. Sous, H. R. Sadeghpour, T. C. Killian, E. Demler, and R. Schmidt, Phys. Rev. Res. **2**, 023021 (2020).

[46] V. Bendkowsky, B. Butscher, J. Nipper, J. B. Balewski, J. P. Shaffer, R. Löw, T. Pfau, W. Li, J. Stanojevic, T. Pohl, and J. M. Rost, Phys. Rev. Lett. **105**, 163201 (2010).

[47] A. Gaj, A. T. Krupp, J. B. Balewski, R. Löw, S. Hofferberth, and T. Pfau, Nat. Commun. **5**, 4546 (2014).

[48] I. C. H. Liu, J. Stanojevic, and J. M. Rost, Phys. Rev. Lett. **102**, 173001 (2009).

[49] C. Fey, M. Kurz, and P. Schmelcher, Phys. Rev. A **94**, 012516 (2016).

[50] M. T. Eiles, J. Pérez-Ríos, F. Robicheaux, and C. H. Greene, J. Phys. B: At. Mol. Opt. Phys. **49**, 114005 (2016).

[51] C. Fey, J. Yang, S. T. Rittenhouse, F. Munkes, M. Baluktsian, P. Schmelcher, H. R. Sadeghpour, and J. P. Shaffer, Phys. Rev. Lett. **122**, 103001 (2019).

[52] M. T. Eiles, C. Fey, F. Hummel, and P. Schmelcher, J. Phys. B: At. Mol. Opt. Phys. **53**, 084001 (2020).

[53] A. L. Hunter, M. T. Eiles, A. Eisfeld, and J. M. Rost, Phys. Rev. X **10**, 031046 (2020).

[54] I. Lesanovsky, P. Schmelcher, and H. R. Sadeghpour, J. Phys. B: At. Mol. Opt. Phys. **39**, L69 (2006).

[55] M. Kurz and P. Schmelcher, J. Phys. B: At. Mol. Opt. Phys. **47**, 165101 (2014).

[56] A. T. Krupp, A. Gaj, J. B. Balewski, P. Ilzhöfer, S. Hofferberth, R. Löw, T. Pfau, M. Kurz, and P. Schmelcher, Phys. Rev. Lett. **112**, 143008 (2014).

[57] A. Gaj, A. T. Krupp, P. Ilzhöfer, R. Löw, S. Hofferberth, and T. Pfau, Phys. Rev. Lett. **115**, 023001 (2015).

[58] T. Niederprüm, O. Thomas, T. Eichert, C. Lippe, J. Pérez-Ríos, C. H. Greene, and H. Ott, Nat. Commun. **7**, 12820 (2016).

[59] F. Hummel, C. Fey, and P. Schmelcher, Phys. Rev. A **99**, 023401 (2019).

[60] F. Engel, T. Dieterle, F. Hummel, C. Fey, P. Schmelcher, R. Löw, T. Pfau, and F. Meinert, Phys. Rev. Lett. **123**, 073003 (2019).

[61] F. Hummel, K. Keiler, and P. Schmelcher, Phys. Rev. A **103**, 022827 (2021).

[62] S. Hollerith and J. Zeiher, arXiv:2212.01673.

[63] R. J. Le Roy, Can. J. Phys. **52**, 246 (1974).

[64] A. Duspayev and G. Raithel, Phys. Rev. A **105**, 012810 (2022).

[65] C. Fey, F. Hummel, and P. Schmelcher, Phys. Rev. A **99**, 022506 (2019).

[66] S. Carter and N. Handy, Mol. Phys. **47**, 1445 (1982).

[67] N. Handy, Mol. Phys. **61**, 207 (1987).

[68] H.-D. Meyer, U. Manthe, and L. S. Cederbaum, Chem. Phys. Lett. **165**, 73 (1990).

[69] M. H. Beck, A. Jäckle, G. A. Worth, and H.-D. Meyer, Phys. Rep. **324**, 1 (2000).

[70] H.-D. Meyer and G. A. Worth, Theor. Chem. Acc. **109**, 251 (2003).

[71] H.-D. Meyer, F. Le Quéré, C. Léonard, and F. Gatti, Chem. Phys. **329**, 179 (2006).

[72] L. J. Doriol, F. Gatti, C. Iung, and H.-D. Meyer, J. Chem. Phys. **129**, 224109 (2008).

[73] H.-D. Meyer, Wiley Interdiscip. Rev.: Comp. Mol. Sci. **2**, 351 (2012).

[74] G. A. Worth, M. H. Beck, A. Jäckle, O. Vendrell, and H.-D. Meyer, The MCTDH Package, Ver. 8.2 (2000); H.-D. Meyer, Ver. 8.3 (2002) and Ver. 8.4 (2007); O. Vendrell and H.-D. Meyer, Ver. 8.5 (2013); Versions 8.5 and 8.6 contain the ML-MCTDH algorithm. Used version: 8.6.1. See http://mctdh.uni-hd.de/.

[75] D. O. Harris, G. G. Engerholm, and W. D. Gwinn, J. Chem. Phys. **43**, 1515 (1965).

[76] F. Hummel, M. T. Eiles, and P. Schmelcher, Phys. Rev. Lett. **127**, 023003 (2021).

Excited state preparation of trapped ultracold atoms via swept potentials [SC3]

Excited-state preparation of trapped ultracold atoms via swept potentials

Daniel J. Bosworth [1,2,*] Maxim Pyzh [1] and Peter Schmelcher [1,2,†]

[1]*Zentrum für Optische Quantentechnologien, Universität Hamburg, Luruper Chaussee 149, 22761 Hamburg, Germany*
[2]*Hamburg Centre for Ultrafast Imaging, Universität Hamburg, Luruper Chaussee 149, 22761 Hamburg, Germany*

We study the out-of-equilibrium dynamics of noninteracting atoms confined within a one-dimensional harmonic trap triggered by dragging an external long-range potential through the system. The symmetry-breaking nature of this moving potential couples adjacent eigenstates in the atoms' effective potential, leading to an energy landscape reminiscent of systems exhibiting trap-induced shape resonances. These couplings may be exploited to selectively excite the atoms into higher vibrational states of the harmonic trap by controlling the motion of the dragged potential. To this end, we consider two protocols designs: The first protocol strives to maintain adiabaticity at critical points during the atoms' dynamics, while the second protocol utilizes the fast tunneling of the atoms within their effective double-well potential. These protocols take place in the few to many millisecond regime and achieve high-fidelity excitation of the atoms into pure vibrational states and superpositions thereof. Overall, our study highlights the significance of dragged potentials for controlling and manipulating atom dynamics and offers intuitive protocols for achieving desired excitations.

DOI: 10.1103/PhysRevA.109.013311

I. INTRODUCTION

Reliable and efficient quantum state engineering techniques are indispensable for emerging quantum technologies from information processing to interferometry and communications. Ultracold quantum gases are particularly suited to the manipulation of quantum states and dynamics due to the exceptional control over interparticle interactions via tunable scattering resonances [1], the ability to prepare ensembles with a well-defined number of particles [2,3], and the flexibility of trapping geometry in terms of shape [4,5], periodicity [6], and dimensionality [7].

For trapped ultracold species, transitions between different vibrational states can be carried out by employing external drives, such as deforming [8] or shaking the trapping potential [9]. The latter approach was implemented in [10] to transfer a Bose-Einstein condensate (BEC) to the collective first excited trap state, which serves as a twin-beam matter wave source upon collisional deexcitation of the atoms. Similar protocols for population inversion have been proposed which rely on adiabatic cycles controlled by the interaction of the BEC with a δ-like impurity [11,12]. Additionally, collective excitations such as solitons and vortices may be generated through appropriately steering a focused laser beam through a condensate [13–17]. State transfer protocols such as those described above have been further combined with sophisticated quantum optimal control techniques [18] and shortcuts to adiabaticity [19,20] in order to manipulate quantum systems with high fidelity on timescales shorter than decoherence times (see, e.g., [21]). Quantum optimal control and shortcuts

to adiabaticity can be used for a wide range of applications, including for example the transport of trapped ions [22,23].

Controlled collisions between species in separate traps provide a further avenue for quantum state engineering. In their theoretical work [24], Stock *et al.* found that the quantized relative motion of a colliding atom pair leads to resonances between trap eigenstates and molecular bound states which would not be present in free space. They termed these trap-induced shape resonances (TISR). Later theoretical works uncovered TISR for colliding atom-ion pairs [25] and proposed using TISR to realize two-qubit quantum gates [26] and excite atoms into higher Bloch bands of an optical lattice [27]. TISR have also been considered in the context of single atoms interacting with multiple impurities [28]. Recently, a landmark experiment by Ruttley *et al.* [29] demonstrated the mergoassociation of single cold RbCs molecules using TISR between the constituent atoms confined in separate optical tweezers.

In this work, we consider a particular case of an external drive which enables fine control over the vibrational state occupation of trapped atoms. Similar to [14–16], the external drive takes the form of dynamically swept external potentials. Our potential however is repulsive at short range with a long-range attractive tail supporting bound states, which offers additional flexibility in terms of protocol design and a more diverse dynamical response of the system. We explore how tuning the shape and drag speed of the external drive can be exploited to excite ground-state atoms into excited trap states or superpositions thereof. We propose two different types of protocols for achieving state transfer which rely on avoided crossings arising in the atoms' discrete energy spectrum due to the swept potential, in a manner analogous to the emergence of TISR. The first protocol, slow yet robust, relies on adiabatic sweeping of the potential around certain critical avoided

*dboswort@physnet.uni-hamburg.de
†pschmelc@physnet.uni-hamburg.de

crossings in the energy spectrum. The second protocol, significantly faster yet requiring precise control over the external potential's position, exploits the ability of the atom to undergo relatively fast tunneling at the avoided crossings.

Our work is laid out as follows. In Sec. II we introduce the setup and discuss the landscape of avoided crossings arising in our system and how these can be used to shuttle the atoms to higher excited states. Sections III and IV focus on the two different state preparation protocols and include proof-of-principle demonstrations for both, as well as a discussion of their limitations. Section V summarizes the present study and discusses directions for future work.

II. SWEPT POTENTIAL MODEL

We begin in Sec. II A by introducing the time-dependent Hamiltonian which models the collision between a dragged external potential and trapped atoms in one spatial dimension. Section II B considers the scenario in which the external potential is swept through the trap at a constant velocity, highlighting the emergence of avoided crossings between eigenstates during the collision and the role played by the potential's profile and speed. This motivates the discussion of the state preparation protocols which are the focus of Secs. III and IV.

A. Model: Collision of trapped atoms with a swept potential

Our system is comprised of atoms of mass m confined within a quasi-one-dimensional (quasi-1D) harmonic trap centered at the origin. The quasi-1D confinement requires $\omega_\parallel \ll \omega_\perp$, where $\omega_\parallel$ and $\omega_\perp$ are the longitudinal and transverse trapping frequencies, respectively. The longitudinal axis is chosen to be parallel to the z axis and the corresponding longitudinal eigenstates and associated eigenenergies are denoted by $\{\phi_n(z)\}$ and $\{\epsilon_n = n + \frac{1}{2}\}$, $n \in \mathbb{N}$. Transverse excitations are neglected throughout this paper such that we restrict ourselves to a one-dimensional problem. Finally, unless stated otherwise, all quantities are given in units defined by the oscillator length $a_{\text{HO}} = \sqrt{\hbar/m\omega_z}$ and the energy spacing $\varepsilon_{\text{HO}} = \hbar\omega_z$ of the longitudinal eigenstates.

At $t = 0$, the atom occupies the trap's vibrational ground state $\phi_0(z)$. For $t > 0$, it experiences an additional time-dependent potential $V_o(z, t)$ which is swept from one side of the system to the other along the z axis. The dragged potential's profile is comprised of a short-range repulsive barrier with an attractive long-range tail and takes the form

$$V_o(z, z_o(t)) = a e^{-b(z-z_o(t))^2} - \frac{1}{2[z - z_o(t)]^4 + 1/c}, \quad (1)$$

where $z_o(t)$ is the displacement of the repulsive barrier from the center of the trap. The model parameters a, b, and c set the height and width of the barrier as well as the depth of the wells formed by the attractive tail, respectively. A plot of the potential is provided in the inset of Fig. 1(a). This potential could be created in an experiment using, for example, a tightly trapped ion [30–32] or a shaped optical potential [4].
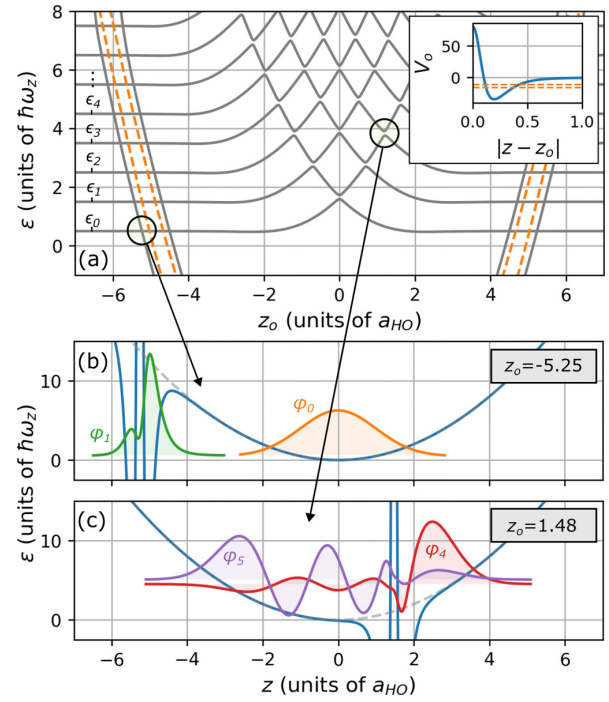

FIG. 1. Instantaneous single-particle energy spectrum. (a) Discrete atomic energy spectrum as a function of the position z_o of the external potential (shown in inset) relative to the trap center. The energies of the lowest few harmonic trap eigenstates are labeled ϵ_i. The dashed lines show the approximate energy shift of the external potential's bound states $\bar{\epsilon}_i + z_o^2/2$ [25] as a function of z_o, where $\bar{\epsilon}_i$ are the energies of the bound states without the harmonic trap. The circles highlight examples of narrowly avoided crossings. Also shown are plots of the instantaneous eigenstates $\{\varphi_i(z; z_o)\}$ near an avoided crossing between (b) a bound state of the dragged potential and a trap state and (c) two trap states. The blue solid line shows the effective potential experienced by the atoms and the gray dashed line is the harmonic trap potential. Eigenstates are vertically offset by their energy. Here we have used the parameters $a = 120$, $b = 4\sqrt{10}c$, and $c = 40$ for the external potential (1).

Summarizing the above considerations, we write the single-atom Hamiltonian as

$$\hat{H}[z_o(t)] = -\frac{1}{2}\frac{d^2}{dz^2} + V_{\text{trap}}(z) + V_o(z, z_o(t)), \quad (2)$$

where $V_{\text{trap}}(z) = z^2/2$ describes the time-independent harmonic trap. Equation (2) is parametrically dependent on the position of the dragged potential z_o and we denote its eigenstates and eigenvalues by $\{\varphi_n(z; z_o)\}$ and $\{\varepsilon_n(z_o)\}$, respectively, to contrast them with those of the pure harmonic trap [$\phi_n(z)$ and ϵ_n].

Hamiltonians of the above form were employed in related works to model atom-ion interactions in the ultracold regime [30,31,33–35]. The atom-ion interaction has a species-dependent length scale R^* and together with the harmonic-oscillator length a_{HO}, these constitute the two characteristic length scales of the system. In this and prior works, we have been interested in the regime where these length

scales are comparable. The form of our Hamiltonian in Eq. (2) is valid for $R^* = a_{\mathrm{HO}}$, which is valid for a variety of species in terms of the atom-ion interaction range and the achievable trapping frequencies. The analysis carried out in the remainder of this work holds for $R^* = a_{\mathrm{HO}}$. However, we emphasize that the proposed protocols would also work for different values so long as the length scales remain comparable. As we mentioned above, the model potential could be realized in one of two ways: (i) a trapped ion and (ii) a shaped optical potential. Thus, we see that the realization with a trapped ion is less flexible since the length scale R^* is set by the choice of species for the atom-ion pair. In contrast, an optical potential would allow greater flexibility since the size of the potential may be tuned in addition to the trapping frequency.

B. Impact of swept potential on the atomic energy spectrum

Let us first solve the time-independent problem to clarify the z_o dependence of the atoms' discrete energy spectrum $\{\varepsilon_n(z_o)\}$. We choose the following model parameters for the external potential (1): $a = 120$, $b = 4\sqrt{10c}$, and $c = 40$ (as used in [30,31,33–35]). For this choice of parameters, the potential supports two bound states with energies $\bar{\epsilon}_0 = -12.2$ and $\bar{\epsilon}_1 = -10.4$, shown in the inset of Fig. 1(a).

Figure 1(a) shows the evolution of the lowest nine eigenvalues with z_o, obtained using exact diagonalization of the Hamiltonian (2). For $|z_o| > 6$, the lowest eigenstates have a regular energy spacing $\hbar\omega_z$ and describe states of the unperturbed harmonic trap. Closer to the trap center [$4 < |z_o(t)| < 6$], the energies of the external potential's bound states are reduced, which leads to level repulsions between the bound states and the trap eigenstates, generating two chains of avoided crossings. The avoided crossings seen here can be considered analogous to trap-induced shape resonances, first predicted by Stock *et al.* for colliding pairs of trapped atoms [24]. That these are indeed a form of shape resonance can be seen in Fig. 1(b), which shows the trap's ground state near its avoided crossing with the lower bound state of the external potential at $z_o = -5.25$. Here these near-degenerate eigenstates are separated by a barrier that forms in the atom's effective potential created by the sum of $V_o(z, z_o)$ and $V_{\mathrm{trap}}(z)$. In addition, a second variety of trap-induced shape resonance analog manifests in this system due this time to the short-range repulsive barrier component of Eq. (1). One such example is shown in Fig. 1(c), where two (perturbed) trap states are separated on either side of the external potential's Gaussian barrier at $z_o = 1.48$. We see therefore that the repulsive and attractive components of (1) each create their own class of avoided crossings. Crucially, both kinds of shape resonances present in Fig. 1 would not appear in the absence of the trap's discrete energy spectrum.

Let us now turn to the time-dependent solution of the Hamiltonian (2). In the remainder of this section, we examine the simplest case of the external potential (1) moving at a constant velocity $\dot{z}_o$ from one side of the system to the other. We are interested in the state of the atoms at long times, i.e., after the external potential has passed into and through the system and excited it on the other side, and which factors influence it.
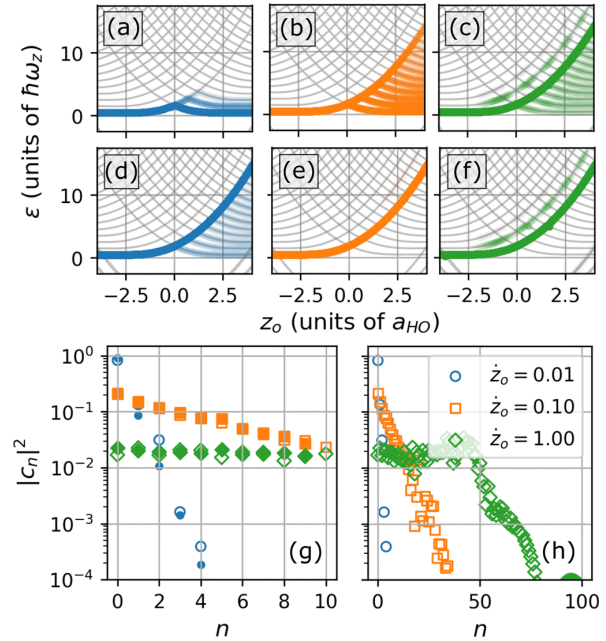

FIG. 2. Path of the atomic state along the energy curves. (a)–(f) Atomic energy spectrum (gray) weighted by the overlap of the atomic state with the instantaneous eigenstates $|\langle \psi(z; z_o)|\varphi_n(z; z_0)\rangle|^2$ of the Hamiltonian (2) as a function of $z_o(t)$ for constant drag speeds (a) $\dot{z}_o = 0.01$, (b) $\dot{z}_o = 0.10$, and (c) $\dot{z}_o = 1.00$. Here we have used the parameters $a = 120$, $b = 4\sqrt{10c}$, and $c = 40$. (d)–(f) Same as (a)–(c) but for a barrier height $a = 320$. (g) and (h) Open circles show the overlap of the final state $|\langle \psi_f(z)|\phi_n(z)\rangle|^2$ with the first (g) 11 and (h) 101 harmonic trap eigenstates $\{\phi_n\}$ ($n = 0, 1, 2, \ldots$) for various drag speeds $\dot{z}_o$. Closed circles in (g) are values obtained using the Landau-Zener formula (3).

At $t = 0$, the atoms occupy the ground state of the trap $\varphi(z, 0) = \phi_0(z)$. We choose the same model parameters for the external potential as before. For numerical purposes, we set the external potential's position at $t = 0$ to be $z_o(0) = -6$, which is sufficiently far removed from the trap center to prevent an immediate quench of the initial atomic state. We determine the atomic dynamics $\psi = \psi(t)$ by solving the time-dependent Schrödinger equation via wave-packet propagation using a dynamically optimized truncated basis representation [36].

We first consider the way in which the dragged potential couples the initial atomic state with other eigenstates during the course of the dynamics. For this purpose, we determine the overlap of the atomic state with the instantaneous eigenstates of the Hamiltonian (2) as a function of $z_o(t)$. Figures 2(a)–2(f) show plots of the energy spectrum [cf. Fig. 1(a)] in which the curves $\{\varepsilon_n(z_o)\}$ are weighted by the overlap integrals $|\langle \psi(t)|\varphi_n(z_o)\rangle|^2$ for different drag speeds $\dot{z}_o$ and heights a of the repulsive barrier. These plots effectively describe how $\psi(t)$ evolves within the Hilbert space of the Hamiltonian (2). We see in Fig. 2(a) that for a sufficiently slow drag speed and small barrier height, the state $\psi(t)$ initially evolves along a single energy curve, with only minor population of neighboring curves occurring after the dragged potential

passes through the trap center. For faster drag speeds and a greater barrier height, the atomic state follows an increasingly diabatic path to higher energy curves. Figure 2 shows that for $\dot{z}_o = 0.01$ and 0.10, diabatic transitions between energy curves take place exclusively at the avoided crossings, since there the coupling between energy curves is greatest and the energy gap smallest. However, this simple picture breaks down at sufficiently fast drag speeds, such as at $\dot{z}_o = 1.00$, which is shown in Figs. 2(c) and 2(f). In both of these cases, the coupling between curves becomes strong enough that additional transitions take place at positions z_o away from the immediate vicinity of the avoided crossings, where the curves have relatively large energy separations. For our purposes, these additional transitions are undesirable since they constitute an additional form of "leakage" between energy curves, which hinders the controlled preparation of a well-defined final atomic state.

A more quantitative understanding of the influence of the drag speed and barrier height on the path of the atomic state in Fig. 2 is provided by the semiclassical Landau-Zener formula [37,38]. This determines the probability P_{ij} for a diabatic transition at an avoided crossing between the energy curves of the eigenstates $\varphi_i(z_o)$ and $\varphi_j(z_o)$:

$$P_{ij} = \exp\left(-2\pi \frac{\Delta_{ij}^2}{\dot{z}_o \alpha_{ij}}\right). \tag{3}$$

Here $\Delta_{ij} = \min(|\varepsilon_i - \varepsilon_j|)/2$ is half the minimum energy gap at the avoided crossing and $\alpha_{ij} = |\frac{d}{dz_o}(\varepsilon_i - \varepsilon_j)|$. For $P_{ij} \to 0$, transitions between the states are suppressed, i.e., the dynamics is adiabatic. This holds for the condition $\Delta_{ij}^2 \gg \dot{z}_o \alpha_{ij}$, whereas for $\Delta_{ij}^2 \ll \dot{z}_o \alpha_{ij}$, $P_{ij} \to 1$ and the dynamics is maximally diabatic.

The closed circles in Fig. 2(g) are predictions for the composition of the atomic state at long times determined by applying Eq. (3) at each crossing encountered by the state. The predictions are in good agreement with the results obtained from the solution of the time-dependent Schrödinger equation (open circles) over a wide range of drag speeds $\dot{z}_o$. Thus, we see that the Landau-Zener formula (3) is a reasonable model for describing the state's path and we may use it to guide our intuition. Figure 2(h) extends the numerical results from Fig. 2(g) up to the 100th excited trap state, highlighting that it is in principle possible to populate arbitrarily highly excited states using the dragged potential. In an experimental setting however, the finite depth of the trapping potential imposes an upper energy limit and any atoms excited beyond this threshold would be lost from the system. This loss could be exploited to our advantage in the following way. We may design a state preparation protocol in which any atoms that do not reach the desired final state are lost from the system, thereby maximizing the fidelity with the target state at the cost of particle number uncertainty. This could be used to circumvent the limitations of the adiabatic state preparation protocol which is the focus of Sec. III.

From Eq. (3) we see that we have three knobs at our disposal for controlling the atoms' path through the energy curves $\{\varepsilon_n(z_o)\}$: Δ_{ij}, α_{ij}, and $\dot{z}_o$. The gap size Δ_{ij} at each avoided crossing is determined by the size of the barrier at the shape resonance since taller, wider barriers lead to more narrowly avoided crossings. Therefore, we can control Δ_{ij} by tuning the model parameters in Eq. (1) as well as the longitudinal trapping frequency ω_z. These will also influence α_{ij}; however, the quadratic dependence of Δ_{ij} in Eq. (3) makes it a more sensitive and thus attractive control parameter. The speed of the dragged potential is also an attractive control parameter since it is a free parameter.

In the following sections, we develop protocols which exploit these control parameters in order to realize deterministic state preparation such that the dragged potential shuttles the atoms into an excited trap state ϕ_n, $n > 0$, or a well-defined superposition of N trap states $\sum_{n=0}^{N} c_n \phi_n$. We denote the target state by ψ_t and the goal of the following sections is to maximize the fidelity measure $\mathcal{F} = |\langle \psi | \psi_t \rangle|^2$. We choose the following fixed set of model parameters: $a = 320$, $b = 4\sqrt{10c}$, and $c = 40$. In particular, we choose $a = 320$, since from Fig. 2(e) we see that for this barrier height, in combination with a drag speed of $z_o = 0.1$, the state's path is predominantly diabatic and transitions between energy curves are to a large extent "clean," by which we mean that the transitions occur chiefly at the avoided crossings and not, as is the case in Figs. 2(e) and 2(f), also in between avoided crossings. Both of these features are crucial for realizing efficient, high-fidelity state preparation protocols.

III. ADIABATIC PROTOCOL

This section introduces the first state preparation protocol, an adiabatic protocol, which seeks to control the path of the atomic state through the energy curves $\{\varepsilon_n(z_o)\}$ using only the intuition provided by the Landau-Zener model (3) discussed in Sec. II. Specifically, we use the drag speed $\dot{z}_o$ of the external potential to control whether the state traverses a given crossing adiabatically or diabatically in order to force it to follow a predetermined path through the energy spectrum. In particular, we demonstrate preparation of the target states $\psi_t^{(1)} = \phi_5$ and $\psi_t^{(2)}(t) = (\phi_4 + e^{i\Phi(t)}\phi_5)/\sqrt{2}$, where we include the phase factor $\Phi(t) = -\omega_z t$ to indicate that the latter target state is not a pure eigenstate of the harmonic trap and hence undergoes periodic dynamics. The demonstration of preparing a mixed state is used to highlight the versatility of the protocol. In principle however, it would be possible to employ similar protocols in order to engineer localized wave packets in anharmonic trap potentials for probing quantum collapse and revival behavior [39].

The adiabatic protocol is outlined in Fig. 3. In particular, Fig. 3(a) illustrates the ideal path through the energy spectrum from the ground state to the fifth excited state of the harmonic trap ϕ_5. Ten narrowly avoided crossings lie along this particular path. Starting from $t = 0$, the state should evolve diabatically at speed v_d until just before it reaches the eighth avoided crossing [indicated by the box in Fig. 3(a)], whereupon the dragged potential is decelerated linearly to the speed v_a, which should be sufficiently slow to fulfill the adiabatic condition $\Delta_{ij}^2 \gg \dot{z}_o \alpha_{ij}$ [see Fig. 3(b)]. If no deceleration occurs, the state will continue to populate higher trap eigenstates, similar to the path seen in Fig. 2(e). After passing this critical eighth avoided crossing, the potential is accelerated once again to v_d and the state continues diabatically through
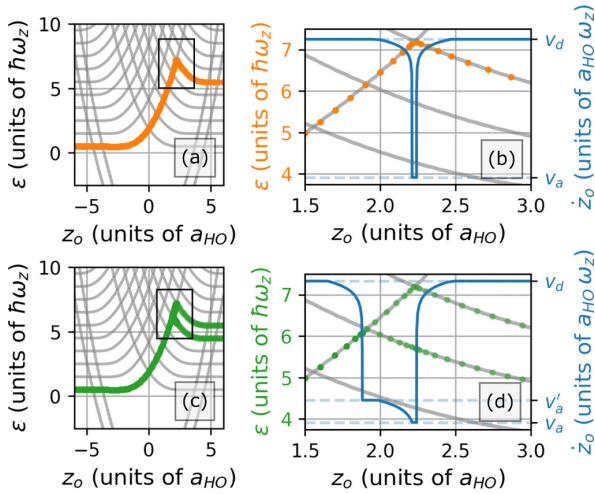
FIG. 3. Schematic of the adiabatic protocol. (a) Ideal state path [orange (dark gray)] through the atomic energy spectrum (light gray) to excite the atom to the fifth excited trap state $\phi_5(z)$. (b) Close-up of the critical region highlighted by the box in (a). The impurity's drag speed is overlaid in [blue (dark gray)], indicating the transition between the diabatic and adiabatic speeds (v_d and v_a, respectively). (c) Ideal state path [green (dark gray)] through the atomic energy spectrum (light gray) to excite the atom to the superposition state $(\phi_4 + e^{i\Phi(t)}\phi_5)/\sqrt{2}$, where $\Phi(t) = -\omega_z t$. (d) Close-up of the critical region highlighted by the box in (c). Note that in both (b) and (d) $\dot{z}_o$ is plotted on a logarithmic scale for the sake of visibility.

the last two avoided crossings, finally reaching the target state $\psi_t^{(1)} = \phi_5$.

Equally, the target state $\psi_t^{(2)}(t) = (\phi_4 + e^{i\Phi(t)}\phi_5)/\sqrt{2}$ may be achieved through a slight modification to the protocol for $\psi_t^{(1)}$. In particular, an additional deceleration step is required such that the state splits equally along the two energy curves at the seventh avoided crossing, as depicted in Fig. 3(c). The speed protocol is shown in Fig. 3(d). The potential is first decelerated from v_d to v_a', whose value is chosen such that an equal mixing between states at the seventh crossing is achieved and can be estimated using Eq. (3).

The results of the simulations for $\psi_t^{(1)}$ are summarized in Figs. 4(a)–4(e). Figure 4(a) shows the actual path followed by the atomic state in each simulation, which agree as expected with the ideal path given in Fig. 3(a). The evolution of the atomic probability density $\rho(z,t) = \psi^*(z,t)\psi(z,t)$ is provided in Figs. 4(b)–4(d) and the external potential's trajectory $z_o(t)$ is indicated by the dashed line. As the potential enters the trap [Fig. 4(b)], the atomic density is swept in the direction of motion of the potential and the dynamics of the state is diabatic. After the external potential is decelerated, the density begins to tunnel to the opposite side of the potential's barrier [Fig. 4(c)]. As the potential leaves the trap [Fig. 4(d)], the atomic density recenters on $z = 0$ and its profile matches approximately that of the fifth excited trap state [see the comparison in Fig. 4(e)]. For this particular simulation, we obtain an overlap of 97.4% with the target state in a time of approximately 1.22×10^4.

TABLE I. Dependence of final fidelity on the adiabatic speed. Column 1 lists the ratio of adiabatic v_a and diabatic v_d speeds, with $v_d = 0.1$ in all cases; column 2 the fidelity with the target state; and column 3 the protocol duration.

v_a/v_d	$\lvert \langle \psi_f \vert \phi_5 \rangle \rvert^2$	t_{tot}
5.0×10^{-3}	25.8	3.20×10^2
5.0×10^{-4}	89.1	1.40×10^3
5.0×10^{-5}	97.4	1.22×10^4

Similar results for the $\psi_t^{(2)}$ protocol are depicted in Figs. 4(f)–4(j). Here we obtain an overlap of 92.6% with the target state. The fidelity is smaller than that obtained for $\psi_t^{(1)}$ in part due to the larger value of v_a used in this example (see the caption of Fig. 4). Consequently, the duration of this protocol is shorter at approximately 6.90×10^3. The final atomic state exhibits regular density oscillations [Fig. 4(i)] with a period matching the time scale set by the energy separation of the neighboring trap states, namely, $2\pi/\omega_z$.

Adiabatic protocols are slow by nature. For a longitudinal trapping frequency of $\omega_z = 2\pi \times 300$ Hz, the examples shown in Fig. 4 would have a duration on the order of seconds. A tighter trapping potential would reduce this of course, since the time unit τ is given by $\tau = 1/\omega_z$ in our unit system. In addition, using larger values of v_a would further reduce the protocol duration but would come at the cost of the fidelity (see Table I). Additional improvements could be made by minimizing the distance over which the potential moves adiabatically via standard optimization techniques.

The final fidelity achieved is strongly influenced by the value of v_a. Nonetheless, there are additional sources of fidelity loss, accounting overall for approximately 1% of the total probability. First, the state's evolution while the potential is dragged at v_d is not perfectly diabatic, which leads to minor losses at each crossing. Diabatic transitions between energy curves away from the avoided crossings are a further source of loss, as we saw for fast drag speeds in Figs. 2(c) and 2(f). No doubt a protocol could be devised to fine-tune the drag speed around particular regions where these transitions become significant. This would however make the overall protocol more complex for rather marginal improvements to the fidelity.

IV. TUNNELING PROTOCOL

The key limiting factor of the protocols described in Sec. III is their long duration: Achieving fidelities with the target state greater than 90% requires 10^3–10^4 units of time, which translates to timescales on the order of seconds for trapping frequencies on the order of 100 Hz. Ideally, we want to be able to significantly reduce the duration of the protocols while still preserving their relative simplicity and high fidelity. This will be the focus of the following section. In Sec. IV A we show how more efficient protocols can be designed by drawing analogies between the dynamics of our system to the tunneling of a particle in a double-well potential and arrive at a condition which enables tunneling to be exploited usefully for state preparation in our system. In Sec. IV B we apply the knowledge from Sec. IV A to realize efficient protocols and
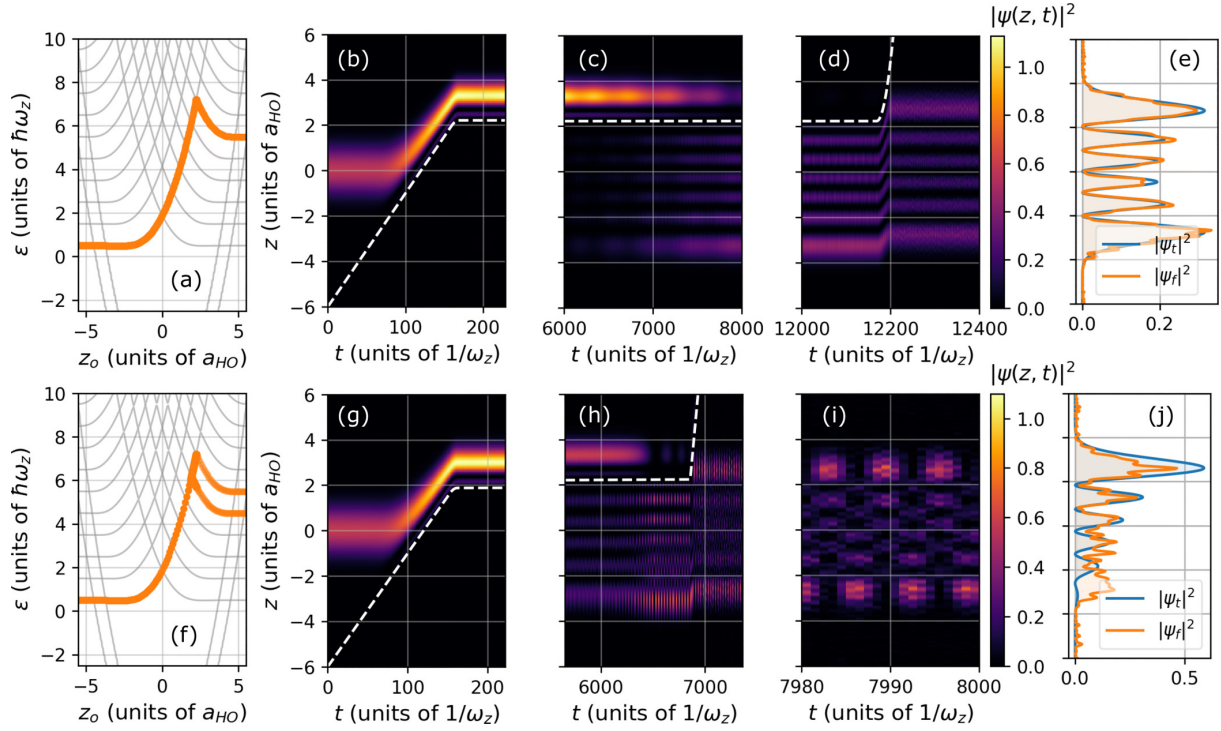
FIG. 4. Adiabatic protocol. (a)–(e) Exciting atoms to the fifth excited trap state $\phi_5(z)$ using the adiabatic protocol. (a) Instantaneous energy spectrum (gray) with the colored line representing the overlap of the atomic state with the instantaneous eigenstates $|\langle \psi(z, z_o)|\varphi_\nu(z, z_o)\rangle|^2$ of (2) as a function of $z_o(t)$. (b)–(d) Atomic probability density $|\psi(z, t)|^2$ for different time intervals during the protocol. The dashed line indicates the trajectory of the moving potential $z_o(t)$. (e) Comparison of the density of the final atomic state $|\psi_f|^2$ to the target state $|\psi_t| = \phi_5|^2$. Here we achieve a fidelity $|\langle \psi_f|\psi_t\rangle|^2$ of 97.4%. (f)–(j) Same as (a)–(e) but for the target state $(\phi_4 + e^{i\Phi}\phi_5)/\sqrt{2}$, where $\Phi(t) = -\omega_z t$. Here we achieve a fidelity $|\langle \psi_f|\psi_t\rangle|^2$ of 92.6%. For both protocols, $v_d = 0.1$. In addition, (a)–(e) $v_a = v_d/20\,000$ and (f)–(j) $v_a = v_d/600$ and $v'_a = v_d/2000$ (v_d, v_a, and v'_a are defined in Fig. 3). Wave functions are normalized such that $\int dz|\psi(z)|^2 = 1$.

present results for the preparation of pure and superposition excited trap states using the two varieties of avoided crossings in our system that were introduced in Sec. II.

A. Condition for complete tunneling

The combination of the harmonic trap and the dragged potential (1) creates an effective potential for the atoms resembling an asymmetric double well [cf. Figs. 1(b) and 1(c)]. For the sake of building intuition, let us first consider the case of noninteracting atoms confined within a symmetric double-well potential, which is realized in our system for $z_o = 0$. The energy spectrum of atoms in a double well is characterized by a series of near-degenerate doublets whose eigenstates have opposite parity. Assume that at $t = 0$ the atoms are in an equal superposition of the lowest two eigenstates: $\psi(z, 0) = [\varphi_0(z) + \varphi_1(z)]/\sqrt{2}$. From the near degeneracy of the eigenstates $\varphi_0(z)$ and $\varphi_1(z)$ and their opposite parity, this wave packet is localized solely within one of the wells. For $t > 0$, the state undergoes unitary time evolution and accumulates a phase Φ, $\psi(z, 0) = [\varphi_0(z) + \exp(i\Phi)\varphi_1(z)]/\sqrt{2}$, where $\Phi = -\Delta\varepsilon t$, which is proportional to the energy gap between the eigenstates $\Delta\varepsilon = \varepsilon_1 - \varepsilon_0$. After a time $T = \pi/\Delta\varepsilon$, the state will have accumulated a phase π such that the wave packet

is now localized within the opposite well: $\psi(T) = (\varphi_0 - \varphi_1)/\sqrt{2}$. For our purposes, we refer to T as the tunneling time.

Based on the size of the energy gaps at the avoided crossings in Fig. 1(a), we can expect tunneling times on the order of 10^2 in our system. This value is one to two orders of magnitude smaller than the time required for the adiabatic protocols discussed in Sec. III [see Figs. 4(c) and 4(h)]. In other words, our estimate of the effective double-well tunneling time T for our system indicates that we could significantly lower the duration of our protocols by simply setting our adiabatic speed all the way to $v_a = 0$, i.e., stopping the potential in the vicinity of the avoided crossing and allowing the state to tunnel freely on timescales set by the atomic energy spectrum.

To exploit tunneling for the purpose of state preparation, we need to understand how to control it. In this regard, two related questions arise. First, what conditions must be fulfilled in the asymmetric double-well system to realize "perfect" tunneling, namely, where the atomic density tunnels completely from one side to the other without leaving behind any residue? Second, can we realize such tunneling for arbitrary positions of the dragged potential? The remainder of this section provides concrete answers to these questions through some straightforward analytical considerations.

We assume that on the approach to the avoided crossing between the instantaneous eigenstates φ_A and φ_B, the atomic state is in a superposition of only these two eigenstates,

$$\psi(z; z_o(t)) = c_A(z_o(t))\varphi_A(z; z_o(t)) + c_B(z_o(t))\varphi_B(z; z_o(t)),$$
(4)

which is valid assuming that the dynamics up to this point has been diabatic. The complex coefficients $c_A(z_o(t))$ and $c_B(z_o(t))$ satisfy $|c_A(z_o(t))|^2 + |c_B(z_o(t))|^2 = 1$ since the atomic wave function is normalized $\langle\psi(z; z_o(t))|\psi(z; z_o(t))\rangle = 1$. The narrowly avoided crossing emerges due to a barrier created in the atoms' effective potential, centered at position z_b. Depending on the type of avoided crossing (see Sec. II for details), z_b may be equal to the position of the dragged potential $z_o(t)$, yet this is not guaranteed. For example, the variety of avoided crossings depicted in Fig. 1(a) is not formed due to the external potential's Gaussian barrier but rather by its long-range attractive tail; hence in this case $z_b \neq z_o(t)$.

At $t = 0$, the dragged external potential is suddenly halted at the position $z_o(0) = z_s$ near the avoided crossing between φ_A and φ_B. Thereafter, the atomic wave function undergoes unitary evolution. Since the Hamiltonian $\hat{H}(z_s)$ no longer has explicit time dependence, the wave function for $t \geqslant 0$ is given by $\psi(z, t; z_s) = e^{-i\hat{H}(z_s)t}\psi(z; z_s)$. In the interest of readability, we drop the z_s parameter notation in equations beyond this point. The atomic probability density $\rho(z, t) = \psi^*(z, t)\psi(z, t)$ at time t is given by

$$\rho(z, t) = |c_A|^2|\varphi_A(z)|^2 + |c_B|^2|\varphi_B(z)|^2$$
$$+ 2c_A c_B \cos(\Delta\varepsilon\, t)\varphi_A(z)\varphi_B(z),$$
(5)

where $\Delta\varepsilon$ is the energy difference between the eigenstates at position z_s and we have assumed that the eigenstates are real valued. For brevity, we label the time-independent and time-dependent contributions to the density as $\bar{\rho}(z) = |c_A|^2|\varphi_A(z)|^2 + |c_B|^2|\varphi_B(z)|^2$ and $\delta\rho(z, t) = 2c_A c_B \cos(\Delta\varepsilon\, t)\varphi_A(z)\varphi_B(z)$, respectively. Note that $\delta\rho(z, t)$ is periodic in time with period $P = 2\pi/\Delta\varepsilon$.

If the dynamics for $t < 0$ has been diabatic, the atoms' probability density at $t = 0$ will be localized on one side of the barrier created in the effective potential, for example, $z > z_b$ [see Fig. 4(b)]. Thus, the atomic density at $t = 0$ fulfills the condition

$$\rho(z, 0) = \bar{\rho}(z) + \delta\rho(z, 0) = 0 \,\forall\, z \leqslant z_b.$$
(6)

Using Eq. (5), we can rewrite the above condition as

$$\bar{\rho}(z) = -\delta\rho(z, 0) = -2c_A c_B \varphi_A(z)\varphi_B(z) \,\forall\, z \leqslant z_b. \quad (7)$$

We now seek the optimal value of the external potential's stopping position, denoted by $\bar{z}_s$, such that the atoms undergo perfect tunneling. This requires that at time $t = P/2$ the atoms are localized on the opposite side of the barrier in the effective potential. Hence, we demand that the atomic density fulfills the following condition:

$$\rho(z, P/2) = \bar{\rho}(z) + \delta\rho(z, P/2) = 0 \,\forall\, z > z_b.$$
(8)

Making use of Eq. (5) and $\cos(\Delta\varepsilon\, P/2) = -1$ yields

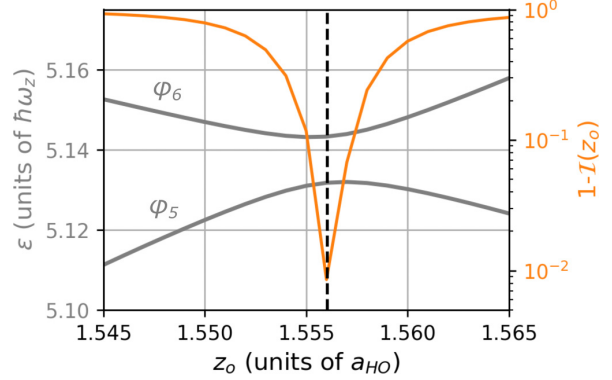$$\bar{\rho}(z) = 2c_A c_B \varphi_A(z)\varphi_B(z) \,\forall\, z > z_b.$$
(9)

FIG. 5. Perfect tunneling condition. Energy curves $\varepsilon(z_o)$ (dark gray) for the eigenstates $\varphi_5(z; z_o)$ and $\varphi_6(z; z_o)$ in the vicinity of their avoided crossing (left axis). Also shown is $1 - \mathcal{I}(z_o)$ [orange (light gray)], where $\mathcal{I}(z_o)$ is the overlap integral $\mathcal{I}(z_o) = \int dz|\varphi_A(z, ; z_o)||\varphi_B(z; z_o)|$ appearing in Eq. (10) (right axis). The dashed line indicates the critical stopping position $\bar{z}_s$.

Finally, we make use of the conditions in Eqs. (7) and (9) and the fact that $\bar{\rho}(z; z_s)$ is normalized to derive

$$1 = \int dz|\bar{\rho}(z)| = \int_{z \leqslant z_b} dz|\bar{\rho}(z)| + \int_{z > z_b} dz|\bar{\rho}(z)|$$
$$= 2|c_A||c_B| \int dz|\varphi_A(z)||\varphi_B(z)|.$$
(10)

In the above, we have used the absolute value in order to write the final expression as a single integral. Equation (10) provides us with a relation between the overlap coefficients $c_i = \int dz\varphi_i(z)\psi(z)$ and the overlap of the eigenstates' absolute magnitudes $\mathcal{I} = \int dz|\varphi_A(z)||\varphi_B(z)|$ which must be fulfilled in order for perfect tunneling to take place, namely, $|c_A||c_B|\mathcal{I} = \frac{1}{2}$.

Since $0 \leqslant |c_A||c_B| \leqslant \frac{1}{2}$ and $0 \leqslant \mathcal{I} \leqslant 1$, the condition in Eq. (10) can only be fulfilled when $|c_A||c_B| = \frac{1}{2}$ and $\mathcal{I} = 1$. This requires (i) the atomic state to be in an equal superposition of eigenstates $\varphi_A(z)$ and $\varphi_B(z)$ (i.e., $|c_A| = |c_B| = 1/\sqrt{2}$) and (ii) that these eigenstates differ at most by the sign of their prefactors [$|\varphi_A(z)| = |\varphi_B(z)| \,\forall z$]. The former condition is rather loose, since it could be realized in general for arbitrary z_s. However, the latter condition provides a strong indication that the optimal stopping position $\bar{z}_s$ is located at the narrowest point of the avoided crossing between the eigenstates. Thus, we have shown that the requirements for perfect tunneling in an asymmetric double well match those of the symmetric double well that we considered at the beginning of this section. We determine $\bar{z}_s$ for a given crossing by evaluating the overlap integral of the eigenstates $|\varphi_A(z)|$ and $|\varphi_B(z)|$ for a range of z_s around their common avoided crossing. Figure 5 shows the results for $|\varphi_5(z)|$ and $|\varphi_6(z)|$. In this case, we confirm that the optimal position $\bar{z}_s$ occurs at the point of closest approach between the energy curves ε_5 and ε_6.

In conclusion, the tunneling protocol cannot be realized for arbitrary z_s. In fact, the ability to tunnel is highly sensitive to the choice of z_s as shown by Fig. 5. Nonetheless, through
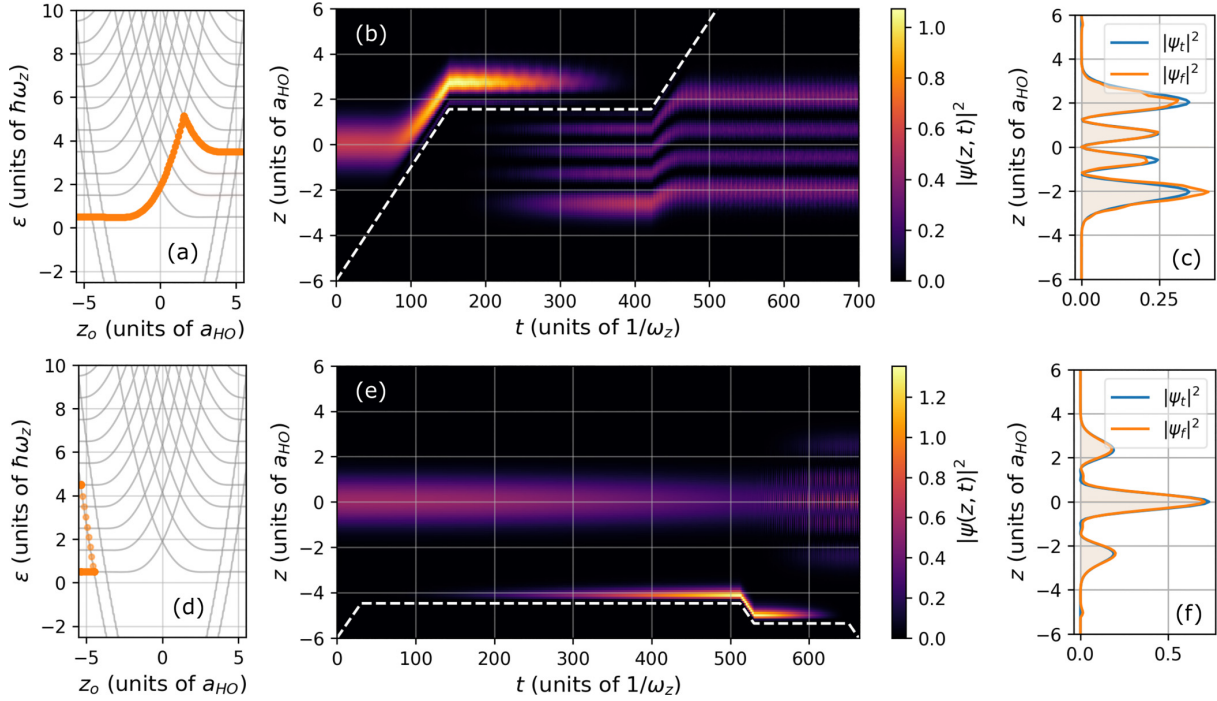
FIG. 6. Tunneling protocol. (a)–(c) Exciting atoms to the third excited trap state ϕ_3 using the tunneling protocol. (a) Atomic energy spectrum, weighted by the overlap of its state with the instantaneous eigenstates $|\langle \psi(z, z_o)|\varphi_v(z, z_o)\rangle|^2$ of Eq. (2) as a function of $z_o(t)$. (b) Atomic probability density $|\psi(z, t)|^2$ throughout the protocol. The dashed line indicates the trajectory of the moving potential $z_o(t)$. (c) Comparison of the density of the atom's final state $|\psi_f|^2$ to the target state $|\phi_3|^2$. Here we achieve a fidelity $|\langle \psi_f|\psi_t\rangle|^2$ of 99.02%. (d)–(f) Same as for (a)–(c) but for the target state $(\phi_0 + e^{i\Phi(t)}\phi_4)/\sqrt{2}$, where $\Phi(t) = -4\omega_z t$. Here we achieve a fidelity $|\langle \psi_f|\psi_t\rangle|^2$ of 99.7%. For both protocols, $v_d = 0.1$. Wave functions are normalized such that $\int dz|\psi(z)|^2 = 1$.

the above analysis we have arrived at the condition $\mathcal{I}(\bar{z}_s) = 1$ which must be fulfilled to achieve perfect tunneling, which provides us with a systematic method for determining the optimal stopping position $\bar{z}_s$. Furthermore, the size of the energy gaps at the avoided crossings mean that the atoms will tunnel over one order of magnitude faster than the adiabatic protocols discussed in Sec. III.

B. Proof of principle

Using the knowledge about the conditions for perfect tunneling gained from the preceding section, we now perform state preparation using with new protocols that execute sudden stops of the dragged potential at relevant avoided crossings in the atomic energy spectrum. The relevant avoided crossings are determined by the desired target state. The duration of each stop is set by the tunneling time $T = \pi/\Delta\varepsilon$ for the given avoided crossing. Between stops, the external potential moves at a constant speed $\dot{z}_o = 0.10$ and the change in its velocity is assumed to be sudden.

Figure 6 summarizes the results of tunneling protocols for target states $\psi_t^{(3)}(z) = \phi_3(z)$ and $\psi_t^{(4)}(z, t) = [\phi_0(z) + e^{i\Phi(t)}\phi_4(z)]/\sqrt{2}$, where $\Phi(t) = -4\omega_z t$. In both cases, we achieve fidelities above 99% for durations of 10^2 time units. In order to prepare the superposition state $\psi_t^{(4)}(z, t)$, we follow a slightly different approach by exploiting instead the avoided

crossings that arise between a bound state of the dragged potential (1) and a vibrational state [see, e.g., Fig. 1(b)]. Using these anticrossings requires us to reverse the direction of motion of the dragged potential, which therefore requires stopping twice during the protocol as compared to only once in the protocol in Figs. 6(a)–6(c). The advantage of this approach is however that there are overall fewer avoided crossings that the state has to traverse, which improves the overall fidelity at the cost of a slightly longer protocol. Finally, we note that by stopping the potential at $\bar{z}_s$ for only half the tunneling time $T/2$, the state will split equally along both paths that meet at the crossing. Using this method, we achieve a fidelity of 99.7% with $\psi_t^{(4)}(z, t)$ in a time of 650 [see Figs. 6(d)–6(f) for further details].

While the tunneling protocols have a distinct advantage in terms of speed, their major drawback is their sensitivity to errors in the stopping position z_s. In Table II we summarize some data which investigate the robustness of the protocol to errors in the stopping position z_s. We find that deviations as small as 0.1% from the optimal stopping position $\bar{z}_s$ can lead to a sizable decrease in the fidelity with $\psi_t^{(3)}(z, t)$. The level of precision in the positioning of the potential might be challenging to meet by current experimental standards.

Additionally, the protocols discussed in this work will be sensitive to deviations in the swept potential from its optimal shape. This effect is investigated in Appendix A 1.

TABLE II. Robustness of the tunneling protocol to error in the stopping position. Column 1 lists the percentage error in the stopping position z_s relative to the optimal stopping position $\bar{z}_s$ and column 2 the fidelity with the target state ϕ_3. The error-free fidelity amounts to 99.02% (see Fig. 6).

Percent error in z_s	$\mid\langle\psi_f\mid\phi_3\rangle\mid^2$
0.01	98.70
0.10	72.14
1.00	1.18

In this work we have demonstrated the preparation of superposition states consisting of at most two trap eigenstates in the population-balanced case. It is possible to modify the protocols to prepare more complicated superposition states, as discussed for the case of the tunneling protocol in Appendix A 2.

V. CONCLUSION

In this work, we explored protocols for exciting individual trapped atoms into higher vibrational states by means of a dynamically swept external potential. In particular, we employed an external potential possessing long-range attractive character and a repulsive barrier at its center, which could be realized via a tightly trapped ion or a shaped optical potential. Excitation of the atoms was facilitated by avoided crossings in the atomic energy spectrum, whose position and gap size may be tuned through the shape of the external potential. The presence of the avoided crossings is a consequence of shape resonances in the effective potential created by the moving external potential, analogous to TISR emerging in collisions between species in separate trapping potentials. The protocols proposed in our work selectively prepare the atoms in excited vibrational states through controlling the speed of the external potential in order to drive the state along a desired path through the atoms' discrete energy spectrum.

The first protocol relies on adiabatic driving around a small number of critical anticrossings, which depend on the desired target state. The protocol's primary limitation is its duration: Achieving fidelities higher than 90% requires durations of 10^3–10^4 in harmonic oscillator units. For a Rb atom with $\omega_z = 2\pi \times 1$ kHz, this would correspond to a protocol duration of approximately 0.1–1.0 s.

In contrast, the second protocol brings the potential to a complete halt at the critical avoided crossings, whereupon the atom undergoes unitary dynamics in its effective potential created by the harmonic trap and the now static external potential. During this period, the atom tunnels through the barrier present at the shape resonance on timescales defined by the energy gap between the eigenstates at the avoided crossing. We found that tunneling occurs over durations of 10^2, which is one to two orders of magnitude faster than the timescales for the adiabatic protocol. The tunneling protocol achieved fidelities higher than 99% with protocol durations of 10–100 ms, assuming a Rb atom with $\omega_z = 2\pi \times 1$ kHz. However, the fidelity of this protocol is highly sensitive to the external potential's stopping position.
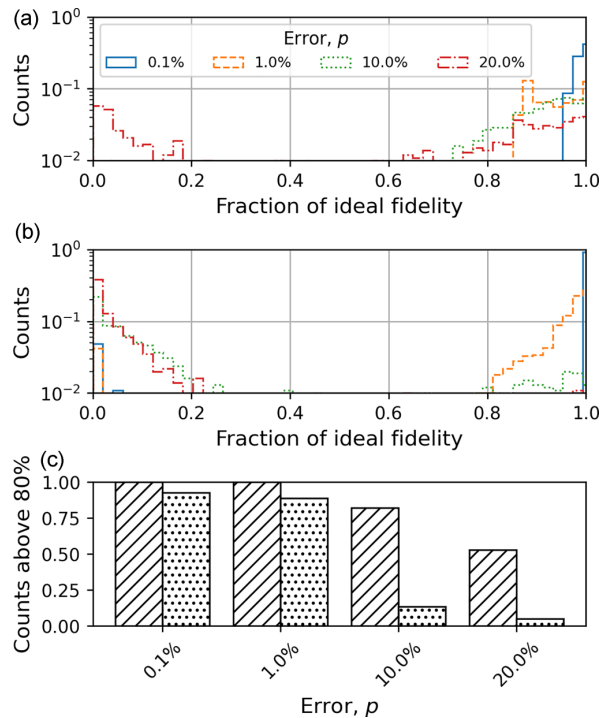

FIG. 7. Robustness of the protocols to deviation in shape of the swept potential. (a) Distribution of fidelities achieved by the adiabatic protocol for varying degrees of error in the model parameters p of the swept potential [see Eq. (1)]. For each value of p, 1000 randomly sampled swept potentials were used. The fidelities are plotted as a fraction of the ideal fidelity with respect to the target state and the counts are normalized. In this case, the target state was the fifth excited trap state ϕ_5 with an ideal fidelity of 97.40%. (b) Corresponding results for the tunneling protocol. In this case, the target state was the third excited trap state with an ideal fidelity of 99.02%. (c) Number of simulations which achieved better than 80% of the ideal fidelity for the adiabatic (slash-hatched) and tunneling (dot-hatched) protocols.

Without any specific attempts at optimization, our protocols can achieve fidelities better than 99% on timescales on the order of milliseconds. While employing quantum optimal control methods would enable us to design protocols with more competitive durations, these protocols would not offer the same level of clarity and intuitiveness as the protocols presented in this work.

Our work may be extended to weakly interacting Bose or Fermi gases to investigate the role of interparticle interactions and particle statistics. Moreover, considering a binary mixture may be of particular interest. For instance, consider a mixture of two components A and B, where species A initially occupies an excited trap state and species B occupies the vibrational ground state. Introducing weak interspecies interactions would mean that species B experiences, in an effective picture, a latticelike background potential created by the density of species A. Additionally, the lattice could be made to vibrate by preparing species A in a superposition of trap states, thus mimicking phononic excitations.
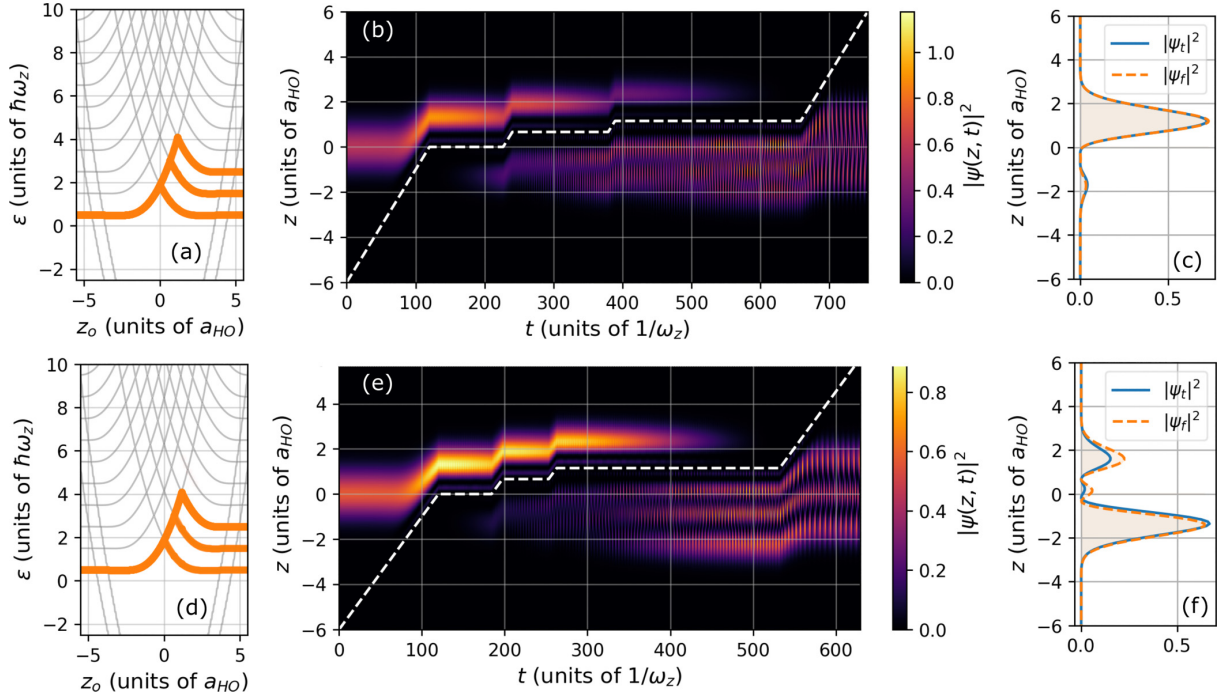
FIG. 8. Tunneling protocol: three-state superposition. (a)–(c) Exciting atoms to the population-balanced three-state mixture (see the text) using the tunneling protocol. (a) Atomic energy spectrum, weighted by the overlap of its state with the instantaneous eigenstates $|\langle \psi(z, z_o)|\varphi_v(z, z_o)\rangle|^2$ of Eq. (2) as a function of $z_o(t)$. (b) Atomic probability density $|\psi(z, t)|^2$ throughout the protocol. The dashed line indicates the trajectory of the moving potential $z_o(t)$. (c) Comparison of the density of the atom's final state $|\psi_f|^2$ to the target state $|\phi_t|^2$. Here we achieve a fidelity $|\langle \psi_f|\psi_t\rangle|^2$ of 99.87%. (d)–(f) Same as (a)–(c) but for the population-imbalanced three-state mixture. Here we achieve a fidelity $|\langle \psi_f|\psi_t\rangle|^2$ of 98.76%. For both protocols, $v_d = 0.1$. Wave functions are normalized such that $\int dz|\psi(z)|^2 = 1$.

Note added. Recently, we became aware of earlier related works [14,15] which propose preparing atoms in pure excited trap states through adiabatic passage of a constant-speed potential well with varying well depth.

APPENDIX

1. Robustness of the protocols to errors in the swept potential

The success of the protocols described in this paper in an experimental setting would rely on the ability to recreate the shaped potential (1) with high precision. Deviations in the shape of the potential, through, e.g., errors in the model parameters, will lead to a reduction in fidelity with respect to the target state. In this section we investigate the robustness of our protocols to deviations in the potential's shape from the ideal, mimicking the impact of experimental errors.

We carried out a series of simulations using swept potentials whose model parameters (a, b, and c) were sampled from Gaussian distributions, where the mean was fixed at the ideal value ($a_0 = 120$, $b_0 = 4\sqrt{10c_0}$, and $c_0 = 40$) and the standard deviation σ was changed to reflect varying degrees

of experimental error. Figure 7 shows the distribution of fidelities achieved for the adiabatic and tunneling protocols with varying standard deviation, defined as a percentage p of the ideal value (i.e., the Gaussian distribution for model parameter a would have a standard deviation $\sigma = pa_0$). To obtain statistics, we performed simulations with 1000 randomly sampled swept potentials for each value of p.

As expected, the protocols perform worse for increasing noise. The tunneling protocol is particularly sensitive: For $p = 0.20$, fewer than 10% of runs achieved a fidelity higher than 80% of the ideal value. In contrast, the adiabatic protocol proved itself more robust, with around 50% of simulations achieving a fidelity better than 80% at $p = 0.20$ [see Fig. 7(c)].

2. Further examples of state preparation

In the main text we showed proof-of-principle results for the preparation of target states involving at most two excited trap states. Nonetheless, the protocols can be applied to realize more sophisticated superpositions of trap states. In this section we show results for the preparation of a superposition of the three lowest-energy trap states

$$\psi_t = \alpha\phi_0 + \beta\phi_1 + \gamma\phi_2. \tag{A1}$$

Figure 8 demonstrates results for the preparation of a population-balanced case ($\alpha = \beta = \gamma = 1/\sqrt{3}$) as well as an

imbalanced case with coefficients in the ratio $\alpha{:}\beta{:}\gamma = 5{:}4{:}16$ using the tunneling protocol. We achieve fidelities of 99.87% and 98.76% for the two cases, respectively. In general, even more complex superpositions of states could be created in this

way. However, guiding the state along more complicated paths in the energy spectrum shown in Fig. 1(a) would require the traversal of an increased number of avoided crossings which, in principle, means a larger overall loss of fidelity.

[1] C. Chin, R. Grimm, P. Julienne, and E. Tiesinga, Rev. Mod. Phys. **82**, 1225 (2010).

[2] A. M. Kaufman, B. J. Lester, C. M. Reynolds, M. L. Wall, M. Foss-Feig, K. R. A. Hazzard, A. M. Rey, and C. A. Regal, Science **345**, 306 (2014).

[3] F. Serwane, G. Zürn, T. Lompe, T. B. Ottenstein, A. N. Wenz, and S. Jochim, Science **332**, 336 (2011).

[4] K. Henderson, C. Ryu, C. MacCormick, and M. G. Boshier, New J. Phys. **11**, 043030 (2009).

[5] O. Morizot, Y. Colombe, V. Lorent, H. Perrin, and B. M. Garraway, Phys. Rev. A **74**, 023617 (2006).

[6] I. Bloch, Nat. Phys. **1**, 23 (2005).

[7] D. S. Petrov, D. M. Gangardt, and G. V. Shlyapnikov, J. Phys. (France) IV **116**, 5 (2004).

[8] S. Martínez-Garaot, E. Torrontegui, X. Chen, M. Modugno, D. Guéry-Odelin, S.-Y. Tseng, and J. G. Muga, Phys. Rev. Lett. **111**, 213001 (2013).

[9] J. J. W. H. Sørensen, M. O. Aranburu, T. Heinzel, and J. F. Sherson, Phys. Rev. A **98**, 022119 (2018).

[10] R. Bücker, J. Grond, S. Manz, T. Berrada, T. Betz, C. Koller, U. Hohenester, T. Schumm, A. Perrin, and J. Schmiedmayer, Nat. Phys. **7**, 608 (2011).

[11] A. Tanaka and T. Cheon, New J. Phys. **18**, 045023 (2016).

[12] A. Tanaka, T. Nakamura, and T. Cheon, Phys. Rev. A **102**, 013308 (2020).

[13] K. W. Madison, F. Chevy, W. Wohlleben, and J. Dalibard, Phys. Rev. Lett. **84**, 806 (2000).

[14] Z. P. Karkuszewski, K. Sacha, and J. Zakrzewski, Phys. Rev. A **63**, 061601(R) (2001).

[15] B. Damski, Z. P. Karkuszewski, K. Sacha, and J. Zakrzewski, Phys. Rev. A **65**, 013604 (2001).

[16] B. Damski, K. Sacha, and J. Zakrzewski, J. Phys. B **35**, 4051 (2002).

[17] I. Hans, J. Stockhofe, and P. Schmelcher, Phys. Rev. A **92**, 013627 (2015).

[18] C. P. Koch, U. Boscain, T. Calarco, G. Dirr, S. Filipp, S. J. Glaser, R. Kosloff, S. Montangero, T. Schulte-Herbrüggen, D. Sugny, and F. K. Wilhelm, EPJ Quantum Technol. **9**, 19 (2022).

[19] S. Deffner and S. Campbell, J. Phys. A: Math. Theor. **50**, 453001 (2017).

[20] D. Guéry-Odelin, A. Ruschhaupt, A. Kiely, E. Torrontegui, S. Martínez-Garaot, and J. G. Muga, Rev. Mod. Phys. **91**, 045001 (2019).

[21] R. Bücker, T. Berrada, S. van Frank, J.-F. Schaff, T. Schumm, J. Schmiedmayer, G. Jäger, J. Grond, and U. Hohenester, J. Phys. B **46**, 104012 (2013).

[22] R. Bowler, J. Gaebler, Y. Lin, T. R. Tan, D. Hanneke, J. D. Jost, J. P. Home, D. Leibfried, and D. J. Wineland, Phys. Rev. Lett. **109**, 080502 (2012).

[23] A. Walther, F. Ziesel, T. Ruster, S. T. Dawkins, K. Ott, M. Hettrich, K. Singer, F. Schmidt-Kaler, and U. Poschinger, Phys. Rev. Lett. **109**, 080501 (2012).

[24] R. Stock, I. H. Deutsch, and E. L. Bolda, Phys. Rev. Lett. **91**, 183201 (2003).

[25] Z. Idziaszek, T. Calarco, and P. Zoller, Phys. Rev. A **76**, 033409 (2007).

[26] H. Doerk, Z. Idziaszek, and T. Calarco, Phys. Rev. A **81**, 012708 (2010).

[27] M. Krych and Z. Idziaszek, Phys. Rev. A **80**, 022710 (2009).

[28] M. Sroczyńska, T. Wasak, K. Jachymski, T. Calarco, and Z. Idziaszek, Phys. Rev. A **98**, 012708 (2018).

[29] D. K. Ruttley, A. Guttridge, S. Spence, R. C. Bird, C. R. Le Sueur, J. M. Hutson, and S. L. Cornish, Phys. Rev. Lett. **130**, 223401 (2023).

[30] J. M. Schurer, P. Schmelcher, and A. Negretti, Phys. Rev. A **90**, 033601 (2014).

[31] J. M. Schurer, A. Negretti, and P. Schmelcher, New J. Phys. **17**, 083024 (2015).

[32] M. Tomza, K. Jachymski, R. Gerritsma, A. Negretti, T. Calarco, Z. Idziaszek, and P. S. Julienne, Rev. Mod. Phys. **91**, 035001 (2019).

[33] J. M. Schurer, R. Gerritsma, P. Schmelcher, and A. Negretti, Phys. Rev. A **93**, 063602 (2016).

[34] J. M. Schurer, A. Negretti, and P. Schmelcher, Phys. Rev. Lett. **119**, 063001 (2017).

[35] D. J. Bosworth, M. Pyzh, and P. Schmelcher, Phys. Rev. A **103**, 033303 (2021).

[36] L. Cao, V. Bolsinger, S. I. Mistakidis, G. M. Koutentakis, S. Krönke, J. M. Schurer, and P. Schmelcher, J. Chem. Phys. **147**, 044106 (2017).

[37] L. Landau, Z. Sowjetunion **2**, 46 (1932).

[38] C. Zener and R. H. Fowler, Proc. R. Soc. London A **137**, 696 (1932).

[39] R. Robinett, Phys. Rep. **392**, 1 (2004).

In situ observation of nonpolar to strongly polar atom-ion collision dynamics [SC4]

In Situ Observation of Nonpolar to Strongly Polar Atom-Ion Collision Dynamics

M. Berngruber,[1,*] D. J. Bosworth[2,3,*,†] O. A. Herrera-Sancho[1,4,5,6] V. S. V. Anasuri,[1] N. Zuber,[1]
F. Hummel[7,‖] J. Krauter,[1] F. Meinert[1] R. Löw,[1] P. Schmelcher[2,3,‡] and T. Pfau[1,§]

[1]*5. Physikalisches Institut, Universität Stuttgart, Pfaffenwaldring 57, 70569 Stuttgart, Germany*
[2]*Zentrum für Optische Quantentechnologien, Universität Hamburg, Luruper Chaussee 149, 22761 Hamburg, Germany*
[3]*Hamburg Centre for Ultrafast Imaging, Universität Hamburg, Luruper Chaussee 149, 22761 Hamburg, Germany*
[4]*Escuela de Física, Universidad de Costa Rica, 2060 San Pedro, San José, Costa Rica*
[5]*Instituto de Investigaciones en Arte, Universidad de Costa Rica, 2060 San Pedro, San José, Costa Rica*
[6]*Centro de Investigación en Ciencias Atómicas, Nucleares y Moleculares,*
Universidad de Costa Rica, 2060 San Pedro, San José, Costa Rica
[7]*Max-Planck-Institute for the Physics of Complex Systems, Nöthnitzer Straße 38, 01187 Dresden, Germany*

The onset of collision dynamics between an ion and a Rydberg atom is studied in a regime characterized by a multitude of collision channels. These channels arise from coupling between a nonpolar Rydberg state and numerous highly polar Stark states. The interaction potentials formed by the polar Stark states show a substantial difference in spatial gradient compared to the nonpolar state leading to a separation of collisional timescales, which is observed *in situ*. For collision energies in the range of $k_\mathrm{B}\mu\mathrm{K}$ to $k_\mathrm{B}\mathrm{K}$, the dynamics exhibit a counterintuitive dependence on temperature, resulting in faster collision dynamics for cold—initially "slow"—systems. Dipole selection rules enable us to prepare the collision pair on the nonpolar potential in a highly controlled manner, which determines occupation of the collision channels. The experimental observations are supported by semiclassical simulations, which model the pair state evolution and provide evidence for tunable nonadiabatic dynamics.

Introduction—Observing, understanding, and controlling individual collisions are prerequisites for many-body physics based on atoms or molecules. Especially in the ultracold regime, where collisions between neutral atoms can be engineered by Feshbach resonances, a high level of control is reached [1]. This makes it possible to study, for example, the study of degenerate molecular gases [2,3], Feshbach molecules [4,5], and Efimov physics [6]. However, when it comes to collisions between charged and neutral particles, reaching the same level of quantum control becomes harder since the range of interactions increases, thus requiring even lower temperatures to reach the quantum regime of scattering [7,8]. More exotic collisions can be studied in systems of laser-cooled Rydberg atoms, which have the advantage of showing long-range interactions, allowing collisions to occur on larger length, slower time, and lower energy scales, making them easier to observe with spatial and temporal resolution. Even exotic bound states between a Rydberg atom and neutral ground state atoms forming ultralong-range molecules have been observed [9–12]. Moreover, the

complex Rydberg level structure can give rise to intriguingly rich potential energy surfaces with avoided crossings and conical intersections providing means to study effects beyond the Born-Oppenheimer approximation [13,14].

More recently, also systems combining Rydberg atoms and ions have become an active field of research [15–21]. Here, we pursue this direction and explore the dynamical processes that lead to a multichannel collision between an ion and a Rydberg atom. Instead of an ion trap we rely on compensating electric fields to work with free-floating ions in an almost net-zero electric field environment. Our high-resolution ion microscope allows us to study collisional dynamics with both spatial and temporal resolution. We are therefore not restricted to only analyzing the initial and final collision partners, but may instead directly observe the dynamics as the collision unfolds.

Theory—The polarizability of highly excited Rydberg atoms gives rise to a long-range charge-induced dipole interaction potential which is shown as a function of the internuclear distance R for the specific case of the $|129S\rangle$ state in Fig. 1. These potential energy curves (PECs) are calculated by exact diagonalization of the electronic Hamiltonian $H_e = H_0 + V_I(R)$, where H_0 describes the unperturbed Rydberg atom and V_I the ion-Rydberg interaction. This interaction term can be written in a multipole

*These authors contributed equally to this work.

†Contact author: dboswort@physnet.uni-hamburg.de
‡Contact author: pschmelc@physnet.uni-hamburg.de
§Contact author: t.pfau@physik.uni-stuttgart.de
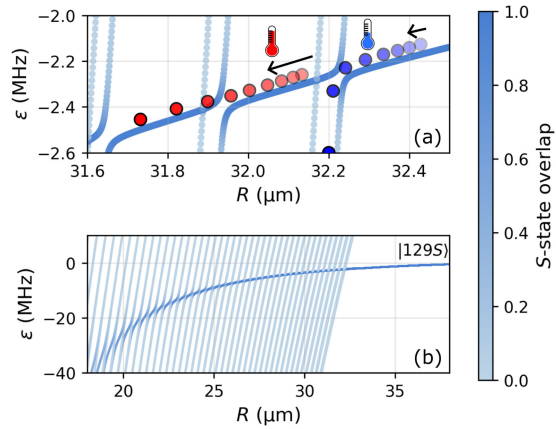‖Present address: Atom Computing, Inc., Berkeley, California, USA.

FIG. 1. Ion-Rydberg collision channels. Adiabatic potential energy curves obtained via exact diagonalization of the electronic Hamiltonian (see Ref. [22]). (a) Close-up around the avoided crossings near the nonpolar $|129S\rangle$ atomic Rydberg state, illustrating the presence of initially slow (red) and fast (blue) collision channels. Counterintuitively, occupation of the fast channels is more probable for initially slower particles. (b) Larger-scale plot of the avoided crossings between the nonpolar S-state and multiple strongly polar Stark states from the neighboring asymptotically degenerate hydrogenic manifold. The overlap of the electronic states with the unperturbed $|129S\rangle$ atomic Rydberg state is denoted by the colorbar. Energies are given relative to the $|129S\rangle$ atomic Rydberg state.

expansion, where we consider terms up to the sixth order (see Ref. [22]). One can distinguish between two regions: the first region is defined in the asymptotic limit for large R, where the potential of the nonpolar S-state falls off with $1/R^4$ due to the charge-induced dipole interaction between the ion and the atomic Rydberg S-state; the second region is found at $R \lesssim 33$ μm for the case of $|129S\rangle$, which is nevertheless approximately 26 times larger than the size of the Rydberg orbit. Here, the ion-induced Stark shift becomes large enough that strongly polar, large angular momentum states from the neighboring $n = 126$ hydrogenic manifold start to cross into the polarization potential and form a series of avoided crossings. For Rydberg S-states in ^{87}Rb, the polarization potential strictly decreases in energy while approaching the ion such that the two collision partners will always be accelerated toward each other. In the direct vicinity of these avoided crossings, the Born-Oppenheimer (BO) approximation is no longer suitable to describe the dynamics properly. Instead, a nonadiabatic, semiclassical model using the Landau-Zener (LZ) formula is employed [28]. This allows us to estimate the probability for an adiabatic transition to a strongly polar state at each crossing and thus can be used to predict the occupation of the different collision channels. The probability P_{ij} to transition nonadiabatically from PEC i to an adjacent curve j is given by $P_{ij} = \exp(-2\pi a_{ij}^2/(\dot{R}\alpha_{ij}))$ [29], where a_{ij} is half the energy gap between the adiabatic PECs at the avoided

crossing and α_{ij} is the differential gradient between the diabatic PECs.

From this formula, it is clear that the probability of undergoing adiabatic dynamics at a given crossing can be experimentally tuned through the relative velocity $\dot{R}$, which is determined in an experimental setting by the atom temperature and the additional kinetic energy acquired upon falling inward on the polarization potential of the nonpolar S-state. Therefore, systems with small relative velocities have an increased probability to follow the PEC adiabatically. In contrast, systems with high relative velocities have a larger probability to traverse the crossing nonadiabatically and thereby remain on the comparatively flat polarization potential. Hence, each avoided crossing provides two collisional channels: one that is mostly populated by systems with low kinetic energy (cold channel) and one that is mostly occupied by high kinetic energy systems (hot channel), see Fig. 1. Interestingly, this leads to a counterintuitive behavior for the overall dynamics: if a cold, low kinetic energy system follows the PEC adiabatically, it will ultimately reach the steep strongly polar potential and thus rapidly accelerate. This results in a faster collision compared to a system with high kinetic energy, which travels along the flat S-state potential and experiences weaker acceleration.

Overview of experimental sequence—The charged ion-Rydberg atom system is realized in a laser-cooled rubidium cloud held in an optical dipole trap of a temperature of about 20 μK. In order to minimize stray electric fields in the system, six electrodes are used to compensate fields well below 100 μV/cm [30]. In that way, the ions can be kept in position for the time of the experiment and no ion trap is needed. An experimental block starts with a 1 μs long ionization pulse, which incorporates a two-photon ionization process, providing just enough energy to overcome the ionization threshold [see Fig. 2(a)]. Next, a Rydberg atom is excited in the electric field of the ion by using a 1 μs long Rydberg excitation pulse, again involving two laser beams [see Fig. 2(b)]. The detuning Δ of the upper 480 nm excitation laser from the bare atomic state in zero field determines the initial radius R_0 at which the Rydberg atom is facilitated around the ion. The radial distribution has a width that is given by the effective linewidth of the two-photon excitation. The verlocity $\dot{R}_0$ is mostly determined by the temperature of the rubidium cloud. This blue laser illuminates the atomic cloud as a thin light sheet in the horizontal direction, thus confining the system for highly excited Rydberg states to a quasi-2D plane, leading to the facilitation of Rydberg atoms located on a ring around the ion (for further details, see Ref. [22]). Afterwards a variable time t_{dyn} can be applied allowing the system to evolve freely. In order to detect the two particles in a distinguishable way, we drag the ion along the optical axis of the ion microscope without displacing it in the imaging plane. To do so, two field electrodes are used to apply a weak electric field of about 1.1 V/cm, which is
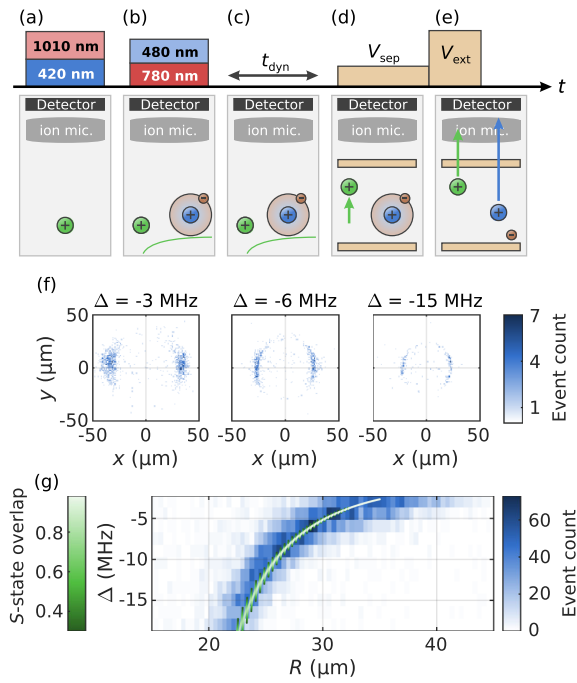
FIG. 2.   Experimental sequence and initial state preparation. (a)–(e) Schematics of the experimental sequence, which consists of the following steps: (a) two-photon ionization to create an ion, (b) two-photon Rydberg excitation in the electric field of the ion, (c) variable interaction time, (d) applying a small separation field which drags the ion along the optical axis of the ion microscope, (e) ionization of the Rydberg atom and imaging of both particles by using a large electric field. Panel (f) shows the Rydberg atom position relative to the ion (located at the origin) for different Rydberg laser detunings Δ from the bare $|129S\rangle$ state in absence of an ion. (g) Histograms of the azimuthally averaged ion-Rydberg atom distance R for various detunings Δ (blue). The theoretically calculated polarization potential is shown in the white to green color code, which indicates the overlap with the bare $|129S\rangle$ state (only overlaps ≥ 0.3 are shown).

small enough to not ionize the Rydberg atom [see Fig. 2(d)]. In the final detection step [Fig. 2(e)], a large electric field of 340 V/cm is applied to field-ionize the Rydberg atom and to accelerate both particles into the ion microscope. Because of the previous separation between the ion and the Rydberg atom, they will arrive at different times at the detector and are therefore easily distinguishable [21,31].

Results and discussion—If the interaction time t_{dyn} in Fig. 2(c) is set to zero, Rydberg atoms initially excited on the flat polarization potential can be directly detected at their original positions. Excitation to the high angular momentum curves is ruled out due to negligible D-state overlap. By scanning the detuning Δ of the Rydberg excitation we can spectroscopically map out the resonance condition for facilitated excitation on the interaction

potential. Figure 2(f) shows examples of averaged *in situ* images of the Rydberg atom position relative to the ion, meaning that the ion is always located at the origin. Owing to the excitation in a quasi-2D plane, a symmetric ring can be observed with the ion microscope. The upper and lower part are not populated due to the finite, elongated shape of the atomic cloud. As it can be clearly seen, the distance between the ion and the Rydberg atom decreases for larger detunings as expected from the facilitation process. Figure 2(g) summarizes the result of such *in situ* images by integrating over the azimuthal angle and showing the data as a function of the internuclear distance R, which represents a direct measurement of the $|129S\rangle$ ion-Rydberg pair state potential. The blue histogram shows the experimentally obtained data, which is in good agreement with the calculated PEC displayed in green.

In the next step, we introduce a variable interaction time $t_{\mathrm{dyn}} > 0$ between the Rydberg excitation and the detection, during which the dynamics take place. This allows the ion-Rydberg pair to move on the interaction potential, such that the system encounters the series of avoided crossings shown in Fig. 1(b). The top row of Fig. 3 shows results for the observed dynamics of the $|129S\rangle$ state at three different detunings. Δ' is the detuning relative to the outermost avoided crossing, such that for $\Delta' > 0$ the system is initialized outside the fan of the hydrogenic manifold. Each panel represents an average over at least 6500 ion-Rydberg events on the detector. Solid and dashed lines indicate the results of semiclassical simulations that account for effects due to finite temperature, effective laser linewidth, experimental timings, as well as the geometry of the setup. We model the observed ion-Rydberg pair dynamics by solving the pair's classical equation of motion along all possible collision channels. Each resulting trajectory is assigned a weight corresponding to the probability of following that particular channel, provided by the LZ formula (for further details, see Ref. [22]). We observe good agreement between the experimental results and the simulations. For negative Δ', one clearly observes faster dynamics overall due to the transition to steep, strongly polar states. At longer times, however, deviations appear which are due to short-range interaction processes. Notably, for $R \lesssim 5$ μm charge transfer of the Rydberg electron can occur. Such processes are beyond the scope of our model and their products cannot be filtered in the experiment.

Our semiclassical model can shed light on the significance of nonadiabatic transitions in the dynamics by studying the change in population of the slow and fast collision channels over time. The bottom row of Fig. 3 shows the population of the strongly polar states over time for LZ simulations (red) and fully adiabatic simulation based on individual, noncoupled PECs (blue). For all Δ', the population growth is slower for LZ simulations due to nonadiabatic transitions. A more quantitative comparison can be made by comparing the times t_e (dashed vertical
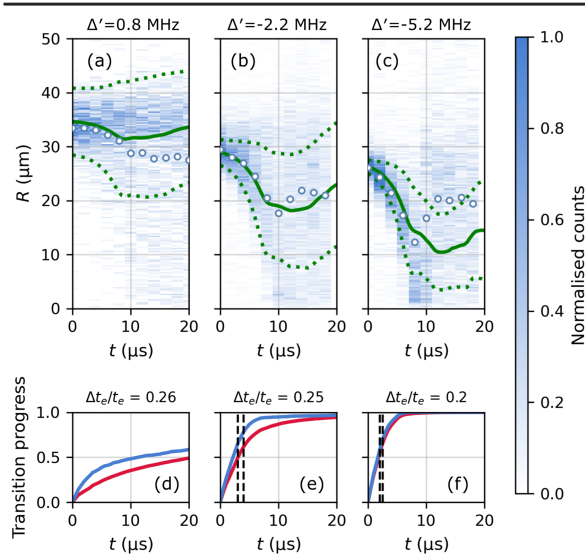
FIG. 3. Ion-Rydberg pair dynamics. (a)–(c) Observed relative atomic dynamics with results of LZ simulations overlaid for different detunings of the Rydberg laser Δ' relative to the outermost avoided crossing at $R \approx 32.2$ μm. The colorbar gives the number of measured counts as a fraction of counts at $t = 0$. Circular data points indicate the mean of the measured distribution for each time step. Solid (dotted) lines indicate the mean (standard deviation) of the theoretical distribution. (d)–(f) Population of the fast collision channels (strongly polar states) over time for both LZ (red) and adiabatic (blue) simulations. Dashed vertical lines (not visible for $\Delta' = 0.8$ MHz in this interval) indicate the time t_e at which the population reaches $1 - 1/e$ (approx. 63%). $\Delta t_e / t_e$ is the relative difference in this time between the LZ and adiabatic simulations. For details of the simulations, see Ref. [22].

lines) at which the population of the nonpolar S-state curve has decayed to $1/e$. The relative difference Δt_e in t_e decreases as the Rydberg atoms are excited further inside the fan, indicating that the motion becomes increasingly adiabatic. This is due to the growing gap size a_{ij} at the avoided crossings at smaller R (see Ref. [22]). In this way the timescale of the dynamics can also be controlled via the laser detuning.

Nonadiabatic transitions are further influenced by the gas temperature T. For high T, ion-Rydberg pairs have a larger probability to follow the slow collision channel due to their initially greater relative velocity. We illustrate this point theoretically in Fig. 4, which shows the transition to fast collision channels over time at different temperatures and two different laser detunings relative to the outermost avoided crossing. The relative difference in t_e increases with T for both detunings [see Fig. 4(d)], indicating that the pairs created in hotter gases spend more time on the slow collision channel created by the nonpolar S-state. Pairs gain kinetic energy as they fall inward along the polarization potential. For $\Delta'_1 = 0.06$ MHz, this gain in kinetic
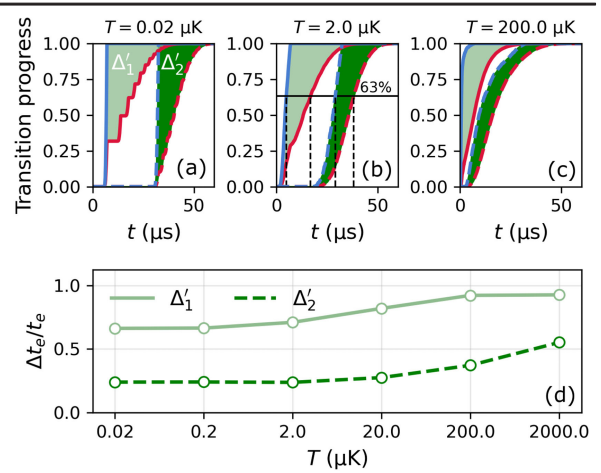

FIG. 4. Predicted impact of temperature on dynamics. Panels (a)–(c) show theoretical results which compare the population of fast collision channels (strongly polar states) over time for both LZ (red) and adiabatic (blue) simulations at different gas temperatures T. Solid (dashed) lines denote an initial laser detuning of $\Delta'_1 = 0.06$ MHz ($\Delta'_2 = 0.31$ MHz) relative to the outermost avoided crossing at $R \approx 32.2$ μm [see Fig. 1(b)]. Panel (d) shows the relative difference in t_e between LZ and adiabatic simulations over a range of gas temperatures. t_e is the time at which the polar state population reaches $1 - 1/e$ (approx. 63%), indicated for the case of $T = 2.0$ μK by the dashed vertical lines in (b).

energy corresponds to approximately 0.4 μKk_B of thermal energy, whilst $\Delta'_2 = 0.31$ MHz is equivalent to 2.0 μKk_B. This additional heating accounts for the negligible change in $\Delta t_e / t_e$ for temperatures below 2 μK [Fig. 4(d)].

Nonadiabatic transitions will also play a more significant role in the dynamics at higher n as a result of the narrowing avoided crossings, whose gap sizes a_{ij} follow a power-law decay with n (see Ref. [22]). The signal of nonadiabatic transitions can thus be enhanced by probing dynamics at larger n.

Summary and outlook—We studied the onset of collisional dynamics between an ion-Rydberg pair in a regime of multiple coupled channels with varying collision timescales. We were able to describe the experimentally observed dynamics with the help of a LZ model. Further, the simulations show that the collisional dynamics can not only be tuned by the initial distance but should also be tunable by other parameters like the principal quantum number. Our work has explored the role of nonadiabatic effects in ion-Rydberg collisions and lays the foundation for future explorations of beyond Born-Oppenheimer physics with Rydberg atoms, such as molecular dynamics in the presence of conical intersections. Precisely understanding nonadiabatic couplings in complicated potential energy landscapes is also a key ingredient to better predict the lifetime of Rydberg molecules such as macrodimers or ion-Rydberg molecules [14]. In this current experimental

realization, the ion-Rydberg complex was photoassociated directly out of a trapped gas of ^{87}Rb. Future experiments might consider using individually trapped atoms in a tweezer setup, which would offer more precise control over the initial separation of the ion-Rydberg pair, thereby further improving the starting conditions of the collision.

---

[1] C. Chin, R. Grimm, P. Julienne, and E. Tiesinga, Feshbach resonances in ultracold gases, Rev. Mod. Phys. **82,** 1225 (2010).

[2] L. De Marco, G. Valtolina, K. Matsuda, W. G. Tobias, J. P. Covey, and J. Ye, A degenerate Fermi gas of polar molecules, Science **363,** 853 (2019).

[3] M. Duda, X.-Y. Chen, A. Schindewolf, R. Bause, J. von Milczewski, R. Schmidt, I. Bloch, and X.-Y. Luo, Transition from a polaronic condensate to a degenerate Fermi gas of heteronuclear molecules, Nat. Phys. **19,** 720 (2023).

[4] T. Köhler, K. Góral, and P. S. Julienne, Production of cold molecules via magnetically tunable Feshbach resonances, Rev. Mod. Phys. **78,** 1311 (2006).

[5] G. Thalhammer, K. Winkler, F. Lang, S. Schmid, R. Grimm, and J. H. Denschlag, Long-lived Feshbach molecules in a three-dimensional optical lattice, Phys. Rev. Lett. **96,** 050402 (2006).

[6] P. Naidon and S. Endo, Efimov physics: A review, Rep. Prog. Phys. **80,** 056001 (2017).

[7] P. Weckesser, F. Thielemann, D. Wiater, A. Wojciechowska, L. Karpa, K. Jachymski, M. Tomza, T. Walker, and T. Schaetz, Observation of Feshbach resonances between a single ion and ultracold atoms, Nature (London) **600,** 429 (2021).

[8] H. Hirzler, R. S. Lous, E. Trimby, J. Pérez-Ríos, A. Safavi-Naini, and R. Gerritsma, Observation of chemical reactions between a trapped ion and ultracold feshbach dimers, Phys. Rev. Lett. **128,** 103401 (2022).

[9] V. Bendkowsky, B. Butscher, J. Nipper, J. P. Shaffer, R. Löw, and T. Pfau, Observation of ultralong-range Rydberg molecules, Nature (London) **458,** 1005 (2009).

[10] D. Booth, S. Rittenhouse, J. Yang, H. Sadeghpour, and J. Shaffer, Production of trilobite Rydberg molecule dimers

[11] T. Niederprüm, O. Thomas, T. Eichert, C. Lippe, J. Pérez-Ríos, C. H. Greene, and H. Ott, Observation of pendular butterfly Rydberg molecules, Nat. Commun. **7,** 12820 (2016).

[12] C. Fey, F. Hummel, and P. Schmelcher, Ultralong-range Rydberg molecules, Mol. Phys. **118,** e1679401 (2020).

[13] F. Hummel, P. Schmelcher, and M. T. Eiles, Vibronic interactions in trilobite and butterfly Rydberg molecules, Phys. Rev. Res. **5,** 013114 (2023).

[14] F. Hummel, M. T. Eiles, and P. Schmelcher, Synthetic dimension-induced conical intersections in Rydberg molecules, Phys. Rev. Lett. **127,** 023003 (2021).

[15] F. Engel, T. Dieterle, T. Schmid, C. Tomschitz, C. Veit, N. Zuber, R. Löw, T. Pfau, and F. Meinert, Observation of Rydberg blockade induced by a single ion, Phys. Rev. Lett. **121,** 193401 (2018).

[16] T. Schmid, C. Veit, N. Zuber, R. Löw, T. Pfau, M. Tarana, and M. Tomza, Rydberg molecules for ion-atom scattering in the ultracold regime, Phys. Rev. Lett. **120,** 153401 (2018).

[17] F. M. Gambetta, C. Zhang, M. Hennrich, I. Lesanovsky, and W. Li, Long-range multibody interactions and three-body antiblockade in a trapped Rydberg ion chain, Phys. Rev. Lett. **125,** 133602 (2020).

[18] L. Wang, M. Deiß, G. Raithel, and J. H. Denschlag, Optical control of atom-ion collisions using a Rydberg state, J. Phys. B **53,** 134005 (2020).

[19] M. Deiß, S. Haze, and J. Hecker Denschlag, Long-range atom–ion Rydberg molecule: A novel molecular binding mechanism, Atoms **9,** 34 (2021).

[20] A. Duspayev, X. Han, M. A. Viray, L. Ma, J. Zhao, and G. Raithel, Long-range Rydberg-atom–ion molecules of Rb and Cs, Phys. Rev. Res. **3,** 023114 (2021).

[21] N. Zuber, V. S. Anasuri, M. Berngruber, Y.-Q. Zou, F. Meinert, R. Löw, and T. Pfau, Observation of a molecular bond between ions and Rydberg atoms, Nature (London) **605,** 453 (2022).

[22] See Supplemental Material at http://link.aps.org/supplemental/10.1103/PhysRevLett.133.083001 for details of the experimental sequence, dynamics simulations, and additional measurements, which includes Refs. [23–27].

[23] S. Weber, C. Tresp, H. Menke, A. Urvoy, O. Firstenberg, H. P. Büchler, and S. Hofferberth, Calculation of Rydberg interaction potentials, J. Phys. B **50,** 133001 (2017).

[24] T. F. Gallagher, *Rydberg Atoms*, Cambridge Monographs on Atomic, Molecular and Chemical Physics (Cambridge University Press, Cambridge, England, 1994).

[25] D. R. Inglis and E. Teller, Ionic depression of series limits in one-electron spectra, Astrophys. J. **90,** 439 (1939).

[26] H. Köppel, W. Domcke, and L. S. Cederbaum, Multimode molecular dynamics beyond the born-oppenheimer approximation, in *Advances in Chemical Physics* (John Wiley & Sons, Ltd., New York, 1984), Vol. 57, pp. 59–246.

[27] M. Schlagmüller, T. C. Liebisch, F. Engel, K. S. Kleinbach, F. Böttcher, U. Hermann, K. M. Westphal, A. Gaj, R. Löw, S. Hofferberth, T. Pfau, J. Pérez-Ríos, and C. H. Greene, Ultracold chemical reactions of a single Rydberg atom in a dense gas, Phys. Rev. X **6,** 031020 (2016).

[28] C. Zener and R. H. Fowler, Non-adiabatic crossing of energy levels, Proc. R. Soc. A **137,** 696 (1932).

[29] J. R. Rubbmark, M. M. Kash, M. G. Littman, and D. Kleppner, Dynamical effects at avoided level crossings: A study of the Landau-Zener effect using Rydberg atoms, Phys. Rev. A **23**, 3107 (1981).

[30] C. Veit, N. Zuber, O. A. Herrera-Sancho, V. S. V. Anasuri, T. Schmid, F. Meinert, R. Löw, and T. Pfau, Pulsed ion microscope to probe quantum gases, Phys. Rev. X **11**, 011036 (2021).

[31] Y.-Q. Zou, M. Berngruber, V. S. V. Anasuri, N. Zuber, F. Meinert, R. Löw, and T. Pfau, Observation of vibrational dynamics of orientated Rydberg-atom-ion molecules, Phys. Rev. Lett. **130**, 023002 (2023).

Supplementary Material: *In situ* Observation of Nonpolar to Strongly Polar Atom-Ion Collision Dynamics

M. Berngruber[¶],[1] D. J. Bosworth[¶],[2, 3, *] O. A. Herrera-Sancho,[1, 4, 5, 6] V. S. V. Anasuri,[1]
N. Zuber,[1] F. Hummel,[7, †] J. Krauter,[1] F. Meinert,[1] R. Löw,[1] P. Schmelcher,[2, 3, ‡] and T. Pfau[1, §]

[1]*5. Physikalisches Institut, Universität Stuttgart, Pfaffenwaldring 57, 70569 Stuttgart, Germany*
[2]*Zentrum für Optische Quantentechnologien, Universität Hamburg,*
Luruper Chaussee 149, 22761 Hamburg, Germany
[3]*Hamburg Centre for Ultrafast Imaging, Universität Hamburg,*
Luruper Chaussee 149, 22761 Hamburg, Germany
[4]*Escuela de Física, Universidad de Costa Rica, 2060 San Pedro, San José, Costa Rica*
[5]*Instituto de Investigaciones en Arte, Universidad de Costa Rica, 2060 San Pedro, San José, Costa Rica*
[6]*Centro de Investigación en Ciencias Atómicas, Nucleares y Moleculares,*
Universidad de Costa Rica, 2060 San Pedro, San José, Costa Rica
[7]*Max-Planck-Institute for the Physics of Complex Systems,*
Nöthnitzer Straße 38, 01187 Dresden, Germany
(Dated: September 30, 2024)

A — Experimental sequence

The experimental sequence starts with the preparation of a cold ^{87}Rb cloud. The atoms originate from an effusive oven source and are subsequentially cooled by employing a Zeeman slower and trapped in a magneto-optical trap (MOT) in a separate MOT-chamber. After a 15 ms long compressed MOT phase followed by a 25 ms optical molasses phase, the atoms are transferred to a movable dipole trap which transports the atoms into the science chamber below the ion microscope. At this point the atoms have a temperature of about 20 µK. In such a sample several thousand experiments can be performed before a new atomic sample has to be loaded.
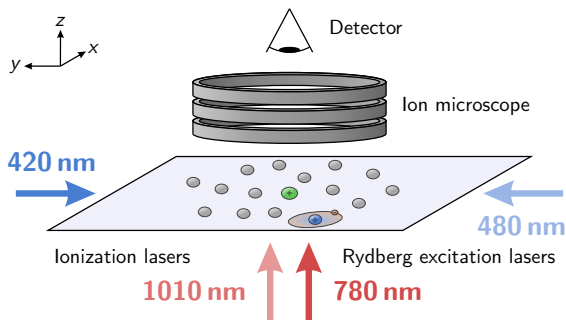

FIG. 1. **Schematic sketch of the experimental configuration.** The imaging plane is shown together with the direction of the laser beams used for ionization and Rydberg excitation of ground state atoms in the atomic sample. The atomic cloud is observed from above with the ion microscope.

———

[¶] These authors contributed equally to this work.

A single experimental block starts with the creation of an ion by using a two-photon ionization process. The first transition is realized by a 420 nm laser beam which is detuned by 80 MHz from the intermediate $|6P_{3/2}, F = 3\rangle$ state. The beam is shone into the atomic cloud in the horizontal direction (see Fig. 1) and has a $1/e^2$ waist of $w_{420} = 7$ µm. The second laser is operated at a wavelength of 1010 nm, providing just enough energy to overcome the ionization threshold. By shining this laser vertically in the experimental chamber with a small $1/e^2$ waist of $w_{1010} = 3.2$ µm one can create a reasonably good ion spot. Both lasers are simultaneously on for 1 µs. In the subsequent step the Rydberg atom is excited in the electric field of the ion, which also takes place within 1 µs. Here, a two-photon process is employed once again, involving a 780 nm laser, 250 MHz detuned from the intermediate $|5P_{3/2}, F = 3\rangle$ state. The second laser is operated at around 480 nm, depending on the desired target Rydberg state. While the 780 nm laser is much larger than the atomic cloud and shone in from below, the 480 nm beam forms a thin light sheet and is introduced horizontally into the chamber. Thus, the system can be approximated by a quasi-2D plane for large Rydberg states.

In the following step a variable interaction time t_{dyn} can be introduced before the two particles are detected. To distinguish them, a small electric field is applied along the z-axis, which drags the ion along the optical axis of the ion microscope but does not yet ionize the Rydberg atom. When the Rydberg atom is field-ionized in the next step by applying the large extraction field of 340 V/cm, the ion and the Rydberg atom have different starting positions and therefore will arrive at different times on the detector. Further details on our ion microscope setup are given in Ref. [1].
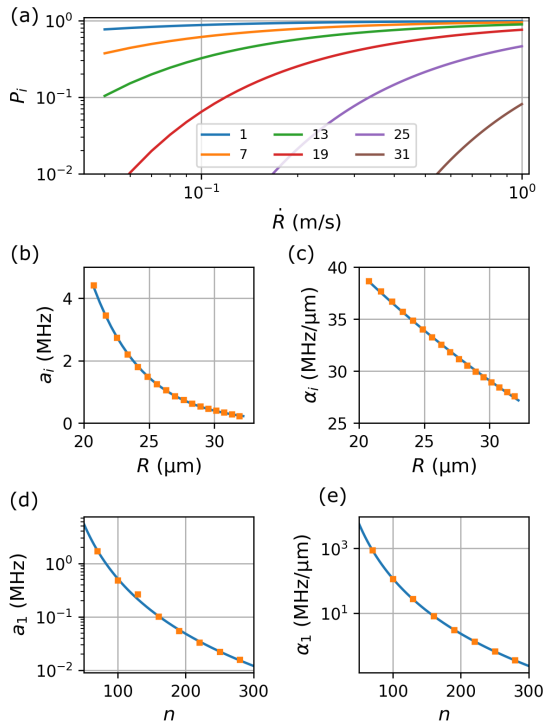
FIG. 2. **Scaling of Landau-Zener transition parameters.** (a) Transition probability as a function of the relative internuclear speed $\dot{R}$ for a selection of avoided crossings in the ion-$129S$ Rydberg system, where the crossings are indexed such that $i = 1$ refers to the outermost avoided crossing. (b),(c) Scaling of the gap size a_i and differential gradient α_i for each crossing in the ion-$129S$ Rydberg system. Solid lines represent fits to exponentially decaying functions of the form $y = Ae^{-bx}$. We find fit values of $b = 0.258 \pm 0.002$ and $b = 0.031 \pm 0.001$ for a_i and α_i, respectively. (d),(e) Scaling of the gap size a_1 and differential gradient α_1 of the outermost avoided crossing with varying principal quantum number n. Solid lines represent fits to power-law-decaying functions of the form $y = Ax^{-b}$. We find fit values of $b = 3.422 \pm 0.075$ and $b = 5.641 \pm 0.009$ for a_1 and α_1, respectively. In (b)-(e), the fits have a root mean square error of less than 10%.

B — Details on the Landau-Zener model for ion-Rydberg pair dynamics

We employ a semiclassical model for the ion-Rydberg pair dynamics, in which the pair's classical motion is determined along the N relevant open collision channels. In the case of $|129S\rangle$, $N = 34$. The open channels are obtained from the adiabatic potential energy curves (PECs) of the system's electronic Hamiltonian H_e, which reads:

$$H_e = H_0 + V_I(R). \qquad (1)$$

Here, H_0 denotes the unperturbed Rydberg atom and V_I describes the interaction between the ion and the Rydberg atom. We are interested in ultralong-range internuclear separations R at which the overlap between the species' charge distributions vanishes, enabling V_I to be approximated using a multipole expansion [2, 3]:

$$V_I(R) = -\sum_{\lambda=1}^{\infty} \sqrt{\frac{4\pi}{2\lambda+1}} \frac{r^\lambda}{R^{\lambda+1}} Y_\lambda^0(\theta, \phi), \qquad (2)$$

where r is the position of the Rydberg electron with respect to the core, $Y_\lambda^0(\theta, \phi)$ are spherical harmonics which are functions of the Rydberg electron's angular position (θ, ϕ) and λ denotes the order of the multipole expansion. The above expansion in Eq. (2) is valid in the regime $R \gg r$. The adiabatic PECs $\{\varepsilon_i(R)\}$ are determined by evaluating eigenvalues of the electronic Hamiltonian in Eq. (1) over a range of internuclear separations R using the *pairinteraction* program [4], which truncates the series in Eq. (2) at $\lambda = 6$.

We are particularly interested in adiabatic PECs which correspond asymptotically to weakly polar atomic Rydberg states. At large internuclear separations, the nonpolar $|nS\rangle$ state acquires an induced dipole moment and the leading-order correction to its energy is given by $\varepsilon_S \propto -n^7/R^4$. In the Rydberg series of ^{87}Rb, the quantum defect-split $|nS\rangle$ state lies below the $n-3$ degenerate hydrogenic manifold. The states in this manifold have an angular momentum of $l > 3$ and acquire a permanent dipole moment at large R due to l-mixing, which makes them strongly polar and gives them a leading-order energy correction of $\varepsilon_l \propto \pm n^2/R^2$.

The competing R-scaling of ε_S and ε_L means that the attractive branches of the Stark-split high-l states eventually become near-degenerate with the $|nS\rangle$ state at sufficiently low R, giving rise to a series of avoided crossings (see Fig. 1(b) in the main article). We refer to this region of internuclear separations R_c as the Inglis-Teller limit, which was defined originally in studies on plasmas as the point at which Stark broadening is sufficient to mix states of different n [5, p. 75]. Based on the asymptotic behaviour of the nonpolar and strongly polar PECs in our system, the onset of this regime should scale roughly as $R_c \propto n^{5/2}$, which is equivalent to a critical electric field strength of $E \propto n^{-5}$ and agrees with earlier results [6].

In the vicinity of these avoided crossings, the adiabatic Born-Oppenheimer approximation is no longer strictly valid and in general it becomes necessary to employ a coupled channel formalism for modelling the vibrational dynamics [7], often at greater computational cost. In contrast, the Landau-Zener (LZ) formula [8] provides a straightforward semiclassical approach for modelling the dynamics of vibrational degrees of freedom in the vicinity of avoided crossings and has been previously applied within the context of ultralong-range Rydberg molecules for predicting electronic transitions due to

nonadiabatic couplings [9]. The LZ formula states that for a wavepacket moving with speed $\dot{R}$ toward an avoided crossing between two coupled PECs $\varepsilon_i(R)$ and $\varepsilon_j(R)$, the system may undergo a nonadiabatic transition between the channels with probability

$$ P_{ij} = \exp\left(- 2\pi \frac{a_{ij}^2}{\dot{R}\,\alpha_{ij}} \right). \qquad (3) $$

Here a_{ij} is half the energy gap at the avoided crossing and α_{ij} is the differential gradient between the curves. For brevity, we rewrite Eq. (3) in terms of a single index i for each avoided crossing $P_{ij} \to P_i$, where $i = 1$ corresponds to the outermost (i.e. large R) avoided crossing in the ion-Rydberg PECs.

As shown in Fig. 2(a) for Rydberg atoms excited to the $|129S\rangle$ state, the ion-Rydberg pair has a finite probability to transition between PECs at the avoided crossings, which opens up a multitude of potential collision channels. The transition probability rises with increasing relative velocity $\dot{R}$ and decreases drastically for avoided crossings at smaller internuclear separations. This is primarily due to the increasing gap size a_i at small R, which can be seen in Fig. 2(b). The quantities featured in Eq. (3) show significant variation with principal quantum number n. The variation in the gap size and gradient at the outermost crossing ($i = 1$) with n is shown in Fig. 2(d) and 2(e). We expect that the quadratic depedence of a_i in Eq. (3) will ensure that its variation dominates the change in transition probabilities compared to variations in the differential gradient α_i. Thus, the probability for nonadiabatic transitions will increase with n. We model the dynamics of the ion-Rydberg pair starting on the $|129S\rangle$ PEC and account for nonadiabatic transitions between collision channels via the LZ formula. The initial conditions $R(0) = R_0$ and $\dot{R}(0) = \dot{R}_0$ of the pair's equation of motion are determined from the Rydberg laser detuning Δ and the gas temperature T, respectively. To ensure a fair comparison with the experimental measurements, it is necessary to account for the finite effective linewidth of the Rydberg excitation laser δ, which broadens the initial separation distribution of the ion-Rydberg pairs $\{R_0\}$. In addition, various time delays are present during the preparation and extraction steps of the experimental sequence due to the finite operation time of the excitation lasers and the time of flight of the ions to the microchannel plate detector, which have also been accounted for in our simulations.

C — n-scaling of nonadiabatic transition probabilities

We now investigate the tunability of the LZ transition probabilities with principal quantum number n. For the initial separation we choose a fixed distance of $33\,\mu m$,

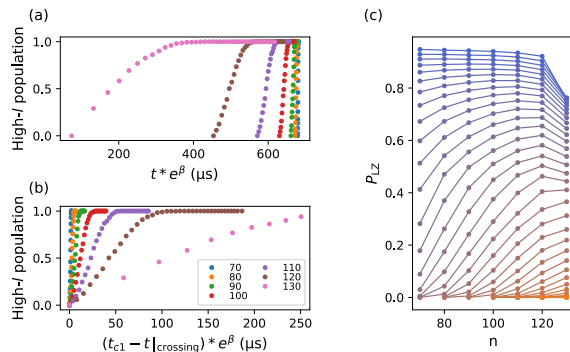FIG. 3. **Dynamics for different principal quantum numbers n.** (a) The population of the strongly polar high-l states is plotted on a rescaled time axis, where $\beta(n)$ is chosen in such a way that the dynamics on the bare S-state potential collapse on the $n = 70$ curve for all n. (b) For better comparison the arrival time of the first crossing is set to zero. Note, that not all data points from (a) are shown here for $n = 130$. (c) Transition probability as a function of n. Colors represent different avoided crossings - ranging from the outermost crossing (blue) to the innermost crossing (orange). Probabilities corresponding to the same crossing are connected by lines to guide the eye.

such that for all n the Rydberg atom is excited onto the $|nS\rangle$ PEC before it crosses into the fan of Stark-split strongly polar states. For simplicity, we set the initial velocity and the effective laser linewidth to zero and consider a one-dimensional case.

The duration of the dynamics varies considerably with n due to the changing length scale and gradient of the PECs (see Fig. 2(d) and 2(e)). To be able to easily compare the relative adiabaticity of the different dynamics, we rescale the time axis by a factor e^β, where β is chosen for each n in such a way that the dynamics on the bare S-state potential collapse onto the same trajectory. Here, we choose $n = 70$ as the reference trajectory. Therefore, $\beta(n{=}70) = 0$ and we find that β strictly increases for larger n, reaching $\beta(n{=}130) \approx 2.2$ for the largest considered principal quantum number.

Fig. 3(a) shows the fraction of systems that populate the strongly polar high-l states as a function of the rescaled time, where each point corresponds to the time at which a crossing is reached. For higher n, the avoided crossings are reached earlier and as a result the population starts to increase at earlier times. In Fig. 3(b), the arrival time at the first crossing is set to zero for all curves, revealing the difference of the adiabaticity inside the fan of the hydrogenic manifold for different n. This is mainly dominated by the density of crossings, since the LZ probability at each individual crossing does not change drastically with n for the first 10 crossings, as can be seen in Fig.3(c). In this figure, we plot the LZ probabilities for all individual crossings, starting with the outermost crossing shown in

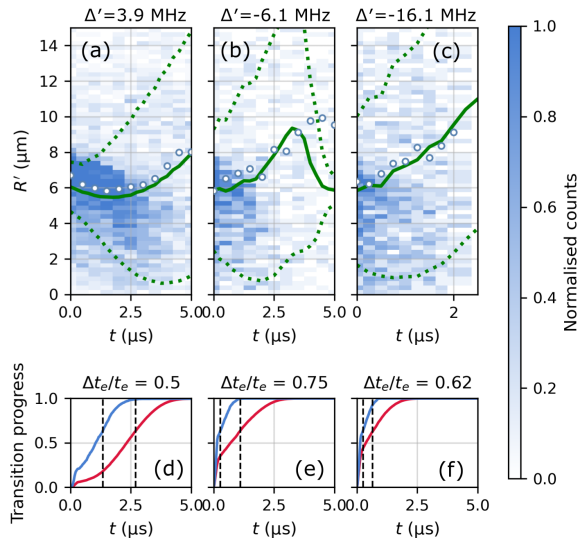C — *n*-scaling of nonadiabatic transition probabilities 4

FIG. 4. **Ion-Rydberg pair dynamics.** (a)-(c) Observed relative atomic dynamics with results of LZ simulations overlaid for different detunings of the Rydberg laser Δ' relative to the outermost avoided crossing between the $|70S\rangle$ atomic Rydberg state and the strongly polar states. The colorbar gives the number of measured counts as a fraction of counts at $t = 0$. Circular data points indicate the mean of the measured distribution for each time step. Solid (dotted) lines indicate the mean (standard deviation) of the theoretical distribution. (d)-(f) Population of the fast collision channels (strongly polar states) over time for both LZ (red) and adiabatic (blue) simulations. Dashed vertical lines (not visible for $\Delta' = 0.8$ MHz in this interval) indicate the time t_e at which the population reaches $1 - 1/e$ (approx. 63%). $\Delta t_e/t_e$ is the relative difference in this time between the LZ and adiabatic simulations.

blue to the deepest considered crossing shown in orange. The deviation from the overall trend at $n = 130$ is due to the fact that the atoms are initialized very close to the first crossing for this state.

D — Ion-Rydberg pair dynamics for the $|70S\rangle$ state

We also observed ion-Rydberg dynamics for the $|70S\rangle$ atomic Rydberg state and the results are shown in Fig. 4. For $|70S\rangle$, the Inglis-Teller regime manifests at smaller internuclear separations than for $|129S\rangle$ ($R_c(n=70) \approx 6.6\,\mu m$ and $R_c(n=130) \approx 32.2\,\mu m$) due to the lower principal quantum number of the Rydberg excitation. Moreover, ion-Rydberg collision pairs at $|70S\rangle$ have fewer open channels than at $|129S\rangle$ due to the smaller number of degenerate high-l states in the neighboring $n = 67$ manifold.

Additionally, in contrast to the measurements taken for

$|129S\rangle$, no 2D-confinement was employed during the experimental sequence and consequently the dynamics unfold in 3D. As a result, the measurements show the *projection* of the internuclear separation R onto the microchannel plate, denoted by R', instead of the true value of R. This has the consequence that the ion-Rydberg separation distribution is extremely broad – even for time $t = 0$ – as can be seen in Fig. 4(a)-(c).

As the ion-Rydberg pairs travel inward to small internuclear separations, they will eventually reach an extreme regime in which the Stark-splitting of neighboring and next-neighboring hydrogenic manifolds becomes far greater than their field-free energetic separation. Thus, the electronic states of the Rydberg atom become highly mixed and an accurate description of the physics becomes increasingly difficult due to the sheer multitude of open channels. We do not aim at a description of the dynamics at such small internuclear separations and instead focus on capturing the physics at intermediate separations at the onset of the Inglis-Teller regime. Therefore, we introduced a short distance cut-off to the simulations which removes particles once they have crossed a certain threshold separation, equal to $2.5\,\mu m$ for the case of $|70S\rangle$. This distance is defined as the internuclear separation for which the energy of the $|70S\rangle$ Rydberg state in zero field is equal to the Coulomb barrier between the ion and the Rydberg core. We overestimate this distance since it does not account for the decrease in the Rydberg electron's energy due to the attractive interaction between the ion and the $|70S\rangle$ Rydberg state. As a result of particles being removed below this threshold value, the mean position of the theoretical distribution of particles is seen to increase over time (see solid green lines in Fig. 4 (a)-(c)). This effect is more pronounced for the dynamics with the $|70S\rangle$ Rydberg state because the collisions happen much faster than at $|129S\rangle$.

When comparing the LZ and adiabatic simulations in the bottom row of Fig. 4, we see that the absolute difference in the transition times Δt_e to the strongly polar curves decreases with decreasing detuning Δ' – indicating, as expected, the increased frequency of nonadiabatic transitions at higher detuning. However, unlike the simulations carried out for $|129S\rangle$, there is no clear trend in the relative difference of these transition times. We attribute this partially to the effective linewidth of the excitation laser $\delta = 3.4$ MHz, which leads to broadening of the initial separation distribution $\{R_0\}$ of the collision pairs. Whilst this broadening is also present for $|129S\rangle$, the effect is amplified in the case of $|70S\rangle$ due to the smaller length scales at which the dynamics occur.

D — Ion-Rydberg pair dynamics for the $|70S\rangle$ state   5

———————

*   dboswort@physnet.uni-hamburg.de
†   Present address: Atom Computing, Inc., Berkeley, CA, USA.
‡   pschmelc@physnet.uni-hamburg.de
§   t.pfau@physik.uni-stuttgart.de

[1] C. Veit, N. Zuber, O.A. Herrera-Sancho, V.S.V. Anasuri, T. Schmid, F. Meinert, R. Löw, and T. Pfau, Phys. Rev. X **11**, 011036 (2021).

[2] A. Duspayev, X. Han, M. A. Viray, L. Ma, J. Zhao, and G. Raithel, Phys. Rev. Res. **3**, 023114 (2021).

[3] M. Deiß, S. Haze, and J. Hecker Denschlag, Atoms **9**, 34 (2021).

[4] S. Weber, C. Tresp, H. Menke, A. Urvoy, O. Firstenberg, H. P. Büchler, and S. Hofferberth, J. Phys. B: At. Mol. Opt. Phys. **50**, 133001 (2017).

[5] T. F. Gallagher, *Rydberg Atoms*, Cambridge Monographs on Atomic, Molecular and Chemical Physics (Cambridge University Press, 1994).

[6] D. R. Inglis and E. Teller, Astrophys. J. **90**, 439 (1939).

[7] H. Köppel, W. Domcke, and L. S. Cederbaum, "Multimode molecular dynamics beyond the born-oppenheimer approximation," in *Advances in Chemical Physics*, Vol. 57 (John Wiley & Sons, Ltd., New York, 1984) pp. 59–246.

[8] C. Zener and R. H. Fowler, Proc. R. Soc. Lond. A **137**, 696 (1997).

[9] M. Schlagmüller, T. C. Liebisch, F. Engel, K. S. Kleinbach, F. Böttcher, U. Hermann, K. M. Westphal, A. Gaj, R. Löw, S. Hofferberth, T. Pfau, J. Pérez-Ríos, and C. H. Greene, Phys. Rev. X **6**, 031020 (2016).

Metastable doubly charged Rydberg trimers [SC5]

Metastable doubly charged Rydberg trimers

Daniel J. Bosworth ●,[1,2,*] Matthew T. Eiles ●,[3] and Peter Schmelcher ●[1,2]

[1]*Zentrum für Optische Quantentechnologien, Universität Hamburg, Luruper Chaussee 149, 22761 Hamburg, Germany*
[2]*The Hamburg Centre for Ultrafast Imaging, Universität Hamburg, Luruper Chaussee 149, 22761 Hamburg, Germany*
[3]*Max-Planck-Institut für Physik komplexer Systeme, Nöthnitzer Straße 38, 01187 Dresden, Germany*

We examine an effectively one-electron system with three positive nuclei composed of a ^{87}Rb* Rydberg atom interacting with a pair of ^{87}Rb$^+$ ions and predict the existence of metastable vibrationally bound states of ^{87}Rb$_3^{2+}$. These molecules are long-range trimers whose stability rests on the presence of core-shell electrons and favorable scaling of the Rydberg atom's quadrupole moment with the principal quantum number n. Unlike recently observed ion-Rydberg dimers, whose binding is due to internal flipping of the Rydberg atom's dipole moment, the binding of ^{87}Rb$_3^{2+}$ arises from the interaction of the ions with the Rydberg atom's quadrupole moment. The stability of these trimers is highly sensitive to n. For $n \leqslant 35$, we estimate that the lifetime of the bound states should be limited by intercore tunneling of the Rydberg electron, which creates an instability in the system. However, we predict that the rate of this process decreases significantly with n, such that already for $n = 38$ it is comparable in magnitude to the rate of spontaneous emission of the Rydberg state. The decreasing depth of the binding potential at larger n will further lead to an increase in the tunneling rate of the vibrational states from the molecular binding potential to dissociative regions of the adiabatic potential energy surface. Nonetheless, at $n = 38$, this mechanism is only relevant for the highest-excited vibrational states in the binding potential.

I. INTRODUCTION

Atomic and molecular ions play significant roles in chemical processes throughout nature. One example can be found inside dense interstellar gases, where proton transfer reactions between H$_3^+$ molecular ions and neutral species contribute to the synthesis of, among other things, water [1,2]. Despite their importance, molecular ions are generally short-lived. This is especially true for multiply charged variants, whose decay releases considerable amounts of stored molecular energy through a Coulomb explosion between their singly charged fragments [3]. This highly exothermic decay has in the past inspired proposals to use molecular dications as a source of propulsive energy [4].

Molecular ions may also form within the ultracold environment of a Bose-Einstein condensate [5–7]. Three-body processes between neutral atoms and an atomic ion can lead to spontaneous formation of bound atom-ion dimers which occupy rovibrational states close to the dissociation threshold. By virtue of the long-range nature of the atom-ion interaction [8], such states are mesoscopic in size, possessing bond lengths on the order of 0.1 μm. These molecules have been well-characterized theoretically [5–7,9–11] and can be

----

*Contact author: dboswort@physnet.uni-hamburg.de

produced in cold hybrid atom-ion experiments by means of laser-assisted spontaneous radiative association [12,13], multiphoton ionisation of neutral precursors [14,15], and, more recently, through binary collisions in the presence of a trapping potential [16]. Moreover, the recent observation of atom-ion Feshbach resonances [17,18] opens the door to magnetoassociation of bound atom-ion pairs, as is currently possible for neutral molecules [19].

By promoting atoms to highly excited states, it is even possible to form *macroscopic* molecular ions, where a single ion binds a Rydberg atom [20–22]. Similar to other species in the zoo of long-range Rydberg molecules [23–31], Rydberg molecular ions exhibit micrometer-size bond lengths and binding energies on scales of mega- or gigahertz for sufficiently large n. The macroscopic size and slow vibrational dynamics of ion-Rydberg systems allow the imaging of molecular dynamics without the need for ultrafast pulses [32,33]. More generally, the high density of states in Rydberg molecules mean they can be utilized to explore and exploit effects beyond the Born-Oppenheimer approximation [34–37].

In this paper, we extend prior work on interacting ion-Rydberg pairs by exploring a three-body system of a ^{87}Rb Rydberg atom interacting with two ^{87}Rb$^+$ cations. Despite the strong Coulomb repulsion between the cations, we find that the presence of quantum defect states [38] and the Rydberg atom's large quadrupole moment give rise to potential wells supporting several vibrationally bound states of ^{87}Rb$_3^{2+}$ above a critical value of the principal quantum number n. Put differently, we reveal that introducing additional energy into the system through a Rydberg excitation can unexpectedly lead to its stabilization. We further explore possible decay

mechanisms and highlight a range of *n* for which we expect these trimers to be stable on timescales comparable to the radiative lifetime of the Rydberg atom. Specifically, we provide semiclassical estimates for the rate of decay of bound states of $^{87}\mathrm{Rb}_3^{2+}$ via nonadiabatic transitions, charge transfer and Coulomb explosion. We model the latter two processes by (i) intercore tunneling of the Rydberg electron and (ii) decay of the vibrational state from the molecular binding potential to the dissociative region of the adiabatic potential energy surface (PESs). We will refer to these distinct processes as electron tunneling (ET) and vibrational state tunneling (VT), respectively.

This paper is laid out as follows. In Sec. II, we discuss ion-Rydberg interactions and derive a lower bound for *n* above which we expect the system to support binding potentials. Section III then presents numerical results for adiabatic potential energy surfaces of the system as well as vibrationally bound states. The possible decay mechanisms of $^{87}\mathrm{Rb}_3^{2+}$ and their variation with *n* is the focus of Sec. IV.

II. SETUP AND INTERACTIONS

In this section, we first describe the $^{87}\mathrm{Rb}_3^{2+}$ system with its competing ion-ion and ion-Rydberg interactions. We then demonstrate that for sufficiently large *n* the ion-Rydberg interaction can be strong enough to counterbalance the destabilizing Coulomb repulsion of the ion pair.

The system under consideration is shown in Fig. 1(a). We consider a single $^{87}\mathrm{Rb}^*$ Rydberg atom interacting with two positively charged $^{87}\mathrm{Rb}^+$ ions at positions $\mathbf{R}_1 = (R_1, 0, 0)$ and $\mathbf{R}_2 = (R_2, \Theta, 0)$ relative to the Rydberg core. The electronic Hamiltonian is given by

$$\hat{H}_e = \hat{H}_0 + \hat{V}_{\mathrm{IR}}^{(1)}(\mathbf{R}_1) + \hat{V}_{\mathrm{IR}}^{(2)}(\mathbf{R}_2) + \hat{V}_{\mathrm{II}}(\mathbf{R}_1, \mathbf{R}_2). \quad (1)$$

$\hat{H}_0$ describes the Rydberg atom with eigenstates $\psi_{n,l,m}(\mathbf{r}) = \frac{u_{n,l}(r)}{r} Y_{l,m}(\theta, \phi)$, where (n, l, m) are quantum numbers. The radial component $u_{n,l}(r)$ includes corrections due to interaction with the core-shell electrons [39,40]. $\hat{V}_{\mathrm{IR}}^{(i)}$ is the interaction of the Rydberg atom with the *i*th ion and $\hat{V}_{\mathrm{II}} = 1/|\mathbf{R}_1 - \mathbf{R}_2|$ is the Coulomb repulsion between the ions. Unless stated otherwise, we assume atomic units throughout this paper. We further neglect the fine structure of the Rydberg atom in our calculations.

For internuclear separations exceeding the Le Roy radius [41] where the overlap between the separate atomic charge distributions vanishes, the ion-Rydberg interaction can be expressed as a multipole expansion [42]:

$$\hat{V}_{\mathrm{IR}}^{(i)}(\mathbf{R}_i) = -\sum_{\lambda=1}^{\infty} \sum_{\mu=-\lambda}^{+\lambda} \frac{4\pi}{2\lambda+1} \frac{r^\lambda}{R_i^{\lambda+1}} Y_{\lambda\mu}(\theta, \phi) Y_{\lambda\mu}^*(\Theta, 0), \quad (2)$$

where $\mathbf{r} = (r, \theta, \phi)$ denotes the position of the Rydberg electron relative to the Rydberg core and $Y_{\lambda\mu}$ are spherical harmonics.

Since it is likely to be the most stable arrangement of the nuclei, in this paper, we focus. in particular, on the symmetric case in which the ions are located on either side of the Rydberg atom with internuclear spacing $|\mathbf{R}_1| = |\mathbf{R}_2| = R$ and $\Theta = \pi$. In this symmetric linear arrangement, the odd-λ terms in $\hat{V}_{\mathrm{IR}}^{(1)}$
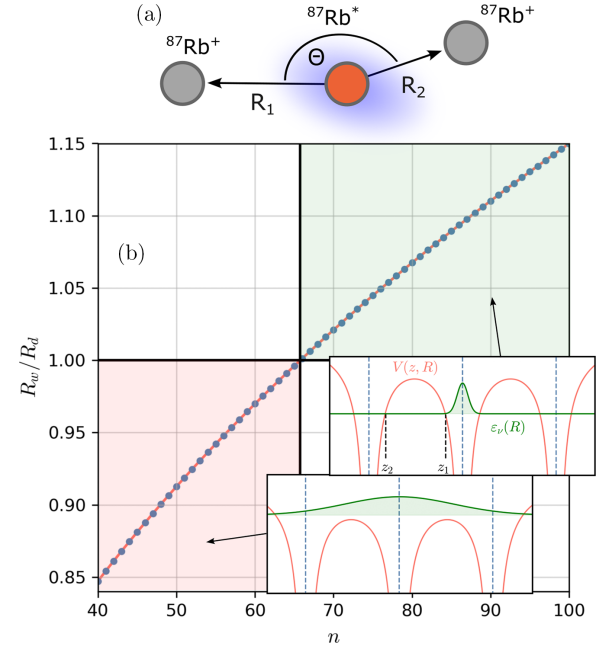

FIG. 1. (a) Schematic of the $^{87}\mathrm{Rb}_3^{2+}$ system, consisting of two $^{87}\mathrm{Rb}^+$ ions and an $^{87}\mathrm{Rb}^*$ Rydberg atom. (b) The scaling of the critical separations R_w and R_d with *n* to first-order approximation (see Sec. II). We find $R_w/R_d = 1$ for a critical *n* value of $n_c \approx 65.8$. The solid line is a fit to a power-law function an^b, with $a = 0.248$ and $b = 0.333$ to three significant figures. The insets depict how the energy of the Rydberg electron relates to the maximum height of the Coulomb barrier in the regimes $R_w/R_d < 1$ and $R_w/R_d > 1$.

exactly cancel out those in $\hat{V}_{\mathrm{IR}}^{(2)}$, such that the leading order term in the net ion-Rydberg interaction is the interaction of the ions with the Rydberg atom's quadrupole moment $V_{\mathrm{quad}}(R) \propto -1/R^3$, corresponding to the term $\lambda = 2$ in Eq. (2). Thus, our setup offers the possibility to explore physics dominated by quadrupole interactions—unlike previously explored systems in which the ion-Rydberg interaction is dominated by the charge-dipole term $\lambda = 1$ [20–22,32,33,43,44]. Potential wells accommodating bound states may form in purely long-range molecular systems due to avoided crossings between different potential energy curves (PEC). For ion-Rydberg dimers [20,21], these avoided crossings occur between a high-field seeking $|nP\rangle$ state and low-field seeking high angular momentum states $|(n-1)l > 3\rangle$ whose leading-order energy corrections are due to the interaction with the Rydberg atom's dipole moment [the charge-dipole term $\lambda = 1$ in the series (2)]. Their anticrossings form binding potentials at internuclear separations approximately one order of magnitude larger than the extent of the Rydberg electron's orbit. The $^{87}\mathrm{Rb}_3^{2+}$ system might also exhibit such crossings between high- and low-field seeking states, possibly giving rise to binding potentials. However, in this case the ion-Rydberg interaction must contend with the Coulomb repulsion of the ion pair and may thus be washed out. Nevertheless, given that matrix elements of the ion-Rydberg interaction terms $\langle\psi_i|\hat{V}_{\mathrm{IR}}^{(j)}|\psi_k\rangle$ scale with *n*, is there a range of *n* for which

the strength of this interaction is comparable to that of the Coulomb interaction?

To answer this question, let us consider two Rydberg states ψ_A and ψ_B connected asymptotically ($R_1, R_2 \to \infty$) to neighboring hydrogenic manifolds n and $n-1$. In the absence of the ion pair, these states have energies $\varepsilon_A^{(0)}$ and $\varepsilon_B^{(0)}$, such that $\varepsilon_A^{(0)} > \varepsilon_B^{(0)}$. In the presence of the ion pair, the states experience energy shifts:

$$\Delta\varepsilon_j^{(1)}(R) = \frac{p_j \, n^4}{R^3} + \frac{1}{2R}. \tag{3}$$

The first term represents the leading-order energy correction resulting from the interaction of the ion pair with the quadrupole moment of the Rydberg atom $\langle \psi_j | 2V_{\text{quad}}(R) | \psi_j \rangle = p_j n^4 / R^3$, where p_j is a constant. This correction lifts the state degeneracy within the hydrogenic manifold. The second term is the energy correction arising from the Coulomb repulsion between the ions $\hat{V}_{\text{II}}$, which contributes a global energy shift of all states.

From Eq. (3), ψ_A will become degenerate with ψ_B at $R = R_w$ when the following holds:

$$\Delta\varepsilon_B^{(1)}(R_w) - \Delta\varepsilon_A^{(1)}(R_w) = \varepsilon_A^{(0)} - \varepsilon_B^{(0)}. \tag{4}$$

However, higher-order energy corrections beyond Eq. (3) will lead to finite mixing between different Rydberg states, ensuring that such degeneracies are prohibited. The resulting level-repulsion between ψ_A and ψ_B may then lead to the formation of a binding potential.

As a first approximation to the possible binding radius of $^{87}\text{Rb}_3^{2+}$, we first consider how the crossing point R_w of the uncoupled energy curves should scale with n. Given that the energy spacing between neighboring Rydberg states decreases according to $\varepsilon_A^{(0)} - \varepsilon_B^{(0)} = q \, n^{-3}$, with q a positive constant, we find from Eq. (4) the following relation:

$$R_w = \sqrt[3]{\frac{2p}{q}} n^{7/3}, \tag{5}$$

where we assume that $p_B = -p_A = p$, with p a positive constant. Thus we see that the binding radius of $^{87}\text{Rb}_3^{2+}$ should increase with n.

However, since we are interested in long-range bound molecular states, at $R = R_w$ the Rydberg electron should remain localized on the central positive core. For three fixed positive ions centered at the origin with equal spacing $|\mathbf{R}|$, the Rydberg electron experiences the net Coulomb potential:

$$V(\mathbf{r}) = -1/|\mathbf{r}| - 1/|\mathbf{r} + \mathbf{R}| - 1/|\mathbf{r} - \mathbf{R}| + 5/2|\mathbf{R}|. \tag{6}$$

Here, the final term is the total repulsive interaction between the positive ions in the system. The maximum height of the Coulomb barrier separating the electron from the two surrounding ionic cores occurs at $r = R/2$, giving a barrier height of $V_b(R) = -13/6R$. Therefore, below a critical internuclear separation R_d, the energy of the Rydberg electron will exceed $V_b(R)$ such that it delocalizes over all three ions, potentially destabilizing the system. Setting $\varepsilon_A^{(0)} + \Delta\varepsilon_A^{(1)}(R_d) = V_b(R_d)$, we find

$$3R_d^3 - 16n^2 R_d^2 + 6pn^6 = 0. \tag{7}$$

To arrive at an estimate of the range of n over which stable long-range bound states may form, we now compare the scaling of R_w and R_d with n. For this, we first determine values for the constants p and q. p is determined by fitting the radial integral appearing in $\langle \psi_j | 2V_{\text{quad}}(R) | \psi_j \rangle$ to the power-law function an^b. For states $|n, l = 4\rangle$, we find $a \approx 2.41$ and $b \approx 4.01$. Given $\langle \psi_j | 2V_{\text{quad}}(R) | \psi_j \rangle = 2\sqrt{4\pi/5} \, \langle \psi_j | r^2 Y_{2,0}(\theta, \phi) | \psi_j \rangle / R^3 = pn^b / R^3$, this yields $p = 1.25$ to three significant figures. Similarly, q is found by fitting the energy splitting of neighboring Rydberg manifolds to qn^c. Here, we find $q \approx 1.14$ and $c \approx -3.02$ to three significant figures.

Figure 1(b) shows the ratio of the two critical separations R_w/R_d as a function of n. The values of R_d were determined through numerical solution of (7). The ratio is found to be monotonically increasing over the range of n shown and exceeds unity for $n \geqslant 66$. The increase of R_w/R_d with n can be understood by considering (7) in the limit of large n, for which it may be approximated as $-16n^2 R_d^2 + 6pn^6 \approx 0$. This yields $R_d \propto n^2$, from which we obtain $R_w/R_d \propto n^{1/3}$. This result agrees with the power-law fit an^b of the data points in Fig. 1(b), where we find $a = 0.248$ and $b = 0.333$ to three significant figures.

In summary, we predict with first-order perturbation theory that R_w scales faster with n than R_d. This means that for sufficiently large n, we may expect the PECs of $^{87}\text{Rb}_3^{2+}$ to exhibit long-range binding potentials in which the Rydberg electron remains localized on the central positive core. Nonetheless, this result should be taken with a grain of salt since we have so far neglected (i) coupling between different Rydberg states and (ii) higher-order multipole interaction terms in the ion-Rydberg interaction series (2). To account for these effects, we will now employ a more sophisticated numerical method for determining the PEC of the electronic Hamiltonian (1). As we will see in the following section, these results point to a significantly lower value of n_c than that given in Fig. 1(b).

III. ELECTRONIC AND VIBRATIONAL STRUCTURE

We now diagonalize the electronic Hamiltonian $\hat{H}_e$ in a finite basis of atomic Rydberg states fulfilling $\hat{H}_0 \phi_\alpha(\mathbf{r}) = \epsilon_\alpha \phi_\alpha(\mathbf{r})$. The eigenvalues $\varepsilon_\nu(\mathbf{R})$ of $\hat{H}_e$ depend on the system's three internal degrees of freedom $\mathbf{R} = (R_1, R_2, \Theta)$ and form PESs which describe the interaction potential between the nuclei. Both the Rydberg Hamiltonian $\hat{H}_0$ and the Coulomb interaction operator $\hat{V}_{\text{II}}(R_1, R_2)$ are diagonal in the Rydberg basis. Matrix elements of the ion-Rydberg interaction terms $\hat{V}_{\text{IR}}^{(i)}(R_i)$ can be evaluated straightforwardly in the Rydberg basis, since analytical results for integrals of multipole moments are generally available [45]. We include the first 16 λ terms in the multipole expansion (2).

In Fig. 2, we show one-dimensional cuts through the adiabatic PES near the $n = 35$ hydrogenic manifold for symmetric linear configurations of the nuclei where $R_1 = R_2 = R$ and $\Theta = \pi$. Figure 2(a) shows the adiabatic PES at the onset of the Inglis-Teller regime [46], where states from different manifolds are mixed [39]. The shaded region indicates electronic states with $\varepsilon_\nu(R) \geqslant V_b(R)$, such that the Rydberg electron delocalizes over all three positive cores. In this regime, our basis of Rydberg states localized on the central positive core
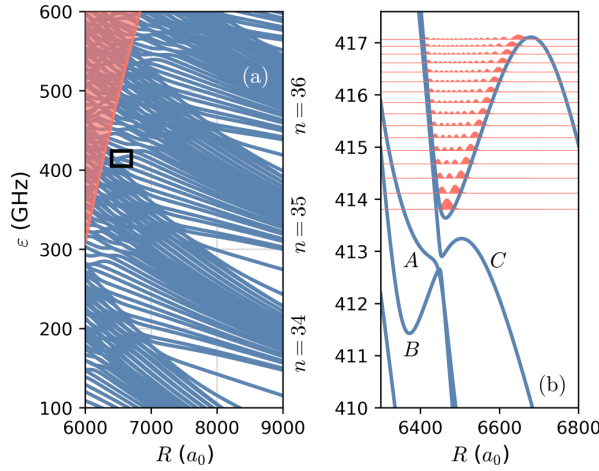
FIG. 2. Adiabatic PES near the $n = 35$ hydrogenic manifold. (a) 1D slice along PES for the symmetric linear configuration $R_1 = R_2 = R$, $\Theta = \pi$. The shaded red region in the upper left indicates the region in which the localized electron ansatz no longer holds. (b) Magnification of the box in (a), showing an example of a molecular binding potential. The filled curves show the probability density of the symmetric stretching modes determined from the effective 1D vibrational Hamiltonian (8). The three neighboring adiabatic PES of the binding potential are labeled $A - C$. Energies given in GHz relative to the $n = 35$ atomic Rydberg state.
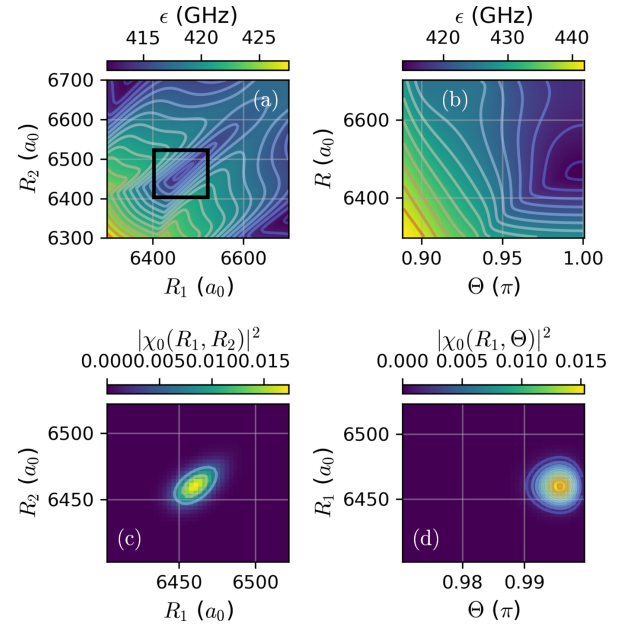

FIG. 3. (a), (b) 2D slices of the binding potential shown in Fig. 2(b) for (a) $\Theta = \pi$ and (b) $R_1 = R_2 = R$, respectively. The adiabatic PES exhibits a local minimum for $R_1 = R_2 = 6460\,a_0$ and $\Theta = \pi$. Energies given in GHz relative to the 35H atomic Rydberg state. (c), (d) Reduced probability density of the vibrational ground state $\chi_0(R_1, R_2, \Theta)$ averaged over (c) Θ and (d) R_2. The states shown here are normalized as $\int dR_1 dR_2 d\Theta |\chi(R_1, R_2, \Theta)|^2 = 1$. The black box in (a) indicates the region spanned by (c).

is no longer an accurate description of the system. To that end, we restrict our focus to regions for which $\varepsilon_v(R) < V_b(R)$ holds.

At large R, the dominant energy correction to the eigenstates is a global positive energy shift stemming from the Coulomb repulsion between the ions. In Fig. 2(a), we see that at $R = 9000\,a_0$ this shift amounts to approximately 400 GHz. This can be seen by looking at the energy of the states in the second manifold from the top of the subplot, which connect asymptotically to the $n = 35$ hydrogenic manifold.

Despite this large global energy shift, we see that there is also a significant Stark-like splitting of the states in the manifolds due to the interaction of the Rydberg atom with the electric field of the ion pair. For approximately $R < 7500\,a_0$, the splitting becomes comparable to the energy separation of the manifolds and the resultant avoided crossings form a variety of well-like structures. One such well is shown in Fig. 2(b). In general, the wells in this region of the energy spectrum have depths ranging from hundreds of MHz to several GHz with local minima positioned at internuclear separations two to three times larger than the expected radius of the Rydberg electron's orbit. In comparison, the binding potentials of diatomic ion-Rydberg molecules arise at internuclear separations roughly one order of magnitude larger than the Rydberg electron's orbit [21,22]. Consequently, we expect that intercore electron tunneling will be more important in our system and we will explore this later in Sec. IV. We further emphasize that the wells seen in Fig. 2 are formed at larger internuclear separations than are predicted by our simplistic analytical model, which from Eq. (5) predicts $R_w \approx 5200\,a_0$ for $n = 35$.

Figures 3(a) and 3(b) show two-dimensional slices of the adiabatic PES of the well in Fig. 2(b) for nonsymmetric nuclear configurations. These plots indicate that the well in Fig. 2(b) is indeed a local minimum for all internal degrees of freedom of the triatomic system, favoring symmetric bond lengths $R_1 = R_2$ and a collinear configuration $\Theta = \pi$.

We determine the vibrational states of the adiabatic PES by solving the vibrational Hamiltonian for a nonrotating triatomic molecule (see Appendix A). We employ a finite difference approach [47], whereby the Hamiltonian is discretised on a three-dimensional grid. The block structure of the matrix Hamiltonian is such that it can be most efficiently constructed when represented on a cubic grid of edge length N. We find that $N = 42$ is sufficient to ensure convergence of the vibrational eigenenergies to the scale of a few MHz. Reduced densities of the vibrational ground state are shown in Figs. 3(c) and 3(d). We find that the well exhibits bending excitations in Θ as well as symmetric stretching excitations in R_1 and R_2, whose first few excitations have spacings of 100 MHz and 135 MHz, respectively. We did not find any antisymmetric stretching excitations among these states.

In addition to the approach described above, we also determined the vibrational states of the symmetric stretch Hamiltonian (8). This is an effective 1D Hamiltonian derived from the full vibrational Hamiltonian (A1) for symmetric

linear configurations of the nuclei and takes the form

$$H_n^{\text{eff}} = -\frac{1}{2\mu}\frac{\partial^2}{\partial R^2} + \varepsilon_i(R), \tag{8}$$

where $\mu = m/2$ with m the mass of ^{87}Rb and $\varepsilon_i(R)$ is a one-dimensional slice of the ith adiabatic PES for $R_1 = R_2 = R$ and $\Theta = \pi$. Using this approach, we find that the binding potential supports sixteen symmetric stretching modes. The probability density of these eigenstates are shown in red in Fig. 2(b). The states have a typical spacing of 250 MHz, which is greater than the energy spacing between states in the 3D model (A1). This is expected due to the reduced dimensionality of the binding potential in the effective model. The difference in energy of the first few symmetric stretching excitations relative to those obtained with the 3D model is less than 1 GHz (see Appendix B).

Finally, we remark that the electronic state of the binding potential in Fig. 2(b) possesses some low-l character. Specifically, at the position of the local minimum the total contribution of S and D states is approximately 15%. Hence, the bound states can in principle be accessed via two-photon excitation transitions (see Appendix D).

IV. ESTIMATING THE TRIMER'S STABILITY

We now estimate the rates of different mechanisms which may limit the lifetime of the trimer states below the radiative lifetime of the Rydberg atom. First, we examine leakage of the vibrational states from the binding potential to neighboring PES via nonadiabatic couplings. We define the rate of nonadiabatic transitions as $\gamma_{\text{NAD}} = \Delta E\, P_{\text{LZ}}$, where ΔE is the average spacing of the vibrational states in the binding potential and $P_{\text{LZ}} = \exp(-2\pi\Gamma)$ is the Landau-Zener formula giving the probability of a nonadiabatic transition [48]. The exponent $\Gamma = \Delta^2/\alpha\dot{R}$ depends on the gap Δ and gradient α parameters of the diabatic curves fitted from the numerically obtained adiabatic PES, in addition to the speed of the molecule $\dot{R}$ at the crossing point R_{cross} of the diabatic curves. Specifically, Δ is defined at R_{cross} as the energy gap between the adiabatic binding potential and the crossing point of the diabatic curves. Similarly, α is defined as the absolute value of the difference in gradient between the diabatic curves. Taking the maximum possible value of $\dot{R}$, set by the energy difference between the maximum height of the binding potential's barrier and the crossing point of the diabatic curves, we find $\gamma_{\text{NAD}} \sim 10^7 - 10^8$ s^{-1} for decay to neighboring adiabatic curves A, B and C [see inset of Fig. 2(b)]. However, if we instead define $\dot{R}$ as the speed of the highest-energy vibrational state at the crossing point $v_{\text{WKB}} = \sqrt{2[E_{15} - V(R_{\text{cross}})]/\mu}$, where E_{15} is the energy of the vibrational state with $\nu = 15$ and μ is the reduced mass of a ^{87}Rb pair, the only significant decay channel is to curve A with $\gamma_{\text{NAD}} \sim 10^4$ s^{-1}. Nonadiabatic decay to curve A is most significant because it has the smallest energy gap Δ. We see, therefore, that the decay rates are highly sensitive to the speed of the bound vibrational state. However, given the large number and complex interwoven form of the adiabatic curves, the applicability of this two-channel semiclassical treatment is unclear. In light of this, a more detailed study of the nonadiabatic coupled-channel equations with vibronic
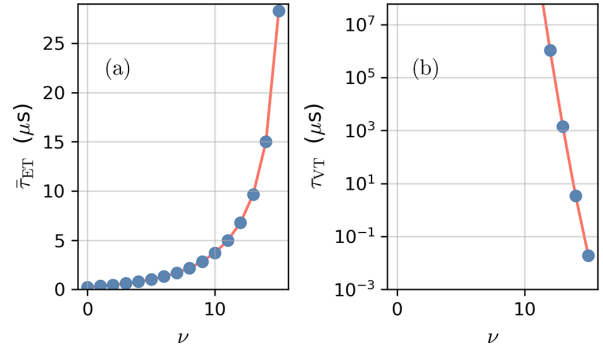

FIG. 4. (a) Expected intercore electron tunneling (ET) times for the symmetric stretching states in the binding potential in Fig. 2(b), with $\nu = 0$ corresponding to the vibrational ground-state. The times have been averaged over the probability density distribution of the vibrational states along R. (b) Expected vibrational state tunneling (VT) times through the barrier in the adiabatic PES [see Fig. 2(b)].

couplings [35] would be an interesting extension of the current paper.

We now consider the rate at which the vibrational states in the molecular binding potential tunnel to the dissociative region of the PES through the barrier shown in Fig. 2(b), which leads to a Coulomb explosion. The rate of such VT is defined as $\gamma_{\text{VT}} = \Delta E\, P_{\text{VT}}(E)$, where $P_{\text{VT}}(E)$ is the semiclassical Wentzel–Kramers–Brillouin (WKB) tunneling probability for a state of energy E (see Appendix C). The tunneling times $\tau_{\text{VT}} = 1/\gamma_{\text{VT}}$ for the bound states are shown in Fig. 4(b). Tunnelling is only relevant for the highest-energy states, where it reaches values as small as tens of nanoseconds.

Charge exchange may also limit the lifetime of the trimer states. We model this process by determining the rate at which the Rydberg electron tunnels through the barrier in the Coulomb potential [see inset of Fig. 1(b)]. We define the rate of this intercore ET as $\gamma_{\text{ET}}(R) = 2f P_{\text{ET}}(R)$, which depends on the semiclassical orbital frequency of the Rydberg electron f and the WKB tunneling probability for an electron of energy $\varepsilon_\nu(R)$ associated with the νth PES (see Appendix C for further details). The factor of 2 accounts for the fact that the Rydberg electron can tunnel through either Coulomb barrier created by the ion pair. The expected tunneling time $\bar{\tau}_{\text{ET}}$ associated to each molecular bound state is determined by averaging $\tau_{\text{ET}}(R) = 1/\gamma_{\text{ET}}(R)$ by probability density of the vibrational state. The results for states in the binding potential at $n = 35$ are shown in Fig. 4(a). For the vibrational ground state, the expected time is approximately 0.24 μs, which is far smaller than the timescale for decay due to spontaneous emission of the Rydberg state. The expected time increases for the excited states, since they show increased probability density around the outer classical turning point of the binding potential [see Fig. 2(b)].

Concluding our discussion of the well at $n = 35$, we expect that the lifetime of the low-energy molecular bound states will be limited by ET, whereas the lifetime of the highest-energy states will be limited by VT. We therefore expect lifetimes on timescales of 0.1–10 μs for the trimer states at $n = 35$.
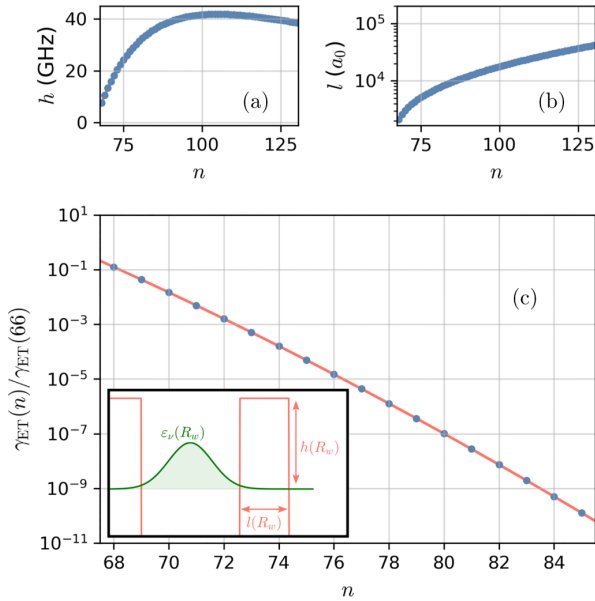
FIG. 5. (a), (b) Scaling of the tunneling barrier height $h(R_w) = V_b(R_w) - \varepsilon(R_w)$ and width $l(R_w) = z_2(R_w) - z_1(R_w)$ with n [see text for definitions and inset in (c)]. (c) The scaling of the rate of intercore electron tunnelling (ET) as a function of n relative to the rate at $n = 66$, with $\gamma_{ET}(66) = 4.02 \times 10^{10}$ s^{-1}. The inset shows a schematic of the Rydberg electron wave function with energy $\varepsilon(R_w)$ in the Coulomb potential, modeled here as a box potential (compare with insets of Fig. 1).

How might the rate of ET change at higher n? To estimate this, we model the Coulomb barrier experienced by the Rydberg electron as a box potential of height $h(R) = V_b(R) - \varepsilon_A^{(1)}(R)$ and width $l(R) = z_2(R) - z_1(R)$ [see inset of Fig. 5(c)]. Here, z_2 and z_1 are classical turning points of the Rydberg electron at position z in the Coulomb potential $V(z, R)$ defined at internuclear separation R [see inset of Fig. 1(b)]. For this simplified case, the WKB tunneling rate (C1) of the Rydberg electron is then given by $\gamma_{ET} = 2f \exp[-2\sqrt{2h(R)}l(R)]$.

Taking $R = R_w$, the n scaling of $h(R_w)$, $l(R_w)$ and γ_{ET} can be determined using the results from perturbation theory given in Eqs. (3) and (5), which we show in Fig. 5. Here, we have additionally made use of the fact that the semiclassical Rydberg orbital frequency f scales as n^{-3} [39].

From Fig. 5, we see that γ_{ET} is monotonously decreasing and highly sensitive to the value of n, ranging over nearly 10 orders of magnitude between $n = 68$ and $n = 85$. This can be understood from the monotonously increasing width of the Coulomb barrier $l(R_w)$ with n, shown in Fig. 5(b). While we do not expect the results of this model to be quantitatively accurate, they do indicate that ET may become less relevant for higher n as the effective width of the Coulomb barrier encountered by the Rydberg electron becomes wider.

To confirm this idea, we calculate adiabatic PESs in the vicinity of the $n = 38$ Rydberg manifold and the associated 1D symmetric stretching modes satisfying the vibrational Hamiltonian (8). We show the results in Fig. 6. The binding
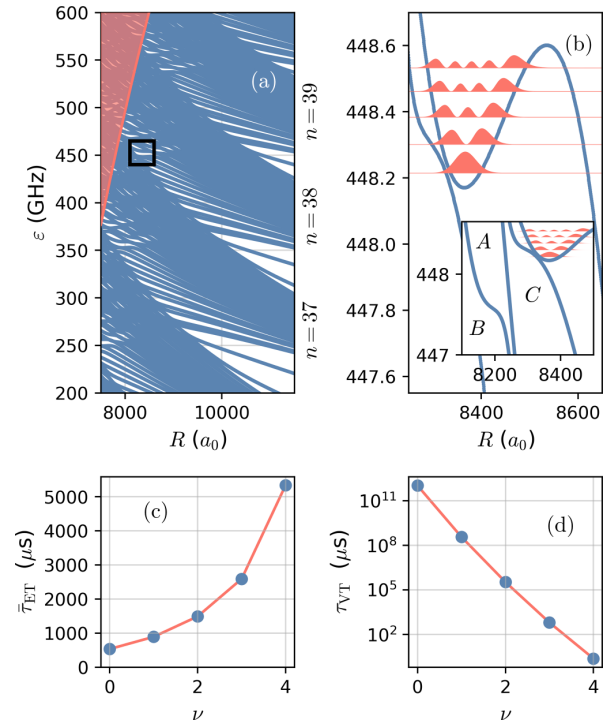
FIG. 6. Adiabatic PES near the $n = 38$ hydrogenic manifold. (a) 1D slice along PES for the symmetric linear configuration $R_1 = R_2 = R$, $\Theta = \pi$. The shaded region indicates the breakdown of the localized electron ansatz. (b) Magnification of the box in (a). The filled curves show the probability density of the symmetric stretching modes determined from the effective 1D vibrational Hamiltonian (8). Inset shows the three neighboring adiabatic PES of the binding potential, labeled $A - C$. Energies given in GHz relative to the $n = 38$ atomic Rydberg state. (c) Expected intercore electron tunneling (ET) times for the symmetric stretching modes in (b). (d) Vibrational state tunnelling (VT) time of the symmetric stretch modes through the barrier in the adiabatic PES visible in (b).

potential at $n = 38$ is shallower than at $n = 35$ and hence supports fewer vibrationally bound states. Despite this, decay via VT remains relevant only for the highest energy states [see Fig. 6(d)]. Furthermore, the expected ET times $\bar{\tau}_{ET}$ shown in Fig. 6(c) are considerably larger than for $n = 35$. For the vibrational ground state, we predict a time of approximately 500 μs, which is more than three orders of magnitude larger than for the ground state of the $n = 35$ binding potential [cf. Fig. 4(a)]. The nonadiabatic decay rates obtained with the maximum speed of a bound state are similar to those at $n = 35$, while those determined with v_{WKB} are vanishingly small for all decay channels.

In summary, we expect bound states of ^{87}Rb$_3^{2+}$ to become longer-lived at higher n due to the decreasing rate of ET. However, with increasing n the depth of the molecular binding potential decreases such that eventually the rate of VT will become the limiting factor in the stability of the trimer.

V. SUMMARY AND OUTLOOK

We predict the existence of metastable doubly charged molecules formed due to long-range bonding between a single ^{87}Rb* Rydberg atom and two ^{87}Rb$^+$ cations. Although such a system is not expected to be stable in the electronic ground state, we find that above a critical value of n the Rydberg atom acquires a sufficiently large quadrupole moment to counterbalance the Coulomb repulsion between the ion pair, forming GHz-deep binding potentials bearing several vibrationally bound states.

We began by considering the competing interactions within the effectively one-electron ^{87}Rb$_3^{2+}$ system. While the Rydberg electron delocalizes below a critical internuclear separation R_d, for suitably large n the ion-Rydberg interaction is strong enough to mix states in neighboring hydrogenic manifolds at separations $R > R_d$. We found that level repulsion between these states gives rise to a multitude of potential wells deep enough to support three-body bound states in the ultracold regime.

Using a semi classical approach, we assessed the stability of these bound states against nonadiabatic decay as well as charge transfer and Coulomb explosion processes. We found that the rate of charge exchange—modeled by intercore tunneling of the Rydberg electron—is highly sensitive to n. In particular, our model predicts that the rate should decrease by over three orders of magnitude from $n = 35$ to $n = 38$. The sensitivity of the charge exchange rate to n may make such few-body atom-ion systems interesting for the study of controlled charge transport [49,50].

At higher values of n, we found that the decreasing depth of the molecular binding potential leads to an increase in the Coulomb explosion rate. This was modeled by the tunneling of the vibrational states from the molecular binding potential to the dissociative region of the adiabatic PES. Nonetheless, at $n = 38$ we estimate the rates of both charge exchange and Coulomb explosion to be comparable in order of magnitude to the rate of spontaneous emission of the Rydberg state.

Nonadiabatic effects will generally be present in systems such as this due to the high density of electronic states. Regimes with strong vibronic couplings may exhibit conical intersections [34] or spontaneous symmetry breaking [51], the latter of which is unique to polyatomic systems [52]. Investigations of such regimes within the context of similar few-body atom-ion systems are left to future work.

Although the molecular bound states are accessible with two-photon excitation transitions, bringing the three atoms together to photoassociate the molecule poses a unique experimental challenge. Optical tweezer setups may be advantageous for this purpose, since they offer precise control over interparticle separation and can be paired with single-atom laser addressing schemes. Beginning with three trapped neutral atoms in their ground state, one could create a pair of cold free-floating ions using schemes demonstrated in recent experiments [22,33,53] and then immediately drive a Rydberg transition of the remaining atom. The successful formation of the trimer state could be confirmed by an absent or delayed Coulomb explosion. Alternatively, the binding could be verified through mass spectroscopic measurements, similar to the approach already employed for ion-Rydberg dimers [22].

While in this paper, we have limited our discussion to ^{87}Rb Rydberg atoms, we expect similar trimer states to exist for other species of alkali metal given that the electronic state of the trimer is chiefly composed of high angular-momentum Rydberg states with vanishing quantum defects.

Despite the practical challenges in observing these unusual molecules, their existence within the parameter space of an otherwise familiar system once more underscores the rich physics which can emerge from exploring the internal structure of atoms.

APPENDIX A: TRIATOMIC VIBRATIONAL HAMILTONIAN

For a nonrotating triatomic molecule, the vibrational Hamiltonian is given by [56,57]

$$
\begin{aligned}
H_n = \frac{1}{m}\Bigg[& -\frac{\partial^2}{\partial R_1^2} - \frac{\partial^2}{\partial R_2^2} - \cos(\Theta)\frac{\partial}{\partial R_1}\frac{\partial}{\partial R_2} \Bigg] \\
& - \frac{1}{m}\left(\frac{1}{R_1^2} + \frac{1}{R_2^2} - \frac{\cos(\Theta)}{R_1 R_2} \right)\left(\frac{\partial^2}{\partial \Theta^2} + \cot(\Theta)\frac{\partial}{\partial \Theta} \right) \\
& - \frac{1}{m}\left(\frac{1}{R_1 R_2} - \frac{1}{R_2}\frac{\partial}{\partial R_1} - \frac{1}{R_1}\frac{\partial}{\partial R_2} \right) \\
& \times \left(\cos(\Theta) + \sin(\Theta)\frac{\partial}{\partial \Theta} \right) + \varepsilon_\nu(R_1, R_2, \Theta), \quad \text{(A1)}
\end{aligned}
$$

where m is the atomic mass of ^{87}Rb and $\varepsilon_\nu(R_1, R_2, \Theta)$ is the νth adiabatic PES. This Hamiltonian acts on wave functions $\chi(R_1, R_2, \Theta)$ normalized as $\int dR_1 dR_2 d\Theta \sin\Theta |\chi(R_1, R_2, \Theta)|^2 = 1$.

APPENDIX B: COMPARING VIBRATIONAL EIGENENERGIES

Table I compares the energies of the first five symmetric stretching excitations obtained with the full 3D vibrational Hamiltonian (A1) and the 1D effective model (8).

TABLE I. Comparison of energies of the first five symmetric stretching eigenstates (including the ground state) of the ^{87}Rb$_3^{2+}$ system obtained with the full (3D) and effective (1D) models. Values are given in GHz to two decimal places.

ν	3D model (A1)	1D model (8)	Absolute difference
0	414.67	413.81	0.86
1	414.81	414.12	0.69
2	414.94	414.41	0.54
3	415.07	414.68	0.54
4	415.20	414.68	0.39

APPENDIX C: SEMICLASSICAL TUNNELING MODEL

The probability for a wave packet of mass m with energy ϵ to tunnel through a 1D barrier $V(z)$ is given in the WKB approach [45,58] by

$$P = \exp\left[-2\sqrt{2m}\int_{z_1}^{z_2} dz\sqrt{V(z) - \epsilon}\right]. \qquad \text{(C1)}$$

The limits of the integral z_1 and z_2 are the inner and outer classical turning points of the barrier, such that $\epsilon = V(z_1) = V(z_2)$.

For estimating the tunneling of the νth vibrationally bound state out of the binding potential (VT), m is given by the reduced mass of a ^{87}Rb pair and $\epsilon = E_\nu$, which corresponds to the energy of the vibrationally bound state determined from the symmetric stretching Hamiltonian (8). The potential V is provided by the adiabatic PEC describing the binding potential, $\varepsilon(R)$. Inserting these quantities into Eq. (C1) and relabelling $z \to R$ gives a vibrational state tunneling probability of

$$P_{\mathrm{VT}} = \exp\left[-2\sqrt{2m}\int_{R_1}^{R_2} dR\sqrt{\varepsilon(R) - E_\nu}\right], \qquad \text{(C2)}$$

where R_1 and R_2 are defined as the inner and outer classical turning points of the barrier in the adiabatic PEC $\varepsilon(R)$ [see, e.g., Fig. 2(b)].

To describe inter-core electron tunnelling (ET), m is the Rydberg electron's mass $m_e = 1$ and ϵ is defined by the R-dependent adiabatic PEC $\varepsilon(R)$ shown in Figs. 2(b) and 6(b). The barrier V is given by the net potential experienced by the Rydberg electron, which is the sum of all Coulomb interactions in the system: $V(\mathbf{r}; R) = -1/|\mathbf{r}| - 1/|\mathbf{r} + \mathbf{R}| - 1/|\mathbf{r} - \mathbf{R}| + 5/2|\mathbf{R}|$. Here, we assume the nuclei are arranged in a symmetric linear configuration, with cations positioned at $\mathbf{R}_1 = (R, 0, 0)$ and $\mathbf{R}_2 = (R, \pi, 0)$ relative to the Rydberg core. This yields an electron tunneling probability of

$$P_{\mathrm{ET}} = \exp\left[-2\sqrt{2}\int_{z_1}^{z_2} dz\sqrt{V(z; R) - \varepsilon(R)}\right]. \qquad \text{(C3)}$$

Here we assume that the motion of the Rydberg electron is restricted along z. z_1 and z_2 are turning points of Rydberg electron in the Coulomb potential [see inset of Fig. 1(b)].
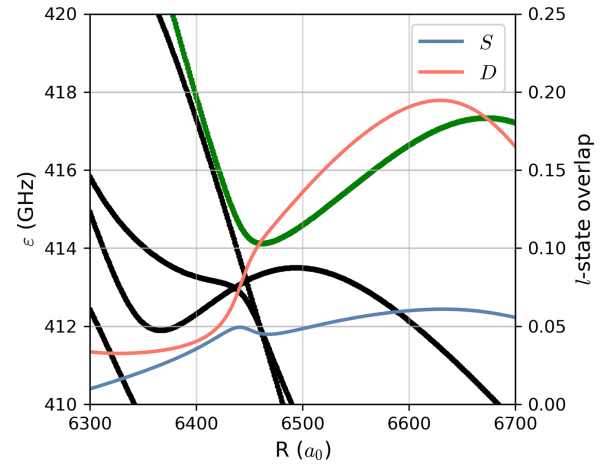

FIG. 7. Adiabatic PES near the $n = 35$ hydrogenic manifold. The secondary axis shows the overlap of the electronic state of the binding potential (green) with S- and D-state atomic Rydberg states.

The ET rate γ_{ET} is then determined by multiplying the result of (C3) with the Kepler frequency of the Rydberg electron's orbit $f = 1/T$, where T is the orbital period. For $n = 35$, we find $f \sim 10^9$ Hz.

APPENDIX D: LOW-l CHARACTER OF ^{87}Rb$_3^{2+}$

We see from Fig. 7 that the electronic state of the ^{87}Rb$_3^{2+}$ binding potential exhibits significant overlap with low angular momentum states (S and D states).

For the symmetric linear configuration considered in Fig. 7 ($R_1 = R_2 = R$), there is a vanishing contribution from P states due to the fact that the leading-order term is a charge-quadrupole interaction. Due to Clebsch-Gordon selection rules, Rydberg states with angular momentum differing only by one are not coupled by such interactions such that the parity of the angular momentum character of the electronic states is preserved. Away from this highly symmetric case, however, parity symmetry is broken.

[1] E. Herbst, S. Miller, T. Oka, J. K.G. Watson, and E. Herbst, The astrochemistry of H$_3^+$, Philos. Transact. A Math. Phys. Eng. Sci. **358**, 2523 (2000).

[2] S. Petrie and D. K. Bohme, Ions in space, Mass Spectrom. Rev. **26**, 258 (2007).

[3] S. Falcinelli and M. Rosi, Production and characterization of molecular dications: Experimental and theoretical efforts, Molecules **25**, 4157 (2020).

[4] C. A. Nicolaides, Energy generation from volcanic ground states. Application to cold He$_2^{2+}$, Chem. Phys. Lett. **161**, 547 (1989).

[5] R. Côté, V. Kharchenko, and M. D. Lukin, Mesoscopic molecular ions in Bose-Einstein condensates, Phys. Rev. Lett. **89**, 093001 (2002).

[6] J. M. Schurer, P. Schmelcher, and A. Negretti, Ground-state properties of ultracold trapped bosons with an immersed ionic impurity, Phys. Rev. A **90**, 033601 (2014).

[7] J. M. Schurer, A. Negretti, and P. Schmelcher, Unraveling the structure of ultracold mesoscopic collinear molecular ions, Phys. Rev. Lett. **119**, 063001 (2017).

[8] R. Côté, From classical mobility to hopping conductivity: Charge hopping in an ultracold gas, Phys. Rev. Lett. **85**, 5316 (2000).

[9] B. Gao, Universal properties in ultracold ion-atom interactions, Phys. Rev. Lett. **104**, 213201 (2010).

[10] Z. Idziaszek, T. Calarco, P. S. Julienne, and A. Simoni, Quantum theory of ultracold atom-ion collisions, Phys. Rev. A **79**, 010702(R) (2009).

[11] D. J. Bosworth, M. Pyzh, and P. Schmelcher, Spectral properties of a three-body atom-ion hybrid system, Phys. Rev. A **103**, 033303 (2021).

[12] F. H. J. Hall, M. Aymar, N. Bouloufa-Maafa, O. Dulieu, and S. Willitsch, Light-assisted ion-neutral reactive processes in the cold regime: Radiative molecule formation versus charge exchange, Phys. Rev. Lett. **107**, 243202 (2011).

[13] S. T. Sullivan, W. G. Rellergert, S. Kotochigova, K. Chen, S. J. Schowalter, and E. R. Hudson, Trapping molecular ions formed via photo-associative ionization of ultracold atoms, Phys. Chem. Chem. Phys. **13**, 18859 (2011).

[14] X. Tong, A. H. Winney, and S. Willitsch, Sympathetic cooling of molecular ions in selected rotational and vibrational states produced by threshold photoionization, Phys. Rev. Lett. **105**, 143001 (2010).

[15] S. Jyothi, T. Ray, S. Dutta, A. R. Allouche, R. Vexiau, O. Dulieu, and S. A. Rangwala, Photodissociation of trapped Rb_2^+: Implications for simultaneous trapping of atoms and molecular ions, Phys. Rev. Lett. **117**, 213002 (2016).

[16] M. Pinkas, O. Katz, J. Wengrowicz, N. Akerman, and R. Ozeri, Trap-assisted formation of atom–ion bound states, Nat. Phys. **19**, 1573 (2023).

[17] P. Weckesser, F. Thielemann, D. Wiater, A. Wojciechowska, L. Karpa, K. Jachymski, M. Tomza, T. Walker, and T. Schaetz, Observation of Feshbach resonances between a single ion and ultracold atoms, Nature (London) **600**, 429 (2021).

[18] F. Thielemann, J. Siemund, D. von Schoenfeld, W. Wu, P. Weckesser, K. Jachymski, T. Walker, and T. Schaetz, Exploring atom-ion Feshbach resonances below the *s*-wave limit, arXiv:2406.13410.

[19] T. Köhler, K. Góral, and P. S. Julienne, Production of cold molecules via magnetically tunable Feshbach resonances, Rev. Mod. Phys. **78**, 1311 (2006).

[20] A. Duspayev, X. Han, M. A. Viray, L. Ma, J. Zhao, and G. Raithel, Long-range Rydberg-atom–ion molecules of Rb and Cs, Phys. Rev. Res. **3**, 023114 (2021).

[21] M. Deiß, S. Haze, and J. Hecker Denschlag, Long-range atom–ion Rydberg molecule: A novel molecular binding mechanism, Atoms **9**, 34 (2021).

[22] N. Zuber, V. S. V. Anasuri, M. Berngruber, Y.-Q. Zou, F. Meinert, R. Löw, and T. Pfau, Observation of a molecular bond between ions and Rydberg atoms, Nature (London) **605**, 453 (2022).

[23] C. H. Greene, A. S. Dickinson, and H. R. Sadeghpour, Creation of polar and nonpolar ultra-long-range Rydberg molecules, Phys. Rev. Lett. **85**, 2458 (2000).

[24] V. Bendkowsky, B. Butscher, J. Nipper, J. P. Shaffer, R. Löw, and T. Pfau, Observation of ultralong-range Rydberg molecules, Nature (London) **458**, 1005 (2009).

[25] C. Fey, F. Hummel, and P. Schmelcher, Ultralong-range Rydberg molecules, Mol. Phys. **118**, e1679401 (2020).

[26] H. Saßmannshausen, J. Deiglmayr, and F. Merkt, Long-range Rydberg molecules, Rydberg macrodimers and Rydberg aggregates in an ultracold Cs gas, Eur. Phys. J. Spec. Top. **225**, 2891 (2016).

[27] S. Hollerith and J. Zeiher, Rydberg macrodimers: Diatomic molecules on the micrometer scale, J. Phys. Chem. A **127**, 3925 (2023).

[28] R. Schmidt, H. R. Sadeghpour, and E. Demler, Mesoscopic Rydberg impurity in an atomic quantum gas, Phys. Rev. Lett. **116**, 105302 (2016).

[29] R. Schmidt, J. D. Whalen, R. Ding, F. Camargo, G. Woehl, S. Yoshida, J. Burgdörfer, F. B. Dunning, E. Demler, H. R. Sadeghpour, and T. C. Killian, Theory of excitation of Rydberg polarons in an atomic quantum gas, Phys. Rev. A **97**, 022707 (2018).

[30] S. T. Rittenhouse and H. R. Sadeghpour, Ultracold giant polyatomic Rydberg molecules: Coherent control of molecular orientation, Phys. Rev. Lett. **104**, 243002 (2010).

[31] R. González-Férez, H. R. Sadeghpour, and P. Schmelcher, Rotational hybridization, and control of alignment and orientation in triatomic ultralong-range Rydberg molecules, New J. Phys. **17**, 013021 (2015).

[32] Y.-Q. Zou, M. Berngruber, V. S. V. Anasuri, N. Zuber, F. Meinert, R. Löw, and T. Pfau, Observation of vibrational dynamics of orientated Rydberg-atom-ion molecules, Phys. Rev. Lett. **130**, 023002 (2023).

[33] M. Berngruber, D. J. Bosworth, O. A. Herrera-Sancho, V. S. V. Anasuri, N. Zuber, F. Hummel, J. Krauter, F. Meinert, R. Löw, P. Schmelcher, and T. Pfau, In situ observation of nonpolar to strongly polar atom-ion collision dynamics, Phys. Rev. Lett. **133**, 083001 (2024).

[34] F. Hummel, M. T. Eiles, and P. Schmelcher, Synthetic dimension-induced conical intersections in Rydberg molecules, Phys. Rev. Lett. **127**, 023003 (2021).

[35] F. Hummel, P. Schmelcher, and M. T. Eiles, Vibronic interactions in trilobite and butterfly Rydberg molecules, Phys. Rev. Res. **5**, 013114 (2023).

[36] R. Srikumar, F. Hummel, and P. Schmelcher, Nonadiabatic interaction effects in the spectra of ultralong-range Rydberg molecules, Phys. Rev. A **108**, 012809 (2023).

[37] M. T. Eiles and F. Hummel, Kato's theorem and ultralong-range Rydberg molecules, Phys. Rev. A **109**, 022811 (2024).

[38] Quantum defect states guarantee significant avoided crossings between potential energy surfaces in the electronic structure. The quantum defect parameters for rubidium have been reported in Refs. [54,55].

[39] T. F. Gallagher, *Rydberg Atoms*, Cambridge Monographs on Atomic, Molecular and Chemical Physics (Cambridge University Press, Cambridge, UK, 1994).

[40] M. T Eiles, Trilobites, butterflies, and other exotic specimens of long-range Rydberg molecules, J. Phys. B: At. Mol. Opt. Phys. **52**, 113001 (2019).

[41] R. J. Le Roy, Long-range potential coefficients from RKR turning points: C6 and C8 for $B(3\Pi_{Ou}^+)$-state Cl_2, Br_2, and I_2, Can. J. Phys. **52**, 246 (1974).

[42] J. D. Jackson, *Classical Electrodynamics*, 3rd ed. (John Wiley & Sons, Hoboken, NJ, 1998).

[43] A. Duspayev and G. Raithel, Nonadiabatic decay of Rydberg-atom–ion molecules, Phys. Rev. A **105**, 012810 (2022).

[44] D. J. Bosworth, F. Hummel, and P. Schmelcher, Charged ultralong-range Rydberg trimers, Phys. Rev. A **107**, 022807 (2023).

[45] H. Friedrich, *Theoretical Atomic Physics*, 4th ed. (Springer International Publishing AG, 2017).

[46] D. R. Inglis and E. Teller, Ionic depression of series limits in one-electron spectra, Astrophys. J. **90**, 439 (1939).

[47] R. J. LeVeque, *Finite Difference Methods for Ordinary and Partial Differential Equations* (Society for Industrial and Applied Mathematics, Philadelphia, PA, 2007).

[48] C. Zener and R. H. Fowler, Non-adiabatic crossing of energy levels, Proc. R. Soc. London A **137**, 696 (1932).

[49] R. Mukherjee, Charge dynamics of a molecular ion immersed in a Rydberg-dressed atomic lattice gas, Phys. Rev. A **100**, 013403 (2019).

[50] A. Pandey, R. Vexiau, L. G. Marcassa, O. Dulieu, and N. Bouloufa-Maafa, Ultracold charged atom-dimer collisions: State-selective charge exchange and three-body recombination, arXiv:2407.14824.

[51] A. Becker, G. M. Koutentakis, and P. Schmelcher, Synthetic dimension-induced pseudo Jahn-Teller effect in one-dimensional confined fermions, Phys. Rev. Res. **6**, 013257 (2024).

[52] I. B. Bersuker, Jahn–Teller and pseudo-Jahn–Teller Effects: From particular features to general tools in exploring molecular and solid state properties, Chem. Rev. **121**, 1463 (2021).

[53] T. Dieterle, M. Berngruber, C. Hölzl, R. Löw, K. Jachymski, T. Pfau, and F. Meinert, Transport of a single cold ion immersed in a Bose-Einstein condensate, Phys. Rev. Lett. **126**, 033401 (2021).

[54] W. Li, I. Mourachko, M. W. Noel, and T. F. Gallagher, Millimeter-wave spectroscopy of cold Rb Rydberg atoms in a magneto-optical trap: Quantum defects of the Ns, Np, and Nd series, Phys. Rev. A **67**, 052502 (2003).

[55] J. Han, Y. Jamil, D. V. L. Norum, P. J. Tanner, and T. F. Gallagher, Rb nf quantum defects from millimeter-wave spectroscopy of cold ^{85}Rb Rydberg atoms, Phys. Rev. A **74**, 054502 (2006).

[56] S. Carter and N.C. Handy, A variational method for the calculation of vibrational levels of any triatomic molecule, Mol. Phys. **47**, 1445 (1982).

[57] N.C. Handy, The derivation of vibration-rotation kinetic energy operators, in internal coordinates, Mol. Phys. **61**, 207 (1987).

[58] D. J. Griffiths and D. F. Schroeter, *Introduction to Quantum Mechanics*, 3rd ed. (Cambridge University Press, Cambridge, UK, 2018).

Chapter 6

Summary and outlook

In this thesis, we have explored atom-ion interactions in ultracold few-body systems, combining ideas from across the fields of neutral quantum gases, (un)trapped ions and Rydberg physics. We discussed the broader development of these areas over the past decades, focusing in particular on the increasing interconnection between them in the last ten to twenty years. This growing interdependence is best encapsulated by the pursuit of ultracold hybrid atom-ion systems, which aim to integrate both charged particles and ultracold quantum gases within a single controlled experimental setup. In future, these systems will serve as novel platforms for quantum information processing and simulation, as well as for explorations of charge-neutral chemistry. Along the way to this goal, interest in the use of Rydberg-state atoms has developed. Rydberg atoms not only facilitate long-range atom-ion entanglement, they also form macroscopic atom-ion bound states. These states exhibit characteristically slow vibrational dynamics, offering a new approach to studying fundamental chemical processes in "slow-motion".

We have presented several scientific contributions in which we investigated static and dynamical behaviours of various few-body systems exhibiting long-range atom-ion interactions. We focused on the interaction of ions with atoms in their electronic ground-state as well as atoms in excited Rydberg states. In this way, we explored interactions on both mesoscopic and macroscopic length scales. Broadly speaking, the goals of our research fell into three categories. Firstly, we sought to understand the interplay of the atom-ion interaction with different competing interactions, such as the van der Waals' interaction between neutral atoms [SC1], the scattering between ground-state atoms and Rydberg electrons [SC2] and the Coulomb repulsion between pairs of cations [SC5]. Our second point of focus was quantum control, which we explored through the use of external drives [SC3] and through influencing the non-adiabatic couplings between collision channels by tuning experimental control parameters [SC4]. The final goal of this thesis was the search for stability in exotic few-body Rydberg systems, where we predicted the formation of ultralong-range trimer states of $^{87}\text{Rb}_3^+$ [SC2] and $^{87}\text{Rb}_3^{2+}$ [SC5]. In what follows, we briefly recount each scientific contribution and discuss possible directions for future work.

In our first work [SC1], we employed the numerical method ML-MCTDHB in order to characterise the low-energy eigenstates of an ion interacting with a pair of bosonic atoms in a quasi-1D system. Studying such few-body quantum systems can prove valuable since they are simpler to treat than many-body systems, yet may still exhibit rich behaviours with implications for fundamental physics and quantum applications. An exciting perspective for this work would be to explore systems with greater numbers of particles. On the one hand, considering many atoms interacting with a single ion would enable the simulation of charged polarons [77, 78] or dissipative properties of ions immersed in degenerate quantum gases [364]. On the other hand, considering multiple ions would be of interest for simulating condensed matter systems. For example, studying chains of ions with state-dependent interactions would enable the investigation of spin-phonon coupling, which was recently proposed as a platform for engineering

strong non-adiabatic couplings [365]. Additionally, ML-MCTDH could be used for exploring charge exchange in systems analogous to the $^{87}Rb_3^{2+}$ complex studied in our work [SC5]. The recent extension of ML-MCTDH to spin systems [177] presents a further opportunity for simulating arrays of trapped atoms and ions. Here, the competition between charge-neutral and neutral-neutral interactions may give rise to rich phase diagrams, similar to those emerging in lattice systems exhibiting resonant and non-resonant dipole couplings [366].

The work [SC3] considered the impact of an externally-dragged ion on a gas of trapped atoms and explored how such mobile impurities can be used to selectively transfer atoms between vibrational trap states. Whilst fine control over quantum states is a fundamental prerequisite for realising any quantum technology, the ability to move quantum states between different vibrational trap states further allows researchers to simulate and study complex quantum phenomena, leading to a deeper understanding of many-body physics, condensed matter systems, and chemical reactions. In our work, we found that the presence of the ion leads to resonances in the vibrational spectrum of the trapped atoms which are reminiscent of trap-induced shape resonances arising in collisions between atoms in separate traps [367]. Such resonances have been used recently to perform "mergoassociation" of ultracold RbCs molecules from individual Rb and Cs atoms initially prepared in separate traps [368]. Inspired by this striking result, we could extend the state preparation protocols in [SC3] for the purpose of preparing polyatomic molecular ions [75] or even ULRM. In the latter case, mergoassociation may provide an alternative approach for associating molecular states that cannot be accessed with dipole-allowed transitions, such as polar ULRM with predominantly high angular momentum character [235, 369–371]. Furthermore, bypassing the restrictions of dipole-allowed transitions may be possible using angular momentum-carrying light [372]. Proposals already exist for using this twisted light for the photoexcitation of circular Rydberg atomic states [373] and for enhancing certain forbidden rovibrational transitions in diatomic molecules [374]. Future work could thus explore similar schemes for associating ULRM.

In [SC4], we developed a semi-classical model for the multi-channel molecular dynamics of ion-Rydberg pairs, complementing *in situ* experimental observations of collisions between these species near the Rydberg *S*-state. Studying collisions provides understanding about a broad range of phenomena, such as thermalisation [350], the catalysis of chemical reactions through enzymes [351] and properties of plasmas [352]. By virtue of their microsecond-scale vibrational dynamics, ion-Rydberg systems offer a unique opportunity to study molecular dynamics without the need for ultrafast pulses [375]. Furthermore, the high density of electronic states and potential for tunability through the principal quantum number mean that Rydberg molecular systems are an excellent platform for exploring physics beyond the BO approximation, which plays a key role in many important biochemical processes in nature [376]. For the system considered in [SC4], the collisional dynamics unfolds over a landscape of multiple collision channels whose characteristic shape mean that initially-slow pairs have a paradoxically greater probability of following fast collision channels. Future extensions of this work could explore ion-Rydberg pair dynamics in different regions of the Rydberg energy spectrum, such as in the binding potential associated with the Rydberg *P*-state in alkali metals [95]. Beyond this, we could explore dynamics in more exotic regimes, such as around conical intersections between adiabatic PES which can already emerge in diatomic systems with the help of Rydberg synthetic dimensions [258, 260]. Furthermore, we could explore optical dressing for the purpose of engineering non-adiabatic couplings in Rydberg systems, leading for example to the emergence of light-induced conical intersections [377, 378].

The remaining scientific contributions [SC2, SC5] focused on stability in three-body systems involving a Rydberg atom and one or more ions, leading to the prediction of long-range triatomic molecular ions. Few-body molecular ions are attractive to work with, since they are simpler to describe than more complex

molecules. They also play a crucial role in many processes throughout nature, such as in the chemistry of the interstellar medium [285] and are further believed to have contributed significantly to the chemistry of the early Universe [379]. Most importantly, our works [SC2, SC5] highlight the rich physics which can emerge within otherwise familiar systems when the atomic structure is treated as another degree of freedom of the system. Rydberg molecules such as these may attract interest in future for studies of fundamental chemical processes, such as observing charge transport [380]. They are also natural systems for exploring singular vibronic couplings [258] and spontaneous symmetry-breaking via the so-called Jahn-Teller effect [173, 381]. Future work may also consider triatomic systems in different regions of the parameter space. For example, the $^{87}\text{Rb}_3^+$ system could be used to study the interaction of ULRM with the inhomogeneous electric field of a distant ion, complementing earlier studies of Rydberg molecules in homogeneous electric fields [174, 382, 383] and providing a novel setup for the study of bound states between charged particles and polar molecules [353–357].

Another avenue could be opened up by exploring few-body systems with multiple Rydberg excitations. This may be particularly interesting for mixtures of different atomic species pairings, such as Rb-Li. As described in appendix B, Li Rydberg atoms differ from Rb and Cs in that their binding potential with the ion is connected asymptotically with the atomic *S*-state instead of the atomic *P*-state. A system of Li and Rb Rydberg atoms interacting with an ion may therefore exhibit strong resonant dipole couplings between the two Rydberg state atoms. It would thus be interesting to explore the competition of this Rydberg-Rydberg interaction with the ion-Rydberg interaction. Finally, one could also consider ion-Rydberg systems involving negatively-charged ions. We show in appendix B that the sign of the ion's charge can lead to dramatic changes in the strength of the non-adiabatic couplings in the system, which would impact the lifetime of molecular states as well as the nature of the vibrational dynamics.

In summary, this thesis has contributed to the understanding of interactions between charged and neutral species across different length scales. Charge-neutral interactions underpin many important processes in nature and developing understanding about the interactions between these species in a few-body context is the first necessary step in learning how to exploit them on a larger scale. A notable example of this is that the insight which led to proposals of the Rydberg blockade mechanism [210] came from a well-developed understanding about interatomic interactions between pairs of Rydberg atoms. Thus, detailed knowledge of the two-body problem resulted in a reliable method of controlling collective excitations in many-body systems, which underpins the modern success of neutral atom quantum computing platforms.

There is no doubt that experiments with hybrid atom-ion systems have exciting years ahead of them. Experimentalists are closing-in on the ultracold temperatures needed to study mixtures of atoms and ions in the *s*-wave scattering regime [83–86], which will open up an entirely new paradigm for quantum simulation and information. It may even be possible to produce optical tweezer arrays of both atoms and ions, with the same degree of single-particle control which is currently enjoyed by neutral atom tweezer arrays today. These can then be further combined with Rydberg dressing for additional flexibility [48, 384, 385]. Ultracold atom-ion systems will further serve as testbeds for exploring charge-neutral chemistry, which may help shed light on, among other questions, the role of simple molecular ions such as H_2^+ in reactions taking place in the interstellar medium [285]. Moreover, precision spectroscopy with ultracold molecular systems can be used for studying the Standard Model and its limitations [2, 386, 387].

Since the recent observation of atom-ion Feshbach resonances [84, 85], the onus is also now on theorists to develop a deeper quantitative understanding of short-range atom-ion interactions and three-body processes. This is a challenging task, given the comparatively high density of atom-ion bound states and current lack of information about atom-ion scattering lengths. Developing a rigorous theoretical

framework would contribute to using Feshbach resonances for precise control over atom-ion interactions and the magnetoassociation of molecular ions in well-controlled states, facilitating state-resolved chemistry [388].

Finally, Rydberg physics – with or without ions – also has a promising future. Macroscopic-sized Rydberg molecules are a testbed for explorations of physics beyond the BO approximation [103, 258–260] and other exotic phenomena, such as Borromean states [237, 238]. Rydberg platforms continue to be a powerful driving force for quantum simulation [48], helping to shed light on complex many-body behaviours. Outside of the ultracold regime, Rydberg physics can be explored in solid state systems through the excited states of electron-hole pairs [180]. Additionally, coherent Rydberg excitations inside thermal vapour cells [389] show great promise as both single-photon sources [390] and radiofrequency sensors [391]. Indeed, Rydberg field sensing technologies are already available to buy [392], making them one of first commercially-available quantum technologies.

Appendix A

Long-range Rydberg – Rydberg interactions

In this appendix, we specify further details about the long-range interaction between pairs of Rydberg atoms and present some analytical results for coupling matrix elements between different Rydberg states due to this interaction.

As discussed in section 3.2.1, the net interaction between a pair of Rydberg atoms with an internuclear separation R exceeding the Le Roy radius [261] is given by [266]:

$$\hat{V} = \sum_{\lambda_1,\lambda_2=1}^{\infty} \frac{\hat{V}_{\lambda_1,\lambda_2}}{R^{\lambda_1+\lambda_2+1}}. \tag{A.1}$$

The interaction terms appearing in the multipole expansion (A.1) $\hat{V}_{\lambda_1,\lambda_2}$ are defined as:

$$\hat{V}_{\lambda_1,\lambda_2} = (-1)^{\lambda_2} \sum_{\mu=-\lambda_<}^{\lambda_<} c_{\lambda_1,\lambda_2,\mu}\, \hat{p}_{\lambda_1,\mu}^{(1)} \cdot \hat{p}_{\lambda_2,-\mu}^{(2)} \quad, \tag{A.2}$$

where $\lambda_< = \min(\lambda_1,\lambda_2)$, $\hat{p}_{\lambda_i,\mu}^{(i)} = \hat{r}_i^{\lambda_i} \cdot Y_{\lambda_i,\mu}(\theta,\phi)$ are multipole operators and $c_{\lambda_1,\lambda_2,\mu}$ are coefficients:

$$c_{\lambda_1,\lambda_2,\mu} = \sqrt{\frac{4\pi}{2\lambda_1+1}}\sqrt{\frac{4\pi}{2\lambda_2+1}}\sqrt{\binom{\lambda_1+\lambda_2}{\lambda_1+\mu}\cdot\binom{\lambda_1+\lambda_2}{\lambda_2+\mu}}. \tag{A.3}$$

We now discuss some general results for matrix elements of the operator $\hat{p}_{\lambda_i,\mu}^{(i)}$ represented in a basis of atomic Rydberg states $\{\psi_{nlm}(\mathbf{r})\}$ describing alkali metal atoms. Alkali metals are conceptually simpler to treat than other kinds of elements since they posses only a single valence electron. The wavefunction of a Rydberg-state alkali metal atom $\psi_{nlm}(\mathbf{r})$ is an eigenfunction of the time-independent Schrödinger equation:

$$\left[-\frac{1}{2}\nabla^2 + V(r)\right]\psi_{nlm}(\mathbf{r}) = \varepsilon\,\psi_{nlm}(\mathbf{r}). \tag{A.4}$$

$V(r)$ is a spherically-symmetric model potential which for large r is well-approximated by the Coulomb potential $1/r$ but includes corrections due to the presence of the core-shell electrons at small r close to the atomic nucleus [127, 192]. The Rydberg wavefunction $\psi_{nlm}(\mathbf{r})$ is represented in spherical coordinates as:

$$\psi_{nlm}(\mathbf{r}) = \frac{u_{nl}(r)}{r}Y_{lm}(\theta,\phi), \tag{A.5}$$

where $Y_{lm}(\theta, \phi)$ are spherical harmonics. The Rydberg wavefunction is normalised as:

$$\langle \psi_{n'l'm'} | \psi_{nlm} \rangle = \int dr d\theta d\phi \, r^2 \sin\theta \, \psi_{n'l'm'}^*(\mathbf{r}) \psi_{nlm}(\mathbf{r}) = \delta_{l'l} \delta_{m'm}. \tag{A.6}$$

The matrix element $\langle \psi_{n'l'm'} | r^\lambda Y_{\lambda\mu}(\theta, \phi) | \psi_{nlm} \rangle$ is determined by evaluating the following integrals over the radial and angular degrees of freedom of the Rydberg electron:

$$I_r = \int dr \, u_{n'l'}^*(r) \, r^\lambda \, u_{nl}(r), \tag{A.7}$$

$$I_\Omega = \int d\Omega \, Y_{l'm'}^*(\Omega) Y_{\lambda\mu}(\Omega) Y_{lm}(\Omega). \tag{A.8}$$

Where $\Omega = (\theta, \phi)$ defines the solid angle with $d\Omega = d\theta d\phi \sin\theta$. If $u_{nl}(r)$ are Coulombic functions (i.e. states with negligible quantum defect), then (A.7) may be solved analytically [383]:

$$\begin{aligned}
I_r = & \frac{2^{l+l'+2}}{n^{l+2}n'^{l'+2}} \sqrt{\frac{(n-l-1)!(n'-l'-1)!}{(n+l)!(n'+l')!}} \\
& \times \sum_{m=0}^{n-l-1} \sum_{m'=0}^{n'-l'-1} \frac{(-2)^{m+m'}}{m!m'!n^m n'^{m'}} \binom{n+l}{n-l-m-1} \\
& \times \binom{n'+l'}{n'-l'-m'-1} (\lambda+m+m'+l+l'+2)! \\
& \times \left[\frac{nn'}{n+n'} \right]^{\lambda+m+m'+l+l'+3}.
\end{aligned} \tag{A.9}$$

However, for quantum defect states [276], I_r must be determined through numerical integration [266]. In contrast, the integral of the angular components (A.8) always has an analytical solution [127]:

$$I_\Omega = \left[\frac{(2l+1)(2\lambda+1)}{4\pi(2l'+1)} \right]^{1/2} \langle l', m' | \lambda, \mu, l, m \rangle \langle l', 0 | \lambda, 0, l, 0 \rangle. \tag{A.10}$$

The above inner products are complex conjugates of Clebsch-Gordan (CG) coefficients. Formally, CG coefficients are defined as $C_{l_1,m_2,l_2,m_2}^{L,M} = \langle l_1, m_1, l_2, m_2 | L, M \rangle$ and $[C_{l_1,m_2,l_2,m_2}^{L,M}]^* = \langle L, M | l_1, m_1, l_2, m_2 \rangle$. These CG coefficients impose restrictions on the values of the numbers $(l', m', \lambda, \mu, l, m)$ appearing in the integral (A.10). Specifically, the coefficient $\langle l_1, m_1, l_2, m_2 | L, M \rangle$ is only non-zero when the following three conditions are fulfilled:

1. $m_1 + m_2 = M$,

2. $|l_1 - l_2| \leq L \leq l_1 + l_2$,

3. $J = l_1 + l_2 + L$ is an even integer.

Appendix B

Long-range ion – Rydberg interactions

In this appendix, we provide further details about the interaction between an ion and a Rydberg atom in the asymptotic limit, including a derivation of the multipole expansion of the interaction in this regime. Furthermore, we discuss the impact of the sign of the ion's charge on the adiabatic PEC, which leads to changes in the size of the energy gap at avoided crossings between neighbouring PEC. As a result of this, we predict the formation of bound states between a Rydberg atom and an anion located in PEC associated asymptotically with the Rydberg D-state. In addition, we present adiabatic PEC for a ^{7}Li Rydberg atom interacting with a ^{7}Li$^+$, revealing long-range bound states in binding potentials connected asymptotically to the Rydberg S-state.

Derivation of the long-range ion-Rydberg interaction term

We consider a Rydberg atom interacting with a single positively-charged ion at internuclear separations exceeding the Le Roy radius [261]. Under such conditions, there is vanishing overlap between the charge distributions of the Rydberg atom and the ion, such that the exchange interaction between their electrons can be neglected. The net ion-Rydberg interaction is then described by the sum of the Coulomb interactions between the different charges in the system:

$$\hat{V} = \frac{1}{|\mathbf{R}|} - \frac{1}{|\mathbf{r} - \mathbf{R}|}.$$

(B.1)

The first term represents the repulsion between the Rydberg core and the ion with internuclear separation $\mathbf{R}$ and the second term describes the attractive interaction between the Rydberg electron at position $\mathbf{r}$ and the ion. In what follows, we describe how to expand the interaction (B.1) in terms of multipole operators [SC2, 92, 93].

Taking $\mathbf{r} = (r, \theta, \phi)$ and $\mathbf{R} = (R, \Theta, \Phi)$, we first rewrite equation (B.1) as:

$$\hat{V} = \frac{1}{|\mathbf{R}|} \left(1 - \frac{1}{\sqrt{1 + h^2 - 2h\cos\alpha}} \right),$$

(B.2)

where $h = |\mathbf{r}|/|\mathbf{R}|$ and α is the angle subtended by $\mathbf{r}$ and $\mathbf{R}$. The second term in (B.2) can be expressed in terms of Legendre polynomials $P_\lambda(\cos\alpha)$ as:

$$\frac{1}{\sqrt{1 + h^2 - 2h\cos\alpha}} = 1 + \sum_{\lambda=1}^{\infty} h^\lambda P_\lambda(\cos\alpha),$$

(B.3)
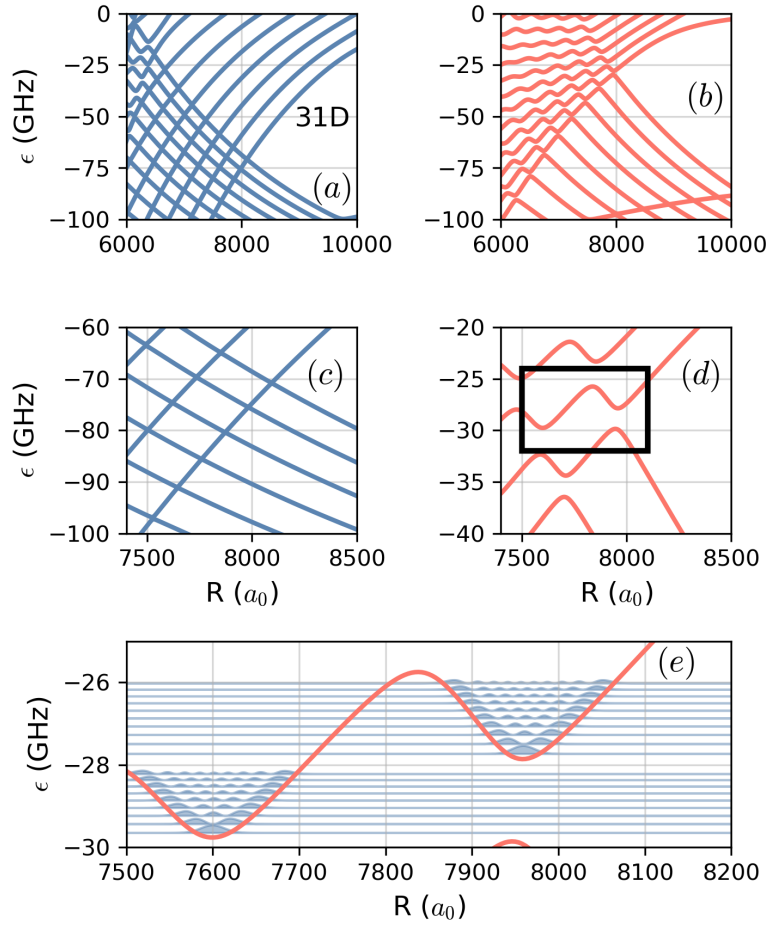
FIGURE B.1: Adiabatic PEC of an ^{87}Rb Rydberg atom interacting with (a),(c) ^{87}Rb$^+$ (b),(d) ^{87}Rb$^-$ near the $|31D\rangle$ atomic Rydberg state. (e) Magnification of the region marked by the black box in (d) showing vibrationally-bound states supported by potential wells formed between the $|31D\rangle$ state and low-field seeking high-l states. Energies are given in GHz relative to the $|31D\rangle$ atomic Rydberg state.

where we have used the fact that $P_0(\cos\alpha) = 1$. The spherical law of cosines further allows us to write $\cos\alpha = \cos\theta\cos\Theta + \sin\theta\sin\Theta\cos(\phi - \Phi)$. Using the spherical harmonic addition theorem [393], we then find:

$$P_\lambda(\cos\alpha) = \frac{4\pi}{2\lambda + 1} \sum_{\mu=-\lambda}^{\lambda} Y_{\lambda\mu}(\theta,\phi)Y_{\lambda\mu}^*(\Theta,\Phi), \tag{B.4}$$

where $Y_{\lambda\mu}$ are spherical harmonics. Inserting (B.3) and (B.4) into equation (B.2), we arrive at the most general form of the interaction between a Rydberg atom and a positive ion in the long-range limit:

$$V(\mathbf{R}) = -\sum_{\lambda=1}^{\infty} \sum_{\mu=-\lambda}^{+\lambda} \frac{4\pi}{2\lambda + 1} \frac{r^\lambda}{R^{\lambda+1}} Y_{\lambda\mu}(\theta,\phi)Y_{\lambda\mu}^*(\Theta,\Phi). \tag{B.5}$$

This may be further simplified by choosing $\mathbf{R} = (R,0,0)$:

$$V_{\Theta=0}(R) = -\sum_{\lambda=1}^{\infty} \sqrt{\frac{4\pi}{2\lambda + 1}} \frac{r^\lambda}{R^{\lambda+1}} Y_{\lambda 0}(\theta,\phi), \tag{B.6}$$
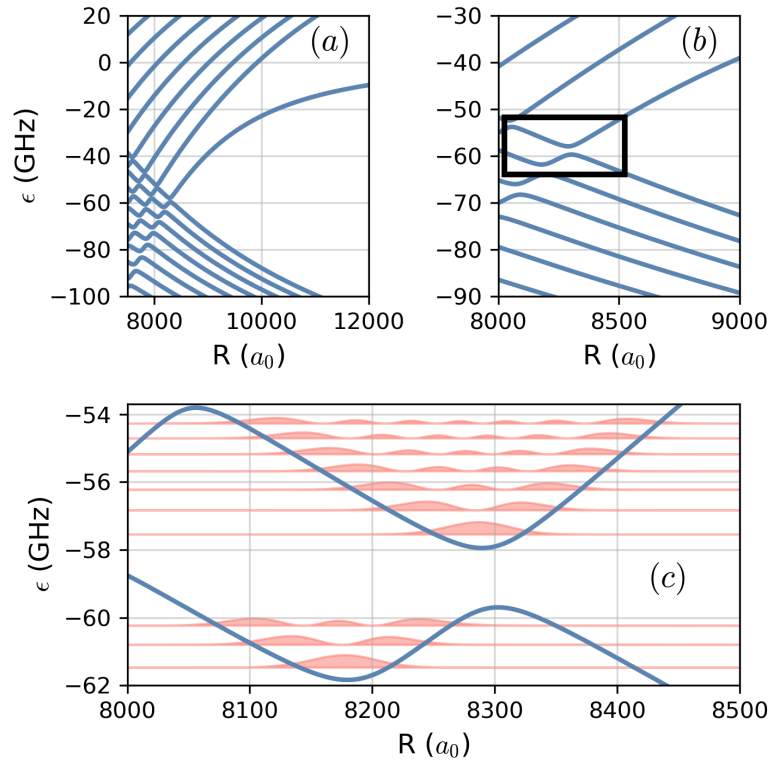
FIGURE B.2: (a),(b) Adiabatic PEC for a ^{7}Li Rydberg atom interacting with a singly-charged positive ion at separation R near the $|30S\rangle$ atomic Rydberg state. (c) Magnification of the region marked by the black box in (b) showing vibrationally-bound states inside the outermost two potential wells formed between the $|30S\rangle$ state and low-field seeking high-l states. Energies are given in GHz relative to the $|30S\rangle$ atomic Rydberg state.

or alternatively by choosing $\mathbf{R} = (R, \pi, 0)$:

$$V_{\Theta=\pi}(R) = -\sum_{\lambda=1}^{\infty} (-1)^\lambda \sqrt{\frac{4\pi}{2\lambda+1}} \frac{r^\lambda}{R^{\lambda+1}} Y_{\lambda 0}(\theta, \phi), \tag{B.7}$$

where we have used the fact that $Y_{\lambda\mu}^*(0,0) = \sqrt{\frac{2\lambda+1}{4\pi}}\delta_{\mu,0}$ and $Y_{\lambda\mu}^*(\pi,0) = \sqrt{\frac{2\lambda+1}{4\pi}}(-1)^\lambda\delta_{\mu,0}$, respectively.

Role of the higher-order multipole interaction terms

In both (B.6) and (B.7), the leading-order term in the multipole interaction series is given by $\lambda = 1$, which represents an interaction of the ion with the dipole moment of the Rydberg atom's charge distribution. This charge-dipole term varies with the internuclear separation as $1/R^2$. For higher-order multipole terms, the order of R in the denominator increases such that their matrix elements are reduced in magnitude relative to the charge-dipole term. Nonetheless, whilst the matrix elements of the $\lambda = 1$ term typically have the largest magnitude, the matrix elements from terms with $\lambda > 1$ must also be included in order to ensure convergence of the adiabatic PEC to a desired energy scale. For example, terms up to $\lambda = 6$ are typically required for convergence to the nearest 10-100 MHz.

The matrix elements of the multipole interaction terms can be determined with help of the analytical results given by equations (A.9) and (A.10). Once again, the radial integrals for quantum defect states

must be evaluated numerically. Whilst the ion-Rydberg interaction leads to coupling between different Rydberg states, we note that multipole terms with even values of λ permit finite diagonal matrix elements in the Rydberg basis, i.e. $\langle \psi_{nlm} | r^\lambda Y_{\lambda 0}(\theta, \phi) | \psi_{nlm} \rangle \neq 0$. Thus, as well as coupling different Rydberg states, the even λ multipole interaction terms additionally contribute energy offsets to individual Rydberg states.

One consequence of these diagonal matrix elements is that the adiabatic PEC for an interacting ion-Rydberg pair are dependent on the sign of the ion's charge [1]. Although this effect is not strong enough to qualitatively change the form of the PEC, it does affect the size of the energy gap at avoided crossings between neighbouring PEC. This can be seen clearly in figure B.1, where we compare adiabatic PEC of an ^{87}Rb Rydberg atom interacting with a cation and an anion, respectively. In particular, near the $|31D\rangle$ Rydberg state, we find that the size of the avoided crossings between the high field-seeking D-state and the low field-seeking high angular momentum states are one order of magnitude larger for the anion system than they are for the cation system. This will have a significant impact on the non-adiabatic couplings between neighbouring PEC: for example, using the Landau-Zener formula (2.8), we estimate that the rates for non-adiabatic transitions of the states shown in figure B.1 (e) to neighbouring PEC are negligible for the anion system. Instead, for the majority of these vibrationally-bound states, we expect the molecular lifetime to be limited by the rate of radiative decay of the Rydberg atom.

Interactions with different atomic species

Finally, we note that the ion-Rydberg systems discussed in the scientific contributions of this thesis have only considered ^{87}Rb Rydberg atoms. Like Rb, Cs is also expected to form long-range binding potentials with an ion through avoided crossings between high field-seeking P-states and low field-seeking high angular momentum states $l > 3$ [92]. However, these are yet to be observed.

For the lighter alkali metal element Li, forming similar long-range wells is not possible because the quantum defect parameter for the P-state is vanishingly small [276]. Indeed, Li only has a significant quantum defect parameter for its S-state. We find that this nonetheless leads to the formation of long-range binding potentials, which arise due to avoided crossings with low-field seeking high angular momentum states (see figure B.2). Whilst the wells are shallower than those seen for ^{87}Rb, at $n = 30$ they are still deep enough to support several vibrational states. Unlike the ion-Rydberg dimers formed with Rb and Cs, these dimers have strong S-state character.

---

[1]The sign of the ion's charge is reflected in the prefactor of the ion-Rydberg interaction series (B.5). The prefactor is negative (positive) for a cation (anion).

Appendix C

Collisional decay of ion-Rydberg dimers

In this appendix, we determine the classical collision rate of a Rydberg atom with background gas atoms and find that these rates agree well with the measured decay rates of ion-Rydberg dimers produced inside an ultracold quantum gas [95].

We consider an ion-Rydberg dimer molecule inside a gas of neutral ground-state atoms with gas density ρ. The mean relative speed between particles of reduced mass μ in a gas at temperature T is given by $\bar{v}_{\text{rel}} = \sqrt{8k_B T / \pi \mu}$ [394]. The rate of collision of the Rydberg atom with atoms of the background gas is then defined by:

$$\gamma_{\text{col}} = \rho \, \sigma \, \bar{v}_{\text{rel}}, \tag{C.1}$$

where σ is the classical scattering cross-section, defined as the geometric cross-section of the Rydberg atom $\pi \langle r \rangle^2$. Given that $\langle r \rangle \propto n^2$, where $\langle r \rangle$ is the expected size of the Rydberg electron's orbit, the cross-section scales as $\sigma \propto n^4$. We find the scaling of the extent of the Rydberg electron's orbit to be $\langle r \rangle \approx 2.4n^2 \, a_0$. We then define the total decay rate of the ion-Rydberg dimer as:

$$\gamma = \gamma_{\text{rad}} + \gamma_{\text{col}}, \tag{C.2}$$

where γ_{rad} is the radiative decay rate of the Rydberg atom.

We now determine the expected lifetime $\tau = 1/\gamma$ of the ion-Rydberg dimer using the experimental parameters quoted in [95]. In particular, we assume a gas temperature $T = 20\,\mu\text{K}$ and minimum and maximum background gas densities of $\rho_{\text{min}} = 1 \times 10^{12} \text{ cm}^{-3}$ and $\rho_{\text{max}} = 5 \times 10^{12} \text{ cm}^{-3}$, respectively. In table C.1, we compare the results for τ to those measured in [95] for dimers in binding potentials formed by the $54P$ and $69P$ states. The measured lifetimes are within the bounds of values predicted using the classical scattering model based off the range of densities quoted in the experiment, indicating that collisional decay may well be responsible for limiting the lifetime of these molecules far below the radiative lifetime of the Rydberg atom.

	Model (µs)		Measured (µs)
	ρ_{min}	ρ_{max}	–
$54P$	5.93	28.23	11.5 ± 1.0
$69P$	2.28	11.31	2.6 ± 0.2

TABLE C.1: Comparison of the expected lifetime of ion-Rydberg dimers predicted by the classical scattering model (C) with those measured in experiment [95].

To confirm the validity of the model , an experiment could be done in which the lifetime is measured systematically for different fixed gas densities ρ. A linear dependence on ρ should be visible in the measured decay rate.

Appendix D

Finite difference representation of the three-atom vibrational Hamiltonian

This appendix presents the finite difference Hamiltonian used to determine the eigenstates and eigenvalues of the vibrational Hamiltonian describing the $^{87}\text{Rb}_3^{2+}$ system studied in [SC5], consisting of a single Rydberg atom interacting with a pair of cations (for a schematic of the system, see figure 1 (a) in [SC5]). A brief introduction to finite difference methods can be found in section 2.5.2.

For a non-rotating triatomic system, the vibrational Hamiltonian is given by [395, 396]:

$$
\begin{aligned}
H_{\text{vib}} = \frac{1}{m} & \left[-\frac{\partial^2}{\partial R_1^2} - \frac{\partial^2}{\partial R_2^2} - \cos(\Theta)\frac{\partial}{\partial R_1}\frac{\partial}{\partial R_2} \right] \\
& - \frac{1}{m}\left(\frac{1}{R_1^2} + \frac{1}{R_2^2} - \frac{\cos(\Theta)}{R_1 R_2} \right)\left(\frac{\partial^2}{\partial \Theta^2} + \cot(\Theta)\frac{\partial}{\partial \Theta} \right) \\
& - \frac{1}{m}\left(\frac{1}{R_1 R_2} - \frac{1}{R_2}\frac{\partial}{\partial R_1} - \frac{1}{R_1}\frac{\partial}{\partial R_2} \right)\left(\cos(\Theta) + \sin(\Theta)\frac{\partial}{\partial \Theta} \right) \\
& + \varepsilon_n(R_1, R_2, \Theta),
\end{aligned}
\tag{D.1}
$$

where m is the atomic mass of ^{87}Rb and $\varepsilon_n(R_1, R_2, \Theta)$ is the nth adiabatic PES, dependent on the bond lengths R_1, R_2 and bond angle Θ. This Hamiltonian acts on vibrational wavefunctions $\chi_\nu(R_1, R_2, \Theta)$ which are normalised as $\int dR_1 dR_2 d\Theta \sin\Theta |\chi_\nu(R_1, R_2, \Theta)|^2 = 1$.

We solve for the eigenstates and eigenvalues of (D.1) by representing the eigenstates on a discrete spatial grid $\chi_\nu \to \chi_\nu^{(ijk)}$. The dimensions of the three-dimensional grid are $N \times M \times L$, where N, M and L are positive integers. $\chi_\nu^{(ijk)}$ represents the amplitude of the νth eigenstate at the grid point $(R_1^{(i)}, R_2^{(j)}, \Theta^{(k)})$, where $R_1^{(i)} = R_1^{(1)} + i\,\Delta R_1$, $R_2^{(j)} = R_2^{(1)} + j\,\Delta R_2$ and $\Theta^{(k)} = \Theta^{(1)} + k\,\Delta\Theta$. The grid spacings ΔR_1, ΔR_2 and $\Delta\Theta$ are defined as $\Delta R_1 = (R_1^{(N)} - R_1^{(0)})/N$, $\Delta R_2 = (R_2^{(M)} - R_2^{(0)})/M$ and $\Delta\Theta = (\Theta^{(L)} - \Theta^{(0)})/L$. We further assume closed boundary conditions, such that χ_{ijk} vanishes for $i = \{0, N+1\}$, $j = \{0, M+1\}$ or $k = \{0, M+1\}$.

We approximate the first-order derivatives using the central finite difference formalism [129], which for derivatives with respect to R_1 take the form of:

$$
\left.\frac{\partial \chi_\nu}{\partial R_1}\right|_{i,j,k} \approx \left[\chi_\nu^{(i+1,j,k)} - \chi_\nu^{(i-1,j,k)} \right]/2\Delta R_1.
\tag{D.2}
$$

Equally, single-variate second-order central finite difference derivatives are approximated as:

$$\left.\frac{\partial^2 \chi_\nu}{\partial R_1^2}\right|_{i,j,k} \approx \left[\chi_\nu^{(i+1,j,k)} - 2\chi_\nu^{(i,j,k)} + \chi_\nu^{(i-1,j,k)}\right]/\Delta R_1^2, \qquad (D.3)$$

whereas multi-variate second-order derivatives are given by:

$$\left.\frac{\partial^2 \chi_\nu}{\partial R_1 \partial R_2}\right|_{i,j,k} \approx \left[\chi_\nu^{(i+1,j+1,k)} - \chi_\nu^{(i+1,j-1,k)} - \chi_\nu^{(i-1,j+1,k)} + \chi_\nu^{(i-1,j-1,k)}\right]/\Delta R_1 \Delta R_2. \qquad (D.4)$$

The remaining derivatives appearing in equation (D.1) are approximated in the same manner.

For brevity, we now adopt a more concise notation: $\chi_\nu^{(i,j,k)} \rightarrow \chi_{i,j,k}$, $R_1^{(i)} \rightarrow R_i$, $R_2^{(j)} \rightarrow R_j$ and $\Theta^{(k)} \rightarrow \Theta_k$. Here, we have dropped the numerical subscripts from R_1 and R_2 since we represent these on identical grids with spacing ΔR. As described in [SC5], this is appropriate as we are interested in nuclear configurations in which the bond lengths are roughly symmetric.

Now, using the approximations (D.2), (D.3) and (D.4), the time-independent Schrödinger equation $H_n \chi_{i,j,k} = E\chi_{i,j,k}$ can be expressed as a system of linear equations, whose number is given by the product of N, M and L. In its full form, the linear equation for the grid point (i, j, k) reads:

$$
\begin{aligned}
-\frac{1}{m}&\left(\frac{1}{\Delta R^2}\left[\chi_{i+1,j,k} + \chi_{i-1,j,k}\right] + \frac{1}{\Delta R^2}\left[\chi_{i,j+1,k} + \chi_{i,j-1,k}\right] - \frac{4\chi_{i,j,k}}{\Delta R^2}\right) \\
&- \frac{\cos\Theta_k}{4m\Delta R^2}\left(\chi_{i+1,j+1,k} - \chi_{i+1,j-1,k} - \chi_{i-1,j+1,k} + \chi_{i-1,j-1,k}\right) \\
&- \frac{1}{m}\left(\frac{1}{R_i^2} + \frac{1}{R_j^2} - \frac{\cos\Theta_k}{R_i R_j}\right)\left[\chi_{i,j,k+1}\left(\frac{1}{\Delta\Theta^2} + \frac{\cos\Theta_k}{2\Delta\Theta}\right) - \frac{2\chi_{i,j,k}}{\Delta\Theta^2} + \chi_{i,j,k-1}\left(\frac{1}{\Delta\Theta^2} - \frac{\cos\Theta_k}{2\Delta\Theta}\right)\right] \\
&- \frac{\cos\Theta_k}{mR_i R_j}\left(\chi_{i,j,k} - \frac{R_j}{2\Delta R}\left[\chi_{i,j+1,k} - \chi_{i,j-1,k}\right] - \frac{R_i}{2\Delta R}\left[\chi_{i+1,j,k} - \chi_{i-1,j,k}\right]\right) \\
&- \frac{\sin\Theta_k}{2mR_i R_j\Delta\Theta}\left(\chi_{i,j,k+1} - \chi_{i,j,k-1} - \frac{R_j}{2\Delta R}\left[\chi_{i,j+1,k+1} - \chi_{i,j+1,k-1} - \chi_{i,j-1,k+1} + \chi_{i,j-1,k-1}\right]\right. \\
&\qquad\qquad\qquad \left. - \frac{R_i}{2\Delta R}\left[\chi_{i+1,j,k+1} - \chi_{i+1,j,k-1} - \chi_{i-1,j,k+1} + \chi_{i-1,j,k-1}\right]\right) = E\chi_{i,j,k}.
\end{aligned}
\qquad (D.5)
$$

This systems of equations can be represented as a matrix eigenvalue problem $\underline{\underline{H}}\mathbf{X} = E\mathbf{X}$, where $\underline{\underline{H}}$ is a square matrix of dimension $(N \times M \times L)^2$, $\mathbf{X} = (\chi_{1,1,1}, \chi_{1,1,2}, \dots, \chi_{N,M,L})$ is a vector whose components give the amplitude of the eigenstate at each grid point and E is the corresponding eigenvalue. Although $\underline{\underline{H}}$ is a sparse matrix, it quickly becomes considerably large in size even for relatively modest numbers of grid points. We found that when using a cubic grid with $N = M = L = D$, the elements $H_{\alpha,\beta}$ of $\underline{\underline{H}}$ form block-like structures which makes the construction of the $D^3 \times D^3$ matrix considerably more efficient.

After constructing the matrix Hamiltonian, the final step is to diagonalise it in order to obtain the eigenvalues and eigenenergies. For the binding potentials considered in [SC5], we find that a value of $D = 42$ is sufficient to ensure convergence of the first twenty vibrational states to the nearest few MHz, which is roughly an order of magnitude smaller than the smallest relevant energy separation for the vibrational states, namely the spacing between vibrational states which is on the order of 100 MHz.

Bibliography

[1] A. Recati and S. Stringari, "Supersolidity in ultracold dipolar gases", Nat. Rev. Phys. **5**, 735 (2023).

[2] M. S. Safronova, D. Budker, D. DeMille, D. F. J. Kimball, A. Derevianko, and C. W. Clark, "Search for new physics with atoms and molecules", Rev. Mod. Phys. **90**, 025008 (2018).

[3] S. Pirandola, "Satellite quantum communications: Fundamental bounds and practical security", Phys. Rev. Res. **3**, 023130 (2021).

[4] C. T. Fancher, D. R. Scherer, M. C. S. John, and B. L. S. Marlow, "Rydberg atom electric field sensors for communications and sensing", IEEE Trans. Quantum Eng. **2**, 1 (2021).

[5] I. H. Deutsch, "Harnessing the Power of the Second Quantum Revolution", PRX Quantum **1**, 020101 (2020).

[6] H. K. Onnes, "Further experiments with liquid helium. C. On the change of electric resistance of pure metals at very low temperatures etc. IV. The resistance of pure mercury at helium temperatures", in *Through Measurement to Knowledge: The Selected Papers of Heike Kamerlingh Onnes 1853–1926*, edited by K. Gavroglu and Y. Goudaroulis (Springer Netherlands, Dordrecht, 1991), pp. 261–263.

[7] M. H. Anderson, J. R. Ensher, M. R. Matthews, C. E. Wieman, and E. A. Cornell, "Observation of Bose-Einstein Condensation in a Dilute Atomic Vapor", Science **269**, 198 (1995).

[8] K. B. Davis, M. O. Mewes, M. R. Andrews, N. J. van Druten, D. S. Durfee, D. M. Kurn, and W. Ketterle, "Bose-Einstein Condensation in a Gas of Sodium Atoms", Phys. Rev. Lett. **75**, 3969 (1995).

[9] C. C. Bradley, C. A. Sackett, J. J. Tollett, and R. G. Hulet, "Evidence of Bose-Einstein Condensation in an Atomic Gas with Attractive Interactions", Phys. Rev. Lett. **75**, 1687 (1995).

[10] C. C. Bradley, C. A. Sackett, and R. G. Hulet, "Bose-Einstein Condensation of Lithium: Observation of Limited Condensate Number", Phys. Rev. Lett. **78**, 985 (1997).

[11] W. Ketterle, "Nobel lecture: When atoms behave as waves: Bose-Einstein condensation and the atom laser", Rev. Mod. Phys. **74**, 1131 (2002).

[12] C. Chin, R. Grimm, P. Julienne, and E. Tiesinga, "Feshbach resonances in ultracold gases", Rev. Mod. Phys. **82**, 1225 (2010).

[13] E. Tiesinga, B. J. Verhaar, and H. T. C. Stoof, "Threshold and resonance phenomena in ultracold ground-state collisions", Phys. Rev. A **47**, 4114 (1993).

[14] S. Inouye, M. R. Andrews, J. Stenger, H. .-. Miesner, D. M. Stamper-Kurn, and W. Ketterle, "Observation of Feshbach resonances in a Bose–Einstein condensate", Nature **392**, 151 (1998).

[15] F. K. Fatemi, K. M. Jones, and P. D. Lett, "Observation of Optically Induced Feshbach Resonances in Collisions of Cold Atoms", Phys. Rev. Lett. **85**, 4462 (2000).

[16] M. Olshanii, "Atomic Scattering in the Presence of an External Confinement and a Gas of Impenetrable Bosons", Phys. Rev. Lett. **81**, 938 (1998).

[17] E. Haller, M. J. Mark, R. Hart, J. G. Danzl, L. Reichsöllner, V. Melezhik, P. Schmelcher, and H.-C. Nägerl, "Confinement-Induced Resonances in Low-Dimensional Quantum Systems", Phys. Rev. Lett. **104**, 153203 (2010).

[18]   V. Dunjko, M. G. Moore, T. Bergeman, and M. Olshanii, "Chapter 10 - Confinement-Induced Resonances", Adv. At. Mol. Opt. Phys. **60**, edited by E. Arimondo, P. R. Berman, and C. C. Lin, 461 (2011).

[19]   J. Herbig, T. Kraemer, M. Mark, T. Weber, C. Chin, H.-C. Nägerl, and R. Grimm, "Preparation of a Pure Molecular Quantum Gas", Science **301**, 1510 (2003).

[20]   J. G. Danzl, E. Haller, M. Gustavsson, M. J. Mark, R. Hart, N. Bouloufa, O. Dulieu, H. Ritsch, and H.-C. Nägerl, "Quantum Gas of Deeply Bound Ground State Molecules", Science **321**, 1062 (2008).

[21]   T. Kraemer, M. Mark, P. Waldburger, J. G. Danzl, C. Chin, B. Engeser, A. D. Lange, K. Pilch, A. Jaakkola, H. .-. Nägerl, and R. Grimm, "Evidence for Efimov quantum states in an ultracold gas of caesium atoms", Nature **440**, 315 (2006).

[22]   S. Knoop, F. Ferlaino, M. Mark, M. Berninger, H. Schöbel, H. .-. Nägerl, and R. Grimm, "Observation of an Efimov-like trimer resonance in ultracold atom–dimer scattering", Nat. Phys. **5**, 227 (2009).

[23]   M. Berninger, A. Zenesini, B. Huang, W. Harm, H.-C. Nägerl, F. Ferlaino, R. Grimm, P. S. Julienne, and J. M. Hutson, "Universality of the Three-Body Parameter for Efimov States in Ultracold Cesium", Phys. Rev. Lett. **107**, 120401 (2011).

[24]   I. Bloch, "Ultracold quantum gases in optical lattices", Nat. Phys. **1**, 23 (2005).

[25]   J. F. Sherson, C. Weitenberg, M. Endres, M. Cheneau, I. Bloch, and S. Kuhr, "Single-atom-resolved fluorescence imaging of an atomic Mott insulator", Nature **467**, 68 (2010).

[26]   C. Weitenberg, M. Endres, J. F. Sherson, M. Cheneau, P. Schauß, T. Fukuhara, I. Bloch, and S. Kuhr, "Single-spin addressing in an atomic Mott insulator", Nature **471**, 319 (2011).

[27]   M. F. Parsons, F. Huber, A. Mazurenko, C. S. Chiu, W. Setiawan, K. Wooley-Brown, S. Blatt, and M. Greiner, "Site-Resolved Imaging of Fermionic ^{6}Li in an Optical Lattice", Phys. Rev. Lett. **114**, 213002 (2015).

[28]   M. Lewenstein, A. Sanpera, V. Ahufinger, B. Damski, A. Sen, and U. Sen, "Ultracold atomic gases in optical lattices: mimicking condensed matter physics and beyond", Adv. Phys. **56**, 243 (2007).

[29]   C. Gross and I. Bloch, "Quantum simulations with ultracold atoms in optical lattices", Science **357**, 995 (2017).

[30]   S. Diehl, A. Micheli, A. Kantian, B. Kraus, H. P. Büchler, and P. Zoller, "Quantum states and phases in driven open quantum systems with cold atoms", Nat. Phys. **4**, 878 (2008).

[31]   R. Labouvie, B. Santra, S. Heun, and H. Ott, "Bistability in a Driven-Dissipative Superfluid", Phys. Rev. Lett. **116**, 235302 (2016).

[32]   J. Benary, C. Baals, E. Bernhart, J. Jiang, M. Röhrle, and H. Ott, "Experimental observation of a dissipative phase transition in a multi-mode many-body quantum system", New J. Phys. **24**, 103034 (2022).

[33]   M. Takamoto, F.-L. Hong, R. Higashi, and H. Katori, "An optical lattice clock", Nature **435**, 321 (2005).

[34]   H. Katori, "Optical lattice clocks and quantum metrology", Nat. Photonics **5**, 203 (2011).

[35]   B. J. Bloom, T. L. Nicholson, J. R. Williams, S. L. Campbell, M. Bishof, X. Zhang, W. Zhang, S. L. Bromley, and J. Ye, "An optical lattice clock with accuracy and stability at the 10^{-18} level", Nature **506**, 71 (2014).

[36]   A. D. Ludlow, M. M. Boyd, J. Ye, E. Peik, and P. O. Schmidt, "Optical atomic clocks", Rev. Mod. Phys. **87**, 637 (2015).

[37]   F. Nogrette, H. Labuhn, S. Ravets, D. Barredo, L. Béguin, A. Vernier, T. Lahaye, and A. Browaeys, "Single-Atom Trapping in Holographic 2D Arrays of Microtraps with Arbitrary Geometries", Phys. Rev. X **4**, 021034 (2014).

[38] W. Lee, H. Kim, and J. Ahn, "Three-dimensional rearrangement of single atoms using actively controlled optical microtraps", Opt. Express **24**, 9816 (2016).

[39] D. Barredo, S. de Léséleuc, V. Lienhard, T. Lahaye, and A. Browaeys, "An atom-by-atom assembler of defect-free arbitrary two-dimensional atomic arrays", Science **354**, 1021 (2016).

[40] M. Endres, H. Bernien, A. Keesling, H. Levine, E. R. Anschuetz, A. Krajenbrink, C. Senko, V. Vuletic, M. Greiner, and M. D. Lukin, "Atom-by-atom assembly of defect-free one-dimensional cold atom arrays", Science **354**, 1024 (2016).

[41] H. J. Manetsch, G. Nomura, E. Bataille, K. H. Leung, X. Lv, and M. Endres, "A tweezer array with 6100 highly coherent atomic qubits", arXiv:2403.12021 (2024).

[42] M. Norcia, H. Kim, W. Cairncross, M. Stone, A. Ryou, M. Jaffe, M. Brown, K. Barnes, P. Battaglino, A. Brown, et al., "Iterative assembly of ^{171}Yb atom arrays in cavity-enhanced optical lattices", arXiv:2401.16177 (2024).

[43] F. Gyger, M. Ammenwerth, R. Tao, H. Timme, S. Snigirev, I. Bloch, and J. Zeiher, "Continuous operation of large-scale atom arrays in optical lattices", arXiv:2402.04994 (2024).

[44] D. Bluvstein, S. J. Evered, A. A. Geim, S. H. Li, H. Zhou, T. Manovitz, S. Ebadi, M. Cain, M. Kalinowski, D. Hangleiter, J. P. Bonilla Ataides, N. Maskara, I. Cong, X. Gao, P. Sales Rodriguez, T. Karolyshyn, G. Semeghini, M. J. Gullans, M. Greiner, V. Vuletić, and M. D. Lukin, "Logical quantum processor based on reconfigurable atom arrays", Nature **626**, 58 (2024).

[45] M. Saffman, "Quantum computing with atomic qubits and Rydberg interactions: progress and challenges", J. Phys. B: At. Mol. Opt. Phys. **49**, 202001 (2016).

[46] L. Henriet, L. Beguin, A. Signoles, T. Lahaye, A. Browaeys, G.-O. Reymond, and C. Jurczak, "Quantum computing with neutral atoms", Quantum **4**, 327 (2020).

[47] M. Morgado and S. Whitlock, "Quantum simulation and computing with Rydberg-interacting qubits", AVS Quantum Sci. **3**, 023501 (2021).

[48] A. Browaeys and T. Lahaye, "Many-body physics with individually controlled Rydberg atoms", Nat. Phys. **16**, 132 (2020).

[49] W. Paul and H. Steinwedel, "Notizen: Ein neues Massenspektrometer ohne Magnetfeld", Z. Naturforsch. A **8**, 448 (1953).

[50] W. Paul, O. Osberghaus, and E. Fischer, *Ein Ionenkäfig*, 1st ed. (VS Verlag für Sozialwissenschaften Wiesbaden, Jan. 1958).

[51] A. Ashkin, "Acceleration and Trapping of Particles by Radiation Pressure", Phys. Rev. Lett. **24**, 156 (1970).

[52] D. J. Wineland, "Nobel Lecture: Superposition, entanglement, and raising Schrödinger's cat", Rev. Mod. Phys. **85**, 1103 (2013).

[53] D. J. Wineland, R. E. Drullinger, and F. L. Walls, "Radiation-Pressure Cooling of Bound Resonant Absorbers", Phys. Rev. Lett. **40**, 1639 (1978).

[54] W. Neuhauser, M. Hohenstatt, P. Toschek, and H. Dehmelt, "Optical-Sideband Cooling of Visible Atom Cloud Confined in Parabolic Well", Phys. Rev. Lett. **41**, 233 (1978).

[55] F. Diedrich, J. C. Bergquist, W. M. Itano, and D. J. Wineland, "Laser Cooling to the Zero-Point Energy of Motion", Phys. Rev. Lett. **62**, 403 (1989).

[56] C. Monroe, D. M. Meekhof, B. E. King, W. M. Itano, and D. J. Wineland, "Demonstration of a Fundamental Quantum Logic Gate", Phys. Rev. Lett. **75**, 4714 (1995).

[57] E. A. Martinez, C. A. Muschik, P. Schindler, D. Nigg, A. Erhard, M. Heyl, P. Hauke, M. Dalmonte, T. Monz, P. Zoller, and R. Blatt, "Real-time dynamics of lattice gauge theories with a few-qubit quantum computer", Nature **534**, 516 (2016).

[58] M. Johanning, A. F. Varon, and C. Wunderlich, "Quantum simulations with cold trapped ions", J. Phys. B: At. Mol. Opt. Phys. **42**, 154009 (2009).

[59] R. Blatt and C. F. Roos, "Quantum simulations with trapped ions", Nat. Phys. **8**, 277 (2012).

[60] C. Monroe, W. C. Campbell, L.-M. Duan, Z.-X. Gong, A. V. Gorshkov, P. W. Hess, R. Islam, K. Kim, N. M. Linke, G. Pagano, P. Richerme, C. Senko, and N. Y. Yao, "Programmable quantum simulations of spin systems with trapped ions", Rev. Mod. Phys. **93**, 025001 (2021).

[61] C. Hempel, C. Maier, J. Romero, J. McClean, T. Monz, H. Shen, P. Jurcevic, B. P. Lanyon, P. Love, R. Babbush, A. Aspuru-Guzik, R. Blatt, and C. F. Roos, "Quantum Chemistry Calculations on a Trapped-Ion Quantum Simulator", Phys. Rev. X **8**, 031022 (2018).

[62] J. Whitlow, Z. Jia, Y. Wang, C. Fang, J. Kim, and K. R. Brown, "Quantum simulation of conical intersections using trapped ions", Nat. Chem. **15**, 1509 (2023).

[63] Z. Davoudi, M. Hafezi, C. Monroe, G. Pagano, A. Seif, and A. Shaw, "Towards analog quantum simulations of lattice gauge theories with trapped ions", Phys. Rev. Res. **2**, 023015 (2020).

[64] S. A. Diddams, T. Udem, J. C. Bergquist, E. A. Curtis, R. E. Drullinger, L. Hollberg, W. M. Itano, W. D. Lee, C. W. Oates, K. R. Vogel, and D. J. Wineland, "An Optical Clock Based on a Single Trapped $^{199}Hg^+$ Ion", Science **293**, 825 (2001).

[65] T. Rosenband, D. B. Hume, P. O. Schmidt, C. W. Chou, A. Brusch, L. Lorini, W. H. Oskay, R. E. Drullinger, T. M. Fortier, J. E. Stalnaker, S. A. Diddams, W. C. Swann, N. R. Newbury, W. M. Itano, D. J. Wineland, and J. C. Bergquist, "Frequency Ratio of Al^+ and Hg^+ Single-Ion Optical Clocks; Metrology at the 17th Decimal Place", Science **319**, 1808 (2008).

[66] A. Härter and J. H. Denschlag, "Cold atom–ion experiments in hybrid traps", Contemp. Phys. **55**, 33 (2014).

[67] M. Tomza, K. Jachymski, R. Gerritsma, A. Negretti, T. Calarco, Z. Idziaszek, and P. S. Julienne, "Cold hybrid ion-atom systems", Rev. Mod. Phys. **91**, 035001 (2019).

[68] M. Deiß, S. Willitsch, and J. Hecker Denschlag, "Cold trapped molecular ions and hybrid platforms for ions and neutral particles", Nat. Phys. **20**, 713 (2024).

[69] C. R. and A. Dalgarno, "Ultracold atom-ion collisions", Phys. Rev. A **62**, 012709 (2000).

[70] R. Côté, "From Classical Mobility to Hopping Conductivity: Charge Hopping in an Ultracold Gas", Phys. Rev. Lett. **85**, 5316 (2000).

[71] R. Côté, V. Kharchenko, and M. D. Lukin, "Mesoscopic Molecular Ions in Bose-Einstein Condensates", Phys. Rev. Lett. **89**, 093001 (2002).

[72] T. C. Killian, S. Kulin, S. D. Bergeson, L. A. Orozco, C. Orzel, and S. L. Rolston, "Creation of an Ultracold Neutral Plasma", Phys. Rev. Lett. **83**, 4776 (1999).

[73] I. Mourachko, D. Comparat, F. de Tomasi, A. Fioretti, P. Nosbaum, V. M. Akulin, and P. Pillet, "Many-Body Effects in a Frozen Rydberg Gas", Phys. Rev. Lett. **80**, 253 (1998).

[74] W. R. Anderson, J. R. Veale, and T. F. Gallagher, "Resonant Dipole-Dipole Energy Transfer in a Nearly Frozen Rydberg Gas", Phys. Rev. Lett. **80**, 249 (1998).

[75] J. M. Schurer, A. Negretti, and P. Schmelcher, "Unraveling the Structure of Ultracold Mesoscopic Collinear Molecular Ions", Phys. Rev. Lett. **119**, 063001 (2017).

[76] W. Casteels, J. Tempere, and J. T. Devreese, "Polaronic Properties of an Ion in a Bose-Einstein Condensate in the Strong-Coupling Limit", J. Low Temp. Phys. **162**, 266 (2011).

[77] G. E. Astrakharchik, L. A. P. Ardila, R. Schmidt, K. Jachymski, and A. Negretti, "Ionic polaron in a Bose-Einstein condensate", Commun. Phys **4**, 94 (2021).

[78] G. E. Astrakharchik, L. A. P. Ardila, K. Jachymski, and A. Negretti, "Many-body bound states and induced interactions of charged impurities in a bosonic bath", Nat. Commun. **14**, 1647 (2023).

[79] P. Zhang, A. Dalgarno, and R. Côté, "Scattering of Yb and Yb^+", Phys. Rev. A **80**, 030703 (2009).

[80] W. W. Smith, O. P. Makarov, and J. Lin, "Cold ion–neutral collisions in a hybrid trap", J. Mod. Opt. **52**, 2253 (2005).

[81] M. Cetina, A. Grier, J. Campbell, I. Chuang, and V. Vuletič, "Bright source of cold ions for surface-electrode traps", Phys. Rev. A **76**, 041401 (2007).

[82] C. Zipkes, S. Palzer, L. Ratschbacher, C. Sias, and M. Köhl, "Cold Heteronuclear Atom-Ion Collisions", Phys. Rev. Lett. **105**, 133201 (2010).

[83] T. Feldker, H. Fürst, H. Hirzler, N. V. Ewald, M. Mazzanti, D. Wiater, M. Tomza, and R. Gerritsma, "Buffer gas cooling of a trapped ion to the quantum regime", Nat. Phys. **16**, 413 (2020).

[84] P. Weckesser, F. Thielemann, D. Wiater, A. Wojciechowska, L. Karpa, K. Jachymski, M. Tomza, T. Walker, and T. Schaetz, "Observation of Feshbach resonances between a single ion and ultracold atoms", Nature **600**, 429 (2021).

[85] F. Thielemann, J. Siemund, D. von Schoenfeld, W. Wu, P. Weckesser, K. Jachymski, T. Walker, and T. Schaetz, "Exploring atom-ion Feshbach resonances below the s-wave limit", arXiv:2406.13410 (2024).

[86] X. Xing, P. Weckesser, F. Thielemann, T. Jónás, R. Vexiau, N. Bouloufa-Maafa, E. Luc-Koenig, K. W. Madison, A. Orbán, T. Xie, T. Schaetz, and O. Dulieu, "Competing excitation quenching and charge exchange in ultracold Li-Ba$^+$ collisions", arXiv:2406.16017 (2024).

[87] K. S. Kleinbach, F. Engel, T. Dieterle, R. Löw, T. Pfau, and F. Meinert, "Ionic Impurity in a Bose-Einstein Condensate at Submicrokelvin Temperatures", Phys. Rev. Lett. **120**, 193401 (2018).

[88] T. Dieterle, M. Berngruber, C. Hölzl, R. Löw, K. Jachymski, T. Pfau, and F. Meinert, "Transport of a Single Cold Ion Immersed in a Bose-Einstein Condensate", Phys. Rev. Lett. **126**, 033401 (2021).

[89] C. Veit, N. Zuber, O. A. Herrera-Sancho, V. S. V. Anasuri, T. Schmid, F. Meinert, R. Löw, and T. Pfau, "Pulsed Ion Microscope to Probe Quantum Gases", Phys. Rev. X **11**, 011036 (2021).

[90] F. Engel, T. Dieterle, T. Schmid, C. Tomschitz, C. Veit, N. Zuber, R. Löw, T. Pfau, and F. Meinert, "Observation of Rydberg Blockade Induced by a Single Ion", Phys. Rev. Lett. **121**, 193401 (2018).

[91] T. Secker, R. Gerritsma, A. W. Glaetzle, and A. Negretti, "Controlled long-range interactions between Rydberg atoms and ions", Phys. Rev. A **94**, 013420 (2016).

[92] A. Duspayev, X. Han, M. A. Viray, L. Ma, J. Zhao, and G. Raithel, "Long-range Rydberg-atom–ion molecules of Rb and Cs", Phys. Rev. Res. **3**, 023114 (2021).

[93] M. Deiß, S. Haze, and J. Hecker Denschlag, "Long-Range Atom–Ion Rydberg Molecule: A Novel Molecular Binding Mechanism", Atoms **9**, 34 (2021).

[94] W. Demtröder, *Molecular Physics: Theoretical Principles and Experimental Methods* (Wiley-VCH, Weinheim, 2005).

[95] N. Zuber, V. S. V. Anasuri, M. Berngruber, Y.-Q. Zou, F. Meinert, R. Löw, and T. Pfau, "Observation of a molecular bond between ions and Rydberg atoms", Nature **605**, 453 (2022).

[96] Y.-Q. Zou, M. Berngruber, V. S. V. Anasuri, N. Zuber, F. Meinert, R. Löw, and T. Pfau, "Observation of Vibrational Dynamics of Orientated Rydberg-Atom-Ion Molecules", Phys. Rev. Lett. **130**, 023002 (2023).

[97] H. Stapelfeldt and T. Seideman, "Colloquium: Aligning molecules with strong laser pulses", Rev. Mod. Phys. **75**, 543 (2003).

[98] F. Krausz and M. Ivanov, "Attosecond physics", Rev. Mod. Phys. **81**, 163 (2009).

[99] A. I. M. Rae, *Quantum mechanics*, 5th ed. (Taylor & Francis, 2007).

[100] M. Born and R. Oppenheimer, "Zur Quantentheorie der Molekeln", Ann. Phys. **389**, 457 (1927).

[101] M. Born and K. Huang, *Dynamical theory of crystal lattices* (Oxford University Press, 1955).

[102] H. J. Monkhorst, "Chemical physics without the Born-Oppenheimer approximation: The molecular coupled-cluster method", Phys. Rev. A **36**, 1544 (1987).

[103]   F. Hummel, P. Schmelcher, and M. T. Eiles, "Vibronic interactions in trilobite and butterfly Rydberg molecules", Phys. Rev. Res. **5**, 013114 (2023).

[104]   G. A. Worth and L. S. Cederbaum, "Beyond Born-Oppenheimer: Molecular Dynamics Through a Conical Intersection", Annu. Rev. Phys. Chem. **55**, 127 (2004).

[105]   W. Domcke, D. Yarkony, and H. Köppel, *Conical intersections: electronic structure, dynamics & spectroscopy*, Vol. 15 (World Scientific, 2004).

[106]   J. Larson, E. Sjöqvist, and P. Öhberg, *Conical intersections in physics* (Springer, 2020).

[107]   W. Domcke and D. R. Yarkony, "Role of Conical Intersections in Molecular Spectroscopy and Photoinduced Chemical Dynamics", Annu. Rev. Phys. Chem. **63**, 325 (2012).

[108]   C. Zener and R. H. Fowler, "Non-adiabatic crossing of energy levels", Proc. R. Soc. Lond. A **137**, 696 (1932).

[109]   D. J. Griffiths, *Introduction to electrodynamics*, 4th ed. (Cambridge University Press, 2017).

[110]   A. Stone, *The Theory of Intermolecular Forces*, 2nd ed. (Oxford University Press, Jan. 2013).

[111]   J. Pérez-Ríos, *An Introduction to Cold and Ultracold Chemistry*, 1st ed. (Springer Cham, 2021).

[112]   T. Karman, M. Tomza, and J. Pérez-Ríos, "Ultracold chemistry as a testbed for few-body physics", Nat. Phys. (2024).

[113]   P. S. Peter Ring, *The Nuclear Many-Body Problem*, 1st ed. (Springer-Verlag Berlin Heidelberg, 1980).

[114]   A. Szabo and N. S. Ostlund, *Modern quantum chemistry: introduction to advanced electronic structure theory*, Dover Books on Chemistry (Dover Publications, 1996).

[115]   M. J. Seaton, "Quantum defect theory", Rep. Prog. Phys. **46**, 167 (1983).

[116]   Z. Idziaszek, T. Calarco, P. S. Julienne, and A. Simoni, "Quantum theory of ultracold atom-ion collisions", Phys. Rev. A **79**, 010702 (2009).

[117]   B. Gao, "Universal Properties in Ultracold Ion-Atom Interactions", Phys. Rev. Lett. **104**, 213201 (2010).

[118]   Z. Idziaszek, T. Calarco, P. S. Julienne, and A. Simoni, "Quantum theory of ultracold atom-ion collisions", Phys. Rev. A **79**, 010702 (2009).

[119]   J. M. Schurer, P. Schmelcher, and A. Negretti, "Ground-state properties of ultracold trapped bosons with an immersed ionic impurity", Phys. Rev. A **90**, 033601 (2014).

[120]   J. Pérez-Ríos and C. H. Greene, "Communication: Classical threshold law for ion-neutral-neutral three-body recombination", J. Chem. Phys. **143**, 041105 (2015).

[121]   A. Krükow, A. Mohammadi, A. Härter, J. H. Denschlag, J. Pérez-Ríos, and C. H. Greene, "Energy Scaling of Cold Atom-Atom-Ion Three-Body Recombination", Phys. Rev. Lett. **116**, 193201 (2016).

[122]   J. Pérez-Ríos and C. H. Greene, "Universal temperature dependence of the ion-neutral-neutral three-body recombination rate", Phys. Rev. A **98**, 062707 (2018).

[123]   A. Mohammadi, A. Krükow, A. Mahdian, M. Deiß, J. Pérez-Ríos, H. da Silva, M. Raoult, O. Dulieu, and J. Hecker Denschlag, "Life and death of a cold BaRb$^+$ molecule inside an ultracold cloud of Rb atoms", Phys. Rev. Res. **3**, 013196 (2021).

[124]   M. Mirahmadi and J. Pérez-Ríos, "Ion-atom-atom three-body recombination: From the cold to the thermal regime", J. Chem. Phys. **158**, 024103 (2023).

[125]   C. R. Harris, K. J. Millman, S. J. van der Walt, R. Gommers, P. Virtanen, D. Cournapeau, E. Wieser, J. Taylor, S. Berg, N. J. Smith, R. Kern, M. Picus, S. Hoyer, M. H. van Kerkwijk, M. Brett, A. Haldane, J. F. del Río, M. Wiebe, P. Peterson, P. Gérard-Marchant, K. Sheppard, T. Reddy, W. Weckesser, H. Abbasi, C. Gohlke, and T. E. Oliphant, "Array programming with NumPy", Nature **585**, 357 (2020).

[126] E. Anderson, Z. Bai, C. Bischof, S. Blackford, J. Demmel, J. Dongarra, J. Du Croz, A. Greenbaum, S. Hammarling, A. McKenney, and D. Sorensen, *LAPACK users' guide*, 3rd ed. (Society for Industrial and Applied Mathematics, Philadelphia, PA, 1999).

[127] H. Friedrich, *Theoretical Atomic Physics*, 4th ed. (Springer International Publishing AG, 2017).

[128] F. Gounand, "Calculation of radial matrix elements and radiative lifetimes for highly excited states of alkali atoms using the Coulomb approximation", J. Phys. France **40**, 457 (1979).

[129] R. J. LeVeque, *Finite Difference Methods for Ordinary and Partial Differential Equations*, 1st ed. (Society for Industrial and Applied Mathematics, 2007).

[130] R. Orús, "Tensor networks for complex quantum systems", Nat. Rev. Phys. **1**, 538 (2019).

[131] U. Schollwöck, "The density-matrix renormalization group", Rev. Mod. Phys. **77**, 259 (2005).

[132] U. Schollwöck, "The density-matrix renormalization group in the age of matrix product states", Ann. Phys. (N. Y.) **326**, 96 (2011).

[133] N. Shibata, "Thermodynamics of the Anisotropic Heisenberg Chain Calculated by the Density Matrix Renormalization Group Method", J. Phys. Soc. Jpn. **66**, 2221 (1997).

[134] A. Mering and M. Fleischhauer, "One-dimensional Bose-Fermi-Hubbard model in the heavy-fermion limit", Phys. Rev. A **77**, 023601 (2008).

[135] A. W. Sandvik, "Ground States of a Frustrated Quantum Spin Chain with Long-Range Interactions", Phys. Rev. Lett. **104**, 137204 (2010).

[136] H.-D. Meyer, U. Manthe, and L. Cederbaum, "The multi-configurational time-dependent Hartree approach", Chem. Phys. Lett. **165**, 73 (1990).

[137] U. Manthe, H.-D. Meyer, and L. S. Cederbaum, "Wave-packet dynamics within the multiconfiguration Hartree framework: General aspects and application to NOCl", J. Chem. Phys. **97**, 3199 (1992).

[138] U. Manthe, H.-D. Meyer, and L. S. Cederbaum, "Multiconfigurational time-dependent Hartree study of complex dynamics: Photodissociation of NO_2", J. Chem. Phys. **97**, 9062 (1992).

[139] M. Beck, A. Jäckle, G. Worth, and H.-D. Meyer, "The multiconfiguration time-dependent Hartree (MCTDH) method: a highly efficient algorithm for propagating wavepackets", Phys. Rep. **324**, 1 (2000).

[140] H.-D. Meyer, F. Gatti, and G. A. Worth, *Multidimensional Quantum Dynamics: MCTDH Theory and Applications*, 1st ed. (Wiley-VCH Verlag GmbH, 2009).

[141] R. Kosloff and H. Tal-Ezer, "A direct relaxation method for calculating eigenfunctions and eigenvalues of the Schrödinger equation on a grid", Chem. Phys. Lett. **127**, 223 (1986).

[142] F. Gatti, B. Lasorne, H.-D. Meyer, and A. Nauts, *Applications of Quantum Dynamics in Chemistry*, 1st ed., Lecture Notes in Chemistry (Springer International Publishing AG, 2017).

[143] H.-D. Meyer and G. A. Worth, "Quantum molecular dynamics: propagating wavepackets and density operators using the multiconfiguration time-dependent Hartree method", Theor. Chem. Acc **109**, 251 (2003).

[144] H. Wang, "Iterative Calculation of Energy Eigenstates Employing the Multilayer Multiconfiguration Time-Dependent Hartree Theory", J. Phys. Chem. A **118**, 9253 (2014).

[145] H. Wang, "Multilayer Multiconfiguration Time-Dependent Hartree Theory", J. Phys. Chem. A **119**, 7951 (2015).

[146] F. Köhler, "Exploring Ultracold Quantum Many-Body Systems with Multi-Layer Multi-Configurational Approaches", PhD thesis (Universität Hamburg, 2023).

[147] H.-D. Meyer, F. L. Quéré, C. Léonard, and F. Gatti, "Calculation and selective population of vibrational levels with the Multiconfiguration Time-Dependent Hartree (MCTDH) algorithm", Chem. Phys. **329**, 179 (2006).

[148] H.-D. Meyer, "Studying molecular quantum dynamics with the multiconfiguration time-dependent Hartree method", WIREs Comput. Mol. Sci. **2**, 351 (2012).

[149] S. Zöllner, H.-D. Meyer, and P. Schmelcher, "Ultracold few-boson systems in a double-well trap", Phys. Rev. A **74**, 053612 (2006).

[150] S. Zöllner, H.-D. Meyer, and P. Schmelcher, "Excitations of few-boson systems in one-dimensional harmonic and double wells", Phys. Rev. A **75**, 043608 (2007).

[151] S. Zöllner, H.-D. Meyer, and P. Schmelcher, "Few-Boson Dynamics in Double Wells: From Single-Atom to Correlated Pair Tunneling", Phys. Rev. Lett. **100**, 040401 (2008).

[152] L. Cao, I. Brouzos, S. Zöllner, and P. Schmelcher, "Interaction-driven interband tunneling of bosons in the triple well", New J. Phys. **13**, 033032 (2011).

[153] H. Wang and M. Thoss, "Multilayer formulation of the multiconfiguration time-dependent Hartree theory", J. Chem. Phys. **119**, 1289 (2003).

[154] U. Manthe, "A multilayer multiconfigurational time-dependent Hartree approach for quantum dynamics on general potential energy surfaces", J. Chem. Phys. **128**, 164116 (2008).

[155] M. Pyzh, K. Keiler, S. I. Mistakidis, and P. Schmelcher, "Entangling Lattice-Trapped Bosons with a Free Impurity: Impact on Stationary and Dynamical Properties", Entropy **23**, 290 (2021).

[156] F. Theel, K. Keiler, S. I. Mistakidis, and P. Schmelcher, "Many-body collisional dynamics of impurities injected into a double-well trapped Bose-Einstein condensate", Phys. Rev. Res. **3**, 023068 (2021).

[157] J. Becker, M. Pyzh, and P. Schmelcher, "Interaction-controlled impurity transport in trapped mixtures of ultracold bosons", Phys. Rev. A **106**, 053314 (2022).

[158] F. Theel, S. I. Mistakidis, K. Keiler, and P. Schmelcher, "Counterflow dynamics of two correlated impurities immersed in a bosonic gas", Phys. Rev. A **105**, 053314 (2022).

[159] F. Theel, S. I. Mistakidis, and P. Schmelcher, "Crossover from attractive to repulsive induced interactions and bound states of two distinguishable Bose polarons", SciPost Phys. **16**, 023 (2024).

[160] N. Gourianov, M. Lubasch, S. Dolgov, Q. Y. van den Berg, H. Babaee, P. Givi, M. Kiffner, and D. Jaksch, "A quantum-inspired approach to exploit turbulence structures", Nat. Comput. Sci. **2**, 30 (2022).

[161] A. I. Streltsov, O. E. Alon, and L. S. Cederbaum, "Role of Excited States in the Splitting of a Trapped Interacting Bose-Einstein Condensate by a Time-Dependent Barrier", Phys. Rev. Lett. **99**, 030402 (2007).

[162] O. E. Alon, A. I. Streltsov, and L. S. Cederbaum, "Multiconfigurational time-dependent Hartree method for bosons: Many-body dynamics of bosonic systems", Phys. Rev. A **77**, 033613 (2008).

[163] J. Caillat, J. Zanghellini, M. Kitzler, O. Koch, W. Kreuzer, and A. Scrinzi, "Correlated multielectron systems in strong laser fields: A multiconfiguration time-dependent Hartree-Fock approach", Phys. Rev. A **71**, 012712 (2005).

[164] E. Fasshauer and A. U. J. Lode, "Multiconfigurational time-dependent Hartree method for fermions: Implementation, exactness, and few-fermion tunneling to open space", Phys. Rev. A **93**, 033635 (2016).

[165] S. Krönke, L. Cao, O. Vendrell, and P. Schmelcher, "Non-equilibrium quantum dynamics of ultracold atomic mixtures: the multi-layer multi-configuration time-dependent Hartree method for bosons", New J. Phys. **15**, 063018 (2013).

[166] L. Cao, S. Krönke, O. Vendrell, and P. Schmelcher, "The multi-layer multi-configuration time-dependent Hartree method for bosons: Theory, implementation, and applications", J. Chem. Phys. **139**, 134103 (2013).

[167]   L. Cao, V. Bolsinger, S. I. Mistakidis, G. M. Koutentakis, S. Krönke, J. M. Schurer, and P. Schmelcher, "A unified ab initio approach to the correlated quantum dynamics of ultracold fermionic and bosonic mixtures", J. Chem. Phys. **147**, 044106 (2017).

[168]   F. Köhler and P. Schmelcher, "Bosonic quantum dynamics following colliding potential wells", Phys. Rev. A **103**, 043326 (2021).

[169]   F. Theel, K. Keiler, S. I. Mistakidis, and P. Schmelcher, "Entanglement-assisted tunneling dynamics of impurities in a double well immersed in a bath of lattice trapped bosons", New J. Phys. **22**, 023027 (2020).

[170]   J. Chen, K. Keiler, G. Xianlong, and P. Schmelcher, "Impurity-induced quantum chaos for an ultracold bosonic ensemble in a double well", Phys. Rev. A **104**, 033315 (2021).

[171]   K. Keiler, S. Krönke, and P. Schmelcher, "Correlation induced localization of lattice trapped bosons coupled to a Bose–Einstein condensate", New J. Phys. **20**, 033030 (2018).

[172]   K. Keiler and P. Schmelcher, "State engineering of impurities in a lattice by coupling to a Bose gas", New J. Phys. **20**, 103042 (2018).

[173]   A. Becker, G. M. Koutentakis, and P. Schmelcher, "Synthetic dimension-induced pseudo Jahn-Teller effect in one-dimensional confined fermions", Phys. Rev. Res. **6**, 013257 (2024).

[174]   F. Hummel, K. Keiler, and P. Schmelcher, "Electric-field-induced wave-packet dynamics and geometrical rearrangement of trilobite Rydberg molecules", Phys. Rev. A **103**, 022827 (2021).

[175]   J. M. Schurer, A. Negretti, and P. Schmelcher, "Capture dynamics of ultracold atoms in the presence of an impurity ion", New J. Phys. **17**, 083024 (2015).

[176]   J. M. Schurer, R. Gerritsma, P. Schmelcher, and A. Negretti, "Impact of many-body correlations on the dynamics of an ion-controlled bosonic Josephson junction", Phys. Rev. A **93**, 063602 (2016).

[177]   F. Köhler, R. Mukherjee, and P. Schmelcher, "Exploring disordered quantum spin models with a multilayer multiconfigurational approach", Phys. Rev. Res. **5**, 023135 (2023).

[178]   C. Fey, F. Hummel, and P. Schmelcher, "Ultralong-range Rydberg molecules", Mol. Phys. **118**, e1679401 (2020).

[179]   S. Hollerith and J. Zeiher, "Rydberg Macrodimers: Diatomic Molecules on the Micrometer Scale", J. Phys. Chem. A **127**, 3925 (2023).

[180]   T. Kazimierczuk, D. Fröhlich, S. Scheel, H. Stolz, and M. Bayer, "Giant Rydberg excitons in the copper oxide Cu2O", Nature **514**, 343 (2014).

[181]   J. Heckötter, M. Freitag, D. Fröhlich, M. Aßmann, M. Bayer, M. A. Semina, and M. M. Glazov, "Scaling laws of Rydberg excitons", Phys. Rev. B **96**, 125142 (2017).

[182]   A. L. Hunter, M. T. Eiles, A. Eisfeld, and J. M. Rost, "Rydberg Composites", Phys. Rev. X **10**, 031046 (2020).

[183]   A. Artusio-Glimpse, M. T. Simons, N. Prajapati, and C. L. Holloway, "Modern RF Measurements With Hot Atoms: A Technology Review of Rydberg Atom-Based Radio Frequency Field Sensors", IEEE Microw. Mag. **23**, 44 (2022).

[184]   O. Firstenberg, C. S. Adams, and S. Hofferberth, "Nonlinear quantum optics mediated by Rydberg interactions", J. Phys. B: At. Mol. Opt. Phys. **49**, 152003 (2016).

[185]   M. Saffman, T. G. Walker, and K. Mølmer, "Quantum information with Rydberg atoms", Rev. Mod. Phys. **82**, 2313 (2010).

[186]   X. Wu, X. Liang, Y. Tian, F. Yang, C. Chen, Y.-C. Liu, M. K. Tey, and L. You, "A concise review of Rydberg atom based quantum computation and quantum simulation", Chin. Phys. B **30**, 020305 (2021).

[187] S. Ye, X. Zhang, F. B. Dunning, S. Yoshida, M. Hiller, and J. Burgdörfer, "Efficient three-photon excitation of quasi-one-dimensional strontium Rydberg atoms with $n \sim 300$", Phys. Rev. A **90**, 013401 (2014).

[188] J. R. Rydberg, "XXXIV. On the structure of the line-spectra of the chemical elements", Philos. Mag. **29**, 331 (1890).

[189] N. Bohr, "I. On the constitution of atoms and molecules", Philos. Mag. **26**, 1 (1913).

[190] W. Pauli, "Über das Wasserstoffspektrum vom Standpunkt der neuen Quantenmechanik", Z. Phys. **36**, 336 (1926).

[191] E. Schrödinger, "Quantisierung als Eigenwertproblem", Ann. Phys. (Berl.) **384**, 361 (1926).

[192] T. F. Gallagher, *Rydberg Atoms*, Cambridge Monographs on Atomic, Molecular and Chemical Physics (Cambridge University Press, 1994).

[193] C. Füchtbauer and F. Gössler, "Entgegengesetzte Unsymmetrie der Verbreiterung bei verschiedenen Linien einer Serie", Naturwissenschaften **21**, 315 (1933).

[194] C. Füchtbauer and F. Gössler, "Verschiebung und unsymmetrische Verbreiterung von Absorptionslinien durch Fremdgase", Z. Phys. **87**, 89 (1934).

[195] C. Füchtbauer, P. Schulz, and A. F. Brandt, "Verschiebung von hohen Serienlinien des Natriums und Kaliums durch Fremdgase, Berechnung der Wirkungsquerschnitte von Edelgasen gegen sehr langsame Elektronen", Z. Phys. **90**, 403 (1934).

[196] E. AMALDI and E. SEGRÉ, "Effect of Pressure on High Terms of Alkaline Spectra", Nature **133**, 141 (1934).

[197] E. Fermi, "Sopra lo Spostamento per Pressione delle Righe Elevate delle Serie Spettrali", Il Nuovo Cimento **11**, 157 (1934).

[198] B. Höglund and P. G. Mezger, "Hydrogen emission line $n_{110} \to n_{109}$: detection at 5009 megahertz in galactic H II regions", Science **150**, 339 (1965).

[199] R. L. Sorochenko and é. V. Borodzich, "Detection of a Radio Line Due to Excited Hydrogen in the Nebula NGC 6618 (Omega)", Dokl. Phys. **10**, 588 (1966).

[200] T. W. Hänsch, "Repetitively Pulsed Tunable Dye Laser for High Resolution Spectroscopy", Appl. Opt. **11**, 895 (1972).

[201] C. Fabre, P. Goy, and S. Haroche, "Millimetre resonances in Na Rydberg levels detected by field ionization: quantum defects and Stark-effect studies", J. Phys. B: At. Mol. Opt. Phys. **10**, L183 (1977).

[202] T. F. Gallagher, L. M. Humphrey, R. M. Hill, W. E. Cooke, and S. A. Edelstein, "Fine-structure intervals and polarizabilities of highly excited p and d states of sodium", Phys. Rev. A **15**, 1937 (1977).

[203] C. Fabre, S. Haroche, and P. Goy, "Millimeter spectroscopy in sodium Rydberg states: Quantum-defect, fine-structure, and polarizability measurements", Phys. Rev. A **18**, 229 (1978).

[204] S. Haroche, "Nobel Lecture: Controlling photons in a box and exploring the quantum to classical boundary", Rev. Mod. Phys. **85**, 1083 (2013).

[205] M. Gross, P. Goy, C. Fabre, S. Haroche, and J. M. Raimond, "Maser Oscillation and Microwave Superradiance in Small Systems of Rydberg Atoms", Phys. Rev. Lett. **43**, 343 (1979).

[206] G. Nogues, A. Rauschenbeutel, S. Osnaghi, M. Brune, J. M. Raimond, and S. Haroche, "Seeing a single photon without destroying it", Nature **400**, 239 (1999).

[207] I. Waki, S. Kassner, G. Birkl, and H. Walther, "Observation of ordered structures of laser-cooled ions in a quadrupole storage ring", Phys. Rev. Lett. **68**, 2007 (1992).

[208] G. Birkl, S. Kassner, and H. Walther, "Multiple-shell structures of laser-cooled ^{24}Mg$^+$ ions in a quadrupole storage ring", Nature **357**, 310 (1992).

[209] D. Jaksch, J. I. Cirac, P. Zoller, S. L. Rolston, R. Côté, and M. D. Lukin, "Fast Quantum Gates for Neutral Atoms", Phys. Rev. Lett. **85**, 2208 (2000).

[210] M. D. Lukin, M. Fleischhauer, R. Cote, L. M. Duan, D. Jaksch, J. I. Cirac, and P. Zoller, "Dipole Blockade and Quantum Information Processing in Mesoscopic Atomic Ensembles", Phys. Rev. Lett. **87**, 037901 (2001).

[211] M. Saffman, "Quantum computing with neutral atoms", Natl. Sci. Rev. **6**, 24 (2018).

[212] J. Kumlin, C. Braun, C. Tresp, N. Stiesdal, S. Hofferberth, and A. Paris-Mandoki, "Quantum optics with Rydberg superatoms", J. Phys. Commun. **7**, 052001 (2023).

[213] C. Boisseau, I. Simbotin, and R. Côté, "Macrodimers: Ultralong Range Rydberg Molecules", Phys. Rev. Lett. **88**, 133004 (2002).

[214] S. M. Farooqi, D. Tong, S. Krishnan, J. Stanojevic, Y. P. Zhang, J. R. Ensher, A. S. Estrin, C. Boisseau, R. Côté, E. E. Eyler, and P. L. Gould, "Long-Range Molecular Resonances in a Cold Rydberg Gas", Phys. Rev. Lett. **91**, 183002 (2003).

[215] N. Samboy and R. Côté, "Rubidium Rydberg macrodimers", J. Phys. B: At. Mol. Opt. Phys. **44**, 184006 (2011).

[216] M. Kiffner, H. Park, W. Li, and T. F. Gallagher, "Dipole-dipole-coupled double-Rydberg molecules", Phys. Rev. A **86**, 031401 (2012).

[217] M. Kiffner, M. Huo, W. Li, and D. Jaksch, "Few-body bound states of dipole-dipole-interacting Rydberg atoms", Phys. Rev. A **89**, 052717 (2014).

[218] H. Saßmannshausen and J. Deiglmayr, "Observation of Rydberg-Atom Macrodimers: Micrometer-Sized Diatomic Molecules", Phys. Rev. Lett. **117**, 083401 (2016).

[219] X. Han, S. Bai, Y. Jiao, L. Hao, Y. Xue, J. Zhao, S. Jia, and G. Raithel, "Cs $62D_J$ rydberg-atom macrodimers formed by long-range multipole interaction", Phys. Rev. A **97**, 031403 (2018).

[220] S. Hollerith, J. Zeiher, J. Rui, A. Rubio-Abadal, V. Walther, T. Pohl, D. M. Stamper-Kurn, I. Bloch, and C. Gross, "Quantum gas microscopy of Rydberg macrodimers", Science **364**, 664 (2019).

[221] F. Robicheaux and J. V. Hernández, "Many-body wave function in a dipole blockade configuration", Phys. Rev. A **72**, 063403 (2005).

[222] H. Weimer, R. Löw, T. Pfau, and H. P. Büchler, "Quantum Critical Behavior in Strongly Interacting Rydberg Gases", Phys. Rev. Lett. **101**, 250601 (2008).

[223] B. Olmos, M. Müller, and I. Lesanovsky, "Thermalization of a strongly interacting 1D Rydberg lattice gas", New J. Phys. **12**, 013024 (2010).

[224] I. Lesanovsky, B. Olmos, and J. P. Garrahan, "Thermalization in a Coherently Driven Ensemble of Two-Level Systems", Phys. Rev. Lett. **105**, 100603 (2010).

[225] T. Pohl, E. Demler, and M. D. Lukin, "Dynamical Crystallization in the Dipole Blockade of Ultracold Atoms", Phys. Rev. Lett. **104**, 043002 (2010).

[226] J. Schachenmayer, I. Lesanovsky, A. Micheli, and A. J. Daley, "Dynamical crystal creation with polar molecules or Rydberg atoms in optical lattices", New J. Phys. **12**, 103044 (2010).

[227] H. Weimer and H. P. Büchler, "Two-Stage Melting in Systems of Strongly Interacting Rydberg Atoms", Phys. Rev. Lett. **105**, 230403 (2010).

[228] I. Lesanovsky, "Many-Body Spin Interactions and the Ground State of a Dense Rydberg Lattice Gas", Phys. Rev. Lett. **106**, 025301 (2011).

[229] R. Mukherjee, J. Millen, R. Nath, M. P. A. Jones, and T. Pohl, "Many-body physics with alkaline-earth Rydberg lattices", J. Phys. B: At. Mol. Opt. Phys. **44**, 184010 (2011).

[230] C. H. Greene, A. S. Dickinson, and H. R. Sadeghpour, "Creation of Polar and Nonpolar Ultra-Long-Range Rydberg Molecules", Phys. Rev. Lett. **85**, 2458 (2000).

[231] V. Bendkowsky, B. Butscher, J. Nipper, J. P. Shaffer, R. Löw, and T. Pfau, "Observation of ultralong-range Rydberg molecules", Nature **458**, 1005 (2009).

[232] V. Bendkowsky, B. Butscher, J. Nipper, J. B. Balewski, J. P. Shaffer, R. Löw, T. Pfau, W. Li, J. Stanojevic, T. Pohl, and J. M. Rost, "Rydberg Trimers and Excited Dimers Bound by Internal Quantum Reflection", Phys. Rev. Lett. **105**, 163201 (2010).

[233] W. Li, T. Pohl, J. M. Rost, S. T. Rittenhouse, H. R. Sadeghpour, J. Nipper, B. Butscher, J. B. Balewski, V. Bendkowsky, R. Löw, and T. Pfau, "A Homonuclear Molecule with a Permanent Electric Dipole Moment", Science **334**, 1110 (2011).

[234] T. Niederprüm, O. Thomas, T. Eichert, C. Lippe, J. Pérez-Ríos, C. H. Greene, and H. Ott, "Observation of pendular butterfly Rydberg molecules", Nat. Commun. **7**, 12820 (2016).

[235] D. Booth, S. T. Rittenhouse, J. Yang, H. R. Sadeghpour, and J. P. Shaffer, "Production of trilobite Rydberg molecule dimers with kilo-Debye permanent electric dipole moments", Science **348**, 99 (2015).

[236] B. Butscher, V. Bendkowsky, J. Nipper, J. B. Balewski, L. Kukota, R. Löw, T. Pfau, W. Li, T. Pohl, and J. M. Rost, "Lifetimes of ultralong-range Rydberg molecules in vibrational ground and excited states", J. Phys. B: At. Mol. Opt. Phys. **44**, 184004 (2011).

[237] I. C. H. Liu and J. M. Rost, "Polyatomic molecules formed with a Rydberg atom in an ultracold environment", Eur. Phys. J. D - At. Mol. Opt. Plas. Phys. **40**, 65 (2006).

[238] I. C. H. Liu, J. Stanojevic, and J. M. Rost, "Ultra-Long-Range Rydberg Trimers with a Repulsive Two-Body Interaction", Phys. Rev. Lett. **102**, 173001 (2009).

[239] C. Fey, M. Kurz, and P. Schmelcher, "Stretching and bending dynamics in triatomic ultralong-range Rydberg molecules", Phys. Rev. A **94**, 012516 (2016).

[240] J. A. Fernández, P. Schmelcher, and R. González-Férez, "Ultralong-range triatomic Rydberg molecules in an electric field", J. Phys. B: At. Mol. Opt. Phys. **49**, 124002 (2016).

[241] P. J. J. Luukko and J.-M. Rost, "Polyatomic Trilobite Rydberg Molecules in a Dense Random Gas", Phys. Rev. Lett. **119**, 203001 (2017).

[242] C. Fey, F. Hummel, and P. Schmelcher, "Building principle of triatomic trilobite Rydberg molecules", Phys. Rev. A **99**, 022506 (2019).

[243] C. Fey, J. Yang, S. T. Rittenhouse, F. Munkes, M. Baluktsian, P. Schmelcher, H. R. Sadeghpour, and J. P. Shaffer, "Effective three-body interactions in Cs($6s$)-Cs(nd) rydberg trimers", Phys. Rev. Lett. **122**, 103001 (2019).

[244] R. González-Férez, H. R. Sadeghpour, and P. Schmelcher, "Rotational hybridization, and control of alignment and orientation in triatomic ultralong-range Rydberg molecules", New J. Phys. **17**, 013021 (2015).

[245] J. Aguilera-Fernández, H. R. Sadeghpour, P. Schmelcher, and R. González-Férez, "Electronic structure of ultralong-range Rydberg penta-atomic molecules with two polar diatomic molecules", Phys. Rev. A **96**, 052509 (2017).

[246] R. González-Férez, S. T. Rittenhouse, P. Schmelcher, and H. R. Sadeghpour, "A protocol to realize triatomic ultralong range Rydberg molecules in an ultracold KRb gas", J. Phys. B: At. Mol. Opt. Phys. **53**, 074002 (2020).

[247] D. Mellado-Alcedo, A. Guttridge, S. L. Cornish, H. Sadeghpour, and R. Gonzalez-Ferez, "Ultralong-range Cs-RbCs Rydberg molecules: non-adiabaticity of dipole moments", arXiv:2401.09618 (2024).

[248] R. Schmidt, H. R. Sadeghpour, and E. Demler, "Mesoscopic Rydberg Impurity in an Atomic Quantum Gas", Phys. Rev. Lett. **116**, 105302 (2016).

[249] F. Camargo, R. Schmidt, J. D. Whalen, R. Ding, G. Woehl, S. Yoshida, J. Burgdörfer, F. B. Dunning, H. R. Sadeghpour, E. Demler, and T. C. Killian, "Creation of Rydberg Polarons in a Bose Gas", Phys. Rev. Lett. **120**, 083401 (2018).

[250] R. Schmidt, J. D. Whalen, R. Ding, F. Camargo, G. Woehl, S. Yoshida, J. Burgdörfer, F. B. Dunning, E. Demler, H. R. Sadeghpour, and T. C. Killian, "Theory of excitation of Rydberg polarons in an atomic quantum gas", Phys. Rev. A **97**, 022707 (2018).

[251] M. T. Eiles, A. L. Hunter, and J. M. Rost, "Ring Rydberg composites", J. Phys. B: At. Mol. Opt. Phys. **53**, 054001 (2020).

[252] M. T. Eiles, A. Eisfeld, and J. M. Rost, "Anderson localization of a Rydberg electron", Phys. Rev. Res. **5**, 033032 (2023).

[253] M. T. Eiles, C. W. Wächtler, A. Eisfeld, and J. M. Rost, "Topological edge states in a Rydberg composite", Phys. Rev. B **109**, 075422 (2024).

[254] J. D. Whalen, S. K. Kanungo, R. Ding, M. Wagner, R. Schmidt, H. R. Sadeghpour, S. Yoshida, J. Burgdörfer, F. B. Dunning, and T. C. Killian, "Probing nonlocal spatial correlations in quantum gases with ultra-long-range Rydberg molecules", Phys. Rev. A **100**, 011402 (2019).

[255] M. O. Vieitez, T. I. Ivanov, E. Reinhold, C. A. de Lange, and W. Ubachs, "Observation of a Rydberg Series in H^+H^-: A Heavy Bohr Atom", Phys. Rev. Lett. **101**, 163001 (2008).

[256] F. Engel, T. Dieterle, F. Hummel, C. Fey, P. Schmelcher, R. Löw, T. Pfau, and F. Meinert, "Precision Spectroscopy of Negative-Ion Resonances in Ultralong-Range Rydberg Molecules", Phys. Rev. Lett. **123**, 073003 (2019).

[257] F. Hummel, P. Schmelcher, H. Ott, and H. R. Sadeghpour, "An ultracold heavy Rydberg system formed from ultra-long-range molecules bound in a stairwell potential", New J. Phys. **22**, 063060 (2020).

[258] F. Hummel, M. T. Eiles, and P. Schmelcher, "Synthetic Dimension-Induced Conical Intersections in Rydberg Molecules", Phys. Rev. Lett. **127**, 023003 (2021).

[259] R. Srikumar, F. Hummel, and P. Schmelcher, "Nonadiabatic interaction effects in the spectra of ultralong-range Rydberg molecules", Phys. Rev. A **108**, 012809 (2023).

[260] M. T. Eiles and F. Hummel, "Kato's theorem and ultralong-range Rydberg molecules", Phys. Rev. A **109**, 022811 (2024).

[261] R. J. Le Roy, "Long-range potential coefficients from RKR turning points: C_6 and C_8 for $B(3\Pi_{Ou}^+)$-state Cl_2, Br_2, and I_2", Can. J. Phys. **52**, 246 (1974).

[262] M. E. Rose, "The Electrostatic Interaction of Two Arbitrary Charge Distributions", J. Math. Phys. **37**, 215 (1958).

[263] P. R. Fontana, "Theory of Long-Range Interatomic Forces. I. Dispersion Energies between Unexcited Atoms", Phys. Rev. **123**, 1865 (1961).

[264] A. Dalgarno and W. Davison, "The Calculation of Van Der Waals Interactions", in Advances in Atomic and Molecular Physics, Vol. 2, edited by D. Bates and I. Estermann (1966), pp. 1–32.

[265] S. Weber and H. Menke, *Pairinteraction - A Rydberg Interaction Calculator*, `https://github.com/pairinteraction/pairinteraction`, 2017.

[266] S. Weber, C. Tresp, H. Menke, A. Urvoy, O. Firstenberg, H. P. Büchler, and S. Hofferberth, "Calculation of Rydberg interaction potentials", J. Phys. B: At. Mol. Opt. Phys. **50**, 133001 (2017).

[267] N. Samboy and R. Côté, "Rubidium Rydberg linear macrotrimers", Phys. Rev. A **87**, 032512 (2013).

[268] M. Kiffner, W. Li, and D. Jaksch, "Three-Body Bound States in Dipole-Dipole Interacting Rydberg Atoms", Phys. Rev. Lett. **111**, 233003 (2013).

[269] A. Urvoy, F. Ripka, I. Lesanovsky, D. Booth, J. P. Shaffer, T. Pfau, and R. Löw, "Strongly Correlated Growth of Rydberg Aggregates in a Vapor Cell", Phys. Rev. Lett. **114**, 203002 (2015).

[270] M. Marcuzzi, J. ř. Miná ř, D. Barredo, S. de Léséleuc, H. Labuhn, T. Lahaye, A. Browaeys, E. Levi, and I. Lesanovsky, "Facilitation Dynamics and Localization Phenomena in Rydberg Lattice Gases with Position Disorder", Phys. Rev. Lett. **118**, 063606 (2017).

[271] S.-y. Ch'en and M. Takeo, "Broadening and Shift of Spectral Lines Due to the Presence of Foreign Gases", Rev. Mod. Phys. **29**, 20 (1957).

[272] I. Beigman and V. Lebedev, "Collision theory of Rydberg atoms with neutral and charged particles", Phys. Rep. **250**, 95 (1995).

[273] N. Allard and J. Kielkopf, "The effect of neutral nonresonant collisions on atomic spectral lines", Rev. Mod. Phys. **54**, 1103 (1982).

[274] A. Omont, "On the theory of collisions of atoms in Rydberg states with neutral particles", J. Phys. France **38**, 1343 (1977).

[275] E. L. Hamilton, C. H. Greene, and H. R. Sadeghpour, "Shape-resonance-induced long-range molecular rydberg states", J. Phys. B: At. Mol. Opt. Phys. **35**, L199 (2002).

[276] M. T. Eiles, "Trilobites, butterflies, and other exotic specimens of long-range Rydberg molecules", J. Phys. B: At. Mol. Opt. Phys. **52**, 113001 (2019).

[277] T. Secker, N. Ewald, J. Joger, H. Fürst, T. Feldker, and R. Gerritsma, "Trapped Ions in Rydberg-Dressed Atomic Gases", Phys. Rev. Lett. **118**, 263201 (2017).

[278] T. Schmid, C. Veit, N. Zuber, R. Löw, T. Pfau, M. Tarana, and M. Tomza, "Rydberg Molecules for Ion-Atom Scattering in the Ultracold Regime", Phys. Rev. Lett. **120**, 153401 (2018).

[279] N. V. Ewald, T. Feldker, H. Hirzler, H. A. Fürst, and R. Gerritsma, "Observation of Interactions between Trapped Ions and Ultracold Rydberg Atoms", Phys. Rev. Lett. **122**, 253401 (2019).

[280] H. Doerk, Z. Idziaszek, and T. Calarco, "Atom-ion quantum gate", Phys. Rev. A **81**, 012708 (2010).

[281] Ø. Burrau, "Berechnung des Energiewertes des Wasserstoffmolekel-Ions (H_2^+) im Normalzustand", Naturwissenschaften **15**, 16 (1927).

[282] C. Barbero-Petrel, P. Schmelcher, and R. González-Férez, "Flipping electric dipole in the vibrational wave packet dynamics of carbon monoxide", arXiv:2403.04065 (2024).

[283] A. Duspayev and G. Raithel, "Nonadiabatic decay of Rydberg-atom–ion molecules", Phys. Rev. A **105**, 012810 (2022).

[284] S. Hollerith, J. Rui, A. Rubio-Abadal, K. Srakaew, D. Wei, J. Zeiher, C. Gross, and I. Bloch, "Microscopic electronic structure tomography of Rydberg macrodimers", Phys. Rev. Res. **3**, 013252 (2021).

[285] E. Herbst, S. Miller, T. Oka, J. K. Watson, and E. Herbst, "The astrochemistry of H_3^+", Proc. R. Soc. Lond. A **358**, 2523 (2000).

[286] S. Kulin, T. C. Killian, S. D. Bergeson, and S. L. Rolston, "Plasma Oscillations and Expansion of an Ultracold Neutral Plasma", Phys. Rev. Lett. **85**, 318 (2000).

[287] T. C. Killian, T. Pattard, T. Pohl, and J. Rost, "Ultracold neutral plasmas", Phys. Rep. **449**, 77 (2007).

[288] D. Ciampini, M. Anderlini, J. H. Müller, F. Fuso, O. Morsch, J. W. Thomsen, and E. Arimondo, "Photoionization of ultracold and Bose-Einstein-condensed Rb atoms", Phys. Rev. A **66**, 043409 (2002).

[289] W. W. Smith, E. Babenko, R. Cote, and H. H. Michels, "On the collisional cooling of co-trapped atomic and molecular ions by ultracold atoms: Ca^+ + Na and $Na_2^+(v^*, J^*)$ + Na", in Coherence and Quantum Optics VIII, edited by N. P. Bigelow, J. H. Eberly, C. R. Stroud, and I. A. Walmsley (2003), pp. 623–624.

[290] O. P. Makarov, R. Côté, H. Michels, and W. W. Smith, "Radiative charge-transfer lifetime of the excited state of $(NaCa)^+$", Phys. Rev. A **67**, 042705 (2003).

[291] L. Ratschbacher, C. Zipkes, C. Sias, and M. Köhl, "Controlling chemical reactions of a single particle", Nat. Phys. **8**, 649 (2012).

[292] P. Puri, M. Mills, E. P. West, C. Schneider, and E. R. Hudson, "High-resolution collision energy control through ion position modulation in atom-ion hybrid systems", Rev. Sci. Instrum. **89**, 083112 (2018).

[293] A. Härter, A. Krükow, M. Deiß, B. Drews, E. Tiemann, and J. H. Denschlag, "Population distribution of product states following three-body recombination in an ultracold atomic gas", Nat. Phys. **9**, 512 (2013).

[294] J. Wolf, M. Deiß, A. Krükow, E. Tiemann, B. P. Ruzic, Y. Wang, J. P. D'Incao, P. S. Julienne, and J. H. Denschlag, "State-to-state chemistry for three-body recombination in an ultracold rubidium gas", Science **358**, 921 (2017).

[295] L. Ratschbacher, C. Sias, L. Carcagni, J. M. Silver, C. Zipkes, and M. Köhl, "Decoherence of a Single-Ion Qubit Immersed in a Spin-Polarized Atomic Bath", Phys. Rev. Lett. **110**, 160402 (2013).

[296] S. Schmid, A. Härter, and J. H. Denschlag, "Dynamics of a Cold Trapped Ion in a Bose-Einstein Condensate", Phys. Rev. Lett. **105**, 133202 (2010).

[297] Z. Idziaszek, T. Calarco, and P. Zoller, "Controlled collisions of a single atom and an ion guided by movable trapping potentials", Phys. Rev. A **76**, 033409 (2007).

[298] L. Oghittu and A. Negretti, "Quantum-limited thermometry of a Fermi gas with a charged spin particle", Phys. Rev. Res. **4**, 023069 (2022).

[299] J. Joger, A. Negretti, and R. Gerritsma, "Quantum dynamics of an atomic double-well system interacting with a trapped ion", Phys. Rev. A **89**, 063621 (2014).

[300] R. Gerritsma, A. Negretti, H. Doerk, Z. Idziaszek, T. Calarco, and F. Schmidt-Kaler, "Bosonic Josephson Junction Controlled by a Single Trapped Ion", Phys. Rev. Lett. **109**, 080402 (2012).

[301] A. Negretti, R. Gerritsma, Z. Idziaszek, F. Schmidt-Kaler, and T. Calarco, "Generalized Kronig-Penney model for ultracold atomic quantum systems", Phys. Rev. B **90**, 155426 (2014).

[302] U. Bissbort, D. Cocks, A. Negretti, Z. Idziaszek, T. Calarco, F. Schmidt-Kaler, W. Hofstetter, and R. Gerritsma, "Emulating Solid-State Physics with a Hybrid System of Ultracold Ions and Atoms", Phys. Rev. Lett. **111**, 080501 (2013).

[303] F. G. Major and H. G. Dehmelt, "Exchange-Collision Technique for the rf Spectroscopy of Stored Ions", Phys. Rev. **170**, 91 (1968).

[304] R. Blatt, P. Zoller, G. Holzmüller, and I. Siemers, "Brownian motion of a parametric oscillator: A model for ion confinement in radio frequency traps", Z. Phys. D **4**, 121 (1986).

[305] Y. Moriwaki, M. Tachikawa, Y. M. Y. Maeno, and T. S. T. Shimizu, "Collision Cooling of Ions Stored in Quadrupole Radio-Frequency Trap", Jpn. J. App. Phys. **31**, L1640 (1992).

[306] J. C. Pearson, L. C. Oesterling, E. Herbst, and F. C. De Lucia, "Pressure Broadening of Gas Phase Molecular Ions at Very Low Temperature", Phys. Rev. Lett. **75**, 2940 (1995).

[307] M. Cetina, A. T. Grier, and V. Vuletić, "Micromotion-Induced Limit to Atom-Ion Sympathetic Cooling in Paul Traps", Phys. Rev. Lett. **109**, 253201 (2012).

[308] Z. Meir, T. Sikorsky, R. Ben-shlomi, N. Akerman, Y. Dallal, and R. Ozeri, "Dynamics of a Ground-State Cooled Ion Colliding with Ultracold Atoms", Phys. Rev. Lett. **117**, 243401 (2016).

[309] C. Schneider, M. Enderlein, T. Huber, and T. Schaetz, "Optical trapping of an ion", Nat. Photonics **4**, 772 (2010).

[310] M. Enderlein, T. Huber, C. Schneider, and T. Schaetz, "Single Ions Trapped in a One-Dimensional Optical Lattice", Phys. Rev. Lett. **109**, 233004 (2012).

[311] C. Schneider, M. Enderlein, T. Huber, S. Dürr, and T. Schaetz, "Influence of static electric fields on an optical ion trap", Phys. Rev. A **85**, 013422 (2012).

[312]   T. Schaetz, "Trapping ions and atoms optically", J. Phys. B: At. Mol. Opt. Phys. **50**, 102001 (2017).

[313]   A. Lambrecht, J. Schmidt, P. Weckesser, M. Debatin, L. Karpa, and T. Schaetz, "Long lifetimes and effective isolation of ions in optical and electrostatic traps", Nat. Photonics **11**, 704 (2017).

[314]   J. Schmidt, P. Weckesser, F. Thielemann, T. Schaetz, and L. Karpa, "Optical Traps for Sympathetic Cooling of Ions with Ultracold Neutral Atoms", Phys. Rev. Lett. **124**, 053402 (2020).

[315]   L. Karpa, "Interactions of Ions and Ultracold Neutral Atom Ensembles in Composite Optical Dipole Traps: Developments and Perspectives", Atoms **9**, 39 (2021).

[316]   B. Höltkemeier, P. Weckesser, H. López-Carrera, and M. Weidemüller, "Buffer-Gas Cooling of a Single Ion in a Multipole Radio Frequency Trap Beyond the Critical Mass Ratio", Phys. Rev. Lett. **116**, 233003 (2016).

[317]   S. Haze, M. Sasakawa, R. Saito, R. Nakai, and T. Mukaiyama, "Cooling Dynamics of a Single Trapped Ion via Elastic Collisions with Small-Mass Atoms", Phys. Rev. Lett. **120**, 043401 (2018).

[318]   E. Trimby, H. Hirzler, H. Fürst, A. Safavi-Naini, R. Gerritsma, and R. S. Lous, "Buffer gas cooling of ions in radio-frequency traps using ultracold atoms", New J. Phys. **24**, 035004 (2022).

[319]   M. Pinkas, O. Katz, J. Wengrowicz, N. Akerman, and R. Ozeri, "Trap-assisted formation of atom–ion bound states", Nat. Phys. **19**, 1573 (2023).

[320]   C. J. Pethick and H. Smith, *Bose–Einstein Condensation in Dilute Gases*, 2nd ed. (Cambridge University Press, 2008).

[321]   D. S. Petrov, G. V. Shlyapnikov, and J. T. M. Walraven, "Regimes of Quantum Degeneracy in Trapped 1D Gases", Phys. Rev. Lett. **85**, 3745 (2000).

[322]   M. D. Girardeau and E. M. Wright, "Breakdown of Time-Dependent Mean-Field Theory for a One-Dimensional Condensate of Impenetrable Bosons", Phys. Rev. Lett. **84**, 5239 (2000).

[323]   T. Kinoshita, T. Wenger, and D. S. Weiss, "Observation of a One-Dimensional Tonks-Girardeau Gas", Science **305**, 1125 (2004).

[324]   S. I. Mistakidis, T. Mithun, P. G. Kevrekidis, H. R. Sadeghpour, and P. Schmelcher, "Formation and quench of homonuclear and heteronuclear quantum droplets in one dimension", Phys. Rev. Res. **3**, 043128 (2021).

[325]   T. Mithun, S. I. Mistakidis, P. Schmelcher, and P. G. Kevrekidis, "Statistical mechanics of one-dimensional quantum droplets", Phys. Rev. A **104**, 033316 (2021).

[326]   I. A. Englezos, S. I. Mistakidis, and P. Schmelcher, "Correlated dynamics of collective droplet excitations in a one-dimensional harmonic trap", Phys. Rev. A **107**, 023320 (2023).

[327]   G. C. Katsimiga, S. I. Mistakidis, G. N. Koutsokostas, D. J. Frantzeskakis, R. Carretero-González, and P. G. Kevrekidis, "Solitary waves in a quantum droplet-bearing system", Phys. Rev. A **107**, 063308 (2023).

[328]   F. Böttcher, J.-N. Schmidt, M. Wenzel, J. Hertkorn, M. Guo, T. Langen, and T. Pfau, "Transient Supersolid Properties in an Array of Dipolar Quantum Droplets", Phys. Rev. X **9**, 011051 (2019).

[329]   J. Hertkorn, J.-N. Schmidt, M. Guo, F. Böttcher, K. S. H. Ng, S. D. Graham, P. Uerlings, H. P. Büchler, T. Langen, M. Zwierlein, and T. Pfau, "Supersolidity in Two-Dimensional Trapped Dipolar Droplet Arrays", Phys. Rev. Lett. **127**, 155301 (2021).

[330]   J. Hertkorn, J.-N. Schmidt, F. Böttcher, M. Guo, M. Schmidt, K. S. H. Ng, S. D. Graham, H. P. Büchler, T. Langen, M. Zwierlein, and T. Pfau, "Density Fluctuations across the Superfluid-Supersolid Phase Transition in a Dipolar Quantum Gas", Phys. Rev. X **11**, 011037 (2021).

[331]   Y. Makhlin, G. Schön, and A. Shnirman, "Quantum-state engineering with Josephson-junction devices", Rev. Mod. Phys. **73**, 357 (2001).

[332]   F. Verstraete, M. M. Wolf, and J. Ignacio Cirac, "Quantum computation and quantum-state engineering driven by dissipation", Nat. Phys. **5**, 633 (2009).

[333] K. T. McCusker and P. G. Kwiat, "Efficient Optical Quantum State Engineering", Phys. Rev. Lett. **103**, 163602 (2009).

[334] M. A. Nielsen and I. L. Chuang, *Quantum computation and quantum information: 10th anniversary edition* (Cambridge University Press, 2010).

[335] V. Giovannetti, S. Lloyd, and L. Maccone, "Quantum Metrology", Phys. Rev. Lett. **96**, 010401 (2006).

[336] R. Bücker, J. Grond, S. Manz, T. Berrada, T. Betz, C. Koller, U. Hohenester, T. Schumm, A. Perrin, and J. Schmiedmayer, "Twin-atom beams", Nat. Phys. **7**, 608 (2011).

[337] S. Martínez-Garaot, E. Torrontegui, X. Chen, M. Modugno, D. Guéry-Odelin, S.-Y. Tseng, and J. G. Muga, "Vibrational Mode Multiplexing of Ultracold Atoms", Phys. Rev. Lett. **111**, 213001 (2013).

[338] J. J. W. H. Sørensen, M. O. Aranburu, T. Heinzel, and J. F. Sherson, "Quantum optimal control in a chopped basis: Applications in control of Bose-Einstein condensates", Phys. Rev. A **98**, 022119 (2018).

[339] A. Tanaka and T. Cheon, "Complete population inversion of Bose particles by an adiabatic cycle", New J. Phys. **18**, 045023 (2016).

[340] K. W. Madison, F. Chevy, W. Wohlleben, and J. Dalibard, "Vortex Formation in a Stirred Bose-Einstein Condensate", Phys. Rev. Lett. **84**, 806 (2000).

[341] Z. P. Karkuszewski, K. Sacha, and J. Zakrzewski, "Method for collective excitation of a Bose-Einstein condensate", Phys. Rev. A **63**, 061601 (2001).

[342] B. Damski, Z. P. Karkuszewski, K. Sacha, and J. Zakrzewski, "Simple method for excitation of a Bose-Einstein condensate", Phys. Rev. A **65**, 013604 (2001).

[343] B. Damski, K. Sacha, and J. Zakrzewski, "Stirring a Bose–Einstein condensate", J. Phys. B: At. Mol. Opt. Phys. **35**, 4051 (2002).

[344] I. Hans, J. Stockhofe, and P. Schmelcher, "Generating, Dragging, and Releasing Dark Solitons in Elongated Bose-Einstein Condensates", Phys. Rev. A **92**, 013627 (2015).

[345] K. Henderson, C. Ryu, C. MacCormick, and M. G. Boshier, "Experimental demonstration of painting arbitrary and dynamic potentials for Bose–Einstein condensates", New J. Phys. **11**, 043030 (2009).

[346] H. Hirzler and J. Pérez-Ríos, "Rydberg atom-ion collisions in cold environments", Phys. Rev. A **103**, 043323 (2021).

[347] L. Wang, M. Deiß, G. Raithel, and J. H. Denschlag, "Optical control of atom-ion collisions using a Rydberg state", J. Phys. B: At. Mol. Opt. Phys. **53**, 134005 (2020).

[348] C. Gross, T. Vogt, and W. Li, "Ion Imaging via Long-Range Interaction with Rydberg Atoms", Phys. Rev. Lett. **124**, 053401 (2020).

[349] R. Robinett, "Quantum wave packet revivals", Phys. Rep. **392**, 1 (2004).

[350] O. Arısoy, S. Campbell, and Ö. E. Müstecaplıoğlu, "Thermalization of Finite Many-Body Systems by a Collision Model", Entropy **21**, 1182 (2019).

[351] S. C. L. Kamerlin and A. Warshel, "At the dawn of the 21st century: Is dynamics the missing link for understanding enzyme catalysis?", Proteins **78**, 1339 (2010).

[352] R. E. Robson, R. D. White, and Z. L. Petrovi ć, "Colloquium: Physically based fluid modeling of collisionally dominated low-temperature plasmas", Rev. Mod. Phys. **77**, 1303 (2005).

[353] J. Turner and K. Fox, "Minimum dipole moment required to bind an electron to a finite dipole", Phys. Lett. **23**, 547 (1966).

[354] J.-M. Lévy-Leblond, "Electron Capture by Polar Molecules", Phys. Rev. **153**, 1 (1967).

[355] K. R. Lykke, R. D. Mead, and W. C. Lineberger, "Observation of Dipole-Bound States of Negative Ions", Phys. Rev. Lett. **52**, 2221 (1984).

[356] C. Desfrançois, "Determination of electron binding energies of ground-state dipole-bound molecular anions", Phys. Rev. A **51**, 3667 (1995).

[357] C. Desfrançois, H. Abdoul-Carime, N. Khelifa, and J. P. Schermann, "From $\frac{1}{r}$ to $\frac{1}{r^2}$ Potentials: Electron Exchange between Rydberg Atoms and Polar Molecules", Phys. Rev. Lett. **73**, 2436 (1994).

[358] E. Fermi and E. Teller, "The Capture of Negative Mesotrons in Matter", Phys. Rev. **72**, 399 (1947).

[359] A. Guttridge, D. K. Ruttley, A. C. Baldock, R. González-Férez, H. R. Sadeghpour, C. S. Adams, and S. L. Cornish, "Observation of Rydberg Blockade Due to the Charge-Dipole Interaction between an Atom and a Polar Molecule", Phys. Rev. Lett. **131**, 013401 (2023).

[360] H. T. Gaenslen, "Electronic potential energy surfaces of ultralong-range Rydberg molecules in the presence of an ion", Bachelor's thesis (Universität Hamburg, 2022).

[361] H. Conroy, "Molecular Schrödinger Equation. IV. Results for One- and Two-Electron Systems", J. Chem. Phys. **41**, 1341 (1964).

[362] H. Medel-Cobaxin, A. Alijah, and A. Turbiner, "About non-existence of the molecular ion H_3^{++}", Collect. Czech. Chem. Commun. **73**, 1271 (2008).

[363] M. L. Glasser, "Quantum mechanics of a simulated trihydrogen dication", J. Math. Chem. **52**, 2119 (2014).

[364] L. Oghittu, J. Simonet, P. Wessels-Staarmann, M. Drescher, K. Sengstock, L. Mathey, and A. Negretti, "Cooling dynamics of a free ion in a Bose-Einstein condensate", Phys. Rev. Res. **6**, 023024 (2024).

[365] J. W. P. Wilkinson, W. Li, and I. Lesanovsky, "Spectral Signatures of Vibronic Coupling in Trapped Cold Ionic Rydberg Systems", Phys. Rev. Lett. **132**, 223401 (2024).

[366] Z. Zeybek, R. Mukherjee, and P. Schmelcher, "Quantum Phases from Competing Van der Waals and Dipole-Dipole Interactions of Rydberg Atoms", Phys. Rev. Lett. **131**, 203003 (2023).

[367] R. Stock, I. H. Deutsch, and E. L. Bolda, "Quantum State Control via Trap-Induced Shape Resonance in Ultracold Atomic Collisions", Phys. Rev. Lett. **91**, 183201 (2003).

[368] D. K. Ruttley, A. Guttridge, S. Spence, R. C. Bird, C. R. Le Sueur, J. M. Hutson, and S. L. Cornish, "Formation of Ultracold Molecules by Merging Optical Tweezers", Phys. Rev. Lett. **130**, 223401 (2023).

[369] J. Tallant, S. T. Rittenhouse, D. Booth, H. R. Sadeghpour, and J. P. Shaffer, "Observation of Blueshifted Ultralong-Range Cs_2 Rydberg Molecules", Phys. Rev. Lett. **109**, 173202 (2012).

[370] M. A. Bellos, R. Carollo, J. Banerjee, E. E. Eyler, P. L. Gould, and W. C. Stwalley, "Excitation of Weakly Bound Molecules to Trilobitelike Rydberg States", Phys. Rev. Lett. **111**, 053001 (2013).

[371] K. S. Kleinbach, F. Meinert, F. Engel, W. J. Kwon, R. Löw, T. Pfau, and G. Raithel, "Photoassociation of Trilobite Rydberg Molecules via Resonant Spin-Orbit Coupling", Phys. Rev. Lett. **118**, 223001 (2017).

[372] K. Y. Bliokh and F. Nori, "Transverse and longitudinal angular momenta of light", Phys. Rep. **592**, 1 (2015).

[373] J. D. Rodrigues, L. G. Marcassa, and J. T. Mendonça, "Excitation of high orbital angular momentum Rydberg states with Laguerre–Gauss beams", J. Phys. B: At. Mol. Opt. Phys. **49**, 074007 (2016).

[374] M. Maslov, G. M. Koutentakis, M. Hrast, O. H. Heckl, and M. Lemeshko, "Charge density model for the interaction of molecules with vortex beams", arXiv:2310.00095 (2023).

[375] J. Zou and S. D. Hogan, "Absolute static-field magnetometry, magnetic gradiometry, and vector electrometry with circular Rydberg atoms", Phys. Rev. A **107**, 062820 (2023).

[376] M. N. R. Ashfold and S. K. Kim, "Non-Born–Oppenheimer effects in molecular photochemistry: an experimental perspective", Philos. Trans. Royal Soc. A **380**, 20200376 (2022).

[377] N. Moiseyev, M. Šindelka, and L. S. Cederbaum, "Laser-induced conical intersections in molecular optical lattices", J. Phys. B: At. Mol. Opt. Phys. **41**, 221001 (2008).

[378] P. V. Demekhin and L. S. Cederbaum, "Light-induced conical intersections in polyatomic molecules: General theory, strategies of exploitation, and application", J. Chem. Phys. **139**, 154314 (2013).

[379] S. Lepp, P. C. Stancil, and A. Dalgarno, "Atomic and molecular processes in the early Universe", J. Phys. B: At. Mol. Opt. Phys. **35**, R57 (2002).

[380] R. Mukherjee, "Charge dynamics of a molecular ion immersed in a Rydberg-dressed atomic lattice gas", Phys. Rev. A **100**, 013403 (2019).

[381] I. B. Bersuker, "Jahn–Teller and Pseudo-Jahn–Teller Effects: From Particular Features to General Tools in Exploring Molecular and Solid State Properties", Chem. Rev. **121**, 1463 (2021).

[382] M. Kurz and P. Schmelcher, "Electrically dressed ultra-long-range polar Rydberg molecules", Phys. Rev. A **88**, 022501 (2013).

[383] M. Kurz, "Ultralong-range diatomic molecules in external electric and magnetic fields", PhD thesis (Universität Hamburg, 2014).

[384] S. Hollerith, K. Srakaew, D. Wei, A. Rubio-Abadal, D. Adler, P. Weckesser, A. Kruckenhauser, V. Walther, R. van Bijnen, J. Rui, C. Gross, I. Bloch, and J. Zeiher, "Realizing Distance-Selective Interactions in a Rydberg-Dressed Atom Array", Phys. Rev. Lett. **128**, 113602 (2022).

[385] L.-M. Steinert, "Spatially tunable spin interactions with rydberg atoms in optical tweezers", PhD thesis (Universität Tübingen, 2024).

[386] J. Taylor, B. Vargo, D. Hoffman, T. J. Price, and R. C. Forrey, "Formation of antihydrogen molecular ions by associative ionization", Phys. Rev. A **109**, 052816 (2024).

[387] D. DeMille, N. R. Hutzler, A. M. Rey, and T. Zelevinsky, "Quantum sensing and metrology for fundamental physics with molecules", Nat. Phys. (2024).

[388] K. Najafian, Z. Meir, M. Sinhal, and S. Willitsch, "Identification of molecular quantum states using phase-sensitive forces", Nat. Commun. **11**, 4470 (2020).

[389] H. Kübler, J. P. Shaffer, T. Baluktsian, R. Löw, and T. Pfau, "Coherent excitation of Rydberg atoms in micrometre-sized atomic vapour cells", Nat. Photonics **4**, 112 (2010).

[390] F. Ripka, H. Kübler, R. Löw, and T. Pfau, "A room-temperature single-photon source based on strongly interacting Rydberg atoms", Science **362**, 446 (2018).

[391] M. Noaman, H. Amarloo, R. Pandiyan, S. Bobbara, S. Mirzaee, K. Nickerson, C. Liu, D. Booth, and J. P. Shaffer, "Vapor cell characterization and optimization for applications in Rydberg atom-based radio frequency sensing", in Quantum Sensing, Imaging, and Precision Metrology, Vol. 12447, edited by J. Scheuer and S. M. Shahriar (International Society for Optics and Photonics, 2023), p. 124470V.

[392] Rydberg Technologies Inc., *Rydberg Field Measurement System*, Available online at: `https://www.rydbergtechnologies.com/products`, last accessed on 21.06.2024.

[393] A. R. Edmonds, *Angular momentum in quantum mechanics*, 4th ed. (Princeton university press, 1996).

[394] P. C. Ellgen, *Thermodynamics and Chemical Equilibrium*, Available online at: `https://chem.libretexts.org/Bookshelves/Physical_and_Theoretical_Chemistry_Textbook_Maps/Thermodynamics_and_Chemical_Equilibrium_(Ellgen)`, last accessed on 28.06.2024 (CreateSpace Independent Publishing Platform, 2014).

[395] S. Carter and N. Handy, "A Variational Method for the Calculation of Vibrational Levels of Any Triatomic Molecule", Mol. Phys. **47**, 1445 (1982).

[396]   N. Handy, "The Derivation of Vibration-Rotation Kinetic Energy Operators, in Internal Coordinates", Mol. Phys. **61**, 207 (1987).

Acknowledgements

These last years have been quite the journey for me, which may sound strange given the fact that for most of this period I could usually be found seated at a desk, frowning over a computer screen. On a personal level however, this was a time of great change. It was not always plain-sailing, but I am grateful for everything I have learned along the way. Below, I'd like to express my sincere gratitude to the following humans, whom I owe a great deal to.

For the opportunity to pursue this PhD in the first place, and for years of support and guidance, I thank my supervisor Peter. For his time and advice, helping me to keep the bigger picture in mind, I also give thanks to my co-supervisor Christof.

In-between the many periods of confusion, came these rare electrifying moments when finally all the pieces of the puzzle would fall into place. For many such wonderful moments, I am indebted to Maxim and Frederic, who provided significant support to me during our projects together and beyond. Thank you for your time, energy and unfailing patience.

For almost three years, I had the pleasure of working with a group of exceptional people in Stuttgart. To my partners in crime, Moritz and Óscar, I give thanks for the many hours of discussions and work together. Thanks are further due to the whole PI5 team for inviting me to join their group retreats, where I experienced blisters the size of eggs and The Bus Trip from Hell. I also got to see the Alps for the first time which, for a lad who grew up only knowing the gentle hills of southern England, was truly a sight to behold. Thank you for it all. To my other collaborator Matt, I would also like to extend a big thank you. I very much enjoyed our time working together.

In addition to the people I worked with directly, I have been fortunate to meet many other smart and inspiring people from around the world. This includes my colleagues in the group of Fundamental Processes in Quantum Physics here in Hamburg – you are simply too many to list! Special mentions are due to Rohan and Zeki for an unforgettable night in Tübingen. Life at the office would also never have been complete without Ansgar and Friethjof, whose bone-dry humour always lightened the mood. Thanks are further due to Anja Cordes, whose daily efforts ensured the smooth running of our group, as well as to all the custodial staff for creating a comfortable and functional working environment.

I am extremely grateful to have belonged to the graduate school of the Centre for Ultrafast Imaging. I want to thank in particular the student representatives – including Rukan, Alessandra, Matt and Susana – for organising the summer schools which will forever remain highlights of my PhD. Thank you also to all CUI members and the h-bar team for allowing me to follow my passion in moonlighting as a pub quiz master.

Hamburg would have never come to feel quite this much like home if it weren't for the friends I made outside of the office. I'd like to say a big thank you my OG housemates Leonardo, Lei Lei, Patrizio, Jesper, Adam, Oleg and, Our Man in The Shed, Christof. You guys are actually the best! I'm also grateful to my friends Alex, Julien, René, Finnja and Sebo for all the times we have spent together. Many thanks are due to Gisa: your excellent German lessons not only helped me get comfortable with the language but also provided a much-needed sense of normality during the strange days of the pandemic.

Last, and in no way least, I give thanks to my family. You made all of this possible.

Affidavit / Eidesstattliche Versicherung

I hereby declare in lieu of an oath that I have written this dissertation myself and have not used any aids or sources other than those stated.

The written version submitted corresponds to the version on the electronic storage medium.

The dissertation has not already been accepted in the submitted or a similar form in a previous doctoral accepted or assessed as unsatisfactory in a previous doctoral procedure.

Hamburg, the 05.07.2024

Daniel Jordan BOSWORTH

Hiermit versichere ich an Eides statt, die vorliegende Dissertationsschrift selbst verfasst und keine anderen als die angegebenen Hilfsmittel und Quellen benutzt zu haben.

Die eingereichte schriftliche Fassung entspricht der auf dem elektronischen Speichermedium.

Die Dissertation wurde in der vorgelegten oder einer ähnlichen Form nicht schon einmal in einem früheren Promotionsverfahren angenommen oder als ungenügend beurteilt.

Hamburg, den 05.07.2024

Daniel Jordan BOSWORTH